PALAEOCLIMATE RECORDS CONSTRUCTED FROM SOUTHERN AUSTRALIAN MODERN, HOLOCENE AND PLEISTOCENE SPELEOTHEMS

Pauline Clare Treble

January, 2003

A thesis submitted for the degree of Doctor of Philosophy of
The Australian National University

DECLARATION

I certify that this thesis does not incorporate without acknowledgment any material previously submitted for a degree or diploma in any university: and that to the best of my knowledge and belief it does not contain any material previously published or written by another person except where due reference is made in the text.

Pauline Clare Treble, January 2003.

ACKNOWLEDGMENTS

Many people have assisted me through the course of this thesis. I am particularly indebted to those who volunteered to collect rainwater and speleothem samples with/or for me. Their time and effort given was extremely generous and I could not have completed this research without their energy and commitment. I thank Ian Houshold, Chester Shaw and Robin Wass (Parks and Wildlife Tasmania), Kevin Kiernan (Forestry Tasmania), Robyn McBeath and Stefan Eberhard (Caveworks WA), Ann Wood and Rob Kwok (CALM, WA) for access and assistance with speleothem sampling. Even for those who love being underground, I am sure I occasionally tested their enthusiasm. I particularly thank Ian for having to spend so much time with me in such small places in arduous conditions. I thank Chester Shaw, Robin Wass, Neil Tindale, Laurie Porter, Chris Morgan, Paul Sofilas, Jol Desmarchelier and authorising bodies Cape Grim BAPS and Caveworks for enthusiastically collecting rainwater samples for me. I thank Graham Farquhar, Hilary Stuart-Williams, Kim Suan Gan and Sue Wood for all their efforts to assist me in analysing these rainwater samples. I thank Prof Bill Budd for granting me access to isotopic data of the Margate rainwater samples and his encouragement and assistance in the data analysis. I thank also Pandora Hope and Nicola Telcik for providing and manipulating Reanalysis data.

The ion microprobe analysis at UCLA would not have been performed without the kind financial assistance from Mervin and Katalin Paterson (Mervin and Katalin Paterson Fellowship) and the interest and support of Prof Mark Harrison. I thank them sincerely, and also Kevin McKeegan and Marty Grove for technical support in LA.

AMS radiocarbon dating was conducted under the assistance of Keith Fifield. I thank him for access to the lab and for AMS measurements. I also thank Guaciara dos Santos for her technical teachings, friendship and wisdom.

At RSES, I thank for their technical support and patience: Joe Cali, Graham Mortimer, Lois Taylor, Charlotte Allen, Heather Scott-Gagan, Joan Cowley, Steve Eggins, Gael Watson, Les Kinsley, Damien Kelleher and Abaz Alimanovic. I particularly thank Mike Shelley for his interest in teaching students a thing or two, both with regards to technical aspects and the real world of research.

I am grateful for the supervision that I have received from many and varied people. I sincerely thank John Chappell for patiently guiding me through this project. I thank also Malcolm McCulloch, Mike Gagan, Albert Goede, Janette Lindesay and Andy Spate for supplementary but essential supervision and encouragement.

The friends that have offered support and endured woes are so numerous that I will inevitably forget to mention several. I apologise if you are not on this list: Juan Pablo Bernal, Roza Passos, Kaylene Thomas, Anna Chappell, Wolfgang Muller, Pauline English, Eleanor Dixon, Prachi Jain, Mathew Wells, Arjun Heimsath, Jol Desmarchelier, Axel Schmitt, Andrew Kiss, Chuck Magee, Geoff Hunt, Helen McGregor, Erica Hendy, Eva Calvo, Carles Pelejero, Claudia Zipfel, Julie Trotter and Rebecca Gresham. I particularly thank you if you read parts of my thesis.

Last but not ever least, I thank my extended family: Paul Rustomji, Sue Treble, Paul Treble, Leigh Toop and Percy Worsnop, for their unconditional love, encouragement, support and patience. They are pure gold.

ABSTRACT

Multiple climate proxy records of late Pleistocene, Holocene and modern-age speleothems from Tasmania and southwestern Australia are presented. The justification for investigating these speleothem records is their individual potential to test methods of speleothem palaeoclimate reconstruction. Tasmanian Pleistocene and Holocene records confirm that $\delta^{18}O$ of drip-water has changed significantly over time, and dominates the speleothem $\delta^{18}O$ signal. For the Pleistocene speleothem from north-central Tasmania, input of glacial melt-water from the Western Tiers drives this $\delta^{18}O$ record in the opposite direction to speleothem $\delta^{18}O$ records in southwestern Australia and New Zealand. This melt-water input precludes the interpretation of this Pleistocene speleothem $\delta^{18}O$ record as a palaeotemperature record.

For the 2.4-0 ka Holocene $\delta^{18}O$ record, drip-water changes are argued to be predominantly due to shifting zonal and meridional-type circulation patterns of the rain-bearing low-pressure systems of the mid-latitudes. This interpretation is based on the first climatic analyses of event-based rainfall samples, performed in this study, which identifies the intensity of the low pressure systems of the mid-latitudes as the dominant control over rainfall amount and $\delta^{18}O$ across southern Australia. The interpretation of the speleothem $\delta^{18}O$ record is supported by speleothem $\delta^{13}C$, Mg concentration and Sr isotopes, which are controlled by residence time, hence rainfall recharge, in the limestone. This record also bears the first evidence for the Little Ice Age in southern Australia, which is interpreted to be characterised by drier and likely cooler conditions between A.D.1450 and 1790.

High resolution measurement of Mg, P, U, Sr, Ba and Na using laser-ablation inductively coupled mass spectrometry (LA-ICP-MS) has revealed clearly resolvable annual cycles in a modern speleothem from southwestern Australia whose age is well-constrained by the dates of emplacement and removal of the boardwalk on which it grew (A.D.1911-1992); allowing for the first confident comparison between the instrumental climate record and speleothem proxies. Mg, P and U mimic the dramatic ~200 mm (20%) decrease seen in rainfall records experienced by this region since the A.D.1960s. This behaviour is due to Mg's sensitivity to residence time and uranyl's strong affinity for, and dependence on, the bio-production of P. Of the other trace elements, Ba and Na appear to be significantly influenced by growth rate while the effects of prior-calcite precipitation appear to be important for Sr. Unique to this study, high resolution (20 µm) ion microprobe analyses on the modern speleothem reveal ~1‰ annual cycles in speleothem $\delta^{18}O$ moving harmoniously with trace element cycles. The positive relationship between $\delta^{18}O$ and Mg cycles strengthens the interpretation of these proxies as effective hydrological indicators.

TABLE OF CONTENTS

LIST OF FIGURES

LIST OF TABLES

CHAPTER ONE

SPELEOTHEMS AS PALAEOCLIMATE RECORDERS

1.1 WHY STUDY PALAEOCLIMATOLOGY?

Beyond the comparatively short instrumental and historical climate records our knowledge of the earth's climate system is derived from proxies preserved in the geological record. The knowledge gained from palaeoclimate reconstruction is the basis of our understanding of its natural rhythms and variability. Most importantly, palaeoclimate records enable us to appreciate that the present climate state could be relatively short-lived and remind us that even in the recent past, ~A.D.1600-1860, small temperature changes significantly disrupted human lives during the so-called "Little Ice Age" (Grove, 1988). More recently, we have learned that the last glacial cycle was punctuated by numerous rapid climate switching events resulting in transitions approaching the range of full glacial-interglacial conditions (Broecker, 2000; Stuiver and Grootes, 2000).

The current climate system is inherited from earth system processes of the Cenozoic. The main climatic drivers of this period are (Zachos *et al.*, 2001):

- Plate tectonics (*e.g.* establishment of the Antarctic Circumpolar Current by the opening and reorganisation of ocean passages (Lawver and Gahagan, 1998) and the uplift of the Himalayas and the Tibetan Plateau (Kutzbach *et al.*, 1993).
- Thermohaline circulation dynamics (Dansgaard-Oeschger events; Broecker and Denton, 1989; Dansgaard *et al.*, 1993) and catastrophic ice sheet surges (Heinrich events; Bond *et al.*, 1992).
- Atmospheric CO_2 (Broccoli and Manabe, 1987; Shackleton, 2000).

Numerous additional perturbations, feedbacks and modes (*e.g.* dust, volcanic eruptions, El Nino Southern Oscillation) also exist. All of these factors overlie the ongoing but more subtle driver of the earth's climate system, that is, astronomical forcing from slow variations of planetary orbital geometry with the dominant period of eccentricity (~92 ka) and secondary periods of obliquity (40 ka) and precession (19 and 21 ka; Imbrie, 1982).

Examples of proxies used for palaeoclimate reconstruction are:

- tree-rings (ring width, stable isotopes);
- ice-cores (stable isotopes, gas inclusions, aerosol content);
- terrestrial and marine sedimentary cores (stable isotopes, faunal assemblages, alkenones, texture);
- geomorphology (lake levels indicated by shorelines, river palaeochannels, remnant glacial features); and
- corals (stable and radiogenic isotopes, trace metals, band width and fluorescence) and speleothems (stable and radiogenic isotopes, trace metals).

Broadly, the key criteria for choosing ideal material for palaeoclimate reconstruction are:

1. that modern material exists for calibration;
2. the chronology may be well constrained;
3. that the proxies are well preserved; and
4. their formation is understood.

The first criterion is that a proxy record from modern material must be calibrated to instrumental climate data. For example, tree rings readily fulfil this condition as ~100 years or so of data may be obtained from coring living trees near to a meteorological station. Part of the record can be used for calibration, for example, ring width to warm-season temperature, and the predictive power of the proxy is tested using the remainder of the record (*e.g.* Cook *et al.*, 1992).

The second criterion is that an accurate chronology can be obtained for the sample material. Chronologies may be constructed from layer counting (*e.g.* tree rings, annual layers in ice cores and varve sediments), or by radionuclides. In the later case, the accuracy of a radionuclide chronology (*e.g.* U-series, radiocarbon) depends on the precision of measurement of the isotope and its closed-system behaviour of the isotopes involved. Obtaining accurate and precise chronologies is highly important for proxy records to be compared. Only when the timing of events can be faithfully slotted together, can cause and effect be separated as climate events take hold.

The third criterion is that proxies are well preserved and that they are free from effects that may corrupt the climate signal *i.e.* contamination and diagenesis. Identifying these

later effects requires adequate criteria for assessment *e.g.* neomorphism and recrystallisation of aragonite corals (Marshall, 1983).

The fourth requirement is that the proxies are directly driven by climate processes, *i.e.* they are not filtered or influenced by non-climatic factors such as position in the landscape, and that the functional response to climatic change is known. The time-scale at which climatic patterns can be resolved ranges from seasonal to millennial, depending on the rate of accumulation of the material and the nature of its functional response.

1.2 WHY USE SPELEOTHEMS?

Speleothems are cave decorations (stalagmites, stalactites, flowstones *etc.*), the majority of which are formed from the precipitation of $CaCO_3$ from drip-water. They are slow growing (~100-1000 micrometers per year; Baker *et al.*, 1993a; Genty *et al.*, 2001) but as they are well protected by the cave, speleothems of 100's ka in age may be preserved, although they may suffer hiatuses because of aridity or glacial cover. An important feature of speleothems is that they are well-datable by U-series disequilibrium methods (Schwarcz, 1980; Ludwig *et al.*, 1992) and, as such, are one of the few terrestrial archives for which precise and accurate chronologies may be constructed.

The potential for using speleothems as palaeoclimate archives was first assessed by Hendy and Wilson (1968) who demonstrated that the oxygen isotopic composition ($\delta^{18}O_{SP}$) of a New Zealand speleothem resembled the form of the Caribbean deep-sea palaeotemperature curve covering the past 80-90 ka. Hendy and Wilson suggested that $\delta^{18}O_{SP}$ was a record of cumulative palaeotemperature effects, primarily cave temperature, but also the dew-point temperature of meteorological precipitation ($\delta^{18}O_P$). $\delta^{18}O_{SP}$ has remained the main speleothem palaeoclimate proxy; however, its interpretation has been problematic. Early studies by Schwarcz (1986); Harmon *et al.* (1978a, 1978b, 1979); Gascoyne (1992); Goede *et al.* (1986, 1990); and several later studies by Lauritzen (1995); Lauritzen and Lundberg (1999) and Desmarchelier *et al.* (2000) persisted with the notion that all $\delta^{18}O_{SP}$ variation could be largely accounted for by temperature effects (cave temperature and meteorological dew-point temperature). However, it is now recognised that other meteorological and climatic effects such as

relative humidity and moisture recycling, may significantly outweigh the dew-point temperature effect on $\delta^{18}O_P$ and thus $\delta^{18}O_{SP}$. This is demonstrated by the high-resolution Holocene records of Ku and Li (1998) and McDermott *et al.* (2001); and the long, continuous, but composite speleothem records of Bar-Matthews *et al.* (1999; 60 ka); and Wang *et al.* (2001; 75 ka). All of these records show shifts in $\delta^{18}O_{SP}$ which are most readily explained by changes in the dominant moisture sources.

In this context, the Devils Hole record from Nevada (Winograd *et al.*, 1992) is important for two reasons. Firstly, it demonstrates that precise chronologies can be obtained from speleothem U-series dates (Ludwig *et al.*, 1992) and secondly, this record indicates that orbital forcing may not be the only climate regulator. This later point is revealed by the timing of glacial terminations in the 500,000 ka record which do not conform to the orbitally tuned SPECMAP chronology (Martinson *et al.*, 1987), widely used for deep sea core records. The Devils Hole record highlights the utility of speleothems for determining the timing of major climate events as they propagate across the continents. This is important information for testing hypotheses of cause and effect relationships of climate events *e.g.* cross-correlating the effects of rapid climatic shifts (Dansgaard-Oeschger events) to improve Greenland ice core (GRIP and GISP2) chronologies (*e.g.* Spötl and Mangini, 2002) and examining the expression of these events on low-latitude regions *e.g.* Wang *et al.* (2001).

Speleothems as climate proxies will be discussed in more depth as the processes behind these are introduced below.

1.3 THE THEORY AND APPLICATIONS BEHIND SPELEOTHEMS AS PALAEOENVIRONMENTAL RECORDERS

1.3.1 Introduction

The palaeoenvironmental information derived from speleothems is primarily based on their stable isotope (Hendy and Wilson, 1968; Harmon *et al.*, 1979; Gascoyne, 1992) and trace element compositions (Gascoyne, 1983; Goede *et al.*, 1998; Roberts *et al.*,

1998; Fairchild *et al.*, 2001). Radioactive isotopes of U and C are measured for chronologies (Schwarcz, 1986; Ludwig *et al.*, 1992; Genty and Massault, 1997) but may also be used as proxy indicators of environmental factors such as soil and atmospheric carbon production and limestone dissolution activity (Genty *et al.*, 1998, Genty and Massault, 1999; Kaufman *et al.*, 1998; Beck *et al.*, 2001). Other potentially useful speleothem properties are fluid inclusion isotopic composition (Schwarcz and Yonge, 1983; Matthews *et al.*, 2000; Dennis *et al.*, 2001); organic acid fluorescence (McGarry and Baker, 2000); growth rate and histograms of dates to indicate growth frequency (Baker *et al.*, 1993a; Ayliffe *et al.*, 1998; Baker *et al.*, 1998) and growth banding (Baker *et al.*, 1993b).

This study has focussed on the interpretation of $\delta^{18}O_{SP}$ and trace elements at both the annual scale and longer periods. $\delta^{13}C_{SP}$ and Sr isotopes are also used to aid the interpretation of trace element trends over decadal to centennial scales. Radioactive isotopes of C and U were investigated solely to construct chronologies and will be reviewed and discussed separately (Chapter 3). This chapter focuses on the mechanisms of speleothem formation and the incorporation of O and C stable isotopes and trace elements into the calcite lattice.

1.3.2 Stable isotope theory

With the exception of speleothems precipitated from high-magnesium dolomite and those formed from sulphates and chlorides in arid areas, the vast majority of speleothems are precipitated as $CaCO_3$ in the rhombohedral calcite structure. Crystals may be at sub-millimetre size at the precipitation front but they gradually fuse to become centimetre scale or larger, a process known as Ostwald ripening (Morse and Casey, 1988; discussed further in Chapter 6). The stable isotopes of oxygen and carbon: ^{18}O, ^{16}O, ^{13}C and ^{12}C in speleothems have been widely used for interpreting climatic and vegetation changes. More recently, stable isotopes of Ca (^{48}Ca to ^{40}Ca) have also been investigated as archives of environmental information (De La Rocha and DePaolo, 2000; Nagler *et al*, 2000); however, recent studies have shown that metabolic effects in organically precipitated calcites are responsible for Ca fractionation (*e.g.* Eisenhauer *et al.*, 2002) and it is thus unlikely to be seen in inorganic carbonates such as speleothems. Galy *et al.*

(2002) have also shown that Mg isotopes may be measured in speleothems, although the environmental implication of this is not yet understood.

The fundamental property of isotopes of an element that results in measurable variations in their relative concentrations in a given compound such as calcite, is that isotopes differ in their mass to charge ratios and thus in physio-chemical properties such as bond strengths and diffusion rate. Lighter isotopes are more reactive owing to weaker bonding capacity (Gat, 1981a) and more rapid diffusion than their heavier counterparts (Merlivat, 1978). Consequently, lighter isotopes are concentrated in reaction products in uni-directional (non-exchange) reactions, *e.g.* evaporation (Gat, 1981b). This preferential partition of isotopes between two substances, A and B, is termed the fractionation, α_{A-B} which is defined by Equation 1.3.1 (*e.g.* Friedman and O'Neil, 1977), where R is the ratio of the heavy to the light isotope *e.g.* $^{18}O/^{16}O$.

$$\alpha_{A\text{-}B} = R_A/R_B \qquad (1.3.1)$$

The rarity of the heavier isotope (*e.g.* abundance of ^{18}O is 0.20% compared to ^{16}O, 99.76%; Holden, 1991) makes it difficult to accurately measure O and C isotopes as absolute abundances, thus they are measured as ratios and reported relative to the known ratio of a standard. Owing to the small difference between the ratio of the unknown (R_x) to that of the standard material (R_{std}), this difference is multiplied by 1000 as shown in Equation 1.3.2 and the units for this fractionation, δ_x, are expressed as parts per thousand (‰; Friedman and O'Neil, 1977).

$$\delta_x = (R_x/R_{std} - 1) * 1000 \qquad (1.3.2)$$

Chemical and physical reactions may proceed under either isotopic or kinetic equilibrium conditions. Isotopic equilibrium is attained when the forward and the reverse reaction rates for the light isotope are equal, and likewise, those for the heavy isotope are equal (R_A does not equal R_B, but $\alpha_{A\text{-}B}$ will always be constant for a given set of reaction conditions). Isotopic equilibrium is a consequence of relative bond strengths and quantum effects and thus the isotopic equilibrium constant, α, is temperature dependent (Gat, 1981a). It is this property that allows for the reaction temperature to be calculated from the measured δ of A and B (in the case of speleothems; from $\delta^{18}O_{SP}$ and drip-water

$\delta^{18}O$ ($\delta^{18}O_{DRIP}$)). This is the basis for deriving palaeotemperature data from $\delta^{18}O$ providing isotopic equilibrium conditions can be reasonably assumed. For C, the temperature dependence is small, Romanek *et al.* (1992) and thus is usually ignored.

Kinetic fractionation dominates over isotopic equilibrium if a reaction proceeds faster than required for isotopic equilibrium, since the isotopic composition of the reaction product becomes rate limited by the diffusion of species to the reactive boundary layer. Since diffusion is proportional to atomic mass, kinetic precipitation results in a higher concentration of lighter isotopes in the reaction product (Turner, 1982). For oxygen, fractionation between calcite and bicarbonate ($\alpha_{calcite\text{-}HCO_3^-}$) is smaller for equilibrium reactions than it is for kinetic reactions (Kim and O'Neil, 1997). For C, the experimental evidence is conflicting; $\alpha_{calcite\text{-}HCO_3^-}$ is argued to be smaller for equilibrium reactions by Turner (1982) and independent of precipitation rate by Romanek *et al.* (1992). For speleothems, this fractionation competes with the effects of rapid degassing which affects the fractionation between bicarbonate and CO_2 ($\alpha_{CO_{2(g)}\text{-}HCO_3^-}$) resulting in isotopically heavier calcite, as isotopically lighter CO_2 is preferentially removed from solution.

Kinetic reactions dominate precipitation of organic carbonates (*e.g.* corals, foraminifera), as here the carbonate is precipitated by a metabolic reaction and is isolated from the reactants by a membrane, inducing so called "vital effects". In this case, and within certain precipitation conditions, these vital effects can often be calibrated to temperature, salinity or light availability (McConnaughey, 1989a; 1989b). However, as speleothems are inorganic calcites, they are useful palaeoenvironmental archives only when precipitation is slow enough for isotopic equilibrium to be maintained, since the effects of kinetic reactions such as rapid degassing, can not be calibrated to environmental conditions (Hendy, 1971).

1.3.3 Trace element theory

Trace elements, those present in concentrations less than 1% (Morse and Mackenzie, 1990), such as strontium (Sr), barium (Ba), magnesium (Mg), manganese (Mn) and

uranium (U) have proven to be useful proxies for environmental conditions such as temperature and salinity in marine corals (*e.g.* Sinclair *et al.*, 1998), marine sediments (foraminifera, *e.g.* Lea *et al.*, 2000) and terrestrial aqueous sediments (*e.g.* de Deckker, 1982). The basis for palaeoenvironmental interpretation of trace elements in low-temperature, low-concentration $CaCO_3$ solutions is that divalent ions with similar ionic radius to Ca^{2+} can substitute directly for Ca^{2+} in the $CaCO_3$ lattice, where its concentration may be related to its concentration in solution, as well as temperature and pressure (Morse and Bender, 1990). However, the uptake of trace elements is a more discriminating process than for stable isotopes as the choice of one trace element over another in solution is primarily dependent on its ionic radius and affinity with HCO_3^- and CO_3^{2-}, relative to Ca^{2+}. Trace elements may also occupy non-lattice positions or lattice defect sites or be adsorbed onto the mineral surface (Veizer, 1983a).

The uptake of a foreign ion over the uptake of Ca^{2+} is defined as its partition coefficient, D. Strictly speaking, the partition coefficient of a trace element between a solid and a solution is a thermodynamically driven process and should therefore be expressed as a function of its activity coefficient ratios (Morse and Bender; 1990):

$$D = K\left[\frac{a_{Me}/a_{ca^{2+}}}{a_{MeCO_3}/a_{CaCO_3}}\right] \qquad (1.3.3)$$

where a is the activity coefficient and Me denotes the metal ion of interest.

Activity coefficients are dependent on the change in free energy due to ionic interactions, which are a function of temperature, pressure, ionic strength and concentrations of the species involved. Since for natural solutions these factors are rarely known, the partition coefficient is usually approximated by a stoichiometric but non-thermodynamic expression (here referred to as $D_{Me/Ca}$; Morse and Bender, 1990; Morse and Mackenzie, 1990):

$$D_{Me/Ca} = \frac{(m_{Me}/m_{Ca})_{solid}}{(m_{Me}/m_{Ca})_{liquid}} \qquad (1.3.4)$$

where m_{Me} and m_{Ca} are the molar concentrations of the metal and Ca^{2+}, respectively.

Similar to stable isotopes, trace element incorporation may be complicated by kinetic effects. Here Equation 1.3.3 is only equivalent to Equation 1.3.4 under equilibrium conditions. Kinetic reactions under faster precipitation rates are usually characterised by $D_{Me/Ca} >> D$ as the faster growing crystal exhibits less discrimination against foreign ions (Morse and Bender, 1990). However, natural systems and most empirical laboratory experiments rarely proceed under equilibrium conditions, and it is often not strictly possible to use empirically determined $D_{Me/Ca}$ to calculate the reaction temperature or the solution composition. Such uncertainties hamper palaeoenvironmental interpretations such as palaeotemperature, palaeosalinity *etc.* based on trace element concentration. Moreover, $D_{Me/Ca}$ of natural and simulated natural systems often deviate from ideal equilibrium behaviour because of the following (Morse and Bender, 1990):

- heterogeneities due to changing solution composition;
- recrystallisation of an initially metastable to a stable compound;
- non-lattice substitution; and
- the presence of other foreign materials (*e.g.* organic ligands) which may poison or enhance metal uptake or affect calcite growth rate.

1.3.4 The incorporation of stable isotopes and trace elements into speleothems

The incorporation of stable isotopes or trace elements into speleothem calcite may preserve environmental information, since deep cave conditions are generally sufficiently humid that speleothem precipitation reactions are slow enough for isotopic equilibrium conditions to be maintained. Potentially, the partitioning of oxygen isotopes and metals such as Mg between solid and solution are temperature dependent (McCrea, 1950; Mucci, 1987; Oomori *et al.*, 1987), and thus are potential recorders of the cave temperature, which for most caves approximates to mean annual temperature. By contrast, the partitioning of stable carbon isotopes and metals such as Sr, Ba and U may preserve information on aquifer residence time, precipitation rate and aspects of soil and vegetation above a cave (Roberts *et al.*, 1998; Hellstrom *et al.*, 1998; Fairchild *et al.*, 2001).

All speleothems used in this study are composed of calcite crystals. The mechanism of calcite precipitation is described by the following equations; where Equations 1.3.5 and 1.3.6 describe the formation of carbonic acid in the soil zone and Equation 1.3.7 is the precipitation of $CaCO_3$ from saturated drip-waters once they enter the cave. Figure 1.3.1 shows the processes of speleothem formation schematically.

$$CO_{2(g)} \Leftrightarrow CO_{2(aq)} \quad (1.3.5)$$

$$CO_{2(aq)} + H_2O \Leftrightarrow HCO_3^- + H^+ \quad (1.3.6)$$

$$H^+ + CO_3^{2-} \Leftrightarrow HCO_3^- \quad (1.3.7)$$

$$Ca^{2+} + CO_3^{2-} \Leftrightarrow CaCO_3 \quad (1.3.8)$$

Equations 1.3.5-1.3.8 are summarised as

$$Ca^{2+} + 2HCO_3^- \Leftrightarrow CaCO_3 + CO_2 + H_2O \quad (1.3.9)$$

Rain equilibrated with atmospheric $CO_{2(g)}$ falls onto the soil where a far greater amount of $CO_{2(g)}$ is added from decay of organic matter and plant-root respiration in the soil (Dorr and Munnich, 1986). The dissolved $CO_{2(g)}$ (Equation 1.3.5) acidifies the soil water by forming H^+ together with carbonate (CO_3^{2-}) and bicarbonate ions (HCO_3^-), which then percolate into the limestone dissolving carbonate and trace elements. Saturation of this solution with respect to Ca^{2+} is achieved quickly and all cave drip-waters are saturated despite the route taken (fast or slow; Fairchild *et al.*, 2000). When it reaches the cave, the solution equilibrates with the P_{CO_2} of the cave atmosphere, which is lower than P_{CO_2} in the soil, thus driving Equation 1.3.9 towards calcite precipitation, which typically occurs at entry points in the cave ceiling forming stalactites, and where solutions drips onto the cave floor forming stalagmites and flowstones (Figure 1.3.1). Trace elements for which $D_{Me/Ca}$ is less than unity, are mostly excluded from the calcite lattice, thus enriching the solution; whereas those for which $D_{Me/Ca}$ is greater than unity, are preferentially taken up, depleting the solution. Within this constraint, variation in the concentration of trace elements in $CaCO_3$ also depends on factors such as their concentration in solution, crystal growth rate and temperature.

In reality, this simplified model consists of numerous kinetic and equilibrium reactions whose cumulative history heavily determines $\delta^{18}O_{SP}$ and $\delta^{13}C_{SP}$ but have less impact on trace element concentration. These reactions can be considered in more detail by dividing the model into 3 stages of speleothem evolution. These are:

1. meteorological processes acting on water molecules as they journey from the ocean to the cave ($\delta^{18}O$ only);
2. the hydrological journey of the water through the soil and limestone where it is joined by soil CO_2; and ultimately,
3. the temperature, reaction rate and PCO_2 of the cave during calcite precipitation.

The first stage of the journey, ocean to cave, is complex as it is imprinted with processes operating in oceanic and atmospheric environments far removed both geographically and climatically from those of the cave. These processes include equilibrium and kinetic fractionation effects at every phase change experienced by a moist air mass on its journey from sea to rainfall at the cave site (Dansgaard, 1961), including sea-water $\delta^{18}O$ ($\delta^{18}O_{SW}$) enrichment due to changes in global ice volume, progressive and preferential rainout of meteoric precipitation $\delta^{18}O$ ($\delta^{18}O_P$), recycling of moist air masses from re-evaporation of water bodies and from plant-leaf respiration. Because of the potentially large variation in $\delta^{18}O_P$ and thus $\delta^{18}O$ in both drip-water and speleothem, these meteorological and physical processes will be considered in a dedicated chapter (Chapter 5).

The second stage of the journey primarily influences the drip-water $\delta^{13}C$ ($\delta^{13}C_{DRIP}$) and may further alter $\delta^{18}O_{DRIP}$. In the simplest karst system (direct and fast through-flow), $\delta^{18}O_{DRIP}$ will closely mimic the surface $\delta^{18}O_P$ annual cycle (the reservoir of O atoms in the rainwater far outweigh any subsequent contribution from soil CO_2 or limestone carbonate). However, the thicker and more porous the limestone, the greater the storage, dilution and mixing of $\delta^{18}O_P$, resulting in attenuation of this cycle.

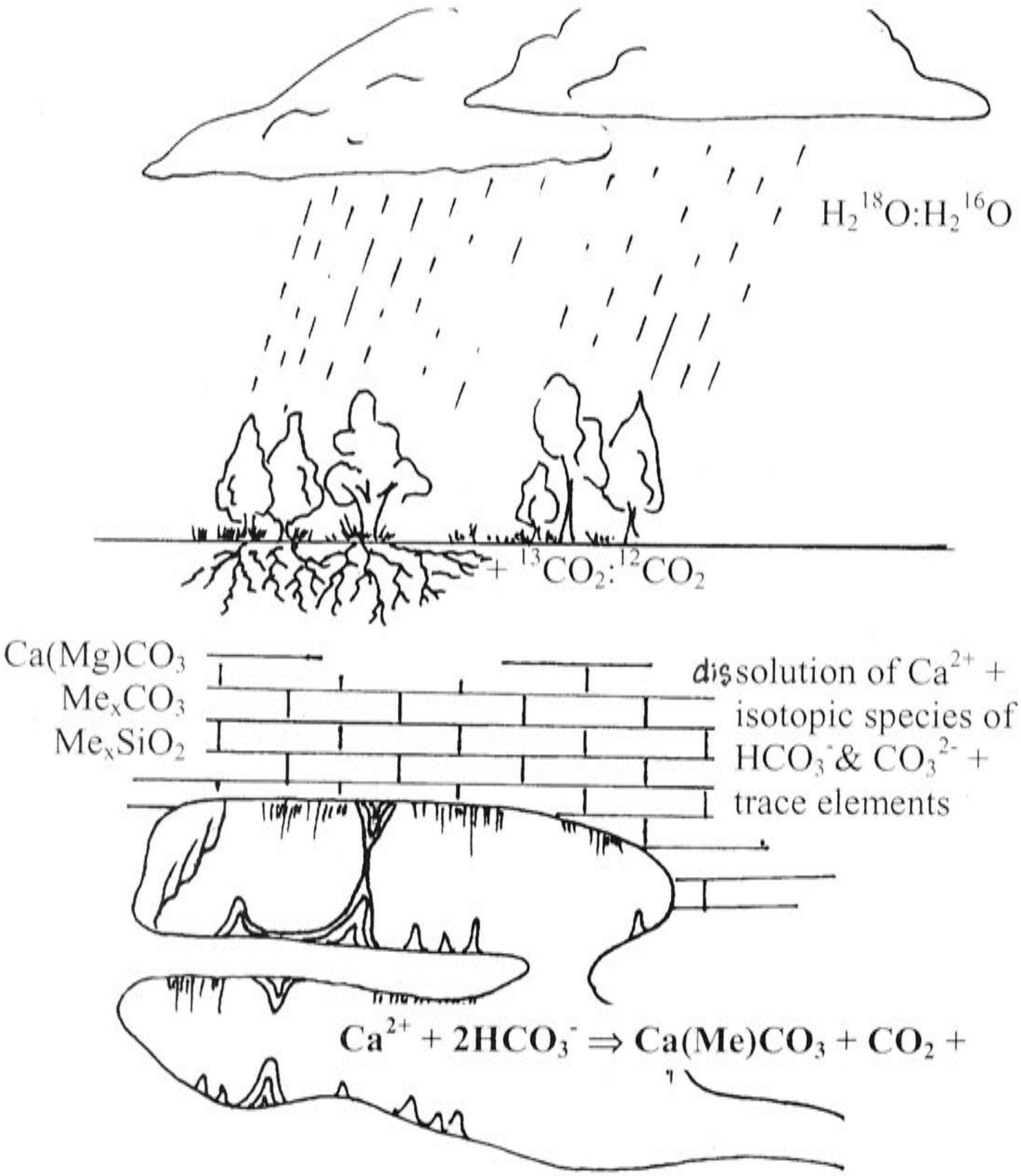

Figure 1.3.1: Schematic diagram of speleothem formation showing major reactions and species involved.

In contrast to O, there are far fewer C atoms in drip-water as their sources are limited by the contributions of atmospheric, plant-root respired and organically decomposed CO_2 ("the soil CO_2 reservoir"), and from the limestone itself, according to Equation 1.3.9 (Genty *et al.*, 2001). The $\delta^{13}C$ of plant CO_2 is determined by its photosynthetic pathway, termed C3 or C4 type (Cerling, 1984). CO_2 from plants using a C3 pathway (trees, shrubs) have a $\delta^{13}C$ of around –27.1‰, while plants using the C4 pathway (typically grasses) have an average $\delta^{13}C$ of –12.7‰. Early interpretations of $\delta^{13}C_{SP}$ proposed that it was driven by the climatically induced abundances of these vegetation types (Dreybrodt,

1980, Dorale *et al.*, 1992; Talma and Vogel, 1992). However unlike $\delta^{18}O_{SP}$, $\delta^{13}C_{SP}$ is sensitive to contribution of C atoms from the dissolution of limestone (Genty and Massault, 1997; Genty *et al.*, 2001) and consequently, is more likely to be the product of end-member mixing between soil CO_2 and the dissolved limestone. In short, the $\delta^{13}C_{SP}$ signal is heavily determined by the amount of C from limestone dissolution, which modifies any vegetation signal (*e.g.* Hellstrom *et al.*, 1998), but may be greatly corrupted by rapid degassing and prior calcite precipitation in highly karstified systems (Baker *et al.*, 1997). This effect will be exacerbated in drier periods.

Hence, $\delta^{18}O_{DRIP}$ and $\delta^{13}C_{DRIP}$ carry signatures of the rainfall $\delta^{18}O_P$ and other palaeo-hydrological information from soil/limestone interactions. Upon entering the cave (stage 3), the mechanism of calcite precipitation (equilibrium, kinetic, evaporative) may complicate the preservation of this information. Speleothems must precipitate under conditions of isotopic equilibrium for both O and C species for palaeoenvironmental information to be decipherable, which demands that the degassing of CO_2 be sufficiently slow that all species in Equations 1.3.5-1.3.8 remain at isotopic equilibrium. The rate of degassing depends on the gradient of PCO_2 between solution and cave atmosphere. This rate is greater for caves that are open to the surface atmosphere, and also for stream caves where flowing water may cause significant air movement. For these reasons, speleothems are generally only sampled from deep cave interiors where relative humidity and PCO_2 are high. Calcite precipitation driven by evaporation of the precipitating film may also cause kinetic effects (Hendy, 1971), however, this effect will be greatest for open caves where the problem of rapid degassing is more significant.

To address the question of determining whether or not a speleothem was precipitated under conditions of isotopic equilibrium, Hendy and Wilson (1968) proposed that sampling along speleothem growth layers would test for kinetic fractionation. While this test appears to be theoretically sound, in practise it is impossible to know if coeval calcite is being sampled. Hendy and Wilson (1968) also postulated that the kinetic process will result in simultaneous enrichment in both $\delta^{13}C_{SP}$ and $\delta^{18}O_{SP}$ and suggested that strongly correlated $\delta^{13}C_{SP}$ and $\delta^{18}O_{SP}$ along the growth axis would also indicate whether kinetic fractionation was present. However, this test is also not definitive as there are non-kinetic processes which may result in $\delta^{13}C_{SP}$ and $\delta^{18}O_{SP}$ being highly

correlated (Hellstrom *et al.*, 1998). However, as argued by Hellstrom (1998), these are more likely evident in the low frequency fluctuations in $\delta^{13}C_{SP}$ and $\delta^{18}O_{SP}$, while kinetic fractionation should be correlated on the highest frequency attained in high resolution sampling.

More recently, this difficult problem of testing for kinetic effects was tackled by Frisia *et al.* (2000) by distinguishing between equilibrium and kinetically precipitated speleothems by their calcite fabric appearance. They found that crystals in isotopic equilibrium with their drip-waters are characterised by columnar, fibrous columnar or microcrystalline fabrics, that had formed from slowly dripping solution with relatively low level of super-saturation. Microcrystalline calcite was considered to form under similar conditions in the presence of growth inhibitors. By contrast, crystals formed under kinetic precipitation conditions were characterised by dendritic patterns comprised of bundles of branching crystallites containing many crystal defects. These dendritic fabrics formed from fast dripping highly super-saturated waters under rapid degassing or evaporation.

Similar to stable isotopes, the partitioning of trace elements from a solution into calcite is dependent on the starting composition of the solution, and kinetic and equilibrium processes. However, in some respects, the interpretation of environmental information by trace elements in speleothems may be less fraught with uncertainties than $\delta^{18}O_{SP}$, since they are dominated by proximal sources in the overlying soil and limestone, and therefore record local environmental conditions. However, like stable isotopes, the partition of ions into calcite may be complicated by kinetic effects.

The partitioning of Mg into calcite has long been known to be temperature dependent (Katz, 1973; Mucci, 1987; Oomori *et al.*, 1987). The first investigations of speleothem trace elements by Gascoyne (1983) compared the distribution of Mg between drip-waters and calcite, and a subsequent study by Goede and Vogel (1991) examined speleothem Mg concentration over the post-glacial warming period (15-12 ka). These studies suggested that speleothem Mg/Sr could be used as a palaeothermometer, using Sr to correct for fluctuations in drip-water concentration. However, further studies by Gascoyne (1992) and Goede (1994) found that correlations between Mg and $\delta^{18}O_{SP}$, also interpreted as a temperature proxy, were low. Roberts *et al.* (1996) found further

evidence against the Mg palaeothermometer, in a high resolution study of three coeval Holocene stalagmites with different Mg/Sr records from the same cave, which indicated that any temperature effect on Mg/Sr variation was greatly overshadowed by hydrological factors. This result turned the focus of speleothem trace element research towards their use as indicators of effective precipitation (Huang *et al.*, 2001; Fairchild *et al.*, 2000).

The exploration of speleothem trace elements has been greatly advanced by improved analytical techniques (Secondary Ionisation Mass Spectrometry, SIMS; and Laser Ablation Inductively Coupled Mass Spectrometry, LA-ICP-MS). This technology led to the detection of annual cycles in trace elements (Roberts *et al.*, 1998), which would be unachievable by conventional bulk-sampling and digestion methods. Sub-annual resolution sampling of trace elements is expanding as more elements are added to the multi-proxy approach to speleothem interpretation (Huang and Fairchild, 2001; Fairchild *et al.*, 2001). The significance of these annual cycles was demonstrated by Baldini *et al.* (2002) who argue that seasonal-scale changes in Sr and P reflect changes in growth rate and rainfall during drier conditions over the 8.2 ka cold reversal.

1.3.5 Sr isotopes

^{87}Sr forms from the radioactive decay of ^{87}Rb (half life 48.8×10^9 years; Faure, 1986). The concentration of radiogenic ^{87}Sr in a mineral depends on the age and Rb/Sr ratio of that mineral. Stable isotopes of Sr; ^{88}Sr, ^{86}Sr and ^{84}Sr, also exist. For marine carbonate rocks, the ratio of the radiogenic to a stable Sr isotope *e.g.* $^{87}Sr/^{86}Sr$ gives a value representative of the seawater from which it precipitated. $^{87}Sr/^{86}Sr$ is thus a suitable tracer for groundwater studies since considerable differences of $^{87}Sr/^{86}Sr$ exist between limestones and rainwater, because the marine $^{87}Sr/^{86}Sr$ ratio has changed considerably over geologic time (Veizer *et al.*, 1983), due to variations in the input of volcanic, sialic and recycling of marine carbonate rocks (Figure 1.3.1).

Since $^{87}Sr/^{86}Sr$ is not fractionated during calcite precipitation (Faure, 1986), the $^{87}Sr/^{86}Sr$ of the speleothem directly records the $^{87}Sr/^{86}Sr$ ratio of the drip-water, which in turn, reflects the mixing between the $^{87}Sr/^{86}Sr$ of the limestone and of rainfall derived from

modern seawater. Hence, $^{87}Sr/^{86}Sr$ in speleothems may indicate residence time and thus may act as a hydrologically-linked climate proxy (Banner *et al.*, 1996; Goede *et al.*, 1998; Ayalon *et al.*, 1999; Bar-Matthews *et al.*, 1999; Verheyden *et al.*, 2000), provided the $^{87}Sr/^{86}Sr$ of the limestone is sufficiently different from modern seawater (Figure 1.3.1).

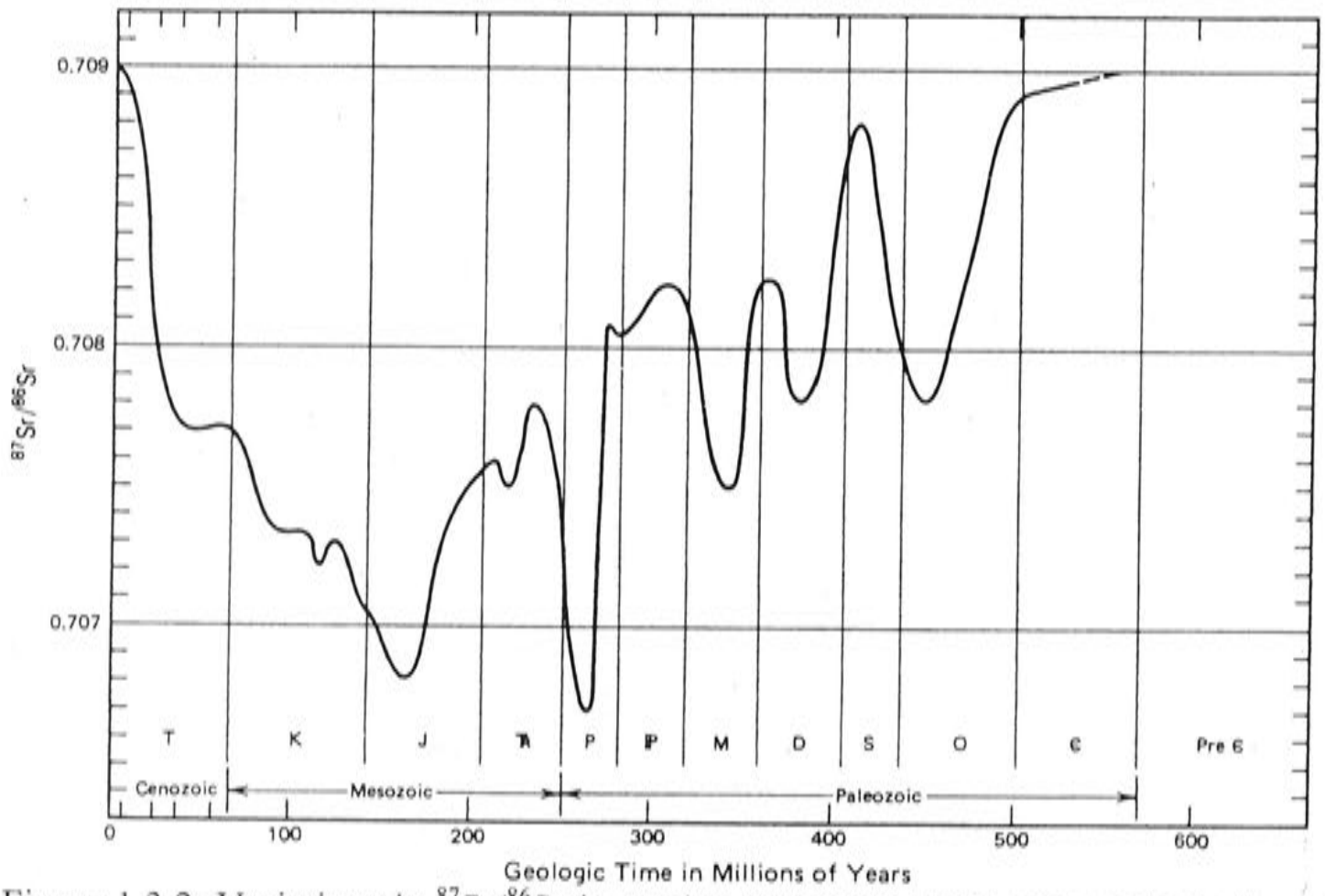

Figure 1.3.2: Variations in $^{87}Sr/^{86}Sr$ in marine carbonate rocks over geologic time. (From Faure, 1986, p. 188.)

1.4 SUMMARY

Speleothems are potentially important records of palaeoclimate proxies. The proxies most widely used in studies are:

- $\delta^{18}O_{SP}$, which carries a composite signature of global ice-volume, meteoric moist air-mass history, meteoric dew-point temperature and cave temperature; and
- $\delta^{13}C_{SP}$, which originates as $\delta^{13}C$ of soil CO_2 from plant-roots and soil organic matter decomposition, but is diluted with, and its isotopic ratio altered by limestone C atoms.

The encoding of stable isotope information in the speleothem calcite depends on the rate of calcite precipitation, which is determined by the difference between soil and cave PCO_2 and also the stability and humidity of the cave atmosphere. Thus, a number of factors influence these two stable isotopes in speleothems, and it is clear that other

information is required, if the effects of different factors are to be decoupled. Recent studies hold some promise that the interpretation of speleothem stable isotopes will be aided by trace elements, which are sourced from rainfall, soil and limestone. Although the relationships between trace elements, their isotopes (*e.g.* $^{87}Sr/^{86}Sr$), and climate is indirect, they are proving themselves to be indicators of recharge and hydrological conditions in the local environment of the cave. The strength of speleothems as proxy climate recorders lies with their well-datable, well preserved multi-proxy records which are essentially the only continuous continental climate records, and yet record information from local, regional and distant climate processes.

CHAPTER TWO

THESIS OVERVIEW AND SAMPLE DESCRIPTIONS

2.1 THESIS OVERVIEW

2.1.1 Introduction to thesis objectives

Smart *et al.* (1996) called for greater scientific rigour in the analysis and interpretation of speleothems, and made the following criticisms of much of the work that had been done previously:

- lack of appreciation for the multiple factors that control $\delta^{18}O_{SP}$;
- lack of multi-proxy and petrographic tools to categorise these factors;
- lack of climate-proxy validation using modern speleothems;
- lack of attempts to reproduce speleothem records;
- lack of appreciation of non-linear growth rate, with little attempt to select an appropriate sampling resolution to detect compressed records.

These criticisms were aimed at research conducted during the 1970's to mid-1990's where the quality of speleothem records was poor, primarily because of analytical limitations. Speleothems are slow growing and prior to the availability of micro-sampling techniques, large sample sizes (1-5 mg) were needed for stable isotope and trace element analyses, which produced coarsely sampled records which were unlikely to be representative of the true variability. The quality of the record was often further compromised by even larger sample sizes (> 5 g) needed for low precision U-series age measurements by alpha-spectrometry. However, speleothem palaeoclimate records can now be tested more rigorously, owing to the development of micro-sampling techniques and increased access to Thermal Ionisation Mass Spectrometry (TIMS) U-series measurements. More recently, advances in in-situ analyses by LA-ICP-MS and SIMS will further improve speleothem proxy climate analysis by allowing annual cycles to be resolved.

This thesis seeks to address the critical issues raised by Smart *et al.* (1996). In its conception, the initial goal of this study was to examine the potential inadequacy of

$\delta^{18}O_{SP}$ as a palaeothermometer in southern Australia, knowing that previous work had suggested that the interpretation of $\delta^{18}O_{SP}$ as a palaeothermometer is highly misleading.

Recognising that several factors affect $\delta^{18}O_{SP}$, Schwarcz (1996) introduced the term speleothem "gamma" or $\gamma = d(\delta^{18}O_{SP}/dT$; T being temperature), which he used to describe the net effect of the conflicting factors of cave temperature, which drives $\delta^{18}O_{SP}$ isotopically heavier during cooler periods, and $\delta^{18}O_P$ which becomes isotopically lighter during cooler periods. This led to speleothem records being classified as being dominated by cave temperature ($\gamma < 0$), or by meteoric precipitation temperature ($\gamma > 0$). The sign of γ at a given site can be detected over periods of known temperature change, usually by comparing Pleistocene $\delta^{18}O_{SP}$ to that of modern cave calcite. The persistent notion that $\delta^{18}O_{SP}$ could be fully accounted for by temperature effects, and the failure to find an adequate way to decouple these effects by methods such as fluid inclusion analysis, which at this time failed to prove itself as a reliable method for decoupling these effects, resulted in over-simplified interpretations of $\delta^{18}O_{SP}$ as a climate proxy recorder.

Two sets of local data highlight this problem.

1. The results of an undergraduate project by this author (Treble, unpublished Honours thesis, 1998) on a Tasmanian Holocene stalagmite (0-2 ka) found $\delta^{18}O_{SP}$ variations that were far greater than could be attributed to temperature.
2. Specimens from climatically and physiographically similar sites in Tasmania and New Zealand show opposite trends of $\delta^{18}O_{SP}$ records (positive and negative γ), bridging the Last Glacial Maximum (LGM)-Holocene transition.

The late Holocene stalagmite record, FC-S3, from the Florentine Valley, Tasmania (Figure 2.1.1) shows $\delta^{18}O_{SP}$ ranges from –3.8‰ to –4.9‰ over 1.2 ka. Tree ring data (Cook *et al.*, 1992) shows that mean temperature over this period varied by less than 1°C which can only account for 0.24‰ of the 1.1‰ variation of the FC-S3 record, which implies that FC-S3 $\delta^{18}O_{SP}$ was driven by meteorologic variations in $\delta^{18}O_P$. This has since been recognised for other records (Ku and Li, 1998; Bar-Matthews *et al.*, 1999; McDermott *et al.*, 2001; Wang *et al.*, 2001).

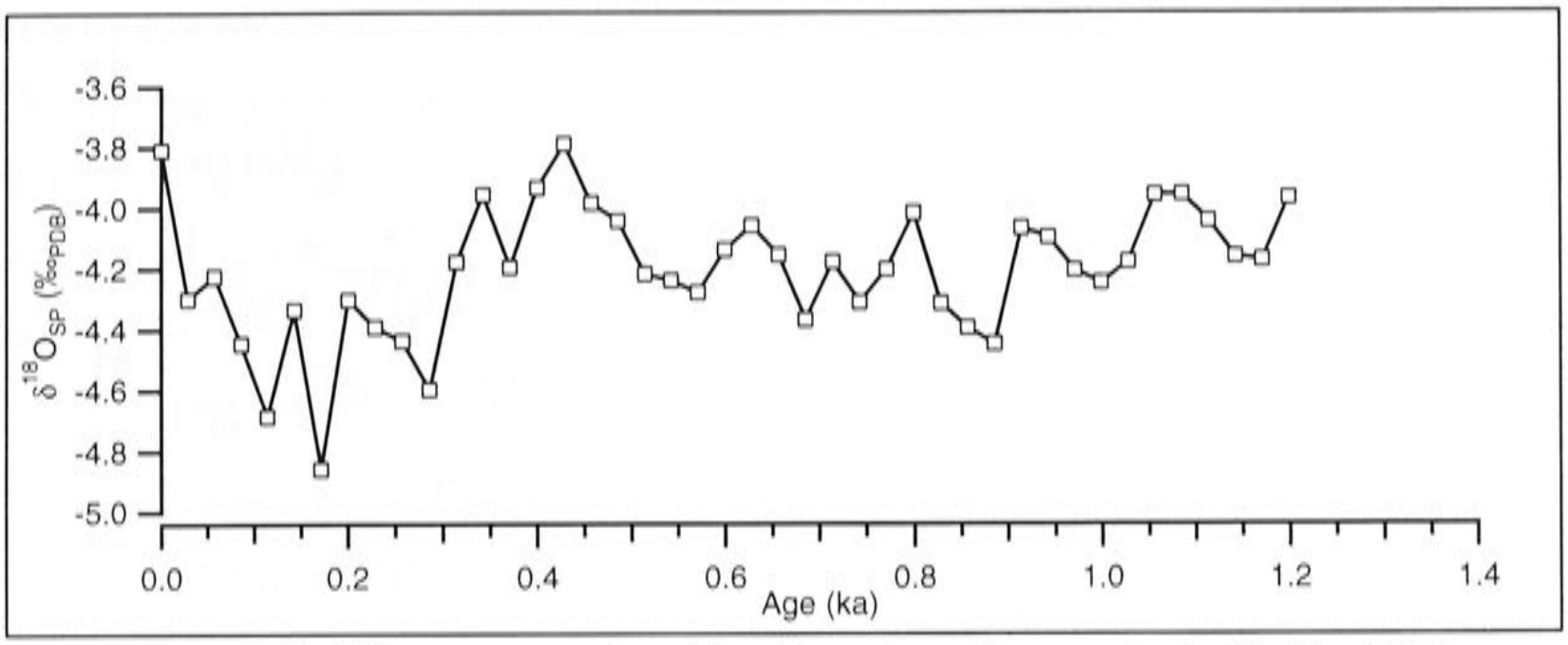

Figure 2.1.1: FC-S3 $\delta^{18}O_{SP}$ curve produced for this authors Honours thesis (Treble, 1998).

Contrasting trends (positive and negative γ) of $\delta^{18}O_{SP}$ Late Quaternary speleothems from records for the climatically similar islands of Tasmania and New Zealand (site locations shown in Figure 2.1.2) cannot simply be explained by meteoric or cave temperature effects, given the similarity of the two sites, both now and at the LGM. Both islands are located in the belt of the westerly wind-flow of the Southern Hemisphere, and speleothems (Tasmania: Goede *et al.*, 1986, 1990, 1994; New Zealand: Hellstrom *et al.*, 1998) were located on the lee-side of west-coast ranges which rise to an average height of 1000-1200 m (summit 1617 m; Tasmania) and 1400 m (summit 1509 m; New Zealand). Consequently, both sites receive winter-dominant annual rainfall of 1200-1400 mm. Each site was near to areas that were glaciated at the LGM, where comparable temperature depressions (4.5-6°C) have been estimated from glacial geomorphology (Porter, 1975; Soons, 1979; Colhoun *et al.*, 1996). It is thus incongruent that Tasmanian speleothem records are positive γ while New Zealand's are negative. Moreover, this behaviour is unlikely to be due to variation in regional rainfall trends as $\delta^{18}O_{SP}$ records from two Australian mainland sites (Buchan, -37°30', 148°09' and Naracoote, -37°02', 140°48') just 580 and 780 km from the Tasmanian sites respectively, have negative γ (Goede *et al.*, 1996; Desmarchelier *et al.*, 2000). Thus, positive γ appears to be isolated to Tasmania.

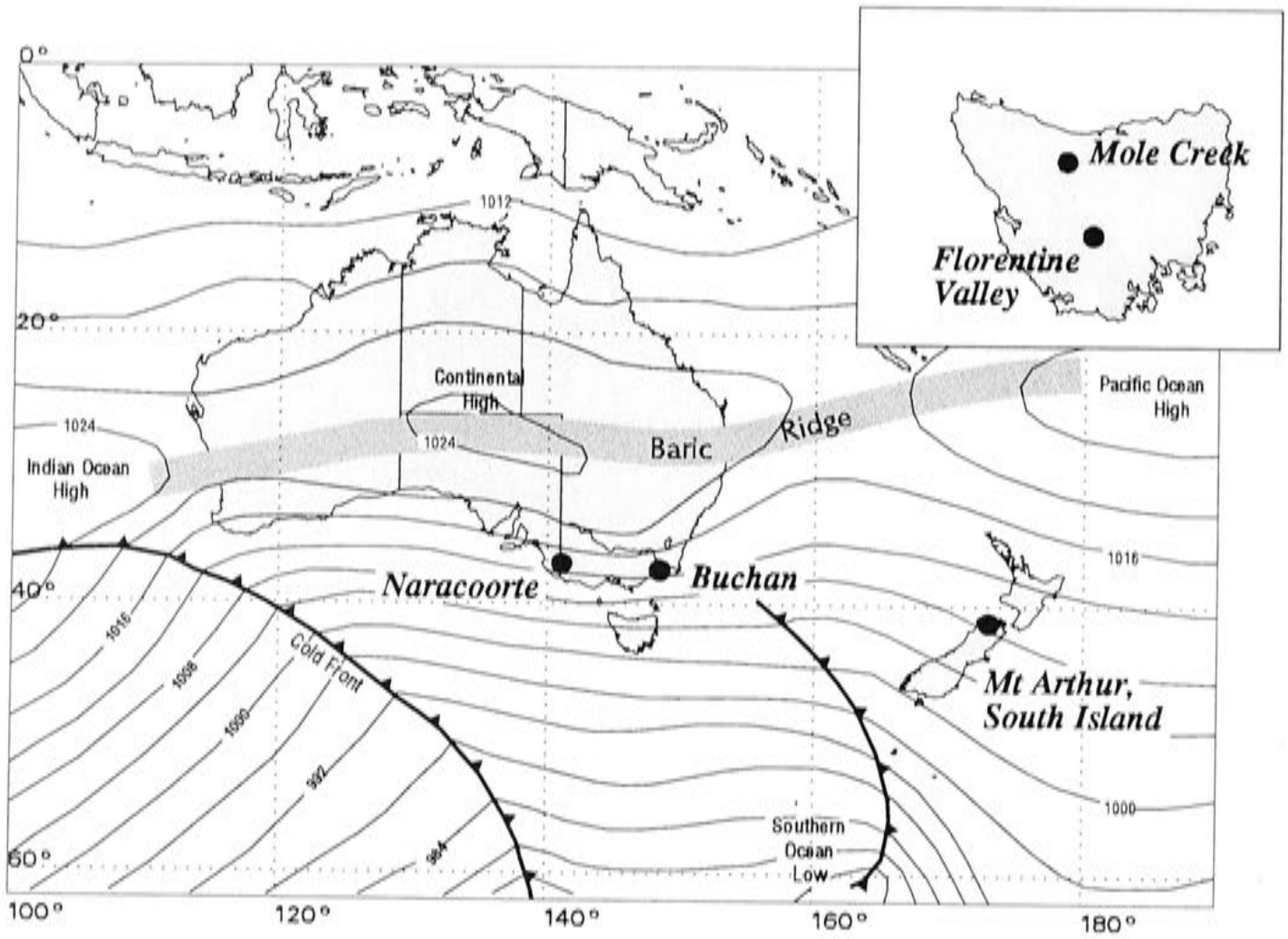

Figure 2.1.2: Site locations of speleothem $\delta^{18}O_{SP}$ records: Florentine Valley and Mole Creek (Tasmania, inset; Goede *et al.*, 1986, 1990, 1994), Mt. Arthur (South Island New Zealand; Hellstrom *et al.*, 1998), Naracoorte (Desmarchelier *et al.*, 2000) and Buchan (Goede *et al.*, 1996). Average synoptic features for Southern Hemisphere winter (Sturnam and Tapper, 1996) are shown.

2.1.2 Justification of speleothem and water sampling and outline of project

Holocene stalagmites: FC-S3 and FC-S8

The late Holocene FC-S3 $\delta^{18}O_{SP}$ record produced for this author's Honours thesis was re-sampled at a higher resolution and extended to 2.2 ka (Chapter 7). Since changes in rainfall $\delta^{18}O_P$ (rainfall amount, moisture source) was the only remaining hypothesis for the large $\delta^{18}O_{SP}$ variation seen in this record, multi-proxies (trace elements and Sr isotopes) were investigated to monitor limestone recharge and residence time. A second stalagmite (FC-S8) from the same cave was also collected to attempt to reproduce the FC-S3 record (Chapter 7). Chronologies for these records were constructed from U-series measurements (Chapter 3) and additional radiocarbon measurements were made on FC-S3 (Chapter 3).

Pleistocene flowstones: MK-F1 and ES-F1

The investigation into the conflicting behaviour of speleothem records of Tasmania and New Zealand, required confirmation that γ is definitely positive for Tasmania since this claim was based on speleothem records from periods within the last glacial cycle where independent temperature estimates for Tasmania were not available (125-55 ka and 14-0 ka), and instead the Vostok deuterium record was used as a temperature proxy (Goede, 1998; Figure 2.1.3). Thus, a speleothem covering the LGM-Holocene transition which could be directly compared with the 31 ka record from New Zealand (Hellstrom, 1998; Hellstrom *et al.*, 1998), was needed.

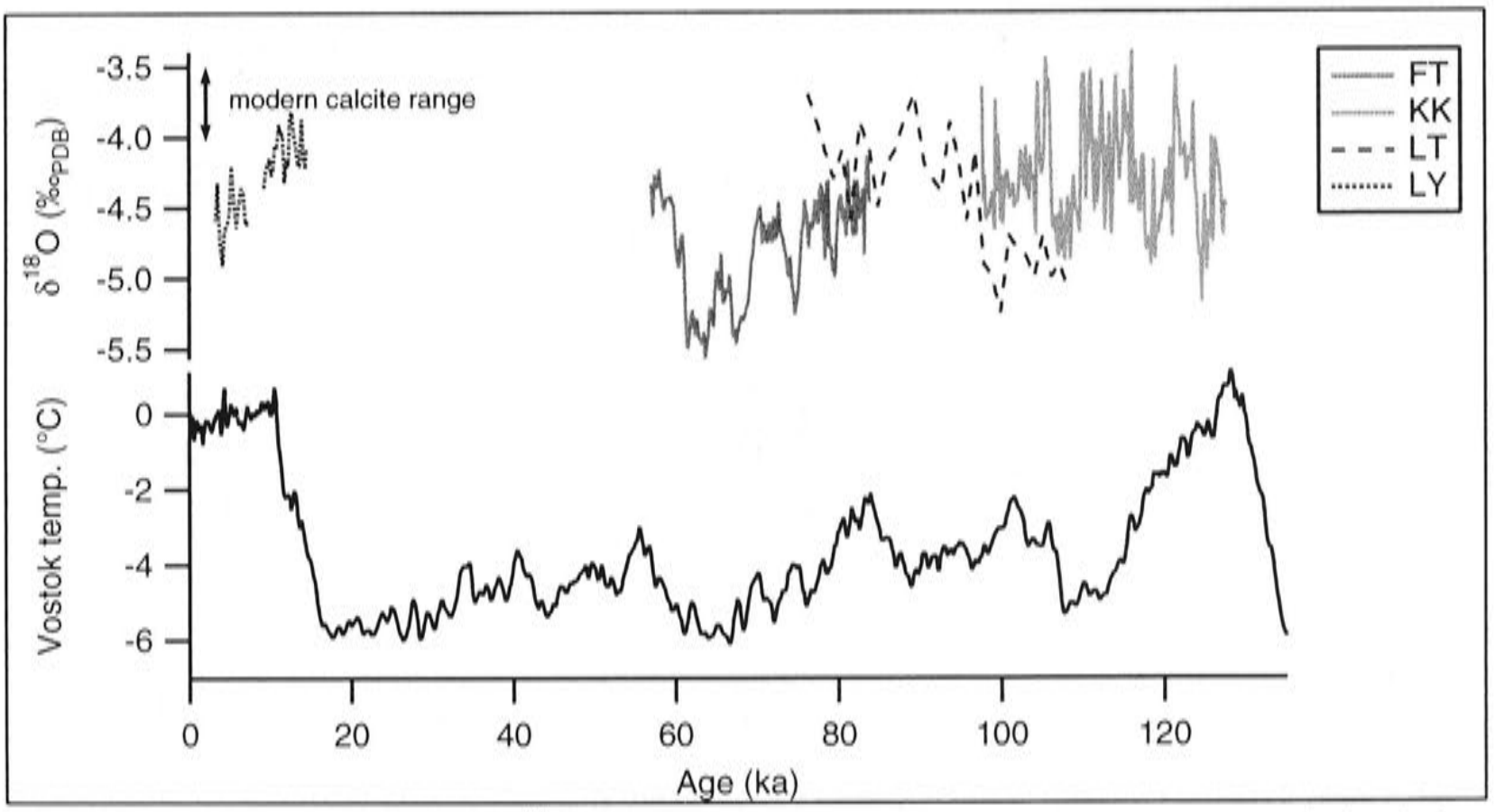

Figure 2.1.3: Trends between $\delta^{18}O_{SP}$ (Goede, 1998) and Vostok temperature derived from deuterium isotopes (Jouzel *et al.*, 1987). (Legend refers to speleothem identification codes given by Goede; details of FT appear in Goede (1994), LT in Desmarchelier and Goede (1996), KK in Goede (1998) and LY in Goede and Hitchman (1984).)

Following the preference of Hellstrom (1998), flowstone, rather than stalagmites, was chosen for sampling. This is because the probability of obtaining a near continuous speleothem record covering the last 20 ka or longer is greater for flowstone, as they are fed by multiple drips rather than a single drip source. It was originally proposed to sample flowstone from the Florentine Valley, as this site receives rainfall only from the west and is thus isolated from moisture sources from mainland Australia. However, as no suitable flowstone could be found, it was instead obtained from Marakoopa Cave (flowstone MK-F1) in the Mole Creek karst (Figures 2.1.2 and 2.1.4). This site, located

north of the Central Plateau, receives predominantly westerly wind-flow moisture, but also receives some moisture from east-coast low depressions in summer.

Flowstone ES-F1, from Margaret River karst in southwestern Australia (Figure 2.1.4), was included. The justification of including this site was that it receives the same rainfall $\delta^{18}O_P$ as Tasmania and New Zealand, but at a site that is both non-glaciated and upstream from the influence of the Australian continent. It was considered necessary to obtain this record, as obviously proximity to glacial sites may greatly influence $\delta^{18}O_{SP}$, as may the exposure of continental shelves north and west of Tasmania if the present-day shoreline was 120 m lower during the LGM (Figure 2.1.4).

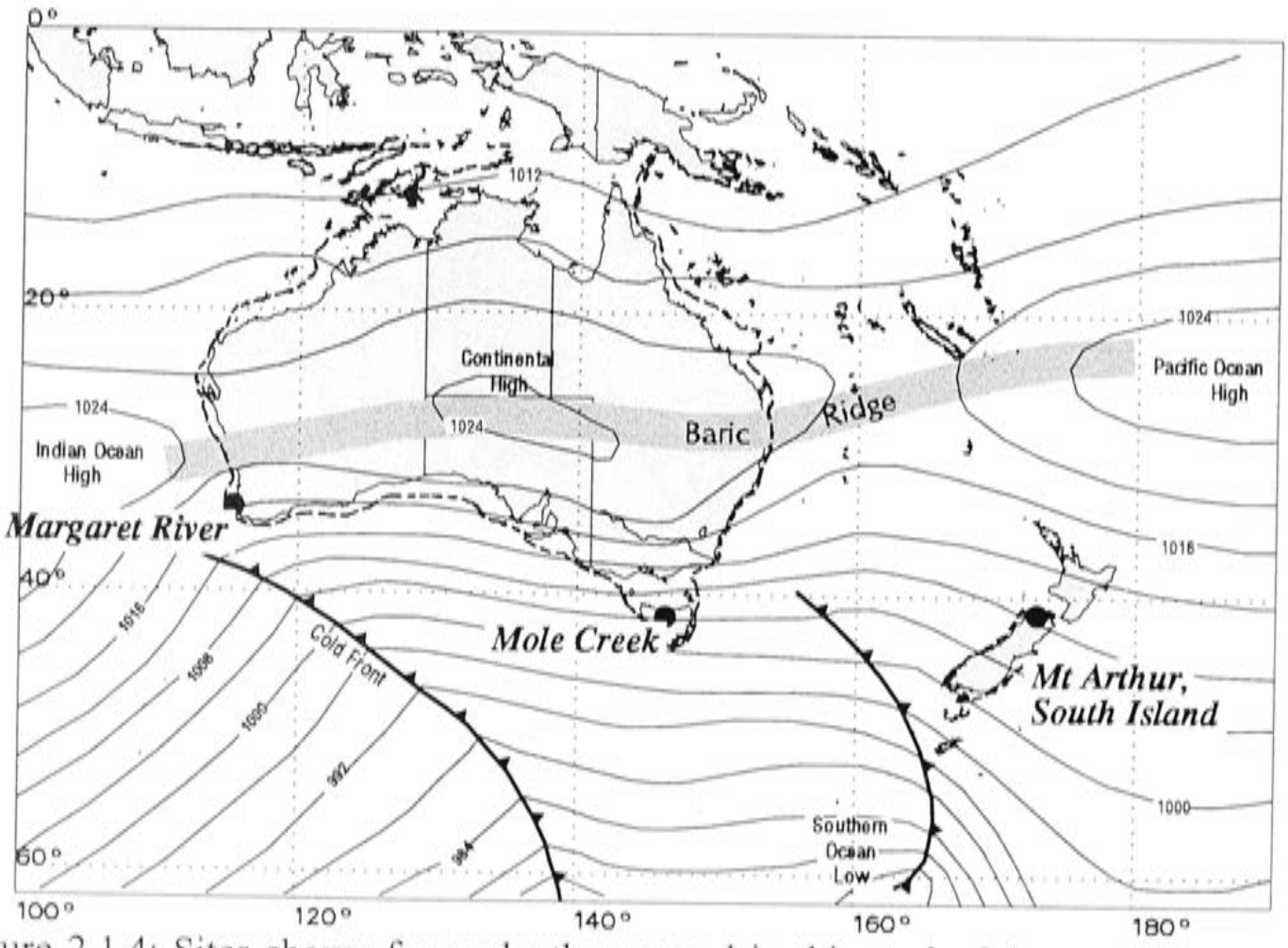

Figure 2.1.4: Sites shown for speleothems used in this study; Margaret River and Mole Creek. Mt Arthur is also shown as the record of Hellstrom *et al.*, 1998 will be used to compare with the records constructed for this study. Dashed line is 120 m isobath indicating LGM shoreline.

Modern stalagmite MND-S1

Included initially as an aside to this project, but in keeping with the main theme of speleothem climate proxy validation, a modern speleothem record from southwestern Australia, MND-S1, was also constructed. The original justification for including this stalagmite was as an appropriate test of annual trace element banding since its age was well-constrained by the date of emplacement (A.D.1911) and removal (A.D.1992) of the

tourist boardwalk on which it grew. However, it soon became apparent that it was a valuable and possibly unique specimen as its relatively fast growth rate (~350 µm/a) permitted clear resolution of annual trace element cycles and, furthermore, these cycles overlapped with instrumental climate records. This specimen also came from a non-agricultural catchment and the land above the cave had not been heavily logged or altered since European settlement. Therefore, a detailed study comparing its $\delta^{18}O_{SP}$ annual trace element cycles with the climate record was warranted.

Water samples

The key question to the Holocene and Pleistocene investigations is how much $\delta^{18}O_P$ might have changed in the past. To fully investigate all possible factors influencing $\delta^{18}O_P$, event-based rainfall samples were collected from Tasmania (Mole Creek and also sites Cape Grim and Hastings), New Zealand (Mt Arthur) and Cape Leeuwin in southwestern Australia for a period of 12 months (Figure 2.1.5).

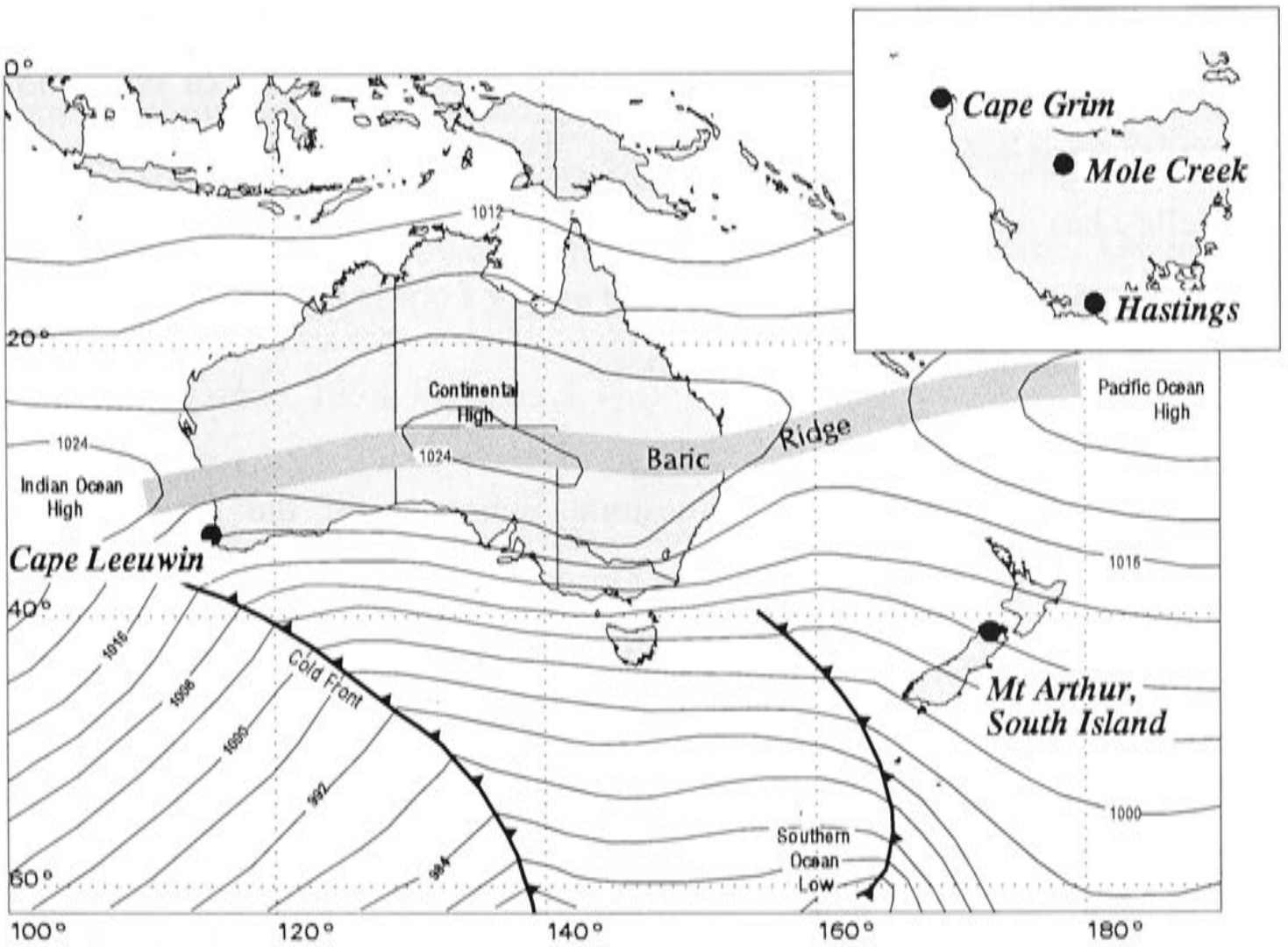

Figure 2.1.5: Sites where event-based rainfall samples were collected.

2.2 FIELD AND SPELEOTHEM SAMPLE DESCRIPTIONS

2.2.1 Tasmania

Florentine Valley (FC-S3 and FC-S8)

Stalagmite FC-S3 was sampled from the Florentine Valley located in south-central Tasmania (Figure 2.1.2) between the ranges of Mount Field West to the east, the Gordon and Tiger Ranges to the west and the Central Plateau to the north (average height of these ranges: 1200, 900 and 1000 m asl, respectively). The Florentine Valley floor itself lies at 348 m asl. 1215 mm of rainfall (BOM, 2002) is delivered to the Valley by the frontal systems of the westerly wind-flow, which are most active during winter.

The lower mountain slopes of the Florentine Valley are covered by dense, cool temperate rainforest (Kiernan, 1971), while the limestone valley floor carries eucalypt forest and sedgeland (Gilbert, 1958), which may owe its existence to regeneration fires after logging. Alpine humus soils developed on the dolerite mountains on the eastern border of the Florentine Valley, consist of dolerite clasts in a matrix of sand and clay developed under periglacial conditions (Wilson, 1990). The impure limestone of the Florentine Valley has weathered to produce a deep yellow podsolic soil (Gilbert, 1958), although the current soil cover over much of the valley floor is highly skeletal, owing to erosion following logging and burning operations.

Caves have formed in the Gordon Limestone Subgroup of the Junee Group of Ordovician and Siluro-Devionian rocks. The Gordon Limestone itself consists of three formations of Middle to Late Ordovician age (Corbett and Banks, 1974). Two of these formations, the Cashions Creek and Benjamin Limestone outcrop in the Florentine Valley. Frankcombe Cave (-42°32', 146°27') is developed in the Benjamin Limestone which overlies the dolomitic Cashions Creek Limestone. A perennial stream sinks on the eastern side of the Cashions Creek Limestone and reappears inside Frankcombe's Cave (Kiernan, 1971). The streamway is active for the first 150 m, while a further 200 m of streamway is only activated during floods.

Frankcombe Cave itself is a horizontal stream system approximately 900 m long with several upper relict passages and many short, blind side passages (Kiernan, 1971). The

entrance to the cave is through a collapsed doline; no other entrance has been discovered. Stalagmite FC-S3 was collected by colleague J. Desmarchelier on the 26th February 1996, approximately 300 m into the cave. It appears that FC-S3 is the top of a longer stalagmite (not located) that had been broken and washed downstream to be deposited in the inactive streamway when it was found. The streamway itself is mostly devoid of decoration, so it is likely that FC-S3 grew in one of the numerous side blind passages where the air appears to be still. A temperature logger placed in one of these pockets reveal a constant annual temperature of 8.25°C.

FC-S3 is 168 mm tall and characterised by easily distinguishable, fine laminae (approximately 600-1000 μm wide) of alternating white and cream to translucent yellow bands. These bands are sub-horizontal and distinguishable to the very edge of the stalagmite until they taper downwards and pinch out. Closer inspection of these bands under a microscope reveal that the prominent banding is due to the crystal structure of small needle-like palisades of translucent white crystals alternating with much larger, yellow translucent crystals. The layers show one probable change in drip-point location, and some minor episodes of re-dissolution are indicated by solution holes between 31-49 mm and 86-103 mm above the base. The calcite also becomes more translucent 95 mm above the base accompanied by an increase in the laminae thickness. The top 55 mm of this stalagmite was analysed for stable isotopes as part of an unpublished Honours thesis by this author (Treble, 1998; Figure 2.1.1).

Stalagmite FC-S8 is 410 mm tall and characterised by frosty-white small crystals (microcrystalline in places) at its core, which grade to translucent large crystals at its flanks. Some banding is evident, both in the core and extending over the flanks, as translucent to white transitions. These layers are sub-horizontal until they taper over the edges. FC-S8 was collected by this author on 2nd May 1999 under a permit issued by Forestry Tasmania. It was active when collected and growing on a small ledge above, but still within the passage of the streamway. Some solution holes are evident predominantly within the basal 60 mm but also intermittently above this.

Mole Creek (MK-F1)

The Mole Creek karst (Figure 2.1.2) lies immediately to the north of the Central Plateau and the Great Western Tiers, which rise to an average height of 1000 and 1200 m

respectively. The township of Mole Creek lies at 460 m asl although the caves which have developed in the Gordon Limestone, described above, may be about 100 m above or below this elevation. Glacial till has been deposited at many sites in the region during the Quaternary; however, the furthest reach of the nearest LGM glacier (Mersey Valley) is not well-known, but may have been as close as ~15 km from Marakoopa and Lynds Caves (Colhoun *et al.*, 1996). Yearly rainfall reaches a maximum of 962 mm recorded at the nearest station of Deloraine (-41°31', 146°39') and is delivered predominantly from the west as fronts in the westerly wind-flow but also from the east as east-coast depressions.

Marakoopa Cave (-41°35', 146°17') is a branched stream cave generally referred to as Marakoopa 1 and Marakoopa 2. Marakoopa 1 operates as a tourist cave, while Marakoopa 2 is a limited access cave. Marakoopa 2 is a 360 m long stream cave with its main entry via Marakoopa 1 cut-off each winter by a flooded sump. There are apparently three other entrances to Marakoopa 2 (Mathews, 1985), although they are not used as they are very small in cross-section.

A flowstone core (MK-F1) was drilled at the end of a blind passageway approximately 50 m from the main stream passage under the supervision of Mr Ian Houshold of National Parks and Wildlife. The site of coring was in a smaller side-pocket of this passageway underneath numerous straw stalactites emerging from the ceiling approximately 0.7 m above the flowstone surface. The flowstone itself continues several tens of metres down the passageway towards the junction with the stream passageway. The core is 685 mm long and 65 mm in diameter. It consists of mostly large crystals occasionally interrupted by flaky calcite intermingled with layers of small (1-2 mm) calcite-covered sediment.

This flowstone was selected because of its position deep within the cave and away from air movement created along streamways, but also because its appearance at the surface, which was of translucent, allogenic-mineral free calcite. Unfortunately, it became clear when it was cored, that this allogenic-free calcite only existed as a thin capping approximately 10 mm thick overlying calcite contaminated with fine clay particles giving MK-F1 an overall pale greyish-pink colour. This allogenic contamination compromised its suitability for U-series dating, however since considerable effort was

invested in obtaining this core it was still used as part of this thesis. Radiocarbon dates corrected for dead carbon proportion are used as a chronology for the stable isotope record. A temperature logger at this site revealed a constant temperature of 8.0°C.

Lynds Cave (LY)

Lynds Cave (-41°34', 146°13') is large stream outflow cave with over 1 km of streamway passage (Mathews, 1985). A stalagmite LY was removed by Dr Albert Goede in the early 1980's. The stalagmite was found lying broken in the streamway but its base was located on the floor of a large aven above the streamway known as the "Ballroom" where airflow was still compared with that in the main stream passageway. A temperature logger at this site revealed an annual temperature range of 8.3-8.9°C with the cave temperature cycle lagging the surface temperature cycle by approximately 2 months. This stalagmite appears in Goede and Hitchman (1984) and Goede (1998: unpublished thesis). Unpublished results of A. Goede's are used in this thesis to compare with the stable isotope record of MK-F1 (Chapter 8). U-series dates have been performed by this author which appear in Chapter 3.

2.2.2 Southwestern Australia

The caves of southwestern Australia lie in the Leeuwin-Naturalist ridge which formed from layers of aeolianite and calcarenite deposited during the high and low sea-level stands of the Late Quaternary. Ages derived for sequences further north (Rottnest Island and adjacent mainland) indicate that deposition began in the Mid-Pleistocene and was still active during substage 5e and the LGM (Stirling *et al.*, 1995; 1998; Price *et al.*, 2001). The sandy-lime soils above the caves support Karri (eucalypt) forest with often dense understoreys of vegetation.

Mean annual temperature for the region is 15.1°C, ranging from 20.0°C in summer to 10.3°C in winter (Manjimup station; BOM, 2002). Rainfall is delivered to this region by the frontal systems embedded in the westerly-wind circulation with the highest rainfall (*e.g.* June 171.5 mm) occurring with the northern most expansion of the westerly-wind zone in the winter months. By contrast, summers are generally dry (*e.g.* January 10.3 mm) when the westerly-wind zone migrates south of the West Australian coast. Overall,

current mean annual rainfall is 795 mm although this is 20% less than for the period A.D.1901-1965 when the average mean annual rainfall was 1011 mm. This decline has prompted a number of investigations into the variability and meteorological behaviour of southwestern Australia's rainfall (Nicholls and Lavery, 1992; Ansell *et al.*, 2000; IOCI, 1999; Smith *et al.*, 2000). Consequently, a high quality data set for rainfall trends has been constructed for this region (Lavery *et al.*, 1992) and will be used to compare with the modern speleothem climate proxy record (MND-S1).

Easter Cave (ES-F1)

Flowstone material was sampled from Easter Cave (-34° 16', 115° 06') under the permission of tourism operator, Caveworks. Easter Cave is a limited access, well-decorated large phreatic cave extending 7655 m underneath approximately 20 m of calcarenite. It is accessed by a pot-hole entrance. No major streams exist in Easter Cave, although it contains intermittent standing and flowing water in sections. Moondyne is a much smaller sink-hole cave system extending 270 m beneath approximately 20 m of calcarenite. Both caves are possibly subject to cold air drainage during the winter months; however, temperature loggers placed at the sites of sample removal reveal a seasonal temperature range of 16.5-16.8° for Easter and 15.9-16.5°C for Moondyne Cave, with the cave temperature cycle lagging that of the surface by ~2 months.

A block of flowstone, ES-F1 of approximate dimensions 200 mm tall by 180×150 mm was removed from the top of a sequence of massive flowstone (~2 m tall) at the junction of passages known as the "Epstein Passage" with the "Main Drag", located 100 m from the entrance. The flowstone sequence had been previously exposed by a large crack formed, presumably, when sediments supporting the flowstone compacted under its weight or were undermined. This flowstone was fed directly from a massive collection of straw stalactites emerging from the cave ceiling which was approximately 2 m from the top surface of the flowstone. This modern surface appeared to still be active at collection, however, the block removed for sampling had separated from, and was no longer in contact with the growing surface. Since the calcite that had been deposited after the cracking was relatively thin (several cm's), then the youngest surface of the block removed was unlikely to be older than late Holocene. No attempt was made to core the entire sequence through the modern surface as this would have been extremely

difficult due to the height and limited space between the modern surface and the ceiling, and may have damaged the formation.

ES-F1 consists of finely laminated translucent yellow bands approximately 1-3 mm thick, interrupted by occasional phases of opaque white microcrystalline fabric. It is free of allogenic minerals apart from one fine layer of red-brown sediment 11 mm from its base, which probably marks a hiatus given that it appears to mark an unconformity between the yellow bands described above it and the distinctly different white mono-crystalline fabric below it.

Moondyne Cave (MND-S1)

A small stalagmite, MND-S1 (33 mm tall) from Moondyne Cave (-34° 16', 115° 05') was chosen because the absolute maximum and minimum ages of this sample are constrained by the date of emplacement and subsequent removal, of a tourist boardwalk upon which it grew. Historical evidence (Hatcher, 1995) indicate this cave was first opened for tourism in A.D.1911 and it has been assumed that the wooden boardwalk was installed just prior to this date. Cave tours ceased in 1959 but MND-S1 remained on the boardwalk in the cave until 1992 when the cave underwent restoration.

This stalagmite was collected still attached to this boardwalk, although some material (~0.5 to 1 mm) was lost when it was removed from the wood. This was unavoidable as the initial calcite deposited had smeared and soaked into, and around, the soft outer fibres of the wood. The calcite consists of several large crystals, white to translucent in colour, and apart from some staining which is isolated to the surface contacting the wood, is free of allogenic contamination. Some layering is just visible, but there are too few visible layers to be considered annual.

CHAPTER THREE

U-SERIES DISEQUILIBRIUM AND RADIOCARBON AGE MEASUREMENTS

3.1 INTRODUCTION

Chronologies constructed for the speleothems used in this study consist of U-series and radiocarbon age measurements. U-series methods have the potential for producing precise and accurate age measurements for speleothems, as in general, they consist of a pure $CaCO_3$ matrix that remains closed to radionuclide migration (*e.g.* Schwarcz, 1980; Ludwig *et al.*, 1992). Radiocarbon age measurements of speleothems by comparison, are far less accurate owing to the variable dilution of ^{14}C atoms by the addition of ^{14}C-free limestone C to the drip-water. However, radiocarbon age measurements were included here for two reasons. Firstly, because technical delays were experienced in obtaining U-series measurements using the Finnigan Triton which was being installed at RSES during the course of this thesis research (U-series measurements on the existing Finnigan MAT261 proved difficult due to the very low U concentrations of the samples). To obtain preliminary chronologies for stable isotope and trace element records, radiocarbon age measurements by conventional counting techniques were employed. Secondly, radiocarbon age measurements by accelerator mass spectrometry techniques (AMS) were used to constrain the topmost age of a stalagmite (FC-S3) that was very low in ^{230}Th. This is because modern-age samples (< A.D.1950) have not yet generated sufficient ^{230}Th to be precisely dated by U-series.

Table 3.1.1 below summarises the details of and method employed for each age measurement. No age measurements were performed for MND-S1 as its chronology is constrained by the dates of emplacement and removal of the tourist boardwalk on which it grew. Further details and chronological methods of MND-S1 are shown in Chapter 6.

Table 3.1.1: Age measurement location and method used. (*Locations in brackets for FC-S3 1D-9D are shown as distance below tip also.)

Site	Speleothem	Samples	Distance above base* (mm)	TIMS U-series	Conventional ^{14}C	AMS ^{14}C
Tasmanian sites						
Frankcombe Cave	FC-S3	U1	13	✓		
		U2	165	✓		
		9D	163.75 (4.25)			✓
		8D	164.25 (3.75)			✓
		7D	164.75 (3.25)			✓
		6D	165.25 (2.75)			✓
		5D	165.75 (2.25)			✓
		4D	166.25 (1.75)			✓
		3D	166.75 (1.25)			✓
		2D	167.25 (0.75)			✓
		1D	167.75 (0.25)			✓
	FC-STRAW	1	(1.5)			✓
	FC-S8	U1	5	✓		
Lynds Cave	LY	U1	28	✓		
		U2	2320	✓		
Marakoopa Cave	MK-F1	TOP	425		✓	
		MID	245		✓	
		BASE	105		✓	
Southwestern Australia sites						
Easter Cave	ES-F1	U1	190	✓		
		U1A	192		✓	
		U2	110		✓	
		U4	111	✓		
		U6	20	✓		
Moondyne Cave	MND-S1	historical age control				

3.2 U-SERIES DISEQUILIBRIUM DATING

3.2.1 Introduction to ^{238}U-series decay

Naturally occurring radioactive isotopes of uranium (U) and thorium (Th) include ^{238}U, ^{235}U, ^{234}U, ^{234}Th, ^{232}Th and ^{230}Th. ^{238}U, ^{235}U and ^{232}Th have half lives greater than 10^8 years and are primary constituents of the earth. ^{234}U is a decay product of ^{238}U, with a half life of 2.45×10^5 years and is the parent of ^{230}Th, which has a half life of 7.54×10^4 years. If a rock containing ^{238}U were undisturbed for more than 1.6 Ma then equilibrium would exist between ^{238}U and its daughter products such that the activity ratio $^{230}Th/^{234}U = 1$ (Gascoyne, 1992). But if the system were disturbed by chemical removal of U, then the system would be in disequilibrium until sufficient time had passed for ^{230}Th and its

daughters to form (and hence re-establish equilibrium) by decay of ^{234}U and ^{238}U (Ivanovich, 1982). Since the half lives (and hence decay constants) of ^{238}U and its daughters are known, the ratio of $^{230}Th/^{234}U$ provides a measure of the time elapsed since the system was disturbed. This is the basis of age determination of deposits using U and Th isotopes, and is one method of U-series disequilibrium decay, termed Th/U dating.

3.2.2 U-series disequilibrium dating of speleothems

The U source for speleothems may be any U-bearing rocks or minerals which the groundwater comes into contact with before it precipitates. Limestone contains around 2 $\mu g\ g^{-1}$ of U (though there is considerable variation around this value) and virtually no Th, though Th may be present in the allogenic component of the limestone as clays and heavy minerals (Gascoyne, 1982). Other sedimentary rocks such as organic rich shales and marine phosphates may have U concentrations up to 1200 $\mu g\ g^{-1}$ (with negligible Th) while silicic igneous rocks typically contain both U (2.2 - 6.1 $\mu g\ g^{-1}$) and Th (8 - 33 $\mu g\ g^{-1}$). The U and Th concentration of metamorphic rocks varies depending on the initial rock composition and the grade of metamorphism (Gascoyne, 1982).

Due to the greatly differing solubilities of U and Th (Th is virtually insoluble), speleothems are in a state of U-series disequilibrium when they are initially formed. Groundwater percolates through the regolith and bedrock over the cave, but since U is soluble while Th is insoluble in most freshwaters, it is considered that no significant Th from the U source in the regolith and bedrock is carried by the groundwater. Since speleothems are precipitated from these groundwaters, only U and no Th is deposited in the speleothem calcite, which effectively resets the $^{230}Th/^{234}U$ clock to zero (Gascoyne and Schwarcz, 1982). Providing that the speleothem remains closed to radionuclide migration, the activity ratio $^{230}Th/^{234}U$ provides a measure of the time since the calcite was precipitated and of the age of the speleothem.

Theoretically, U-series disequilibrium dating may be used to date samples in the range 1 to 600 000 years old if closed system conditions exist. Closed system conditions ensure that changes in the abundance of U and Th isotopes result only from radioactive decay and may be assumed if there is no evidence of the following:

- weathering;
- recrystallisation;
- secondary mineral formation.

Such features are the result of post-depositional alterations, which can cause radionuclide migration (Gascoyne, 1978) that can occur through the preferential leaching of U, causing the measured Th/U ratio to be misleadingly high, and making the apparent age older. The ratio $^{234}U/^{238}U$ at time of mineral deposition, which is used as a quality control test for closed system conditions in corals since the $^{234}U/^{238}U$ ratio of seawater has not changed by more than several per mil over the last several hundreds of thousands of years (Henderson, 2002), can not be used to assess post-depositional alteration in speleothems since the $^{234}U/^{238}U$ ratio of groundwater varies greatly in time and space and is also dependent on the varying pathways undergone by the source waters, soil redox conditions and limestone residence time (*e.g.* Kaufman *et al.*, 1998; Hellstrom and McCulloch, 2000). In the case of speleothems, stratigraphic age consistency along the speleothem growth axis is a broad test for post-depositional alteration. Secondary mineralisation revealed by thin section analysis of calcite may also indicate open systems.

Allogenic contamination can corrupt dates by introducing Th and/or U from carbonate (the limestone) or non-carbonates (silicates and oxides). Because these sources differ greatly in their U and Th content and age, the effect produced by their incorporation is unpredictable. This unpredictability is further complicated by the fact that preferential leaching of either U or Th from non-carbonates differs greatly between materials depending on their chemical properties and those of the leaching solution. Allogenic contamination may be indicated by high ^{232}Th values, which is not a product of the ^{238}U radioactive decay. Therefore, high values of ^{232}Th (or low $^{230}Th/^{232}Th$ since the degree of contamination is relative to the ^{230}Th accumulated from U decay in the pure carbonate component) suggests that Th and U have been introduced into the system by allogenic material. Kaufman *et al.* (1998) suggest that the threshold value for ages needing to be corrected for allogenic contamination should lie $\sim ^{230}Th/^{232}Th < 30$, although this value is debated *e.g.* Ludwig and Paces (2002) show allogenic corrections for samples with $[^{230}Th_{SA}/^{232}Th_{SA}]_{activity} > 10$ are small.

The ratio $^{230}Th/^{238}U$ and $^{234}U/^{238}U$, the later expressed in per mil deviation from secular equilibrium, $\delta^{234}_{(0)}$, '0' indicating the ratio at time of measurement, can be used for calculating U-series ages. The decay constants (the rate of decay) of ^{230}Th and ^{234}U (λ_{230} and λ_{234} respectively) are known, and the time elapsed (t) since the calcite was deposited may be calculated iteratively using Equation 3.2.1:

$$1-\left[\frac{^{230}Th}{^{238}U}\right] = e^{-\lambda_{230}T} - \frac{\delta^{234}U_0}{1000} \times \left(\frac{\lambda_{230}}{\lambda_{230}-\lambda_{234}}\right)\left(1-e^{(\lambda_{234}-\lambda_{230})T}\right) \qquad (3.2.1)$$

where square brackets indicate activity ratios. The activity of a sample is the number of disintegrations per unit time which were the units used when ages were measured by alpha-spectrometry. Ages determined by mass spectrometry convert atomic ratios to activity ratios using λ, shown in Equation 3.2.2 for $[^{230}Th/^{238}U]$:

$$\left[\frac{^{230}Th}{^{238}U}\right] = \frac{^{230}Th}{^{238}U} \times \frac{\lambda_{230}}{\lambda_{238}} \qquad (3.2.2)$$

In addition, $\delta^{234}U_T$, which is the $^{234}U/^{238}U$ ratio corrected for the time elapsed between disequilibrium and measurement, is calculated using:

$$\delta^{234}U_T = \delta^{234}U_0 e^{\lambda_{234}T} \qquad (3.2.3)$$

3.3 METHOD OF U-SERIES DATING

3.3.1 Sample preparation

Samples weighing approximately 5 g or less (aiming for at least 100 ng of ^{238}U) were cut using a diamond blade saw and/or a dental burr. The samples were etched in 5% v/v HCl and then ultrasonically cleaned using alternate washes of acetone and supra-pure H_2O (H_2O with a resistance not less than 18 MΩ/cm, hereafter referred to as MQ H_2O) to remove any surface contaminants.

Initially, organic material was destroyed by firing samples at 800°C for 4 hours. However, Bischoff and Fitzpatrick (1991) concluded that firing increases ^{232}Th and also ^{230}Th that is leached from allogenic minerals, possibly influenced by the amount of

allogenic aluminosilicates which are converted to more soluble calcium-metasilicates when heated. Hence, for most samples the removal of organic material was done by treatment with H_2O_2 after sample dissolution. Samples that were fired are indicated in Table 3.4.1 but were not repeated, as they are not critical measurements for this thesis.

3.3.2 Chemical separation of U and Th

Spike preparation

A spike containing calibrated concentrations of ^{229}Th, ^{230}Th, ^{233}U, ^{234}U, ^{235}U and ^{238}U was added to each sample so that U and Th yields could be determined after mass spectrometry. The amount of spike used for each sample was calculated according to the mass and U concentration of the sample with $^{233}U_{SPIKE}/^{235}U_{SPIKE+SA}$ (where subscript SA indicates sample) between 0.1 and 1.0. Samples less than 100 ppb generally had ratios of 0.5 to 1.0. The U concentration of the samples were determined prior to spiking by measuring the concentration of ^{238}U using solution inductively-coupled plasma mass spectrometry (ICP-MS) by direct calibration.

U and Th separation

The sample was dissolved by the step-wise addition of concentrated HNO_3 after which the was spike added. The solution was refluxed with H_2O_2 to oxidise organic material. A few drops of $FeCl_3$ were added, diluted to approximately 15 mls with 1N HNO_3 and U and Th co-precipitated with $Fe(OH)_3$ by adding NH_4OH. The precipitate was collected after centrifugation and the supernatent discarded. The precipitate was washed twice with MQ H_2O and then dissolved by adding 7N HNO_3 to make up the final volume to 1 ml. The sample was then loaded into columns filled with anion exchange resin which had been washed with alternating cycles of MQ H_2O and concentrated HNO_3 and conditioned with 5N HCl. The U fraction was collected first with MQ H_2O and then the Th fraction with 5N HCl. The columns were not reconditioned between U and Th collection as trace amounts of ^{238}U in the Th sample aid in focusing the ion source of samples with low U concentrations such as those investigated in this study. Two drops of dilute graphite (to tag the sample) and five drops of concentrated HNO_3 were added to the collected fractions which were left overnight to evaporate to dryness.

3.3.3 Thermal Ionisation Mass Spectrometry (TIMS)

Filament loading

The U and Th samples obtained by chemical separation were dissolved in approximately 2 ml of 1N HNO_3. The Th samples were loaded onto single zone-refined Re filaments between two layers of graphite, while the U samples were loaded onto double zone-refined Re filaments. All filaments were evaporated to dryness under a current of 0.8 A.

Mass spectrometry

Early measurements (April 1999 to May 2000) made on a Finnigan MAT 261 thermal ionisation mass spectrometer (TIMS) proved to be difficult, particularly for Th. This was due to the fact that the samples were very low in ^{238}U (typically less than 100 µg/g) and also young in age (30,000 years) yielding ^{230}Th levels typically below 0.1 pg/g. Measurements ceased until a new Finnigan Triton was installed. The advantage of the Triton lies primarily in its superior secondary electron multiplier (SEM), improved ion transmission and optics, compared with the MAT 261. In addition, the darknoise of the Triton was significantly lower than that of the MAT 261 (~1 cps) which reduces the instrumental error in collecting low level Th.

The U isotopes were measured in the following line order (bold font indicates mass collected on the SEM while the other masses are simultaneously collected on adjacent Faraday cups):

1. 233-**234**-235-238
2. **235**-238
3. **233**-235

Providing that ^{235}U was sufficient to be simultaneously measured in a Faraday cup, the ratio $^{235}U_{SEM}$:$^{235}U_{Faraday}$ is used to correct $^{234}U_{SEM}$/$^{235}U_{Faraday}$ for the differences in gain between the SEM and the Faraday cups. If the ^{235}U signal was insufficient to be measured on a Faraday, then ^{233}U, ^{234}U and ^{235}U are 'peak hopped' into the SEM which avoids the need to perform a gain correction, but has the disadvantage that ^{235}U can not be simultaneously measured, therefore any possible fluctuations in beam intensity occurring between masses cannot be cancelled out *i.e.* no multicollection.

The concentration of ^{234}U and ^{238}U in the sample are then determined by removing the contribution of ^{238}U, ^{235}U and ^{234}U from the spike by standard isotope dilution techniques and then correcting $^{238}U/^{235}U$ for mass bias (fractionation between masses as the lighter isotopes are preferentially removed from the hot filament over time), using an exponential mass bias law.

Th data was acquired by peak hopping ^{229}Th, ^{230}Th and ^{232}Th on the SEM, counting for relatively long periods (typical integration time of 32 s for each species) which produced data with significantly lower statistical counting errors than initial acquisitions of shorter but more frequent integrations.

Concentrations of ^{230}Th were determined directly by using the known amount of $^{229}Th_{SPIKE}$ ($^{230}Th_{SPIKE}$ concentration is around five orders of magnitude less than that in the youngest of these samples and thus $^{230}Th_{SA}$ does not need to be calculated using isotope dilution). The ratio $[^{230}Th_{SA}/^{232}Th_{SA}]_{activity}$ is calculated as it is typically used as an indicator of allogenic Th.

Finally, the sample age was calculated iteratively using Equation 3.2.1 and spreadsheet software.

Calculation of errors

The age error is dominated by systematic uncertainty in decay constants (mostly ^{230}Th; Meadows *et al.*, 1980) and statistical counting uncertainty. However, the uncertainty in the decay constants λ_{230} and λ_{234} were not considered for the samples used in this study since these uncertainties only become significant for ages much older than ~30 ka (Ivanovich and Harmon, 1982). The uncertainty of the calculated age, termed here 'age error' was calculated by propagating the uncertainties of $[^{230}Th/^{238}U]_{activity}$, $\delta^{234}U_O$ ($\delta^{234}U$ at time of measurement) and the uncertainty of $\delta^{234}U_T$ ($\delta^{234}U$ at time of calcite formation) was calculated by propagating the uncertainties of $\delta^{234}U_O$ and age according to the equations below.

According to Equation 3.2.1, age (t), is a function of [$^{230}Th/^{238}U$] and $\delta^{234}U_O$, *i.e.*

$$t = f\left([^{230}Th/^{238}U],\ \delta^{234}U_o\right),$$

thus the age error, Δt is also a function of these:

$$\Delta t = f'\left(\Delta[^{230}Th/^{238}U],\ \Delta\delta^{234}U_o\right)$$

To write an expression for Δt, the age Equation 3.2.1 is re-written as

$$\omega = 0 = -1 + \left[\frac{^{230}Th}{^{238}U}\right] + e^{-\lambda_{230}t} - \frac{\delta^{234}U_o}{1000} \times \left(\frac{\lambda_{230}}{\lambda_{230} - \lambda_{234}}\right)\left(1 - e^{(\lambda_{234} - \lambda_{230})t}\right) \quad (3.3.1)$$

where $$\omega = f''\left([^{230}Th/^{238}U], \delta^{234}U_o, t\right) \quad (3.3.2)$$

and thus $$\Delta\omega = f'''\left(\Delta[^{230}Th/^{238}U], \Delta\delta^{234}U_o, \Delta t\right) \quad (3.3.3)$$

and the age error is solved by partial differentiation of Equation 3.3.1 with respect to the variables in Equation 3.3.2. Solving and re-arranging becomes:

$$\Delta t = \sqrt{\frac{\left(\frac{\partial\omega}{\partial A}\right)^2 \times \Delta A^2 - \left(\frac{\partial\omega}{\partial\delta^{234}U_o}\right)^2 \times \Delta\delta^{234}U_o{}^2}{\left(\frac{\partial\omega}{\partial t}\right)^2}} \quad (3.3.4)$$

Similarly, the uncertainty in $\delta^{234}U_T$ is calculated by propagating the uncertainties of $\delta^{234}U_O$ and t through Equation 3.3.5 below:

$$\delta^{234}U_T = \delta^{234}U_o e^{-\lambda_{234}t} \quad (3.3.5)$$

such that

$$\Delta\delta^{234}U_T = \sqrt{\left(\frac{\partial\delta^{234}U_T}{\partial\delta^{234}U_o}\right)^2 \times \Delta\delta^{234}U_o^2 + \left(\frac{\partial\delta^{234}U_T}{\partial t}\right)^2 \times \Delta t^2} \quad (3.3.6)$$

3.4 RESULTS OF U-SERIES DATING

3.4.1 MK-F1 U concentration results

U concentration of sub-samples of speleothem cut for U-series dating were determined by solution ICP-MS. By measuring ^{232}Th also, this method served as a screening for samples that are significantly contaminated with allogenic minerals. The U and Th concentration results for MK-F1, the core obtained from Marakoopa Cave, confirmed

that this flowstone core contained high levels of allogenic minerals (Figure 3.4.1). Figure 3.4.1 shows that ^{232}Th concentrations are very high, rising to over 400 ppb, an order of magnitude greater than ^{238}U (average is 39 ppb, n = 17). The combination of high ^{232}Th (hence high allogenic ^{230}Th) with low ^{238}U, would greatly bias the apparent age of these samples if dated using the above methods without any corrections.

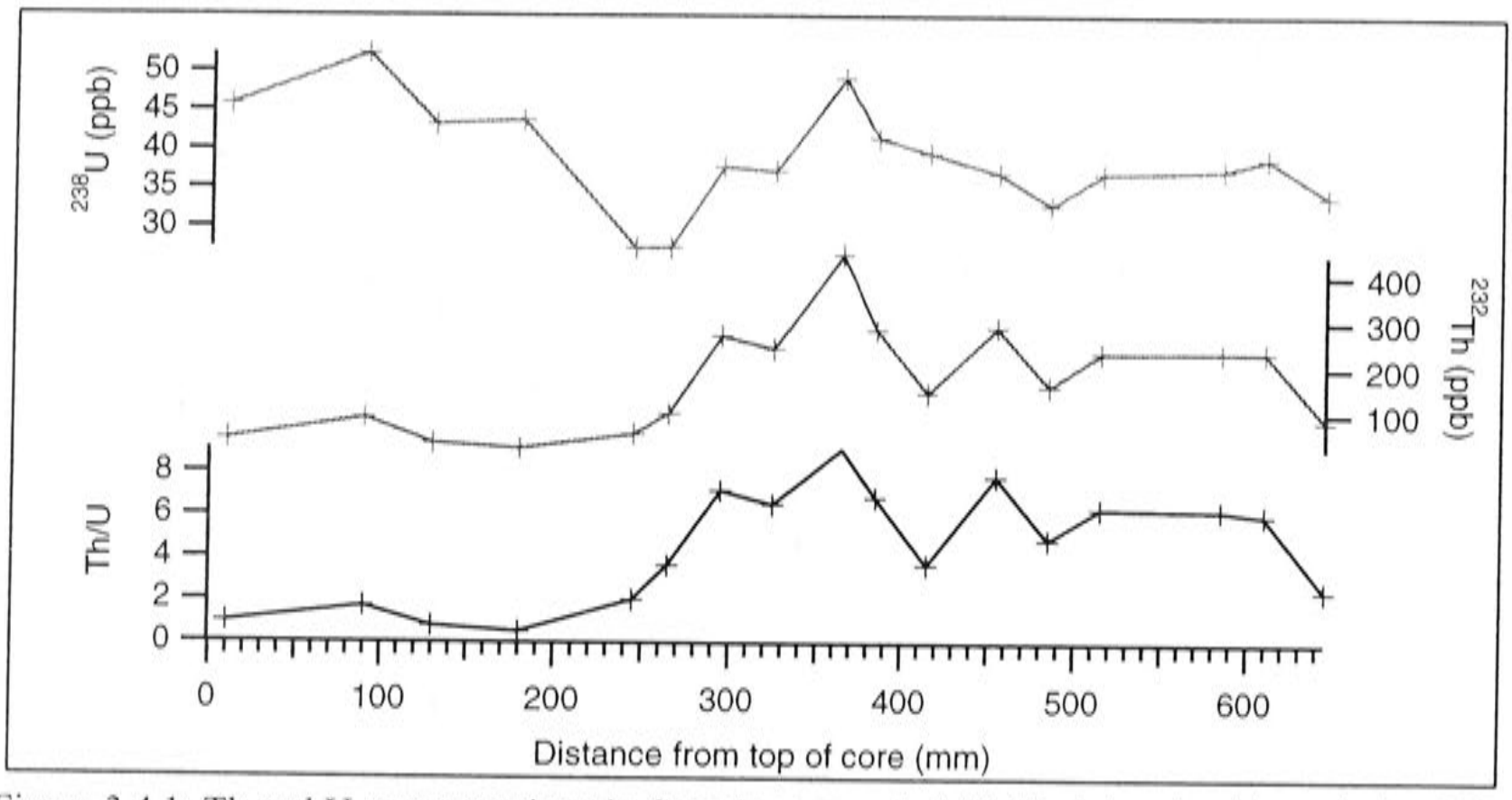

Figure 3.4.1: Th and U concentrations in flowstone sample MK-F1 determined by solution ICP-MS.

Theoretically, allogenic contribution of U and Th may be corrected for by numerical methods applied to measurements of coeval samples with differing allogenic proportions of ^{238}U, ^{234}U and ^{230}Th (Bischoff and Fitzpatrick, 1991; Luo and Ku, 1991; Ludwig and Titterington, 1994). This technique relies on the principle that if measurements of a suite of coeval samples with differing ^{238}U, ^{234}U and ^{230}Th can be made, then allogenic-free $^{234}U/^{238}U$ and $^{230}Th/^{238}U$ values can be extracted by interpolating the mixing-line to the allogenic-free end-member. There are several ways of performing this extrapolation using different ratio combinations of ^{238}U, ^{234}U, ^{232}Th and ^{230}Th, using either the slope or intercept of the extrapolated line (see Luo and Ku, 1991; Kaufman, 1993; Ludwig and Titterington, 1994). The critical requirement of this technique is that the values used produce ratios that are dispersed along both the X and Y axes, but with little scatter (high r^2), and yet are coeval. Previously, this spread was produced by processing both the leachate and insoluble residue (Ku and Liang, 1984) or several extracts of the leachate during dissolution with different strength acids (Schwarcz and Latham, 1989). However,

these leaching methods were found to fractionate the isotopes, which affected the ages (Bischoff and Fitzpatrick, 1991). The only reliable method found for producing the suite of ratios is to analyse whole coeval fragments separately (Bischoff and Fitzpatrick, 1991; Ludwig and Paces, 2002). Thus, significantly larger amounts of coeval material are required. As the amount of material required is larger for low ^{238}U samples, the number of coeval samples may be limited by availability. The analytical limitations here require that each analysis have at least 100 ng of ^{238}U, and thus at least 5 g of each coeval sample must be digested. Since this technique would require at least 5-6 analyses, then this equates to 25-30 g of coeval $CaCO_3$. Unfortunately, after digesting this much $CaCO_3$, there would remain little confidence that coeval material was being used, given the slow growth rate of flowstone (< 50 µm/a). Taking in to account the larger volume of sample digested for analysis would increase the age error substantially.

While it is common for much effort to go into producing age measurements for valuable specimens such as hominoids where the allogenic contamination levels may be similar, although U concentration is usually higher (*e.g.* McDermott *et al.*, 1996; Thorne *et al.*, 1999), the effort required for producing more precise age measurements than the conventional ^{14}C age measurements produced for MK-F1 was questionable, and certainly beyond the time permitted for this thesis. Thus, U-series age measurements were not performed for MK-F1 and radiocarbon age measurements are used as an alternative, albeit potentially flawed chronology, which will be discussed in Section 3.5.

3.4.2 Age measurements

The U-series data for this study appear in Table 3.4.1 below (Appendix I contains dates and brief descriptions of all U-series measurements processed by this author during the course of her PhD research). Table 3.4.1 shows that all age measurements are stratigraphically ordered where more than one age measurement was performed for the same speleothem. The basal age measurement of the Frankcombe Cave (Tasmanian) stalagmites, FC-S8 (2.99 ± 0.17 ka) is similar to the basal age measurement of FC-S3 (3.67 ± 0.21 ka) and thus, these two speleothems from the same cave overlap in their growth periods, making them suitable for the reproducibility study (the tip of FC-S8 did

not need to be dated as it was collected whilst it was still active). This reproducibility study, primarily focusing on stable isotopes, was outlined in Chapter 2 and appears in Chapter 7.

An age measurement of 14.54 ± 1.13 ka for the base of the stalagmite, LY, from Lynds Cave, Mole Creek, agrees very well with an earlier combined radiocarbon/electron spin resonance age of 14.6 ka (Goede and Hitchman, 1984; Goede, 1998). However, the topmost age measurement (6.47 ± 0.76 ka) is significantly older than the combined radiocarbon/electron spin resonance age of 2.9 ka (Goede, 1998). Each age measurement is flawed, however. Goede and Hitchman (1984) assume that the dead carbon age offset is constant through time and can be estimated by correcting the age-depth slope between two radiocarbon ages by the slope between their ESR equivalent dose measurements, and derive a dead carbon reservoir correction of 2,200 years. The conventional radiocarbon age of 5250 ± 70 years BP (Pta-2979) thus was considered to be 2.9 ka (Goede and Hitchman, 1984). The associated error of this corrected age was not propagated with the statistical error, but would be large owing to the error associated with the equivalent dose measurement and assumptions regarding constant dead carbon proportion and constant equivalent dose. For the TIMS U-series age conducted by this author, the low $^{230}Th/^{232}Th$ (~13) indicates the measured age is older than the true age owing to allogenic contamination (Table 3.4.1). The true age of the top of LY is likely to lie between the U-series and corrected-radiocarbon age, ~4.7 ka.

Age measurements of the southwestern Australian flowstone, ES-F1 (25.54 ± 2.37 to 2.28 ± 0.50 ka) indicate it grew through the LGM-Holocene transition, which on the basis of its chronology only, makes it a suitable specimen for determining the trend of $\delta^{18}O_{SP}$ with temperature, or the sign of speleothem 'γ', over this transition (Chapter 2; this investigation appears in Chapter 8).

One further feature to compare is $\delta^{234}U_T$ which differs greatly between samples from different caves *i.e.* Frankcombe Cave samples range from ~565 to 710‰, Lynds Cave samples from ~1240 to 1670‰ and Easter Cave samples from ~60 to 85‰. $\delta^{234}U_T$ indicates the degree of $^{234}U/^{238}U$ disequilibrium in cave groundwaters and has been

interpreted as a function of soil redox conditions and limestone weathering rate (Kaufman *et al.*, 1998; Hellstrom and McCulloch, 2000). This proxy was not investigated here owing to the small number of samples processed, but may be investigated in the future.

Table 3.4.1: The results of thermal ionisation mass spectrometry on samples used in this study. The concentration of Th is shown for younger material. Also shown are age measurements for FC-S3, marked with an asterisk. These were conducted for this author's Honours thesis (Treble, 1998), but are included here as they are discussed below.

Sample	Median distance above base (mm)	Sample fired?	Mass (g)	$^{238}U_{conc}$ ($\mu g\ g^{-1}$)	$[^{230}U/^{238}U]$ activity	$\delta^{234}U_T$ $\pm 2\sigma$ error	$[^{230}Th/^{232}Th]$ activity	Age $\pm 2\sigma$ error (ka)
FC-S8 U1	5	Y	5.12	0.096	0.0427 $\pm$ 0.0025	569 $\pm$ 4.43	2.596	2.99 $\pm$ 0.17
LY-STAL1 U1	28	N	5.27	0.031	0.3292 $\pm$ 0.0108	1664.30 $\pm$ 115.67	43.26 $\pm$ 1.84	14.54 $\pm$ 1.13
LY-STAL1 U2	2320	N	5.50	0.019	0.1291 $\pm$ 0.0130	1246.48 $\pm$ 7.01	12.60 $\pm$ 1.34	6.47 $\pm$ 0.76
ES-F1 U1	190	N	5.26	0.066	0.0225 $\pm$ 0.0011	84.40 $\pm$ 1.89	1.87 $\pm$ 0.15	2.28 $\pm$ 0.50
ES-F1 U2	110	N	4.81	0.062	0.0795 $\pm$ 0.0015	61.02 $\pm$ 1.10	78.51 $\pm$ 1.20	8.47 $\pm$ 0.90
ES-F1 U6	20	N	5.03	0.017	0.2265 $\pm$ 0.0218	79.44 $\pm$ 4.62	2.01 $\pm$ 0.12	25.54 $\pm$ 2.37
FC-S3 U2*	165	N	4.43	0.500	0.0036 $\pm$ 0.0012	706.00 $\pm$ 2.88	1.033	0.23 $\pm$ 0.08
FC-S3 U1*	13	N	5.03	0.304	0.0557 $\pm$ 0.0032	673.24 $\pm$ 4.20	1.692	3.67 $\pm$ 0.21

3.4.3 Possible sources of error in U-series dates

The age errors shown in Table 3.4.1 are statistical, calculated by propagating the statistical errors of the measured ratios using Equations 3.3.4 and 3.3.6.

U concentrations of speleothems may range from < 0.03 to 100 $\mu g\ g^{-1}$ (Ivanovich and Harmon, 1982)). Table 3.4.1 shows that speleothems measured by this author range in U concentration from 0.017 to 0.500 $\mu g\ g^{-1}$, with the lowest concentrations found for ES-F1 U6 and for LY-STAL U1 and U2. Low U concentrations produced low-intensity beams increasing the statistical age error; consequently these samples produced some of the larger age uncertainties (Table 3.4.1).

Most samples contain significant values of allogenic ^{232}Th *i.e.* $^{230}Th/^{232}Th < 30$, hence allogenic ^{230}Th, which particularly for very young samples, *e.g.* FC-S3 U2, FC-S3 U1, FC-S8 U1, LY-STAL U2, ES-F1 U6 and ES-F1 U1 may significantly affect the age. As discussed above, to correct for allogenic contamination requires analysis of multiple coeval samples to produce a mixing line, such that an age for an uncontaminated end-member may be calculated. However, given the limited amount of material available for these dates (dictated by the low U concentrations) prevented this further analysis. Examination of corrections for Holocene speleothems in Kaufman *et al.* (1998) showed age bias for samples with $^{230}Th/^{232}Th < 30$, result in apparent ages on the order of ~2 ka older than the corrected age. The possible age bias for samples with the measurements shown in Table 3.4.1 may be speculated if two assumptions are made:

1. that the actual topmost age measurement for FC-S3 U2, 0.23 ± 0.08 ka (Table 3.4.1), is modern and thus the activity ratios determined for this sample represent the allogenic end-member; and
2. that FC-S3 U1 and U2 received identical amounts of allogenic contamination with U and Th isotope ratios at secular equilibrium.

It is stressed here that these assumptions are only made in order to speculate about the possible magnitude of age bias for FC-S3 U1. It is recognised that allogenic contamination of drip-waters will change over time, and that FC-S3 U2 will contain some ^{230}Th from the pure carbonate, but it is assumed that this is insignificant here compared with the allogenic fraction. The $^{230}Th/^{234}U$ and the $^{230}Th/^{238}U$ activity ratios of FC-S3 U1 were corrected by the 'detrital ratios' of FC-S3 U2 using Equation 3.4.1 (Kaufman *et al.*, 1998):

$$\left[\frac{230Th}{234U}\right]_C = \frac{1-\left(\left[\frac{232Th}{230Th}\right]_S \times \left[\frac{230Th}{232Th}\right]_D\right)}{\left[\frac{234U}{230Th}\right]_S - \left(\left[\frac{232Th}{230Th}\right]_S \times \left[\frac{230Th}{232Th}\right]_D\right)} \qquad (3.4.1)$$

which assumes that the allogenic component is in secular equilibrium. Subscript C denotes pure carbonate member; S, the sample containing pure carbonate and allogenics, and D, the detrital member.

This speculation produces a corrected age of 1.39 ± 0.19 ka for FC-S3 U1, which is far younger than 3.67 ± 0.21. Since the validity of this new age cannot be verified by performing multiple coeval dates, it would be desirable to obtain another independent age estimate. For speleothem records where trace elements are measured, this may be done by counting annual cycles (see Chapters 6 and 7), provided that the date when the speleothem ceased growing is known (*i.e.* FC-S8 was collected whilst it was still active). For FC-S3 U2 itself, the only way of determining the time when it ceased growing, is to check for a ^{14}C spike produced by nuclear weapons testing using radiocarbon methods. This technique has the potential to constrain the time when FC-S3 ceased growing to either pre- or post-A.D.1956 (Genty and Massault, 1997; Genty *et al.*, 1998; Genty *et al.*, 2001).

3.5 RADIOCARBON DATING OF SPELEOTHEMS

3.5.1 Introduction to radiocarbon dating

^{14}C, ^{13}C and ^{12}C are naturally occurring isotopes of carbon. ^{13}C and ^{12}C are stable isotopes, while ^{14}C is radioactive and has a half-life of 5730 years (Godwin, 1962). All ^{14}C atoms are cosmogenically produced in the upper atmosphere from the collision of a nitrogen atom (${}^{14}_{7}N$) and a neutron (${}^{1}_{0}n$) as shown by Equation 3.5.1:

$$ {}^{14}_{7}N + {}^{1}_{0}n \rightarrow {}^{14}_{6}C + {}^{1}_{1}H \qquad (3.5.1) $$

Cosmogenically produced ^{14}C becomes incorporated into all living organisms (plants, animals) and material derived from these (*e.g.* peats, humus), as well as inorganic C-bearing material (*e.g.* speleothem calcites, ocean water). Radiocarbon (^{14}C) dating of these materials involves measuring the ratio of ^{14}C:^{12}C atoms by β-counting or for higher precision, by accelerator mass spectrometry (AMS). Radiocarbon dating can be used to determine the age of material to around 40,000 years BP by standard techniques, or greater when appropriate C purification procedures are combined with very low laboratory backgrounds and AMS counting (*e.g.* Bird *et al.*, 1999).

Radiocarbon dating is not an ideal method for determining *absolute* ages of speleothems as the process of incorporation of atmospheric ^{14}C is less direct for speleothem calcite than it is for living organisms, because the C atoms in speleothem calcite are a mixture of atmospheric and inorganic C of vastly different ages and ^{14}C activity. Beginning with the organic C reservoir above the cave, the delay of conversion of atmospheric CO_2 to soil CO_2 by soil organic matter (SOM) can range from seasonal (*e.g.* grass) to more than 100 years (*e.g.* large trees) (Dorr and Munich, 1986; Genty and Massault, 1997). The ^{14}C atoms, now soil $^{14}CO_2$, may then be further diluted by the process of dissolution of radioactively "dead" limestone, as most limestones are of considerable age and therefore contain only ^{13}C and ^{12}C but no ^{14}C atoms. The proportion of limestone C atoms in the speleothem is termed the 'dead carbon proportion' (DCP). Researchers that choose to date speleothems using the ^{14}C method must correct their dates by this proportion. This proportion is expressed by Equation 3.5.2 (Genty and Massault, 1997):

$$DCP = \left(1 - \frac{A^{14}C_{SP}}{A^{14}C_{ATM}}\right) \times 100\% \qquad (3.5.2)$$

where $A^{14}C_{SP}$ and $A^{14}C_{ATM}$ are the activities of ^{14}C atoms in the speleothem and the atmosphere, respectively, expressed as percent modern carbon (PMC).

To determine DCP; $A^{14}C_{ATM}$, which varies over time (Stuiver *et al.*, 1998; Beck *et al.*, 2001), needs to be known for the time of speleothem precipitation and hence the approximate age of the sample also must be known. Attempts to constrain the possible age use the following methods:

- collecting the sample while it was actively forming (Williams *et al.*, 1999); or
- determining the age of the sample by interpolation between U-series dates (Vogel, 1983); or
- using a sample that grew through the period of nuclear weapons testing, which for the Southern Hemisphere, raises $A^{14}C_{ATM}$ above 100 PMC after A.D.1956 (Manning and Melhuish, 1994). By this method, the rise and decay of $A^{14}C_{ATM}$ ("bomb spike") may be seen, but in an attenuated or delayed form due to the soil organic matter decomposition process (Genty and Massault, 1997, Genty *et al.*, 1998; Genty and Massault, 1999).

Typical DCP results derived by D. Genty who has pioneered much of the previous research on speleothem DCP, range from ~9 to 22 ± 1.5% at sites in Belgium, France and Slovenia (Genty and Massault, 1997; Genty *et al.*, 1998; Genty *et al.*, 1999) and a estimate of 15 ± 5% is commonly quoted based on these results and calculations from literature (Genty and Massault, 1997). However, the most recent study on Scottish speleothems highlights that DCP may be greater than this estimate (38%), supposedly due to development of a peat bog above a cave through the Holocene and consequently, an increase in the age of SOM carried in the drip-water (Genty *et al.*, 2001).

3.5.2 Samples dated by radiocarbon methods in this study

MK-F1/ES-F1

As outlined in Section 3.4, the high allogenic mineral content of MK-F1 indicated by the high ^{232}Th values, would have produced a large bias for the U-series age measurements. Radiocarbon age measurements by conventional counting methods were performed here as an alternative. The disadvantages of this radiocarbon chronology, primarily the uncertainty created by the DCP dilution, is discussed with the results below. U-series age measurements for ES-F1 were successfully obtained (Table 3.4.1), however, the results of the radiocarbon age measurements, performed prior to the U-series, are presented here to allow a comparison of the two techniques.

FC-S3

In this study, the tip of stalagmite FC-S3 was known to be very young as U-series age measurements (Table 3.4.1) showed the top 10 mm of stalagmite had an age of 230 ± 76 years. Since this sample was very low in both ^{238}U and ^{230}Th, then the true age of the tip of FC-S3 is likely to have been significantly younger than this U-series age, possibly modern. To further constrain the youngest age of FC-S3, ^{14}C dating was employed to detect the presence or absence of a bomb spike (> 100 PMC) which would indicate if the tip of FC-S3 grew before or after $A^{14}C_{ATM}$ rose above 100 PMC (A.D.1956 for the Southern Hemisphere; Manning and Melhuish, 1994). To determine the DCP, a straw (soda straw stalactite) tip from the same cave was also analysed. This straw (FC-STRAW1) was actively growing when collected in May 1999. According to in-situ

measurements by Desmarchelier (1999), the average growth rate of straws from Frankcombe Cave is 680 μm per year. Thus, the ~15 mg of straw tip removed for analysis represented approximately 4 years growth, and an average age of A.D.1997 ± 2.

3.6 RADIOCARBON AGE MEASUREMENTS BY CONVENTIONAL COUNTING

3.6.1 Sample preparation

Samples weighing approximately 2 g were pre-cleaned with a dental drill to remove any visible contaminants and ultrasonically washed in MQ H_2O. These samples for conventional radiocarbon ages were submitted to the Radiocarbon Dating Laboratory at RSES, ANU, for measurement by liquid scintillation counting methods (see Gupta and Polach, 1985 for details).

3.6.2 Results and discussion

Table 3.6.1 shows the results of the conventional radiocarbon age measurements. These conventional radiocarbon ages were calculated based on the initial assumption that $A^{14}C_{ATM}$ at the time of speleothem formation is 100 PMC and have not yet been corrected for reservoir effects (DCP for speleothems), or the isotopic fractionation between $^{14}C/^{12}C$ due to photosynthesis and $CaCO_3$ precipitation, based on measured $^{13}C/^{12}C$ ($\delta^{13}C$), which has approximately half the fractionation of $^{14}C/^{12}C$ (Equation 3.6.2; Stuiver and Polach, 1977).

Table 3.6.1: Results of radiocarbon age measurements by conventional counting techniques for flowstones MK-F1 and ES-F1. Conventional radiocarbon age is that reported by the laboratory and is neither corrected for reservoir effects or isotopic fractionation.

Sample	Laboratory code	Distance above base (mm)	$d^{14}C$ (‰)	$D^{14}C$ (‰)	Conventional radiocarbon age (years BP)
MK-F1 top	ANU-11519	425	-810.6 ± 3.5	-820.1 ± 3.4	13,780 ± 160
MK-F1 mid	ANU-11520	245	-944.0 ± 1.9	-946.8 ± 1.8	23,560 ± 280
MK-F1 base	ANU-11521	105	-972.3 ± 1.7	-973.7 ± 1.6	29,230 ± 520
ES-F1 U1A	ANU-11392	192	-239.0 ± 12.6	-277.0 ± 12.3	2,610 ± 140
ES-F1 U4	ANU-11393	111	-647.8 ± 7.8	-665.4 ± 7.4	8,790 ± 180

In order to obtain more accurate radiocarbon ages, several corrections need to be made. For the radiocarbon measurements, three equations are critical (Stuiver and Polach, 1977):

$$d^{14}C\,(‰) = \left(\frac{A_{SN}}{A_{ON}} - 1\right) \times 1000 \qquad (3.6.1)$$

$$D^{14}C\,(‰) = d^{14}C - 2\left(\delta^{13}C + 25\right)\left(1 + \frac{d^{14}C}{1000}\right) \qquad (3.6.2)$$

$$\text{radiocarbon age (years BP)} = -8033 \ln\left(1 - \frac{D^{14}C}{1000}\right) \qquad (3.6.3)$$

where $d^{14}C$ is the difference between the activity of sample to standard (A_{SN}/A_{ON}) in per mil (Equation 3.6.1). $D^{14}C$ is $d^{14}C$ corrected for $\delta^{13}C$ fractionation and normalised to wood (Equation 3.6.2), and Equation 3.6.3 is the age equation.

Since the dilution of speleothem $^{14}C/^{12}C$ by limestone ^{12}C will have the effect of reducing the sample activity (A_{SN}) by the proportion of ^{12}C dissolved, this dilution needs to be accounted for by correcting the A_{SN}/A_{ON} ratio below:

$$d^{14}C'(‰) = \left\{\left(\left(1 - \frac{DCP}{100}\right) \times \frac{A_{SN}}{A_{ON}}\right) - 1\right\} \times 1000 \qquad (3.6.4)$$

$d^{14}C'$ is then corrected for $\delta^{13}C_{SP}$ and normalised to wood ($D^{14}C'$; Equation 3.6.2) and the conventional age re-calculated by Equation 3.6.3 (Table 3.6.2). The errors associated with the DCP estimate (15 ± 5%, see Genty and Massault, 1997 for literature review) was determined by calculating the upper and lower estimates of the age based on a probable DCP range of 10 to 20% rather than by the propagation method outlined for U-series, because of the asymmetric nature of the age equation (Equation 3.6.3) and are shown in Table 3.6.2.

These conventional DCP-corrected radiocarbon ages were then calibrated to calendar years using the CALIB program (Stuiver and Reimer, 1993) which has been updated using the INTCAL98 calibration by Stuiver *et al.* (1998; Table 3.6.2). Unfortunately, this calibration could not be performed for MK-F1 base and MK-F1 mid as the calibration only extends to 24, 000 years BP and accepts ages younger than ~22,000 radiocarbon

years. For age measurements older than this, there is no internationally agreed calibration. Here the Lake Suigetsu record (Kitagawa and van der Plicht, 1998) was used, as it is the highest resolution calibration record spanning the period 24 - 45 ka. However, the uncertainty of this calibration record is highlighted by a study by Beck *et al.* (2001) using a U-series and radiocarbon dated speleothem, which suggests that large $A^{14}C_{ATM}$ variations do exist for this period, possibly changes in the marine C reservoir induced by changes in the thermohaline circulation.

Table 3.6.2: Conventional radiocarbon ages re-calculated after correcting for DCP and $\delta^{13}C_{SP}$. Calibrated ages are calculated using INTCAL98 (0-24 ka) and *Lake Suigetsu (24-45 ka) calibrations (see text). Errors are 1 σ.

Sample	Distance above base (mm)	$d^{14}C'$ (‰; DCP corrected)	$\delta^{13}C_{SP}$	$D^{14}C'$ (‰; $\delta^{13}C$ corrected)	Re-calculated conventional radiocarbon age (years BP)	Calibrated age measurement (years BP)
MK-F1 top	425	-782.2 ± 6.7	-10.71	-788.4 ± 3.1	12476 ± 494	14806 ± 728
MK-F1 mid	245	-935.6 ± 6.0	-9.44	-937.6 ± 13.0	22286 ± 608	*~25500
MK-F1 base	105	-968.1 ± 6.0	-9.93	-969.1 ± 4.7	27932 ± 814	*~31600
ES-F1 U1A	192	-124.9 ± 13.6	-13.02	-145.8 ± 50.9	1266 ± 479	1165 ± 452
ES-F1 U4	111	-595.0 ± 9.4	-8.61	-608.2 ± 25.3	7528 ± 518	8457 ± 538

The DCP error out-weighs the statistical uncertainty of the $d^{14}C$ measurement, resulting in an expansion of the age uncertainty by ~ ± 500 years. However, as the proportion of the age estimate that this represents diminishes with increasing age, this results in age errors of, in some cases, smaller than those generated for low ^{238}U speleothems. This, and the accuracy of the two methods may be compared by considering both the U-series and radiocarbon age measurements for ES-F1 (Figure 3.6.1). DCP-corrected calibrated radiocarbon and U-series age measurements for ES-F1 U2 and U4 at ~110 mm agree extremely well. $^{230}Th/^{232}Th$ for U2 is high (78.5) and indicates negligible allogenic Th. For ES-F1 U1 and U1A (190-192 mm), allogenic Th ($^{230}Th/^{232}Th = 1.9$) appears to make the U-series age ~1100 years too old.

This exercise suggests that more precise ages may be obtained from radiocarbon age measurements of these low-U speleothems. Where the age measurements are able to be calibrated on the INTCAL98 curve, this may also produce similarly accurate ages also. A significant uncertainty, of course, still remains if the DCP is much greater than the estimated 15 ± 5%. This possibility is further explored for FC-S3, in the following

Section (3.7). Unfortunately, for MK-F1, only a radiocarbon chronology may be constructed. While the favourable cross-dating comparison obtained for ES-F1 suggests that the age 'MK-F1 top' may be close to an accurate age estimate, the other two ages 'MK-F1 mid' and 'MK-F1 base' are almost certainly less accurate as they fall outside the range of the INTCAL98 calibration range.

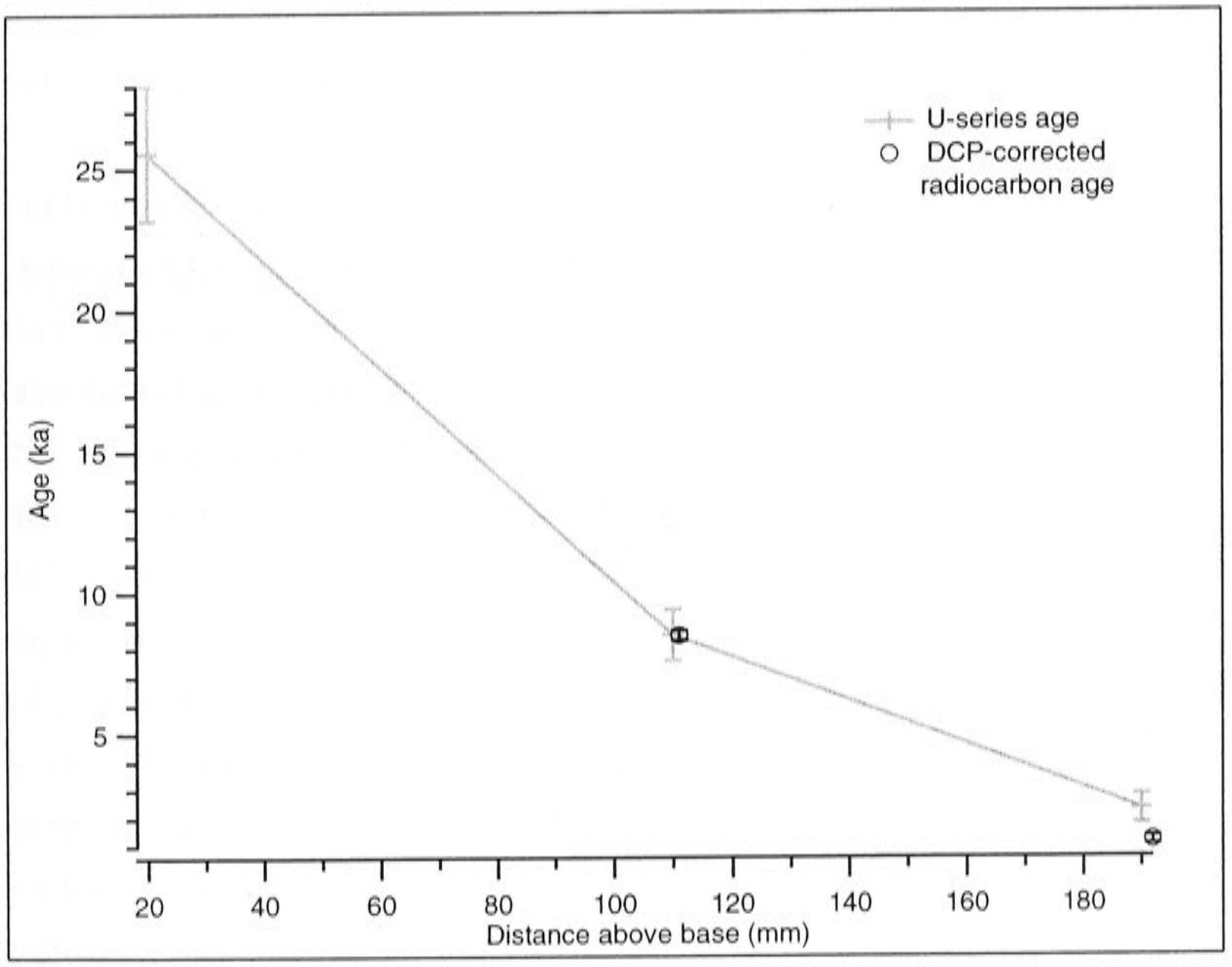

Figure 3.6.1: Flowstone ES-F1 DCP-corrected radiocarbon ages in calendar years and U-series age measurements.

3.7 RADIOCARBON AGE MEASUREMENTS BY AMS

To determine the age of the top of the FC-S3 stalagmite, which is significant for the overall aims of this study, a series of closely-spaced AMS ^{14}C measurements were made, with the expectation of locating a ^{14}C peak corresponding to the post-A.D.1956 bomb testing peak.

3.7.1 Methods

The samples used for ^{14}C dating were an aliquot of the same sample previously used for $\delta^{18}O_{SP}$ and $\delta^{13}C_{SP}$ analysis (Chapter 4, Section 4.2 for method and Chapter 7 for results). Approximately 15 mg of these samples were each weighed into a reaction vessel fitted with a side arm that was filled with 104% (saturated) H_3PO_4. The reaction vessel was attached to a ^{14}C preparation line at the Research School of Physical Sciences and Engineering (RSPhysSE) (for details of the line see Yokoyama, 1999). The line and vessel were evacuated and CO_2 evolved from the sample by reaction with H_3PO_4 at an approximate temperature of 90°C for 20 minutes. The CO_2 was passed through two traps containing an ethanol/dry-ice mixture to capture water and heavy volatiles. The separated CO_2 fraction was further purified by cryogenically freezing the CO_2 into a liquid nitrogen trap and pumping any remaining light volatiles from the trap. The CO_2 was then heated and allowed to equilibrate between two calibrated volumes of 50 and 10 ml. The 50 ml volume of gas was used for graphitisation on re-reduced Fe powder (the ratio of C:Fe being 1-1.2) at 650°C for 6 hours in excess H_2. Carbon atoms from the graphitised samples were counted by AMS at RSPhysSE and normalised to the activity of ANU sucrose (150.81 percent modern carbon (PMC)). The remaining 10 ml of CO_2 were transferred to and sealed in a quartz tube which was then used to measure $\delta^{13}C$ on the multiport device which is connected to a Finnigan MAT 251 mass spectrometer at the Research School of Earth Sciences (RSES).

The results for each sample are reported as the ^{14}C activity of the speleothem calcite normalised to ANU sucrose ($a^{14}C_{SP}$ expressed as PMC) and $A^{14}C_{SP}$ normalised to the $\delta^{13}C$ of wood (-25‰ PDB) using:

$$A^{14}C_{SP} = a^{14}C_{SP}\left(1 - \frac{(\delta^{13}C + 25)}{1000}\right) \quad (3.7.1)$$

which is adapted from Stuiver and Polach (1977) for determining $A^{14}C_{SP}$ based on the measured ratio $^{14}C/^{13}C$. Atmospheric CO_2 activity ($A^{14}C_{ATM}$) has also been normalised to wood. $A^{14}C_{ATM}$ values used for the Southern Hemisphere are from Wellington in New Zealand (Manning and Melhuish, 1994).

3.7.2 Results and discussion: FC-S3

Table 3.7.1 shows that the $A^{14}C_{SP}$ value for FC-STRAW1 (105.4 PMC) is greater than 100 PMC. This confirms that it formed after nuclear weapons tests commenced. Using this value and $A^{14}C_{ATM}$ for Wellington for the average age of the sample analysed (~114 PMC at A.D.1997 ± 2), a DCP of 7% was calculated (Equation 3.5.2). This is lower than the range of DCPs quoted of 15 ± 5% (Genty and Massault, 1997). FC-S3 1D $A^{14}C_{SP}$ at 98.8 PMC is slightly lower than 100 PMC, but given the high probability that FC-S3 1D must have a DCP of at least 7%, leaves no doubt that the $A^{14}C_{ATM}$ that was incorporated into FC-S3 1D must have been greater than 100 PMC, and thus post-nuclear weapons testing (A.D.1956). This age estimate (> A.D.1956) is substantially younger than, and demonstrates the uncertainty of, the U-series age measurement for the top of this very young speleothem with low ^{238}U and $^{230}Th/^{232}Th$ (0.23 ± 0.08 ka: FC-S3 U2, Table 3.4.1).

Figure 3.7.1 shows the behaviour of $A^{14}C_{SP}$ through time. FC-S3 9D to 6D (4.25 – 2.75 mm below tip) range from 84 to 89 PMC (Figure 3.7.1). Given that the external reproducibility on the AMS measurements is ± 2 PMC (2 σ), these values are statistically close. $A^{14}C_{SP}$ of samples FC-S3 3D to FC-S3 5D, are significantly lower than 6-9D (84-89 PMC), while samples 2D and 1D are the highest $A^{14}C_{SP}$ values, indicating they have the most modern carbon.

Theoretically, $A^{14}C_{SP}$ should follow the trend of $A^{14}C_{ATM}$ shown in Figure 3.7.2, but attenuated by the lag time for transfer of soil CO_2 and by the DCP. That is, if $A^{14}C_{SP}$ measurements spanned the entire period prior to A.D.1956 to post ~A.D.1965, then the form of $A^{14}C_{SP}$ should show a constant episode (pre-A.D.1956) followed by a peak and then a slow fall (Figure 3.7.2). This expression of the $A^{14}C_{ATM}$ is shown for a speleothem from southwest France by Genty and Massault (1999; Figure 3.7.3). There should be no large depression in $A^{14}C_{SP}$ values as seen for samples FC-S3 5D to 3D. This depression, in an otherwise generally increasing trend, suggests that there was a significant disruption to the C system, which must have been an increase in old carbon either from the limestone or organic C or both.

Table 3.7.1: $a^{14}C_{SP}$ and $A^{14}C_{SP}$ results for FC-S3 and FC-STRAW1 in PMC.

Sample I.D.	Distance from tip (mm)	$a^{14}C_{sp}$ (PMC)	$A^{14}C_{sp}$ (PMC)
FC-STRAW1	0 – 3	108.1 ± 0.9	105.4 ± 0.9
FC-S3-1D	0 – 0.5	100.8 ± 0.9	98.8 ± 0.9
FC-S3-2D	0.5 – 1.0	96.9 ± 0.9	95.1 ± 0.9
FC-S3-3D	1.0 – 1.5	81.3 ± 1.4	79.9 ± 1.4
FC-S3-4D	1.5 – 2.0	72.6 ± 0.9	71.3 ± 0.9
FC-S3-5D	2.0 – 2.5	76.2 ± 0.8	74.8 ± 0.8
FC-S3-6D	2.5 – 3.0	88.5 ± 0.8	86.9 ± 0.8
FC-S3-7D	3.0 – 3.5	87.1 ± 0.9	85.5 ± 0.9
FC-S3-8D	3.5 – 4.0	85.5 ± 0.7	84.0 ± 0.7
FC-S3-9D	4.0 – 4.5	90.6 ± 0.9	89.0 ± 0.9

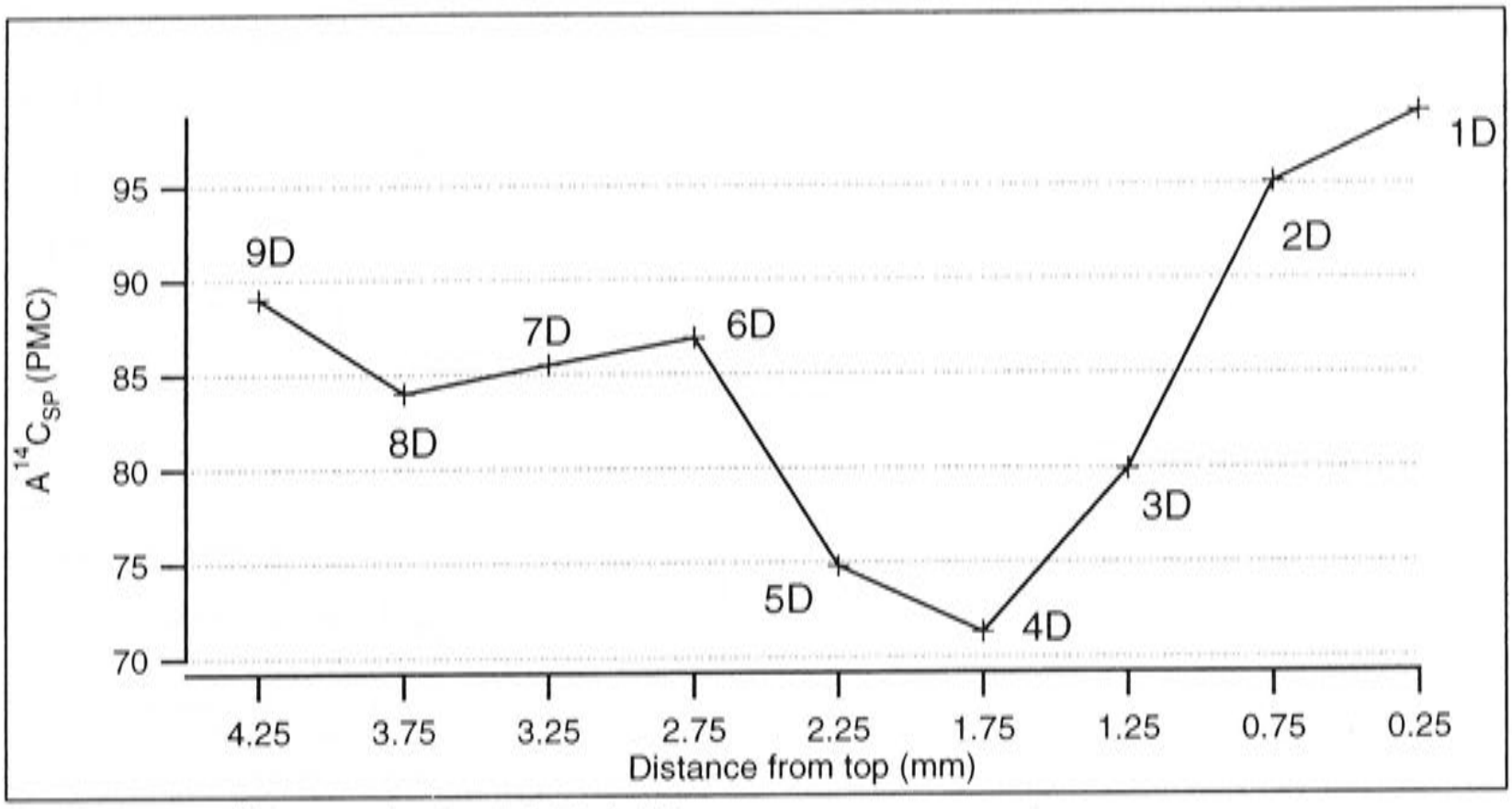

Figure 3.7.1: $A^{14}C_{SP}$ results for FC-S3 1-9D.

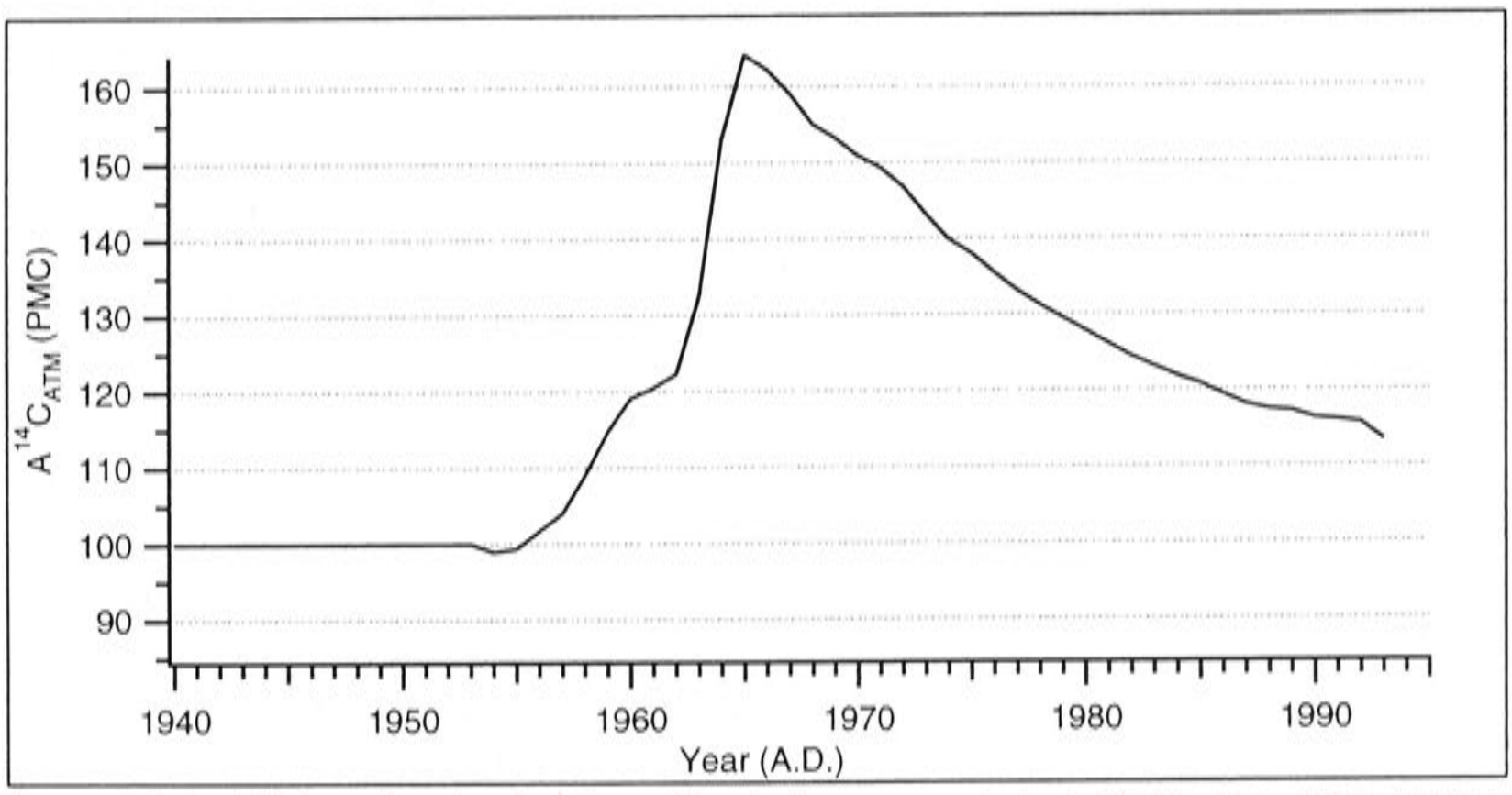

Figure 3.7.2: $A^{14}C_{ATM}$ for the Southern Hemisphere, recorded at Wellington, New Zealand (Manning and Melhuish, 1994).

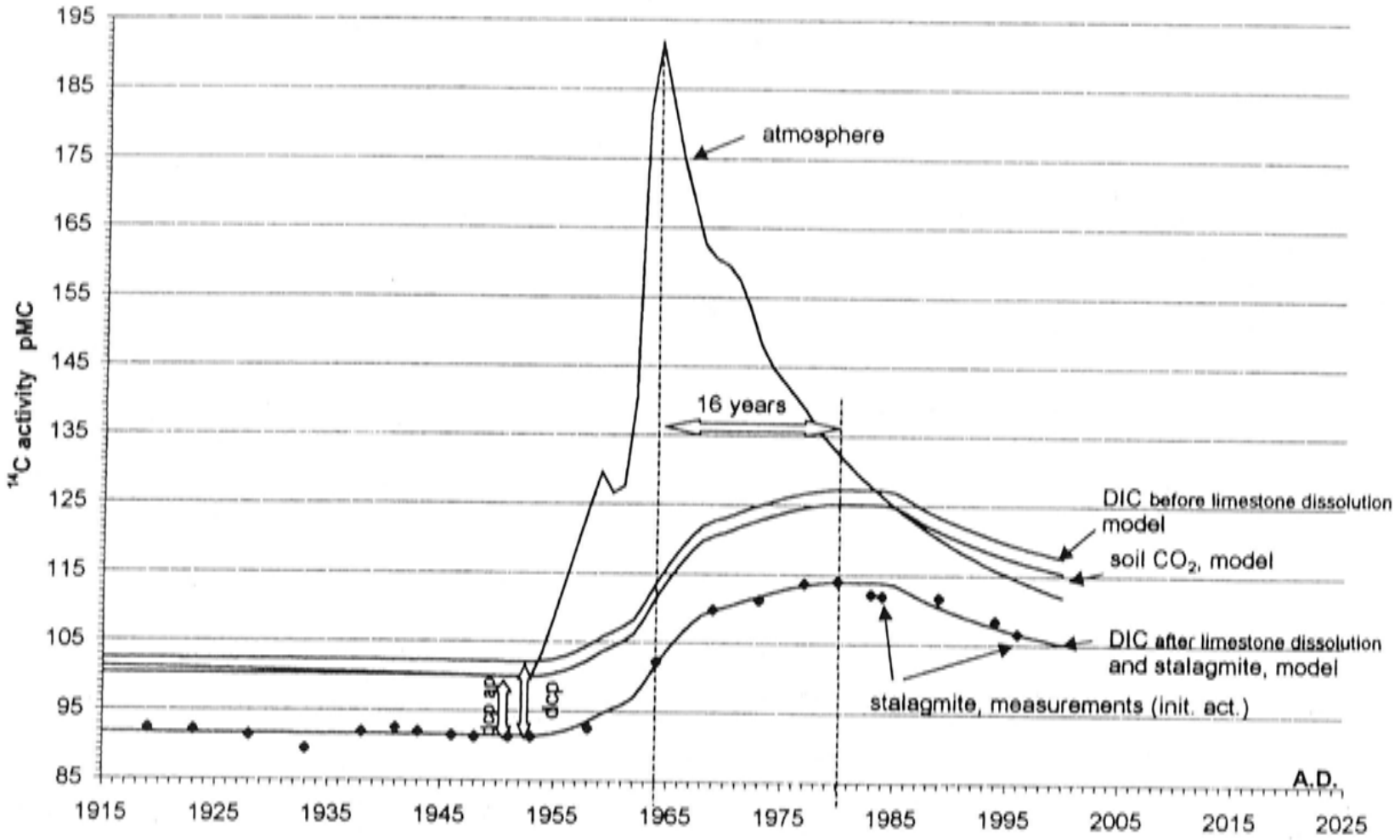

Figure 3.7.3: $A^{14}C_{SP}$ time series for La Faurie Cave stalagmite. Shown also are models for dissolved inorganic carbon before and after limestone dissolution and a model for soil CO_2. Source: Genty and Massault (1999).

Genty and Massault (1999) modelled a $A^{14}C_{SP}$ time series for the stalagmite from southwest France (Figure 3.7.3) based on the $A^{14}C_{ATM}$ curve for the Northern Hemisphere and estimates of:

- DCP (10.5%);
- the relative contribution of the slow and fast decomposing soil organic matter (SOM); and
- the turnover time for the slow and fast decomposing SOM.

These last two estimates were based on measurements of ^{14}C content of soil CO_2 collected from sites with differing proportions of grassland and forest in the Rhine Valley, Germany (Dorr and Munnich, 1986).

Following the steps outlined for Genty and Massault's model, a theoretical speleothem curve was attempted here. Genty and Massault's model simulates the transfer of the $A^{14}C_{atm}$ signal to the speleothem drip-water by splitting and passing it through several smoothing filters representing the uptake and release of organic C through compartments of vegetation with differing turnover times *i.e.* 10% of 10 year, 32% of 22 year and 58% of 130 year turnover, was used by Genty and Massault for their grassland model. This

produces the soil CO_2 curve, and in turn, by applying fractionations (which are small in comparison to the other variables), produces the dissolved inorganic C (DIC) curve (Figure 3.7.3). The $A^{14}C_{SP}$ curve is produced by reducing the DIC curve by the DCP. The model, essentially an attenuation of the $A^{14}C_{ATM}$ signal, is highly sensitive to the estimates given for the relative contribution and turnover times of the SOM components and DCP, with higher estimates of organic carbon delaying and smoothing the signal, and higher estimates of DCP shifting the curve downwards.

To attempt such a model for FC-S3, the DCP for FC-STRAW1 (7%) may be adopted as a first estimate, however no measurements of SOM turnover are available for the Florentine Valley. Genty and Massault (1997) report SOM turnover times and proportions for 3 sites; grassland, woodland and mixed. All three of these models are shown on Figure 3.7.4A to represent the envelope of possible $A^{14}C_{SP}$ produced by these ecotones, constructed using the Southern Hemisphere $A^{14}C_{ATM}$ curve from Wellington, New Zealand (Manning and Melhuish, 1994) and a DCP of 7%.

$A^{14}C_{SP}$ measurements are shown on Figure 3.7.4A; the placement of these values on the time-scale is roughly based on the estimate that the calcite sampled along this growth axis is equivalent to approximately 100 years, based on the average growth rate (< 45 µm/a) estimated from the basal U-series age measurement of 3.7 ka (which is a maximum age due to low $^{230}Th/^{232}Th$) and the collection year A.D.1996. The DCP of 7% is underestimated for FC-S3 as FC-S3 6-9D are much lower (84-89 PMC) than the model shows (95 PMC). If the time span estimated from the growth rate based on the U-series data (100 years) is close to the true span, then FC-S3 6D-9D probably formed prior to nuclear weapons testing, which would suggest the DCP at this time was approximately 14%, which agrees well with estimates given in other studies reviewed by Genty and Massault (1997). Altering the model for a DCP of 14% produces the curves shown in Figure 3.7.4B, which results in a closer agreement between the measured and modelled $A^{14}C_{SP}$. However, as the results from FC-S3 do not express a rise, plateau and fall in $A^{14}C_{SP}$, either because FC-S3 ceased growing before $A^{14}C_{SP}$ peaked, or because the sampling resolution is too coarse to resolve this, it is not possible to constrain the age of 1D and 2D better than anywhere between A.D.1965-1995, resulting an age estimate for the top of FC-S3 of A.D.1980 ± 15 years.

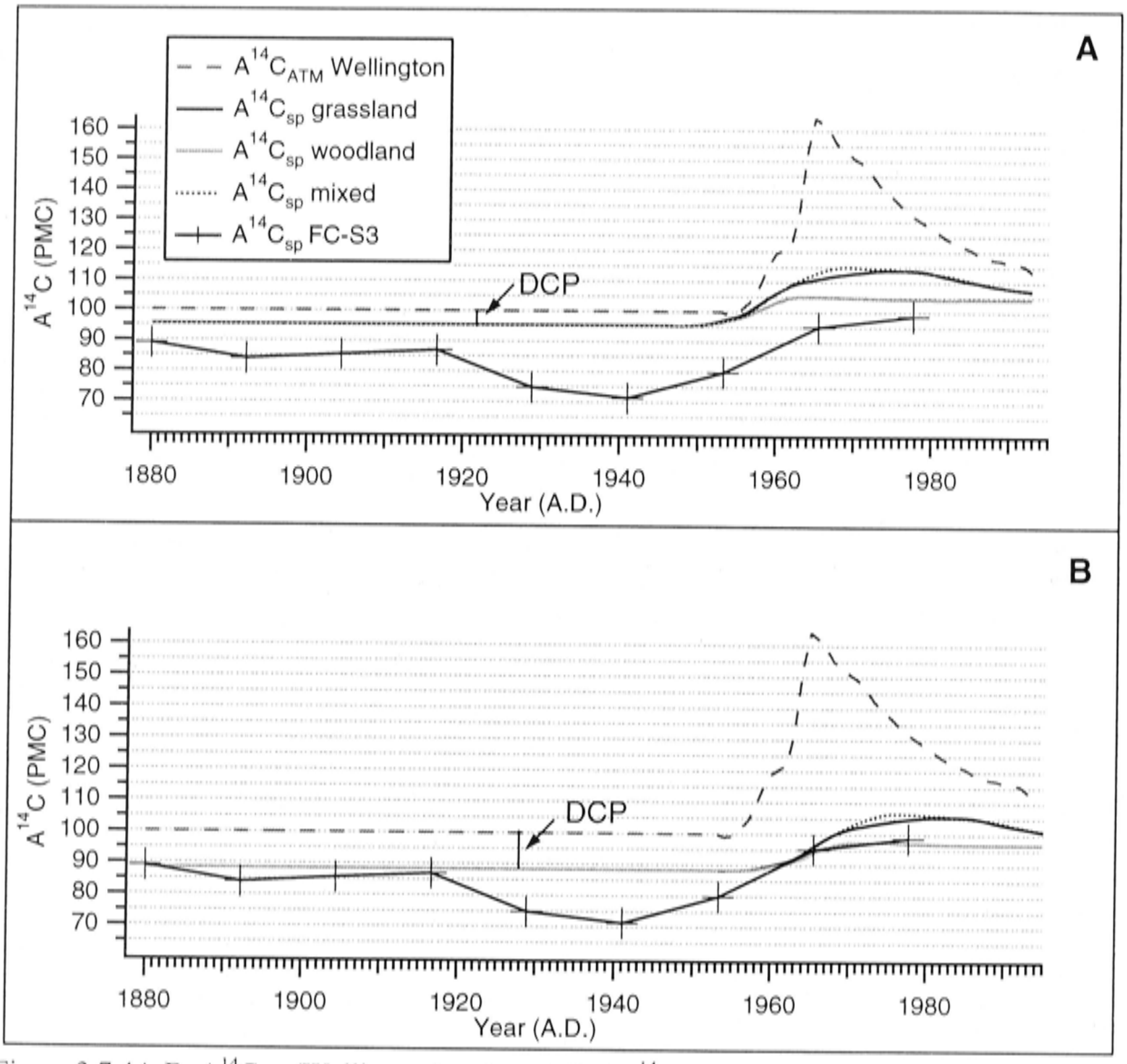

Figure 3.7.4A-B: $A^{14}C_{atm}$ (Wellington) and modelled $A^{14}C_{SP}$ for a DCP of 7% (A) and 14% (B).

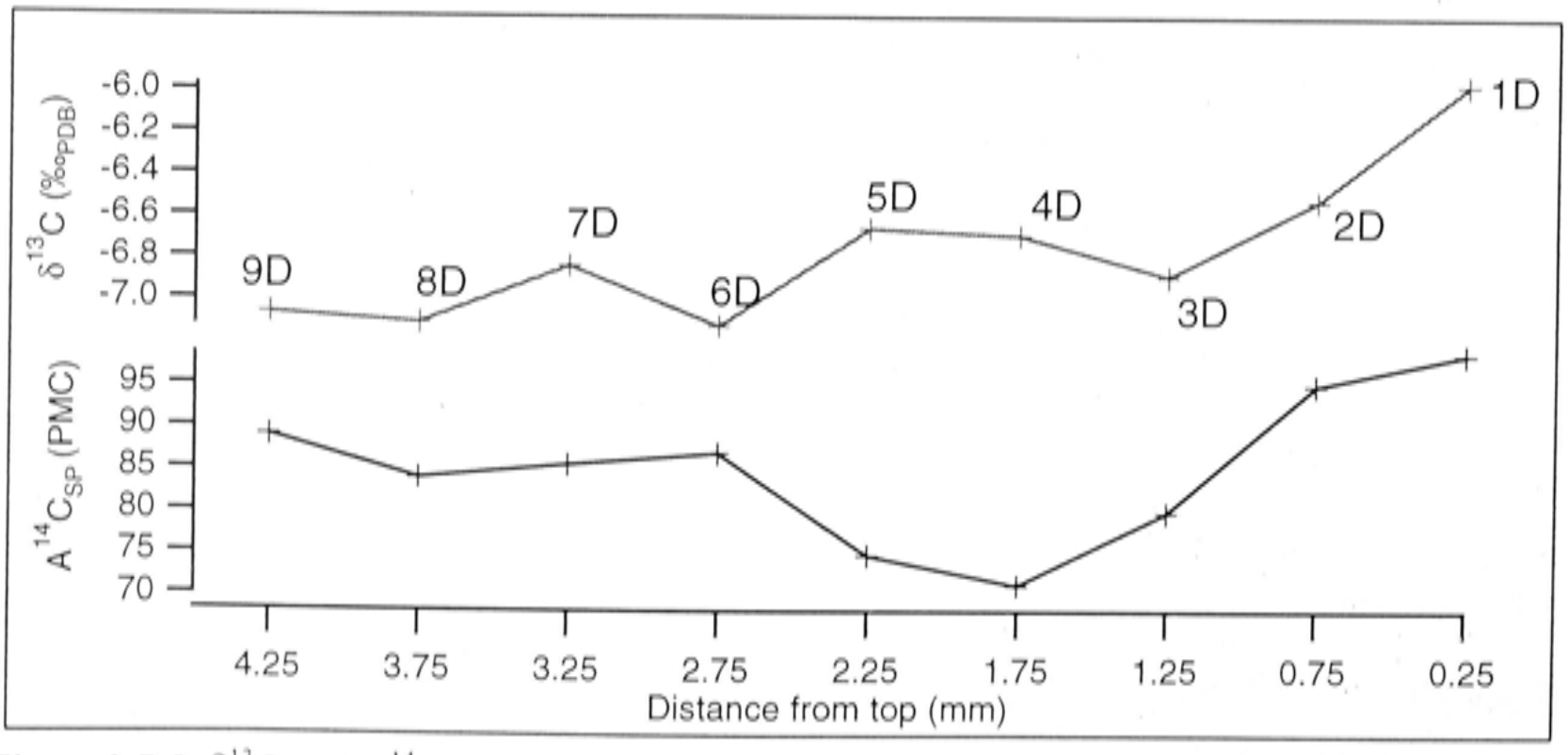

Figure 3.7.5: $\delta^{13}C$ and $A^{14}C_{SP}$ measurements for samples FC-S3 1-9D.

The depression in $A^{14}C_{SP}$ values between ~A.D.1920-1960 corresponds to a DCP of 30%, which may be due to an increase in slow turnover organic carbon or increase in inorganic C. An increase in inorganic carbon would result in a correlation between DCP and $\delta^{13}C$, as the greater uptake of limestone C would also be reflected in the $\delta^{13}C$ values (Genty *et al.*, 2001). Such a relationship may be appropriately investigated here, since stable isotope and $A^{14}C_{SP}$ measurements were performed on aliquots of the same sample and are thus coeval. The Pearson's correlation coefficient for $A^{14}C_{SP}$ and $\delta^{13}C$ is only moderate and not significant at $p < 0.1$ ($r = +0.4$). However, Figure 3.7.5 shows that $\delta^{13}C$ does shift to slightly heavier values when $A^{14}C_{SP}$ is lower (FC-S3 5-3D), although this enrichment is small (+0.4‰). Increasing the (inorganic) DCP from 14 to 30% produces a enrichment of 4‰ in $\delta^{13}C$ of the C species in drip-water, and thus the lower $A^{14}C_{SP}$ values are more likely to be due to an injection of older organic C.

A possible mechanism for injecting old C into the drip-water at samples 5-3D are large bushfires in the Florentine Valley documented for A.D.1807, 1934 and 1948 (Gilbert, 1958), and clear felling and regeneration burning between A.D.1976-1978 (R. Eberhard, *pers. comm.*). Logging and burning vegetation readily converts 'old' organic matter into SOM, raising the relative contribution of old C greatly. This effect would be greater for logging as a greater proportion of the oldest material (core of the trunk) would be added to the SOM. The $A^{14}C_{SP}$ depression is less likely to reflect the A.D.1976-78 logging/regeneration burning, as the speleothem extends 2.5 mm in height above sample 5D, which would be equivalent to ~60 years of growth, if the true growth rate is close to the average growth rate calculated earlier (45 µm/a). Moreover, there is no hint of higher $A^{14}C_{SP}$ due to the bomb-spike prior to 5D which would be expected if the beginning of this depression began ~A.D.1976.

For now, it can only be concluded from the $A^{14}C_{SP}$ measurements that the top of FC-S3 formed post-A.D.1956, and that the modelling study may further constrain this estimate by placing the depression in $A^{14}C_{SP}$ at 5D (2.25 mm below the top) at either A.D.1934 or 1948. Allowing for time to form another 2.5 mm of calcite, any of these later constraints would suggest that FC-S3 ceased growing just prior to its collection in A.D.1996, however, until the timing of the depression can be better constrained, it is only reasonable to suggest that FC-S3 ceased growing post-A.D.1965.

3.8 SUMMARY

This study employed U-series disequilibrium and radiocarbon age measurements to provide a chronology framework for speleothem deposition, so that palaeoclimatic signals such as those derived from O isotope analysis, may be placed within a reliable chronological framework. Samples that were relatively free of allogenic contamination were able to be dated by U-series methods. However MK-F1, suffering from both low ^{238}U and high allogenic mineral contamination could only be dated by conventional radiocarbon dating methods. Where both methods were employed on the speleothem ES-F1, the comparison of age measurements suggested that reliable radiocarbon age measurements could be obtained for ~22 ka to Holocene age speleothems. However, two of the three radiocarbon age measurements for MK-F1 fall outside the accepted range that may be calibrated to radiocarbon years and thus are subject to greater uncertainty.

AMS radiocarbon age measurements along the growth axis of FC-S3 enabled the top of FC-S3 to be constrained to an age of post-A.D.1965 years. In this low ^{230}Th speleothem with significant allogenic contamination, radiocarbon age measurements proved to be more precise and accurate than U-series age measurements.

CHAPTER FOUR

METHODS

4.1 RAINFALL METHODS

4.1.1 Rainfall collection

Samples collected for this study

Rainfall samples collected for $\delta^{18}O$ analyses come from sites near speleothem study areas: Cape Grim, Mole Creek and Hastings (Tasmania), Cape Leeuwin Lighthouse (southwestern Australia), Mt Arthur (South Island New Zealand) and also unpublished data from Margate, Tasmania (Prof W. F. Budd, University of Tasmania) (Figure 2.1.5, Chapter 2). Samples were collected at all sites as surface event rainfall and in addition at the Hastings and Mole Creek locations, simultaneous collections were taken of monthly surface and cave drip-water. The collection of these samples was made possible with the kind assistance of Mr Chester Shaw (Tasmania Parks and Wildlife Service), Mr Robin Wass (Tasmania Parks and Wildlife Service), Mr Larry Porter (Cape Grim Baseline Air Pollution Station), Mr Chris Morgan (Hortresearch, New Zealand) and Mr Paul Sofilas (Cape Leeuwin Lighthouse, Western Australia).

Event-based rainfall collections were taken from a 1 litre Nalgene bottle fitted with a funnel in which sat a plastic ball acting as a valve to minimise evaporation (the ball was prevented from blowing out of the funnel by wiring it through the neck of the funnel to a button larger in diameter than the funnel neck). The water sample was collected by emptying the Nalgene bottle into a 10 ml amber glass bottle with polypropylene lid. The seal of the bottles was improved by wrapping teflon tape around the thread of the bottle before it was capped tightly. Further measures were taken to minimise evaporation by storing the bottles upside down in refrigeration where possible. Monthly rainfall collections were collected from a 25 or 60 l polypropylene drum fitted with a funnel. In the later case, evaporation was minimised by the addition of a thick film of paraffin oil floating on the water surface. A sample of the drum water was collected each month in a 50 ml amber glass bottle in the same manner as the event samples. The drum water was

emptied by opening a tap at its base so that the water could escape while retaining most of the paraffin oil. The oil was changed if spoiled by algae or faeces.

4.1.2 Water isotope methods

$\delta^{18}O$ analysis by off-line equilibration technique at RSES

$\delta^{18}O$ analysis by off-line equilibration technique was performed at the Research School of Earth Sciences (RSES) following methods established by Dr M. K. Gagan. 2 ml aliquots of water were transferred to 20 ml blood serum vials inside a glove bag flushed with CO_2 of known isotopic composition at atmospheric pressure. The H_2O in each vial is then equilibrated with the CO_2 in a constant temperature (25°C) water bath for 30-40 hours. The CO_2 is then extracted into an evacuated line where it is purified firstly by a dry ice/ethanol trap to remove water and secondly by liquid nitrogen to remove volatile organic vapours. The CO_2 is sealed into a pyrex tube which is later broken in a multiport device connected to a Finnigan MAT 251 mass spectrometer. The sample CO_2 peak is measured alternately against that of a reference gas with the dual inlet system of the MAT 251. The $\delta^{18}O$ composition is calculated according to Equation 4.1.1

$$\delta^{18}O_{sample} = \left(\frac{R_{sample}}{R_{reference}} - 1 \right) \qquad (4.1.1)$$

where R is the ratio $^{12}C^{18}O^{16}O:^{12}C^{18}O_2$; $R_{reference} = +0.63 \pm 0.07‰_{VSMOW}$.

Finally, the $\delta^{18}O$ content of the sample is corrected to that of the known internal standards run (here ANU-HP1 and either ANU-OW1 or ANU-LP2 kindly supplied by M. K. Gagan, RSES ANU) which had been calibrated to the external standards SLAP (-55.5‰$_{VSMOW}$) and GISP (-24.82‰$_{VSMOW}$). One standard error is typically 0.3‰.

ANU-HP1	-5.54‰$_{VSMOW}$
ANU-OW1	+0.50‰$_{VSMOW}$
ANU-LP2	-11.95‰$_{VSMOW}$

$\delta^{18}O$ analysis at the Research School of Biological Sciences (RSBS)

The quantity of rainfall event samples collected for this study was too great for all to be measured by the off-line CO_2 equilibration technique at RSES. Instead, $\delta^{18}O$ analysis was conducted at the Research School of Biological Sciences (RSBS) using on-line pyrolysis which provides a rapid sample turn-over with the sacrifice of some precision (one standard error is 0.5‰$_{VSMOW}$).

The method of $\delta^{18}O$ analyses at RSBS is documented in Farquhar *et al.* (1997). Briefly, 0.7μL of water is injected into a tin cup flushed with argon and immediately crimp sealed. The ^{18}O:^{16}O content is determined by decomposing the H_2O by pyrolysis at 1080°C over a nickelized carbon column to carbon monoxide (CO), which is then oxidised to CO_2 using iodine pentoxide. A stream of ultra-high purity helium (He) carries the CO_2 through a gas chromatograph column, where it is separated from other gases (primarily N_2), and into a Micromass Isochrom mass spectrometer. The $^{12}C^{18}O$:$^{12}C^{16}O$ ratio is calculated relative to a known CO reference gas which is injected briefly before the sample CO peak arrives (background is achieved before arrival of sample gas). The $\delta^{18}O$ content of the sample is then determined using Equation 4.1.1 and is reduced to $\delta^{18}O_{VSMOW}$ using the internal standards, ANU-HP1, ANU-OW1 and ANU-LP2.

Significant delays were experienced in obtaining reproducible data from the on-line pyrolysis technique. Achieving routine internal precision (σ < 0.5‰) relies on minimising the memory effects thought to arise from the adsorption or slow release of O from the nickelized carbon packing in the pyrolysis column. These effects are minimised by changing the column packing after 400 samples have been run (Farquhar *et al.*, 1997). Unfortunately, for the duration of access to this equipment, these memory effects were significant through much of the life of the column and poor internal precision (> 1-2‰) and poorer external reproducibility (often >2‰) resulted. Several sources of error including such as sample quality and user variation in sample pippetting were checked; however, filtering samples and having experienced technicians load the samples did not resolve what was probably a technical problem with the mass spectrometer or pyrolysis unit. In the end, the only precaution that could be taken was to run triplicate samples; the

first to 'prime' the column with the $\delta^{18}O$ composition of the sample, and then average the following two samples. The standard error resulting from this was typically ~1‰.

4.2 SPELEOTHEM SAMPLE PREPARATION

4.2.1 Mass spectrometry stable isotope analyses

Sections of speleothem for sampling were cut into slabs typically ~1 cm thick. These sections were cleaned by ultrasonic agitation in MQ H_2O and were mounted on a motorised stage that could be manoeuvred in x and y directions beneath a machine mill dedicated to carbonate micro-sampling. As a further pre-cleaning step, the outer material of the slab were removed by continuous milling along the faces forming the edge to be sampled. Typically, samples weighing several micrograms were milled every 0.5 mm along this edge with a cross-sectional area of 2 x 2 mm using a 2 mm diameter tungsten-carbide drill bit and pre-programmed coordinate commands (Figure 4.2.1). This follows the general method used for sampling corals at RSES (Gagan *et al.*, 1994).

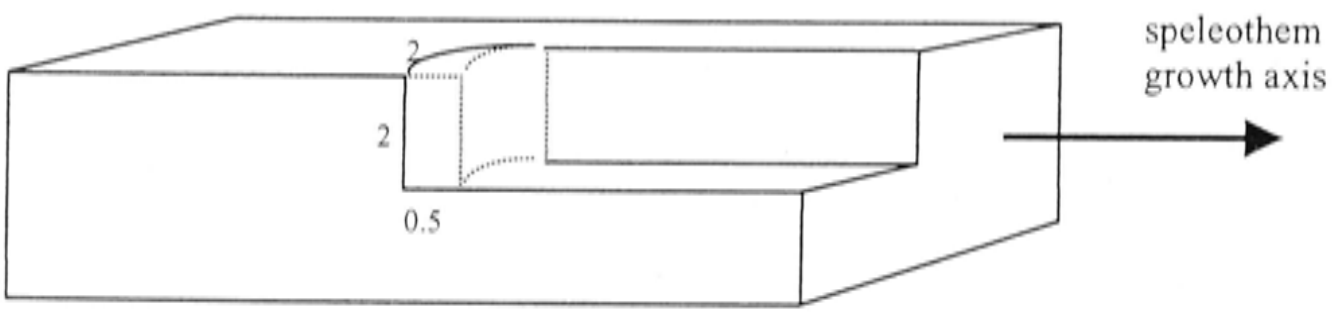

Figure 4.2.1: Sampling procedure for conventional stable isotopes. Units are in mm.

4.2.2 LA-ICP-MS and ion microprobe

Using a 300 µm wafer saw, samples were cut to size for epoxy-mounting in either 7.5 x 2.5 cm sections for Laser Ablation Inductively Coupled Plasma Mass Spectrometer (LA-ICP-MS) or 2.5 cm diameter discs if both LA-ICP-MS and ion microprobe techniques were used. To minimise sample loss due to saw cuts, samples were sub-divided by cutting obliquely to the growth axis as shown in Figure 4.2.2. This enabled the samples

to be divided without loss of data since the last analyses of one track would be repeated as the first analyses on the next section. This also assisted in registration when reassembling or 'stitching' data sections into one array by matching data trends and checking by measuring the overlap of matching growth bands. Typical saw cuts were 300 µm wide and sequential track offsets were ~0.5 to 1.0 mm allowing for ~200 to 700 µm of data overlap.

Samples were mounted in epoxy and polished with 1200 grade sanding paper followed by 12 µm paper and finally on a Kent polisher using 1 µm diamond paste. They were then cleaned by ultrasonic agitation in AR grade alcohol and MQ H_2O.

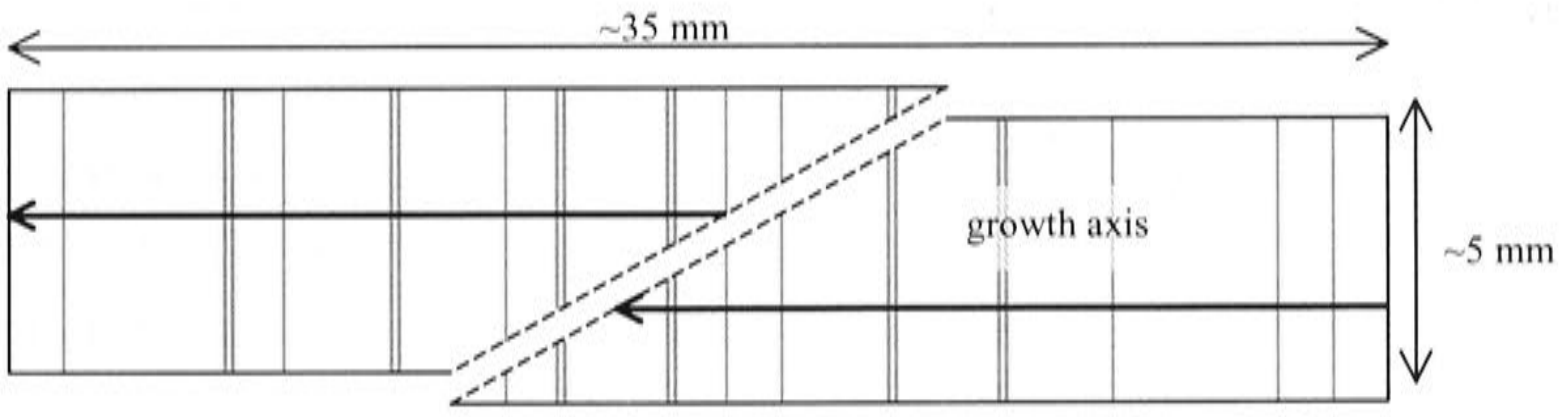

Figure 4.2.2: Samples were cut obliquely and the analyses were conducted along tracks (indicated by arrows) that were laterally offset such that the start and end of each track overlapped enabling sequential tracks to be 'stitched' together. (Grey lines indicate hypothetical growth layers.)

Registration between LA-ICP-MS and ion microprobe data was achieved by creating a scale by timing the Excimer laser, masked to 5 x 50 µm, to fire for every 50 µm of stage travel. This scale was used as a 'ruler' to determined the co-ordinates of a ion microprobe pit relative to the beginning of a LA-ICP-MS track. Figure 4.2.3 shows the ion microprobe pits alongside the 'ruler' and LA-ICP-MS track.

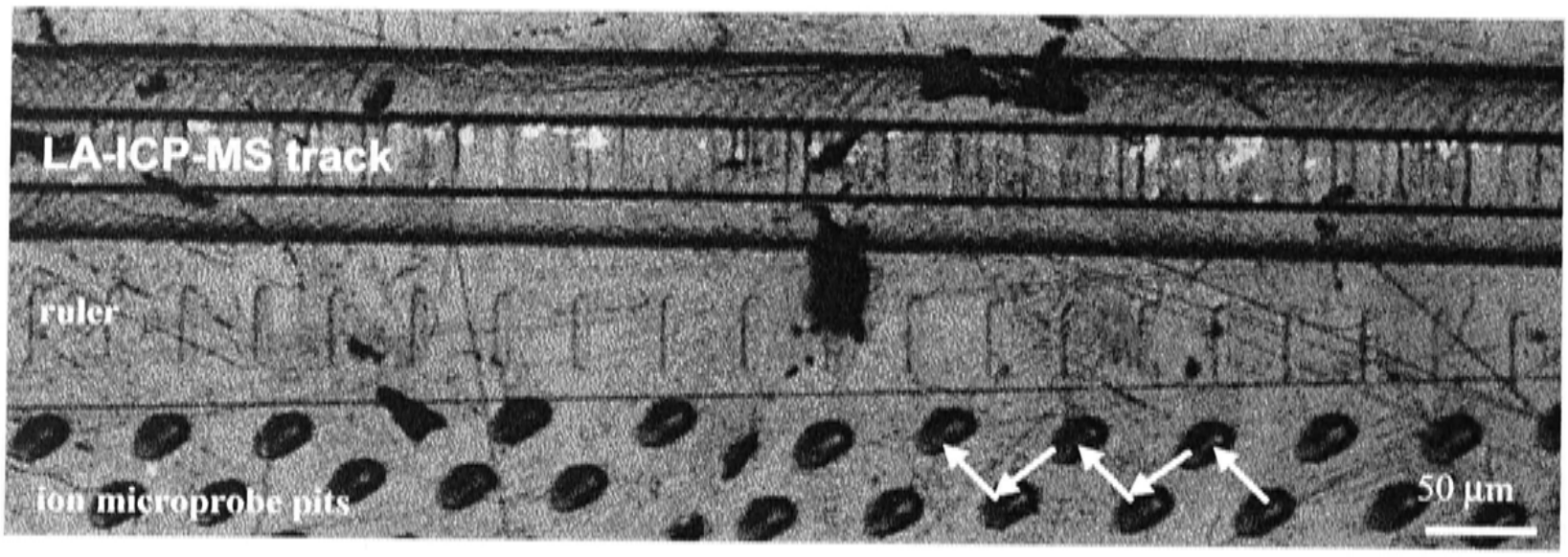

Figure 4.2.3: Registration of ion microprobe pits alongside LA-ICP-MS track by 'ruler' created by firing the laser at 50 µm intervals. The LA-ICP-MS track shows that the data acquisition track (50 µm) is ablated inside a previous track (~120 µm) that was created by ablating the surface twice to remove contaminants. Arrows indicate the order and direction of ion microprobe analyses that form a ion microprobe 'track' referred to in text.

4.3 Trace Element Methods

4.3.1 LA-ICP-MS

Trace element data were measured using the 193 nm Excimer LA-ICP-MS at RSES, ANU (described by Sinclair *et al.*, 1998; ICP-MS is model Agilent 7500s). The epoxy-mounted samples were held inside a motorised micrometer stage under the Excimer laser which was masked to a desired circular or rectangular spot. To achieve a high resolution sampling interval, the motor was run at 1 mm/min while the laser was pulsed at high frequency (20 Hz). This produced a data set close to continuous scanning mode. National Institute of Standards (NIST) glass standard (612) was used to correct the data to absolute concentrations adopting values of Pearce *et al.* (1996). Matrix effects arising from employing a glass matrix to correct for a carbonate matrix (*e.g.* Sinclair *et al.*, 1998) may be a significant problem if precise absolute concentrations are needed. However, the primary interest in this study is not the absolute concentration but the relative variation of the trace elements on inter and intra-annual scales and thus the interpretation of the data produced in this study is not affected by matrix dissimilarities between the sample and standard.

In choosing a spot size, trade-offs must be made to achieve comparable sensitivity over the measurement range of ~0.2 ppm (^{238}U) to 54 000 ppm (^{43}Ca) (a large dynamic range

may be analysed with the quadrapole ICP-MS by a dual electron multiplier which operates simultaneously in the analogue and pulse modes; Thomas (2002)). The highest resolution work attempted here (5 x 50 μm slit) was restricted to the most abundant elements: Mg, Sr, Ba, whereas elements such as U and P could only be measured with a spot size of at least 32 μm. Figure 4.3.1 demonstrates that trends produced by 32, 54 (spots) and smoothed 5 x 50 μm slit are very similar; but it appears that more subtle features are suppressed, such as the initial decrease in mean Ba concentration in the 0 to 0.5 mm using the 54 μm spot due to averaging over the ablation area, but also information using the highest resolution (5 x 50 μm slit) is lost due to smoothing during data reduction. In this instance, the most appropriate spot is 32 μm which captures as much peak-to-trough variation as the smoothed 5 x 50 μm slit and also second-order trends. In general, the data presented here are produced by firing the 100 mJ laser at 20 Hz to produce a 32 μm spot. 7 elements (^{43}Ca, ^{25}Mg, ^{138}Ba, ^{88}Sr, ^{31}P, ^{23}Na, ^{238}U; and additionally ^{27}Al and ^{29}Si for the mapping exercises) were counted sequentially in the quadrapole mass spectrometer over counting intervals of 0.05 s for each element. Measurements of B, S, Mn, Fe, Y, La, Ce and Th were also attempted but were not present in sufficient quantities at any resolution.

Finally, later analyses performed to map sections of MND-S1, were run without H present in the carrier gas flow. H is commonly added to the carrier gas as it increases the sensitivity of the LA-ICP-MS, possibly by increasing the ionisation of the ablated material by the energy released when hydride bonds are broken and reformed in the plasma, however the exact reason is unknown (J. M. G. Shelley, *pers. comm.*). While the presence of H may increase the general analytical sensitivity it can have a detrimental effect on elements with a mass interference with hydrides that are abundant in the carrier gas *e.g.* ^{23}Na and $^{22}Ne^{1}H$. Since the co-variation of Na with the other elements was of

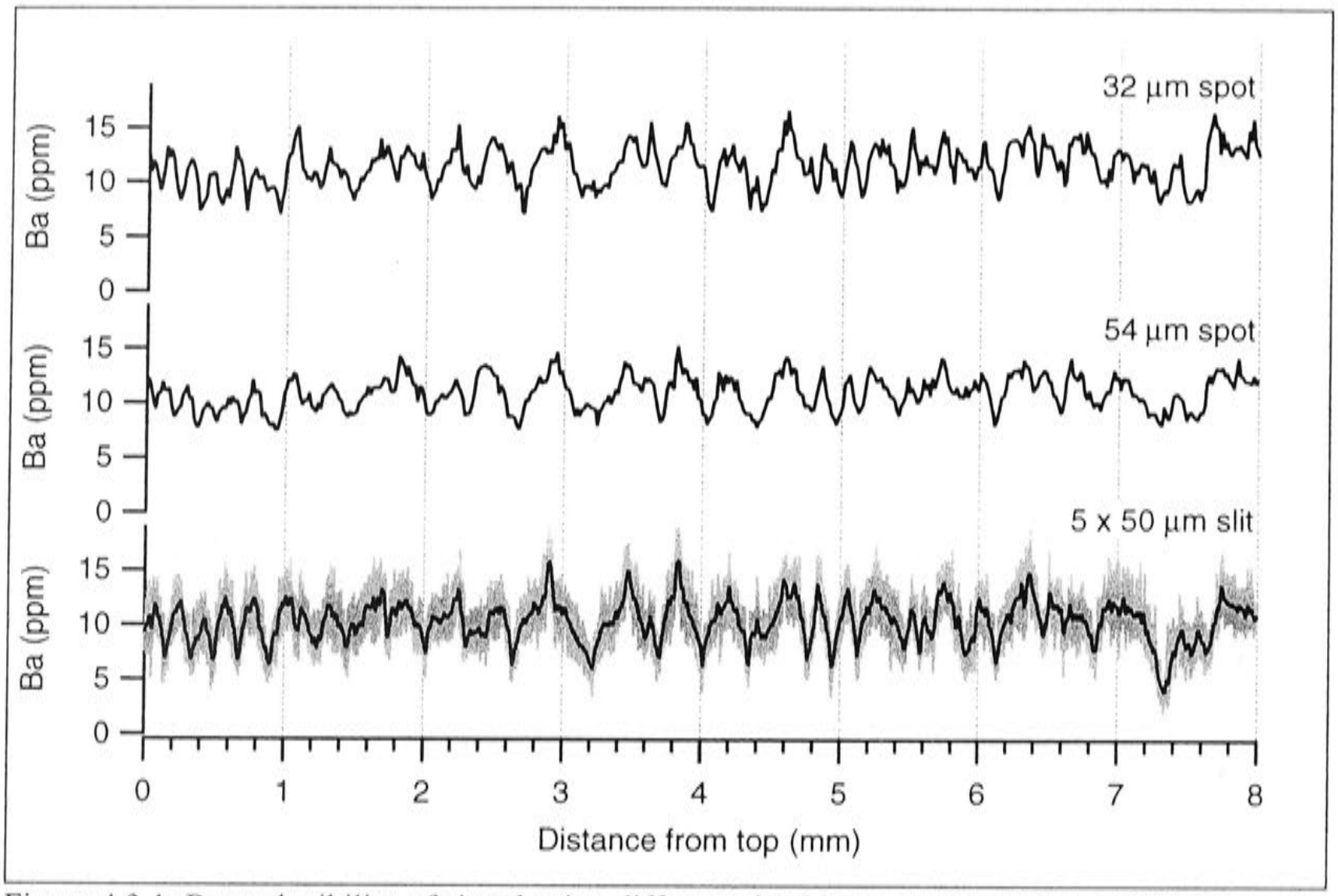

Figure 4.3.1: Reproducibility of signal using different sized laser masks. 32 µm and 54 µm spots are raw data. 5 x 50 µm slit is raw data shown in grey with black smoothed line.

interest to this study, the mapping exercises shown in Chapter 5 were conducted without H. For these exercises, the relative sensitivity of the other elements appears unaffected by the absence of H.

4.3.2 LA-ICP-MS data reduction

Firstly, data were corrected for background counts by subtracting the interpolated slope between backgrounds measured before and after the sample run. Sample runs included measurements of NIST-612 before and after the sample run. For the elements presented here, the backgrounds were typically insignificant (<1%). Drift was corrected by a linear interpolation between standard counts measured before and after the sample. Both standard and sample data were then smoothed with a 3-point moving box to dampen outliers before being corrected for fluctuations in beam intensity or the volume of $CaCO_3$ ablated, by dividing the both sample and standard counts by Ca counts (here Ca counts are used as an internal standard). The metal/Ca ratio is then converted to absolute concentrations using Equation 4.3.1.

$$\text{Sample conc.}(\text{nmolg}^{-1}) = [\text{Ca}]_{SA} \times \left[\frac{\text{X}}{\text{Ca}}\right]_{STD} \times \left(\frac{I_x}{I_{Ca}}\right)_{SA} \Big/ \left(\frac{I_X}{I_{Ca}}\right)_{STD} \qquad (4.3.1)$$

Where X is the element being measured and I is the signal intensity; SA denotes sample and STD denotes NIST standard; square brackets denote concentration. $[Ca]_{SA}$ is assumed to be 40.04%w/w and $[Ca]_{STD}$ is 8.47%w/w.

Initially, ^{46}Ca was used as the internal standard as it was present in sufficiently low quantities to be measured in pulse mode (thus avoiding potential uncertainty in applying a pulse-analogue conversion factor since many elements of interest were acquired in pulse mode). However, it was realised that an isobaric interference with ^{46}Ti had been overlooked, which had little impact on the sample counts as it contains negligible Ti, but the NIST-612 glass standard contains significant Ti concentrations (the ratio of absolute abundance of ^{46}Ti to ^{46}Ca in the NIST-612 glass is 1:1), thus halving the apparent concentrations of the sample. The choice of internal standard was switched to ^{43}Ca which is free of such interferences but its higher abundance ($^{43}Ca/^{46}Ca$ is 33.75) meant it was restricted to analogue counting.

Further data quality checks involved patching sections where large fluctuations in Ca had occurred, with smoothed values. This was considered necessary since it was apparent, irrespective of whether Ca was measured in either analogue or pulse mode, that it did not vary proportionately with other isotopes when the variation in Ca was large, *i.e.* mass bias. This is illustrated in Figure 4.3.2. The upper section of this Figure (4.3.2A) shows two troughs in Ca counts which coincide with troughs in Mg and Sr counts. Ratioing to Ca produces two peaks in Mg but two troughs in Sr that are obviously an artefact of the correction process (4.3.2B). Peaks and troughs are of primary interest to this project and it is alarming that data reduction methods produce such artefacts.

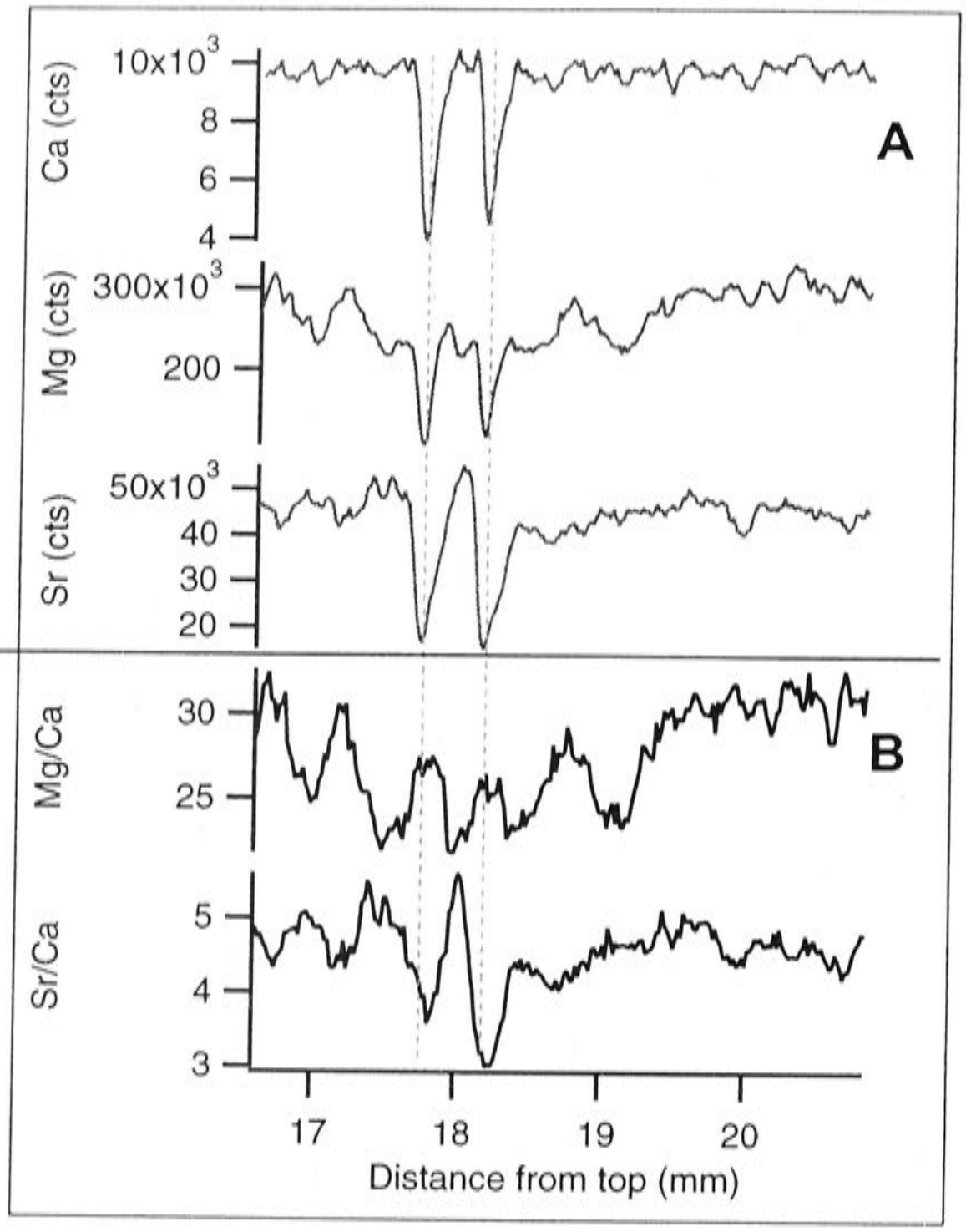

Figure 4.3.2A-B: Correcting for beam fluctuations in Ca may enhance undesirable mass bias effects if the Ca concentration changes by a large amount. In the case here, large drops in Ca due to holes in the surface produce significant peaks in Mg/Ca and significant troughs in Sr/Ca ratios. ('Cts' are raw sample counts.) In the final record, these sections were carefully patched with smoothed data.

Finally, all 32 μm spot data were twice smoothed by a 9-point second-order Savitzsky-Golay filter. Filters were 'bounced' at the beginning and end of data arrays to reduce edge effects. Considering that 1800 data points were produced per mm of sample, this smoothing method only suppresses variations with wavelengths considerably smaller than features of interest in this data.

4.3.3 Mapping LA-ICP-MS data

Multiple adjacent scans were performed to check the spatial homogeneity of the elements of interest. In general, trends were reproduced in adjacent tracks although, there were often variations in smaller amplitude features, which are analogous to 'false rings' or 'missing rings' in dendrochronology (*e.g.* Fritts, 1976). It is therefore, insufficient to perform just one scan, and similar to the principles of dendrochronology,

multiple scans need to be appropriately unified to produce one 'master' sequence that encompasses the trends common to all or most scans but also reduces the variability where sections are less reproducible. Two methods were investigated to do this:

1. Contour mapping by loading the data into spatial contouring software in x, y, z format; where x and y are 2-D coordinates and z are element concentrations. This method has the advantage that an anisotropy could be dictated when smoothing the data grid. This allowed for preferential smoothing in the direction of greater variability (across adjacent tracks rather than along the tracks). This had the effect of minimising noise and maximising their contrast with common, larger amplitude signals. Typically the smoothing method used here was a 3-point triangulation smoother.
2. Stacking the data by subjectively matching peak and trough patterns between adjacent scans. The criteria used to assess matching patterns was loosely based on the methods of dendrochronology (Fritts, 1976; Schweingruber *et al.*, 1990), except that here multiple scans of the same stalagmite rather than multiple independent specimens (*i.e.* a stand of trees) are being used. The emphasis in this method was on capturing distinctive cycles common to most scans ('pointer years'; in this case, usually the largest amplitude cycles), as well as sections where longer trends were reproducible, regardless of the amplitude of the cycles ('pointer intervals' or 'signatures'). In the case where multiple distinct cycles in most scans merge into a single broad peak in one or a few scans, the distinct cycles were retained and the broader peak was omitted. Minor cycles were also omitted if they appeared to be false cycles. These cycles were matched by numbering, then interpolated to 12 points using Analyseries (Paillard *et al.*, 1996), and stacked by calculating an average and standard deviation value for each point in matched cycles.

The first method (contour mapping) was more appropriate for investigating the relationship between crystal habit and element concentration and elemental homogeneity along growth banding. The second method (stacking) was far more time consuming but eventually deemed necessary for constructing a master sequence. The obvious disadvantage is that it is more subjective, and it also may overlook years when growth was limited, affecting the timing or chronology of the master sequence. For this reason, quantitative comparison with instrumental climate data may be difficult. However, it is

sufficient to investigate the parity between instrumental and speleothem data, and more rigorous statistical dendro-techniques could be investigated at a later stage.

4.4 Stable isotope methods

4.4.1 Conventional on-line mass spectrometer analyses

Approximately 200 μg of each sample was weighed out for isotopic analysis. Samples were run on a Finnigan MAT 251 mass spectrometer fitted with a Kiel extraction device. The reaction is performed in the Kiel device at 90°C by the addition of saturated (anhydrous) H_3PO_4 to produce CO_2 gas, which is purified in liquid nitrogen traps and measured alternately against a reference gas on the dual inlet system of the MAT 251, where ^{18}O:^{16}O of the sample and unknown are measured in static mode on Faraday cups for a total of 4 cycles. The data are presented relative to the V-Pee Dee Belemnite (VPDB; Coplen, 1994) standard corrected against the standard NBS-19 and NBS-18, so that the presentation of data is equivalent to that of the CO_2 prepared by the McCrea (1950) method at 25°C for more than 8 hours in 105% H_3PO_4. NBS-19 is enriched relative to VPDB by $\delta^{18}O$ = -2.20‰ and $\delta^{13}C$ = +1.95‰ and NBS-18 is enriched relative to VPDB by $\delta^{18}O$ = -23.00‰ and $\delta^{13}C$ = -5.00‰.

4.4.2 Ion microprobe analyses

Oxygen isotopes were measured on the Cameca ims-1270 microprobe at the Department of Earth and Space Sciences, University of California Los Angeles in collaboration with Prof. T. M. Harrison, Prof. K. D. McKeegan and Dr M. Grove.

Samples were sputtered with a ~ 2nA Cs^+ primary beam to produce negative secondary ions with a mean intensity of ~2.5×10^9 cps (^{16}O) and ~6.5×10^6 cps (^{18}O) from a crater of approximately 20 μm in diameter. ^{18}O and ^{16}O were collected simultaneously in Faraday cups positioned in multi-collection mode after pre-sputtering the area for 180 s. Signals were measured for 10 blocks which yielded a typical internal precision of 0.09‰ (1 σ).

Each analysis took approximately 5 mins. Background measurements were performed for approximately every 10 unknowns but were insignificant when subtracted from sample measurements. $\delta^{18}O$ analysis on the Cameca ims-1270 is described in more detail in Fayek *et al.* (2001) and McKeegan *et al.* (2002).

Successive samples were spaced approximately 40 μm apart. This was necessary as secondary ion generation and trajectories are sensitive to topography created by analysis pits. These effects are particularly strong for insulating materials since they require charge neutralisation by flooding with a normal incidence electron gun in addition to Au coating. With these limitations in mind, achieving the highest possible sampling resolution without introducing topographic effects, was done by offsetting the analysis pits at a 45° angle from the previous, such that the pits lay in a zig-zag pattern along the axis of speleothem growth (Figure 4.2.3).

Analyses were corrected to the VPDB scale using the mean bulk $\delta^{18}O$ determined from conventional analyses (section 4.2.1). While it would have been desirable to measure a standard on the same mount, it was not possible in the short time available for these analyses, as the mounts were prepared at RSES where only standards NBS-18 and NBS-19 were available. It was not certain whether these standards would be have been appropriate, as their homogeneity on the scale of the microprobe measurements was unknown. It was decided that correcting the results to the mean bulk $\delta^{18}O$ of the sample which had been standardised as described in 4.3.1 would be sufficient for this pilot study, since the aim of this experiment was to assess reproducibility of trends in adjacent tracks in order to evaluate the suitability of this technique for very high resolution analysis of speleothem $\delta^{18}O$.

4.5 Sr isotope and concentration methods

Samples used for Sr analyses were aliquots of the powders milled for conventional $\delta^{18}O$ and $\delta^{13}C$ analyses. Approximately 300 μg of $CaCO_3$ were weighed into teflon beakers along with 0.1 g of spiked solution (LORBSR; RSES internal standard) to yield an approximate $^{84}Sr/^{86}Sr$ ratio of 1. The sample was dissolved in concentrated HNO_3 and

evaporated to dryness. The spiked sample was then redissolved in 0.5 ml 2N HNO_3 before being loaded onto a micro-column containing pre-cleaned "Sr spec" anion exchange resin. Following successive washings with 2N HNO_3, the spiked sample is eluted with MQ H_2O and evaporated to dryness.

Approximately 1.5 µl of TaF_5 solution (containing also HF, HCl and H_3PO_4) is loaded onto a single outgassed Re filament. Approximately 100 ng of the purified spiked sample is dissolved in 2 µl of 1N HNO_3 and loaded into the TaF_5 solution. This solution is evaporated to dryness by passing a current of 0.8 A through the filament. The filament is finally flashed to 1.6 A.

Loaded filaments were run on a Finnigan MAT261 operating in static mode. Data were acquired by measuring masses ^{88}Sr, ^{87}Rb, ^{86}Sr, ^{85}Rb and ^{84}Sr in Faraday cups after the ^{88}Sr signal had risen to 3 V.

CHAPTER FIVE

$\delta^{18}O$ OF SOUTHERN AUSTRALIAN RAINFALL

5.1 INTRODUCTION TO WATER ISOTOPES

5.1.1 Why water isotopes were investigated

This Section reviews the climatic effects leading to fractionation of water isotopes presented by Dansgaard (1961; 1964) and subsequent authors, as an introduction for the analysis of water isotopes collected for this study across southern Australia and New Zealand (Section 5.2).

Recapping from Chapter 2, Section 2.1; rainfall samples were collected at sites in southwestern Australia, Tasmania and South Island New Zealand to measure their oxygen isotopic composition ($\delta^{18}O_P$), and to examine the relationships between these isotopes and climate. The impetus for this, initially arose from the two lines of investigation pursued for this thesis:

- Firstly, $\delta^{18}O_{SP}$ variation of the Tasmanian Holocene speleothem (FC-S3) was too large to be solely due to cave-temperature, suggesting meteorological precipitation effects were driving $\delta^{18}O_{SP}$.
- Secondly, the opposite sign of speleothem γ, or trend of $\delta^{18}O_{SP}$ with temperature over the LGM-Holocene transition for Tasmanian and New Zealand speleothems, also suggested that precipitation effects were greatly influencing one or both of these records.

5.1.2 $\delta^{18}O_P$ and δD_P properties and mechanisms of fractionation

In 1961 the International Atomic Energy Association (IAEA) established the collection of monthly rainfall samples for isotopic analysis with the cooperation of the globally distributed stations of the World Meteorological Organisation (WMO). This program became the Global Network of Isotopes in Precipitation (GNIP). Dansgaard (1961; 1964) first published these data, presenting the relationships between oxygen and

deuterium isotopic compositions and climatic variables (temperature, rainfall amount, relative humidity). Dansgaard also demonstrated that precipitation became isotopically lighter with cooler temperatures at increasing latitude, following the relationship +0.69‰/°C (Figure 5.1.1). This finding, which led to the hypothesis that the isotopic composition of precipitation was dependent on temperature, persists to today although its appropriate use is debated (Jouzel *et al.*, 1997a; Cole *et al.*, 1999). This is because the temperature relationship is based on a latitudinal gradient, *i.e.* it has a spatial slope, which may have changed over time.

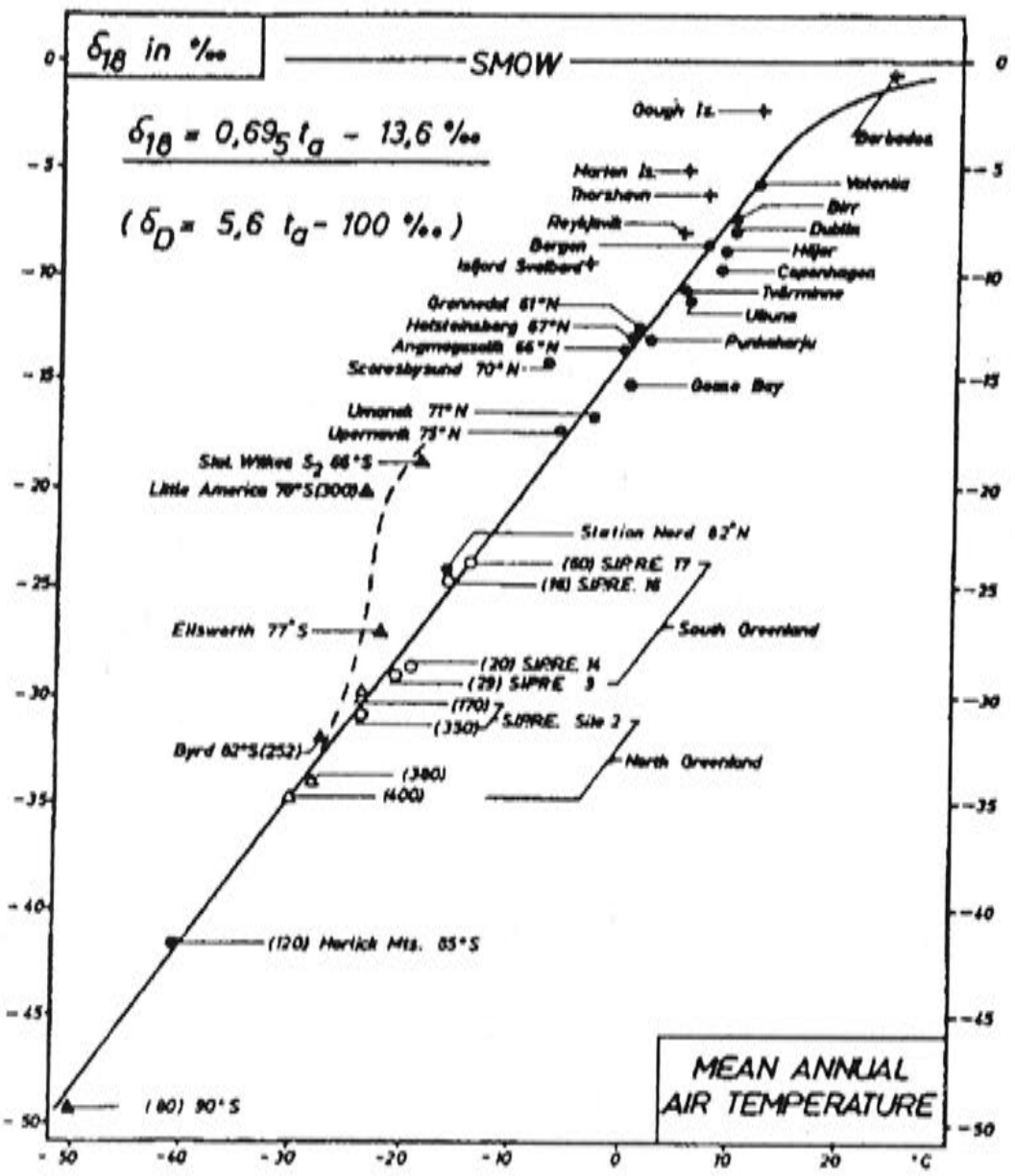

Figure 5.1.1: Relationship between mean annual $\delta^{18}O_P$ and mean annual temperature for an equator-pole gradient. (From Dansgaard, 1964.)

Of all the possible stable isotopes of water, only $^{1}H_2{}^{16}O$, $^{1}H^{2}H^{16}O$ and $^{1}H_2{}^{18}O$ are of measurable natural abundance. The abundance of ^{2}H (or D) and ^{18}O in any species are expressed as a ratio measured relative to that of a known standard, Vienna Standard Mean Ocean Water, VSMOW (Coplen, 1994). The relative distribution of these isotopes in the hydrological cycle (cryosphere, ocean, atmospheric vapour) is distinct since they differ in their relative vapour pressures, P; where $P_{H_2{}^{16}O} >> P_{HD^{16}O}$ or $P_{H_2{}^{18}O}$, hence ^{18}O and D are thermodynamically favoured in a condensed phase, while ^{16}O and ^{1}H are favoured in a vapour phase (Dansgaard, 1961). This fraction, $\alpha_{H_2O_{(g)}-H_2O_{(l)}}$, is therefore temperature

dependent. Values for $\alpha_{H_2O_{(g)}-H_2O_{(l)}}$ (Table 5.1.1), imply that for a vapour-liquid two-phase equilibrium system at 20°C and for a liquid at 0‰$_{VSMOW}$, that the isotopic composition of the vapour will be –80‰ and –9‰$_{VSMOW}$ for δD and $\delta^{18}O$ respectively. Conversely, condensation under isotopic equilibrium will result in condensate enriched by the same magnitude with respect to the vapour.

However, natural systems are rarely at thermodynamic equilibrium, since it requires that the vapour be at 100% relative humidity. If the humidity is less, then excess vapour will be drawn from the liquid-vapour interface, and since the speed of diffusion, D, differs between species (Table 5.1.1), there will be an additional fractionation of the vapour as it moves into the atmosphere. This second fractionation, is termed a kinetic fractionation and is a function of relative humidity rather than temperature.

Table 5.1.1 shows that the equilibrium fractionation is nearly an order of magnitude greater for δD than it is for $\delta^{18}O$ ($\alpha_{HD^{16}O}/\alpha_{H_2{}^{18}O} \sim 9$), while their diffusion coefficients (kinetic fractionation) are roughly the same ($\varepsilon_{HD^{16}O}/\varepsilon_{H_2{}^{18}O} = 0.88$). Thus, δD is more sensitive to equilibrium effects than is $\delta^{18}O$. For this reason, Jouzel (1986) and Jouzel *et al.* (1997) point out that δD should be the preferred species for calculating the degree of equilibrium fractionation *i.e.* temperature. It follows that if both $\delta^{18}O$ and δD can be measured then the magnitude of kinetic effects *i.e.* evaporation may be estimated. In practical terms this is done by calculating the deuterium excess, d_o, defined as $d_o = \delta D - s\delta^{18}O$, where s is the slope of the linear equilibrium or non-equilibrium relationship between δD and $\delta^{18}O$ (Dansgaard, 1964). For both evaporation and conditions under isotopic equilibrium, s = 8.9 (Table 5.1.1). If evaporation is rapid (*i.e.* including kinetic effects) then $s < 8.9$ (since $s = \delta D/\delta^{18}O$ and $H_2{}^{16}O$ is more volatile than $HD^{16}O$). Subsequent condensation will result in $\delta^{18}O$ and $\delta D > 0_{VSMOW}$ and hence a deuterium excess, d_o. Together the three variables; $\delta^{18}O$, δD and d_o can be used to estimate the amount of equilibrium and kinetic fractionation experienced by a parcel of moisture so as to build a more complete picture of source temperatures and relative humidity, and site temperatures (Petit *et al.*, 1991). Databases of modern and palaeowaters may then be used to infer changes in source variation, hence atmospheric circulation through time (Cuffey and Vimeux, 2001).

Table 5.1.1: Properties of water isotopes.

Property	
Mass (a.m.u.; Holden 1991)	
$H_2{}^{16}O$	18.01057
$HD^{16}O$	19.01674
$H_2{}^{18}O$	20.01481
Relative abundance (%)	
D/H	0.016
$^{18}O/^{16}O$	0.201
Equilibrium α vapour-liquid (Majoube, 1971 cited in Gat 1981b)	
	$HD^{16}O$ $H_2{}^{18}O$
20°C	1.084 1.0098
$\frac{\alpha_{HD^{16}O}-1}{\alpha_{H_2{}^{18}O}-1} \approx \left(\frac{\delta_{H^{18}O}}{\delta_{H_2{}^{18}O}}\right) = 8.9$	
Molecular diffusion coefficient, $D_x/D_{H_2{}^{16}O}$ (Merlivat, 1978)	
$D_{HDO}/D_{H_2{}^{16}O}$	0.9755 ± 0.0009
$D_{H_2{}^{18}O}/D_{H_2{}^{16}O}$	0.9723 ± 0.0007
Resulting fractionation into vapour by diffusion, $\varepsilon = (1 - D_i/D)$ at 21°C	
$HD^{16}O$	25.1
$H_2{}^{18}O$	28.5
Relative diffusive effect	
$\varepsilon HDO/\varepsilon H_2{}^{18}O$	0.88

The complexity of equilibrium and kinetic fractionation in natural systems can be illustrated with the example of raindrop formation, imagining a parcel of cloud vapour whose isotopic composition will be lighter than that of seawater, since it will have undergone both equilibrium and kinetic fractionation when it initially evaporated from the sea. The first stage of this process, cloud condensation, is dominated by isotopic equilibrium since the relative humidity within the cloud is high and the fractionation of isotopes as they change from vapour to liquid will be strongly related to the cloud temperature (dew-point temperature). But as soon as the drops leave the cloud base and begin their descent through a less humid atmosphere, the lighter isotopes will be preferentially evaporated under isotopic equilibrium at the surface, but driven overall by kinetic fractionation as vapour is drawn into the atmosphere from the surface (Stewart, 1975). This kinetic fractionation by evaporation, results in isotopic enrichment of the drop, which overprints the previous equilibrium fractionation. The temperature-dependent fractionation, which is of primary interest will only be preserved if the

subsequent kinetic fractionations are minimised by high humidity of the atmospheric column and/or freezing the drops as is the case for snow or hail. Thus, the resulting isotopic composition of any precipitation depends on (Dansgaard, 1961):

- the isotopic composition of the source;
- the number (and magnitude) of phase changes undergone; and
- the temperature and relative humidity at which these phases changes occurred.

Since the source for the majority of rainfall is the ocean, which is of relatively uniform composition (0‰$_{VSMOW}$), it is therefore the subsequent processes undergone by moisture vapour that characterise its resulting isotopic composition. On the global scale; physiographic effects such as topography, distance from the equator and continentality, produce large fractionations in water isotopes; and to these are added local factors such as seasonality and rainfall intensity. These effects are summarised below.

5.1.3 Isotopic fractionation of water in the hydrologic cycle

The temperature effect

Following from above, if cloud vapour condenses under conditions of isotopic equilibrium and all other meteorological conditions are relatively uniform, then the fractionation at condensation should be dependent on the dew-point temperature of the cloud base. This effect is likely to be present in many precipitation events, but masked by larger fractionating processes once the condensate has left the cloud (*i.e.* diffusive kinetic effects at the vapour-liquid boundary; Stewart, 1975). It follows that the temperature effect is likely to be preserved if the precipitation falls as ice thus reducing the subsequent effects of evaporation because diffusion is suppressed in the solid state (Jouzel and Merlivat, 1984), or if the meteorological conditions are more consistent *i.e.* frontal (convective) rather than cyclonic rain (Lawrence *et al.*, 1982; Gedzelman and Lawrence, 1990).

The temperature effect has been well studied in the Antarctic region since it contains the longest isotopic records from ice cores (*e.g.* Lorius *et al.*, 1985; Jouzel *et al.*, 1987). The temperature was reconstructed for the Vostok core using the isotope-temperature relationship determined between Mean Annual Temperature (MAT) and δD of annual

snow samples collected in a transect across the Antarctic interior (Jouzel and Merlivat; r = +0.99; n = 35). However, such an impressive relationship is rare, and likely only occurs here, because the precipitation falls as snow reducing non-equilibrium effects and because the Antarctic interior is climatically stable (coastal stations where there are complex orographic effects and multiple source regions that may have weakened this relationship were not included). Subsequent studies using temporal rather than spatial sampling methods, have shown that even in this region the real relationship between water isotopic composition and temperature is far more complex than originally considered (Kato, 1978; Aristarain *et al.*, 1986; van Ommen and Morgan, 1997; Noone and Simmonds, 1998).

Continental and altitude effects

As an air mass travels inland or in altitude, condensation of the vapour is induced by isobaric cooling with distance travelled inland and/or by adiabatic cooling with altitude, resulting in rainfall that is isotopically lighter than its vapour. This behaviour has been shown for several transects, *e.g.* in an west-east trajectory from the northwest Pacific across the United States (Welker, 2000); and a similar west-east transect of European stations (Rozanski *et al.*, 1982). Seasonal patterns may enhance the continental effect as the distillation is greatest in winter when the air is coolest and driest, and counteracted in summer by enhanced moisture recycling by higher transpiration and evaporation rates; *e.g.* as shown for the Northern Hemisphere mid-latitudes by Koster *et al.* (1986) and also for the Amazon Basin (Salati *et al.*, 1979; Gat and Matsui, 1991).

Evaporation and transpiration have differing capacities to lower summer atmospheric $\delta^{18}O$ since evaporation fractionates groundwater to produce an isotopically lighter vapour while transpiration pumps unfractionated $\delta^{18}O$ vapour back into the atmosphere (Tang and Feng, 2001). The contribution from each process will be site specific although results from a GCM isotopic water balance study suggest that globally, transpiration provides more recycled H_2O than does evaporation, and for the Northern Hemisphere mid-latitudes, recycled moisture contribution and temperature accounted for approximately equal variance in summer $\delta^{18}O$ precipitation (Koster *et al.*, 1993). Examples where evaporation is likely to be significant are few, and only if a site is close to a large water body (*e.g.* Great Lakes, United States; Gat *et al.*, 1994).

The altitude effect is the isotopic fractionation created by both adiabatic cooling and changes in the lapse rate when water vapour is uplifted either orographically or by convection. This effect was first observed in precipitation collected as an air mass ascended the slope of a warm front (Dansgaard, 1953) and can account for the depleted vapour found in cyclonic vortices (Lawrence *et al.*, 1998) and precipitation created by orographic uplift (Epstein, 1956). The fractionation by cooling with elevation may be further enhanced if the vapour is equilibrating with depleted vapour at higher altitude (assuming a general profile of decreasing $\delta^{18}O$ and δD with decreasing temperature and humidity with height). Lawrence and Gedzelman (1996) calculated from their observations of $\delta^{18}O$ during tropical cyclones, that this effect was actually far greater than the effect of adiabatic cooling.

The rainfall amount effect

$\delta^{18}O/\delta D$ appears to be negatively correlated to rainfall amount for some stations, particularly tropical islands but also some mid-latitude stations (*e.g.* Dansgaard, 1964; Yurtsever and Gat, 1981; Gedzelman *et al.*, 1987; Lawrence and Gedzelman, 1996). It is thought that this occurs primarily at the condensation stage, since deeply convective clouds attain greater height in the atmosphere where the water vapour is more efficiently cooled resulting in large quantities of isotopically depleted rainfall (Dansgaard, 1964; Yapp, 1982). This effect may be further enhanced after condensation as the droplets fall through the atmosphere, since:

1. evaporation and diffusion occurs with the surrounding vapour which result in isotopically heavier droplets. Since evaporation is a function of specific humidity, this process will be strongest for lighter events and least for heavier events, and
2. longer duration events will deplete their source such that rainfall will become isotopically lighter with storm duration (Dansgaard, 1964).

Gedzelman and Arnold (1994) further develop the amount effect model using their observations of the isotopic composition of rainfall collected for extra-tropical cyclones (Gedzelman *et al.*, 1987; Gedzelman and Lawrence, 1990). By comparing rainfall collected under the passage of warm fronts and under cyclonic vortices, they argue that it is not the convective nature (strongest for fronts) but the degree of moisture recycling (strongest for vortices) that produces the lightest isotopes. In these cyclonic systems, rainfall is widespread around the centre such that the vortex is drawing vapour inwards

and upwards that has been previously highly depleted by processes 1 and 2 above. This same mechanism was also identified to be driving the amount effect first recognised in tropical cyclones (Lawrence and Gedzelman, 1996).

Other seasonal effects

The term 'seasonal effects' is used by some authors to explain the increase in the amplitude of the seasonal $\delta^{18}O/\delta D$ cycle with latitude which is in-phase with seasonal evaporation flux, transpiration flux, storm track frequency and migration (Rozanski *et al.,* 1993). However, it may be argued that as they are driven by seasonal insolation changes, that they are therefore broadly temperature driven, or a combination of other effects described above. Nonetheless, it is worth discussing some of these 'seasonal effects' as they may be relevant models or analogies when considering that seasonality is likely to have changed significantly in the past, and therefore may offer an additional perspective for interpreting palaeoclimate records.

Cole *et al.* (1999) investigated these seasonal effects by correlating simulated monthly anomalies (seasonal cycle removed) of temperature, moisture source area and precipitation amount against $\delta^{18}O$ for a global network of stations. They found that precipitation amount and vapour source accounted for far more variability than did temperature. In particular, the simulations also show that variability in source regions is high, especially for mid to high latitudes (excluding continental interiors) and that this could significantly alter $\delta^{18}O$ since the values of rainfall arriving from proximal and distal sources differed according to the degree of fractionation by rainout along its trajectory.

The problem of source variation is hotly debated for the Greenland ice core sites as some authors believe this effect can account for a significant portion of the variance in the isotopes (Charles *et al.*, 1994; 1995), which detracts from the temperature effect. Charles *et al.* (1994; 1995) model the precipitation contributions from the North Pacific, North Atlantic, Greenland-Norwegian Seas with additional evapotranspiration from surrounding continents using a coupled ocean-atmosphere GCM. The basis for their argument is that the $\delta^{18}O$ of the present day precipitation from the main two contributing regions (Pacific and Atlantic) can differ by as much as 15‰, and considering the shift in contributing sources suggested in LGM simulations, they suggest that source variation

accounts for a significant portion of the $\delta^{18}O$ shift between the LGM and today, rather than temperature. They support their argument by suggesting that the magnitude of $\delta^{18}O$ observed for the present day sources accounts for the differences in $\delta^{18}O$ observed between spatially distributed ice cores; Summit (central Greenland), Dye 3 (southern Greenland) and Camp Century (northwest Greenland). This view was debated by Krinner & Genthon (1997) who, using GCM simulations, suggest that greater southwards migration of winter sea-ice reduces the moisture available for winter cyclonic advection to the Summit, hence the $\delta^{18}O$ recorded here has a summer bias *i.e.* represents warmer temperatures. Krinner & Genthon (1997) favour this theory over that of Charles *et al.* (1994; 1995) to explain the difference in temperatures inferred from $\delta^{18}O$ and measured directly from the ice boreholes.

5.2 THIS STUDY: ISOTOPES IN SOUTHERN AUSTRALIAN RAINFALL

Intensive studies of isotopes of rainfall are geographically biased towards the high latitudes because of their significance for palaeoclimate interpretation of the long ice-core records (*e.g.* Kato, 1978; Koster *et al.*, 1992; Charles *et al.*, 1994; Jouzel *et al.*, 1997a; Noone and Simmonds, 1998). Elsewhere, our understanding of rainfall isotopic composition comes from global studies utilising the IAEA/GNIP data; which may reveal sites that do not comply with the Dansgaard spatial slope model (+0.69‰/°C; *e.g.* Cole *et al.*, 1999) but are not detailed enough to identify the regional significance of these effects. Where exceptions exist, *i.e.* where high resolution event-based $\delta^{18}O$ collection studies have been undertaken, it has been to understand the climatic effects on $\delta^{18}O$ for a specific region where it is required for palaeoclimate interpretation (*e.g.* White and Gedzelman, 1984, for USA tree-rings records; Ayalon *et al.*, 1998, for Israeli speleothems). (Henceforth, $\delta^{18}O$ will be denoted by either 'P' to indicate meteoric precipitation or 'SP' to indicate speleothem calcite to avoid confusion when the data are compared in the remaining chapters.)

Since the difference in speleothem γ between Tasmanian and New Zealand shows that the variation in $\delta^{18}O_P$ recorded in speleothems from the LGM-Holocene transition cannot be solely attributed to temperature, the likely role of other potential isotopic fractionation effects must be examined. To do this, samples were collected on an event

(9 am-to-9 am rain-day) basis, rather than monthly aggregate samples collected by the IAEA, permitting an investigation between $\delta^{18}O_P$ and local synoptic effects.

Rainfall samples were collected for this study from Cape Grim, Mole Creek and Hastings (Tasmania), Cape Leeuwin Lighthouse (southwestern Australia), Mt Arthur (South Island New Zealand; Chapter 2; Figure 2.1.5, site specifications given in Table 5.2.1 below). This collection was intended to expand the longer unpublished data set collected by Prof W. F. Budd (University of Tasmania) at his home in Margate ~20 km from Hobart and analysed at the Antarctic CRC (University of Tasmania). The primary objective was to focus on this Margate data set in conjunction with synoptic analysis, as it is the longest event-based data set in the region. The collection of rainfall samples at the other sites was established for one year, to check whether relationships found for the Margate data held regionally. However, as mentioned in Chapter 4, Section 4.1, considerable technical problems were experienced analysing these samples using the mass spectrometer at RSBS, ANU. Because of this, many samples could not be analysed, and samples had to be prioritised according to their importance for the study, *e.g.* Cape Leeuwin was given highest priority as this site was furthest and likely to differ from the Margate $\delta^{18}O_P$ records. These samples were run in triplicate as a minimum.

Table 5.2.1: Collection site specifications (Cape Grim: Tindale *et al.*, 2001; Hastings, Margate, Mole Creek, Cape Leeuwin: BOM, 2002; Mt Arthur: C. Morgan, *pers. comm.*; Metservice 2002).

Site	Longitude/ latitude	Altitude (m asl)	MAT (°C)	Annual rainfall (mm)	Duration of collection
Margate, TAS	147°19' -42°58'	52	11.7	677	Jan 1994 - Jun 2000
Cape Grim, TAS	144°41' -40°41'	94	12.4	806	Sep 2000 - Oct 2001
Hastings, TAS	146°52' -43°25'	38	11.5	1381	Apr 2000 - Nov 2000
Mole Creek, TAS	146°23' -41°31'	460	10.3	962 (Deloraine station)	Apr 2000 - Nov 2000
Cape Leeuwin, WA	115°08' -34°22'	13	16.8	999	Oct 2000 - Oct 2001
Mt Arthur, NZ	172°47' -41°12'	445	12.3 (Nelson station)	2100	Jan 2000-Dec 2000

5.3 RESULTS

$\delta^{18}O_P$ of the Margate event-based rainfall samples is highly variable, ranging from close to 0‰$_{VSMOW}$ to less than −14‰$_{VSMOW}$. Figure 5.3.1 shows $\delta^{18}O_P$ for a typical year (1994) alongside rainfall amount (rainfall is represented as the square root of rainfall for scaling convenience) and mean daily temperature. Mean daily temperature is calculated as the mean of the daily maximum of the previous day (~3 pm) and the daily minimum of the rain day (~3 am), to account for the offset between a 24 hour 'rain day' which is 9 am-to-9 am and a 24 hour standard day which is 12 am-to-12 am. Figure 5.3.1 shows that $\delta^{18}O_P$ appears to be strongly related to the inverse of rainfall amount on an event by event basis *i.e.* high rainfall events deliver isotopically lightest precipitation. This is supported by the Pearson correlation coefficients (Table 5.3.1) which shows the correlation between $\delta^{18}O_P$ and rainfall using raw data is $r = -0.61$ ($p < 0.001$), compared with a more moderate relationship with temperature ($r = +0.41$, $p < 0.001$). Detrending the data by subtracting the mean seasonal cycle for years 1994-2000, in all cases strengthens the correlation between $\delta^{18}O_P$ and rainfall while it weakens the correlation between $\delta^{18}O_P$ and temperature (Table 5.3.1). This shows that a significant portion of the correlation between $\delta^{18}O_P$ and temperature is at the lower frequency of the annual cycle, while the higher correlation with rainfall is on the event-by-event scale.

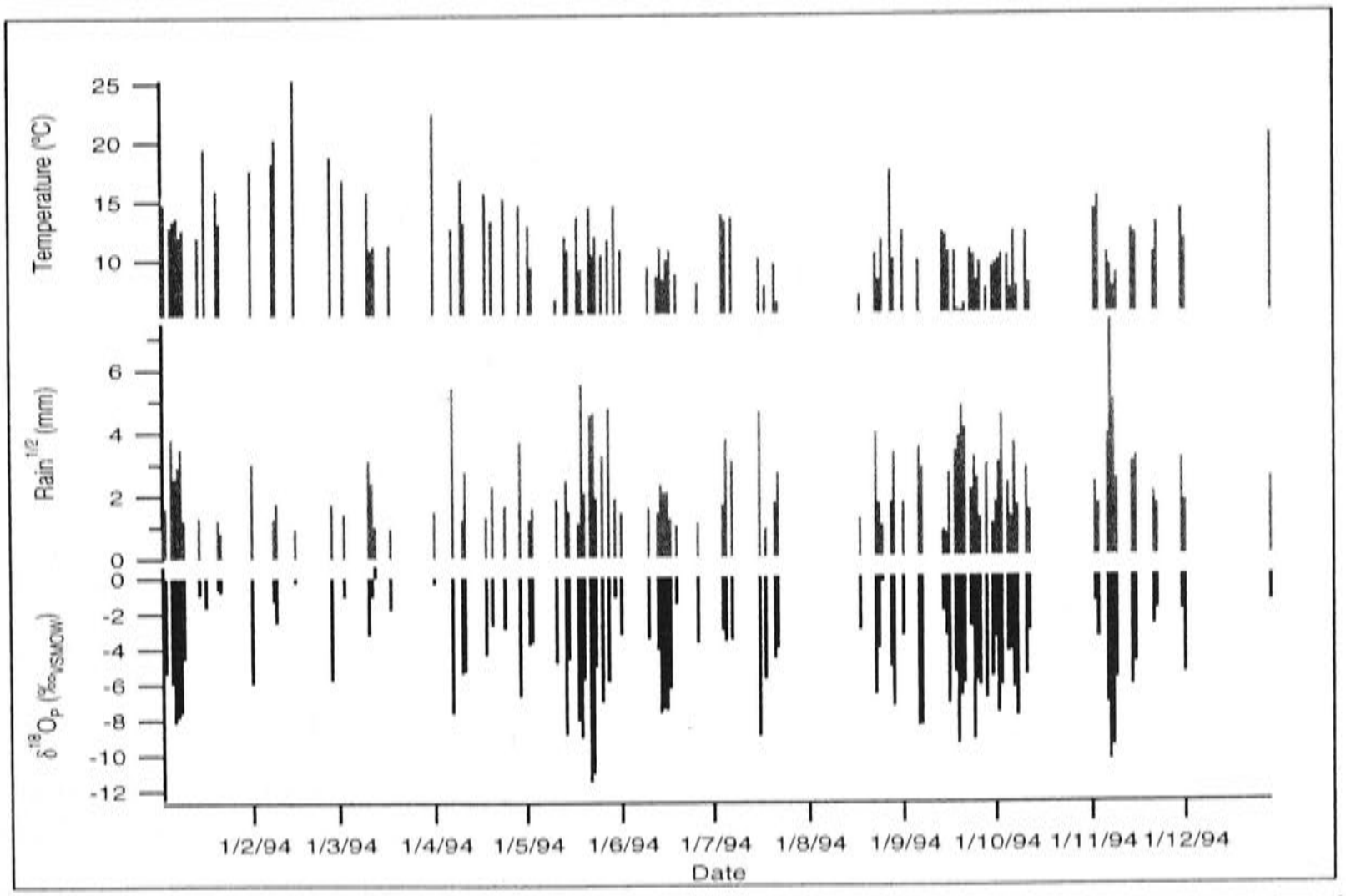

Figure 5.3.1: Event-based $\delta^{18}O_P$ compared with daily rainfall and mean daily temperature for Margate, 1994.

Table 5.3.1: Correlations between $\delta^{18}O_P$ with rainfall and temperature for both raw and detrended (seasonal cycle removed) data for Margate. Rainfall is the amount of rainfall collected in the gauge when the sample was collected. Temperature is that recorded at Hobart, Ellersley Road (data source: Australian Bureau of Meteorology). (Values in bold are significant at the $p < 0.01$ level. *1995 is January-March only.)

Year	r				
	n	$\delta^{18}O_P$:T	$\delta^{18}O_P$:T detrended	$\delta^{18}O_P$:rain	$\delta^{18}O_P$:rain detrended
1994	103	**+0.41**	**+0.34**	**-0.61**	**-0.62**
1995*	32	-0.02	-0.11	-0.42	-0.43
1996	127	**+0.27**	+0.14	**-0.42**	**-0.44**
1997	99	**+0.24**	+0.09	**-0.30**	**-0.40**
1998	95	**+0.22**	-0.02	**-0.34**	**-0.45**
1999	96	**+0.22**	+0.12	**-0.47**	**-0.52**
2000	46	+0.21	+0.19	-0.19	-0.20
all years	598	**+0.29**	**+0.14**	**-0.40**	**-0.47**

The strength of the seasonal cycle in these variables may be clearly seen in Figure 5.3.2, which shows the mean monthly $\delta^{18}O_P$ (1994-2000) alongside mean monthly temperature (constructed using only the days when rain was collected at Margate), and also the mean monthly amount of rainfall collected. Here, $\delta^{18}O_P$ exhibits an annual cycle that is nearly symmetrical about mid-winter, but whose distribution is slightly biased towards August, with an annual range of around 2‰. Temperature is similar to $\delta^{18}O_P$ in that it also shows a smooth cycle, although asymmetrical about mid-winter; with its distribution biased towards June. The correlation between smoothed $\delta^{18}O_P$ and temperature on the annual scale is much higher ($r = +0.85$). Rainfall by contrast, appears to follow $\delta^{18}O_P$ in an antiphase trend until October, after which it continues to rise in the same manner as $\delta^{18}O_P$, peaking in December. This annual trend of rainfall is also present in longer-term records (20-30 years) from surrounding meteorological stations (Margate, Kingston and Hobart). Thus, on the monthly sampled annual scale, there is a much stronger relationship between $\delta^{18}O_P$ and temperature ($r = +0.85$); and a weaker antiphase trend between $\delta^{18}O_P$ and rainfall ($r = -0.20$) which deviates in the last 3 months of the year where the relationship switches from negative to positive.

This exercise, which exemplifies the climatic relationship seen with $\delta^{18}O_P$ depending on event or monthly collections, shows that conflicting interpretations may be drawn depending on the sampling interval. That is, sampling on the higher event frequency reveals that there is a stronger relationship between $\delta^{18}O_P$ and rainfall amount, which contrasts with the higher correlation between $\delta^{18}O_P$ and temperature if monthly sampling intervals are selected. This finding is supported by detrending the event-based data which confirms that the correlation between temperature and $\delta^{18}O_P$ is biased by the similarity of the annual cycles of these variables; whereas the correlation between rainfall and $\delta^{18}O_P$ strongly lies on the event scale (Table 5.3.1). Thus, false deductions would be drawn that the temperature effect was greater if bulk monthly collections were used.

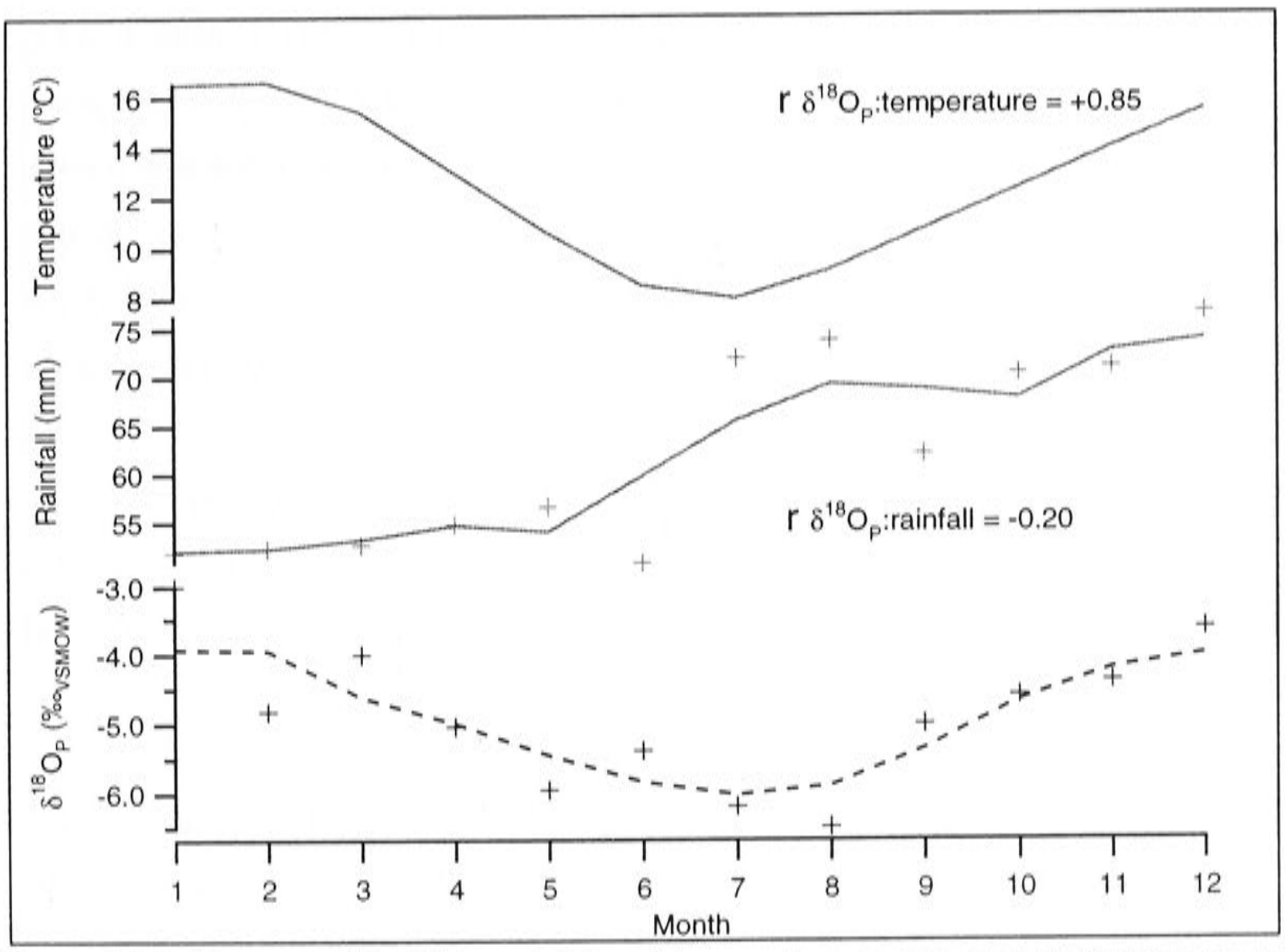

Figure 5.3.2: Mean monthly $\delta^{18}O_P$, rainfall and temperature on rain-days at Margate for 1994-2000. Rainfall and $\delta^{18}O_P$ curves are 3-point running averages.

The results indicate that $\delta^{18}O_P$ at Margate is dominated by the 'amount effect'. This effect is common at tropical stations for monthly collection intervals (Dansgaard, 1964; Yurtsever and Gat, 1981), and is suggested to be a combined result of highly convective storms deeply cooling the moisture mass at high altitude, bringing large amounts of isotopically lighter rainfall, combined with enhanced isotopic enrichment of lower

rainfalls owing to evaporation in lower relative humidity. This effect has also been identified at mid-latitude stations where event-based sampling was undertaken (Gedzelman *et al.,* 1987; 1990). Here, the effective moisture recycling and high rainfall producing extra-tropical cyclones overprint the expected equilibrium temperature effect.

Synoptic effects

Rainfall quantity is dependent on the humidity of an air mass and atmospheric stability, which may be identified by synoptic patterns. To investigate why $\delta^{18}O_P$ and rainfall are correlated on an event basis requires rigorous examination of the synoptic conditions responsible for the rainfall events. This was done by initially examining the synoptic mean sea level pressure (mslp) charts published in the Monthly Weather Review (BOM, 1994-2000) for extreme events in the Margate data set. These extreme events were identified by standardising each month's $\delta^{18}O_P$ and rainfall amount to the mean monthly average, allowing anomalies to be identified. For rainfall, standardising was performed by subtracting the (3-pt smoothed) long-term Hobart 1970-2000 mean for that month, and dividing by the long-term standard deviation. $\delta^{18}O_P$ was treated similarly, except that $\delta^{18}O_P$ values were precipitation weighted and only the mean monthly totals of the Margate record could be used for standardisation, rather than 30 years as was done for rainfall. The monthly rainfall and $\delta^{18}O_P$ anomalies are shown in Figure 5.3.3. It was considered sufficient and convenient to use monthly intervals to identify these event-based anomalies since one or two extreme events dominated the monthly total, and also the temporal deviation in the annual trend could be resolved at monthly resolution (Figure 5.3.2).

To describe the anomaly patterns which appear in Figure 5.3.3, the following classes were devised, where winter and summer are distinguished for cases I/II and IV/V:

I. $\delta^{18}O_P$ light/high winter rainfall (May 1994, November 1994).

II. $\delta^{18}O_P$ light/high summer rainfall (February 1996, February 1998, February 1999).

III. $\delta^{18}O_P$ average/high rainfall (April 1996, March 1997, January 1997, November 1996).

IV. $\delta^{18}O_P$ heavy/low winter rainfall (June 1997, June 1999).

V. $\delta^{18}O_P$ heavy/low summer rainfall (December 1994, March 1994, March 1995, January 1998, January 1999).

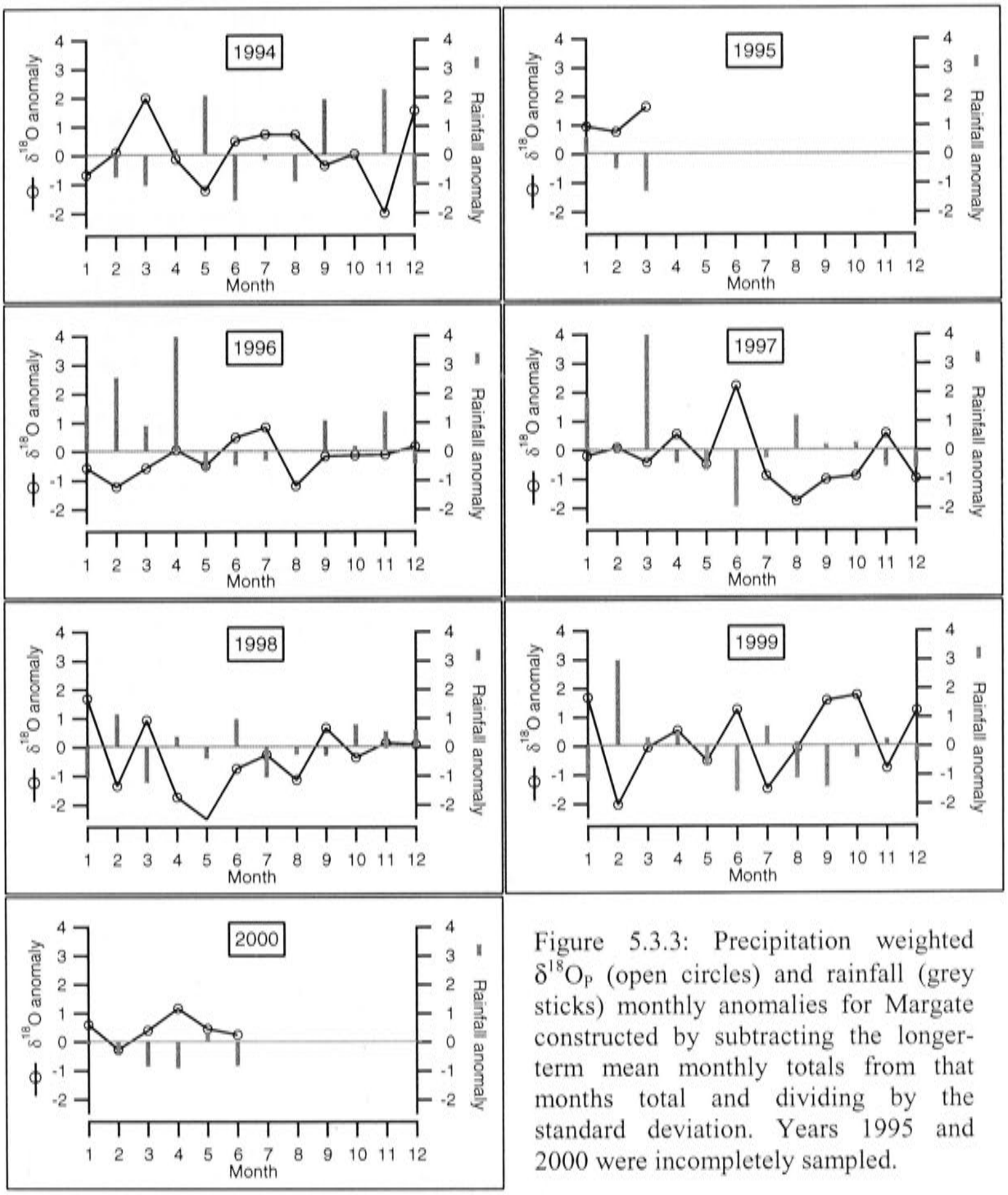

Figure 5.3.3: Precipitation weighted $\delta^{18}O_P$ (open circles) and rainfall (grey sticks) monthly anomalies for Margate constructed by subtracting the longer-term mean monthly totals from that months total and dividing by the standard deviation. Years 1995 and 2000 were incompletely sampled.

All events recorded for these months that appear in the cases above are listed in Table 5.3.2 below. From this table, the extreme events that are responsible for producing the anomaly were identified and are shown in bold font. The mslp charts of these selected events was then examined to identify possible common synoptic causal processes.

Table 5.3.2: Examples of months (all events shown) for each case. Events in bold are the extreme events contributing to the monthly anomaly.

Date	Rainfall (mm)	$\delta^{18}O_P$ (‰)	Date	Rainfall (mm)	$\delta^{18}O_P$ (‰)
Case I			Case III		
2/5/94	1.5	-3.80	**1/4/96**	**20.4**	**-6.60**
3/5/94	2.5	-3.65	**2/4/96**	**16.5**	**-8.00**
11/5/94	3.5	-4.81	**3/4/96**	**18**	**-6.00**
14/5/94	6	-8.85	4/4/96	2.5	-3.40
15/5/94	2.2	-4.64	6/4/96	2.5	-5.20
18/5/94	1.2	-8.09	8/4/96	8.4	-8.30
19/5/94	**30.2**	**-9.04**	9/4/96	11.9	-4.30
20/5/94	4.2	-5.76	10/4/96	10.2	-4.70
22/5/94	**20.3**	**-11.53**	11/4/96	10	-4.40
23/5/94	**21**	**-11.04**	12/4/96	4.7	-3.40
24/5/94	3.5	-5.06	15/4/96	2.9	-3.40
26/5/94	**10.4**	**-7.03**	16/4/96	2	-7.70
28/5/94	**22.5**	**-5.86**	**17/4/96**	**30.5**	**-5.20**
30/5/94	3.5	-1.17	**18/4/96**	**55.3**	**-6.30**
Total rain/ mean $\delta^{18}O_P$	*132.5 mm*	*-8.26‰*	**19/4/96**	**40**	**-6.30**
Case II			20/4/96	11.5	-3.90
5/2/99	4.7	-2.08	22/4/96	8.3	-9.20
7/2/99	**92**	**-10.63**	25/4/96	2	-6.90
8/2/99	**30**	**-11.58**	28/4/96	3.3	-3.20
12/2/99	**17**	**-7.65**	*Total rain/ mean $\delta^{18}O_P$*	*260.9 mm*	*-5.96‰*
13/2/99	**29.5**	**-7.14**	Case IV		
15/2/99	3	-5.14	2/6/99	1	-5.50
18/2/99	6	-7.28	7/6/99	3.5	-4.75
24/2/99	9	-3.64	11/6/99	1.6	-5.26
Total rain/ mean $\delta^{18}O_P$	*191.2 mm*	*-9.25‰*	14/6/99	10.5	-4.49
			19/6/99	3	-3.79
			30/6/99	4	-6.09
			Total rain/ mean $\delta^{18}O_P$	*23.6 mm*	*-4.81‰*
			Case V		
			3/3/94	2	-1.06
			11/3/94	**9.8**	**-3.22**
			12/3/94	**5.7**	**-1.07**
			13/3/94	1	0.69
			18/3/94	0.9	-1.79
			Total rain/ mean $\delta^{18}O_P$	*19.4 mm*	*-2.10‰*

In general, common synoptic scenarios could be identified and distinguished between each case. Events with lightest $\delta^{18}O_P$ and highest rainfall (case I) were produced by intensive and extensive low pressure systems (mid-latitude cyclones generated from the high latitudes of the Southern Ocean) tracking close to Tasmania (*e.g.* Figure 5.3.4I). Low pressure systems are common in winter, however in case I, a late spring outbreak of polar maritime air is accelerated by the positioning of the Australian continental high slightly south of its normal winter latitude, producing fast moving polar air chilling warmer maritime air resulting in high rainfall amounts and snowfalls to Tasmania.

Where large amounts of isotopically light rainfall occur for summer months (case II), a different situation occurs. Here, unseasonally frequent appearance of low pressure systems interact with moisture from over the continent (northwest cloudbands or dispersed subtropical lows), or as east coast troughs (Figure 5.3.4II).

The opposite extreme, $\delta^{18}O_P$ heavy and lower rainfall, are more frequent in the summer months (case V). Here, the positioning of two high pressure systems, one in the southern Indian Ocean and the other in the Tasman Sea, southeast of Tasmania, create a trough where the Indian Ocean high draws tropical moisture southwards to interact with cold southern maritime air drawn up from the south by the high in the Tasman (Figure 5.3.4V). The positioning of summer monsoonal lows over northwest Australia can moisten this air, which brings some rain (but typically less than the fronts of the Southern Ocean) which is isotopically heavier than moisture generated in the Southern Ocean.

For the few winter months where $\delta^{18}O_P$ is heavy and rainfall is low, (case IV) an extended belt of high pressure cells, almost forming a continuous baric ridge from the Indian Ocean to the Pacific Oceans, occurs (Figure 5.3.4IV). Fronts are rarer in this stable atmosphere, owing to the restricted interaction between southern maritime and sub-tropical air masses. When fronts do occur, they are weak and consequently deliver much less rainfall, and the low pressure systems responsible for these, are tracking much further south than usual.

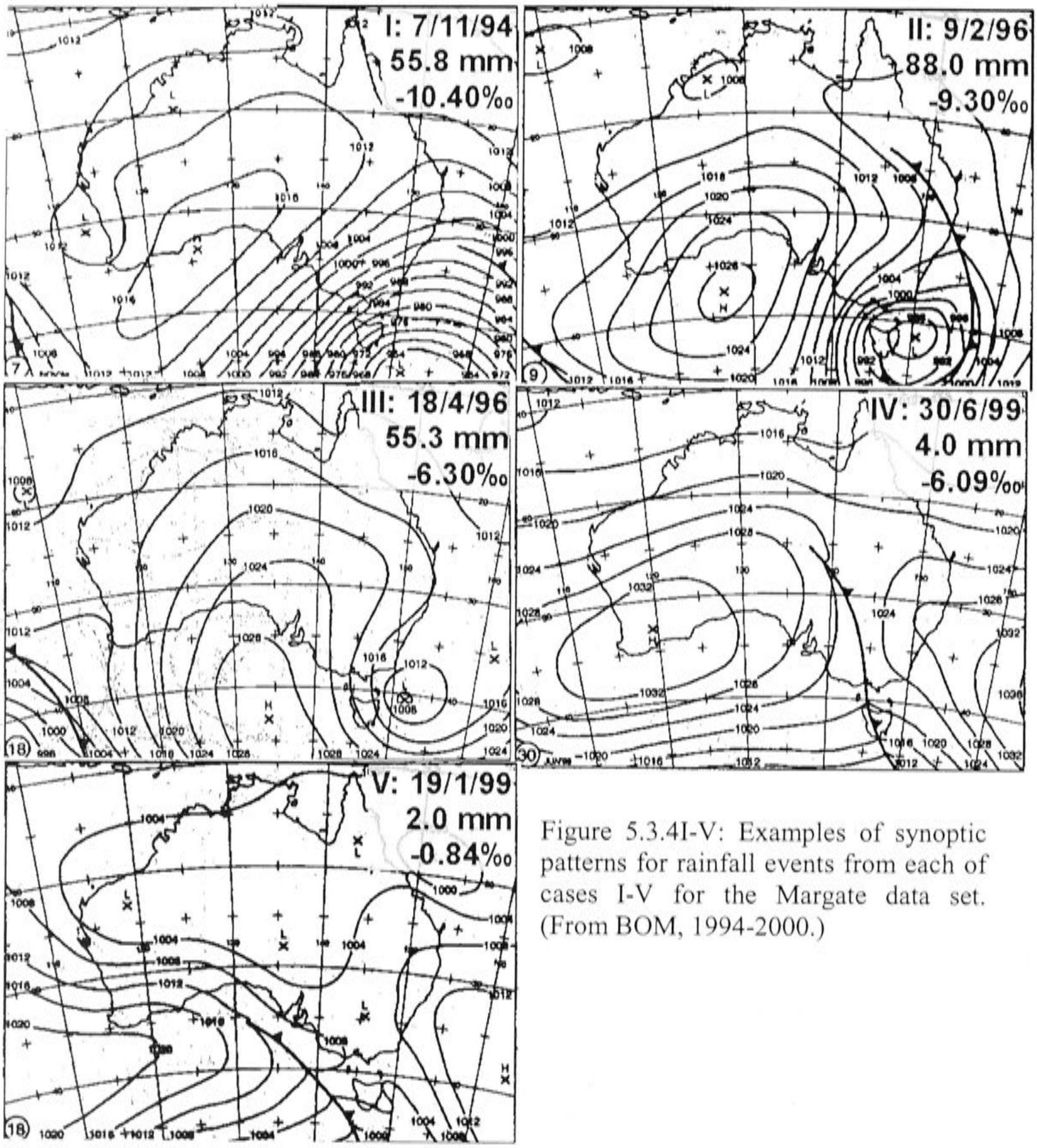

Figure 5.3.4I-V: Examples of synoptic patterns for rainfall events from each of cases I-V for the Margate data set. (From BOM, 1994-2000.)

Between these two opposite end-members of cases I/II and IV/V, is case III where $\delta^{18}O_P$ is close to average. In its mslp pattern, case III appears similar to cases I and II, but this low pressure system formed from the trough between highs located either side of Tasmania, forming an east coast low or trough, which draws in a large volume of tropical/sub-tropical moisture (Figure 5.3.4III). This continental moisture must have been isotopically heavy itself, probably because of its origin in the tropics, where warmer air has isotopically heavier vapour (Dansgaard, 1964; Araguas-Araguas *et al.*, 2000). In these cases where the mslp charts indicate possible tropical/sub-tropical moisture, it was verified by checking Out-going Longwave Radiation (OLR) images as a proxy for cloud cover at http://www.cdc.noaa.gov/cdc/data.interp_OLR.html (obviously,

satellite infra-red images could have been used to assess cloud source however, these were prohibitively expensive and resolution required was adequate from OLR images).

Because communicating these processes using mslp charts on a case by case basis is tedious and sometimes subjective, a way of objectively presenting an average of the synoptic cases was investigated. To do this, assistance was sought from a fellow PhD student, Ms P. Hope (Earth Sciences, University of Melbourne) who had access to numerical meteorological data sets derived from modelled data tuned to fit with available mslp recorded at global station networks (Reanalysis-2, Kanamitsu *et al.*, 1999) and software for manipulating them. Using Reanalysis-2, average mslp isobars were calculated by averaging the 6 hourly slices of simulated mslp over each 2.5° grid of latitude and longitude for the same region shown in the BOM (1994-2000) charts (the events used are shown in bold in Table 5.3.2).

This method produced the following maps (Figures 5.3.5-8) which capture the common features while smoothing the irregularities to produce synoptically distinct scenarios for each of the cases discussed above. These maps summarise the features and support the interpretations presented above, but in addition, some strongly contrasting patterns stand out. Considering again the two extreme winter cases I (Figure 5.3.5) and IV (Figure 5.3.6), shows that case I is dominated by southwest to northeast flow while case IV is dominated by straight west-east flow governed by an west-east baric ridge. These mslp synoptic cases reflect the behaviour of meridional (north-south) versus zonal (west-east) flow pattern of the troposphere.

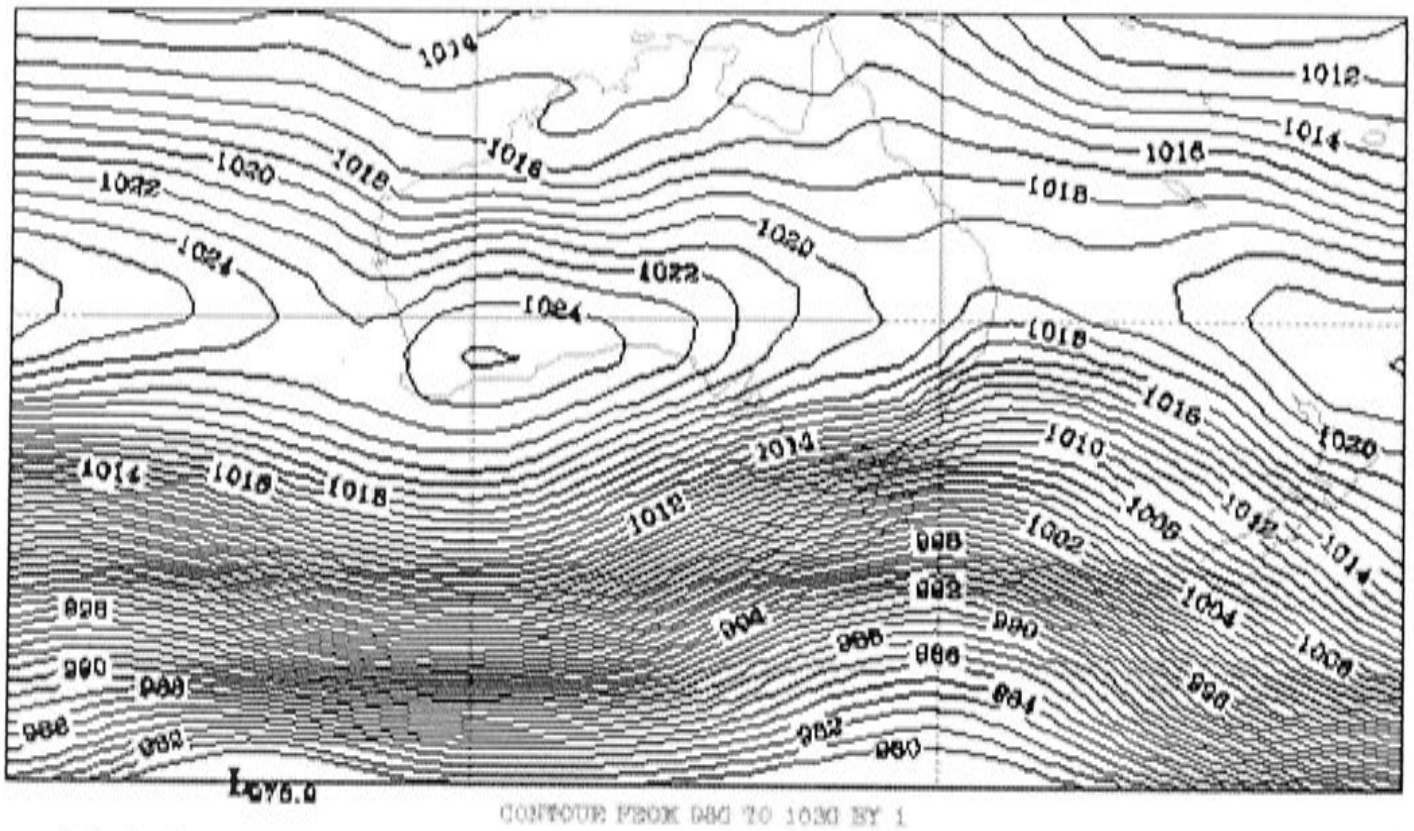

Figure 5.3.5: Case I constructed by averaging all anomaly events using Reanalysis-2 data.

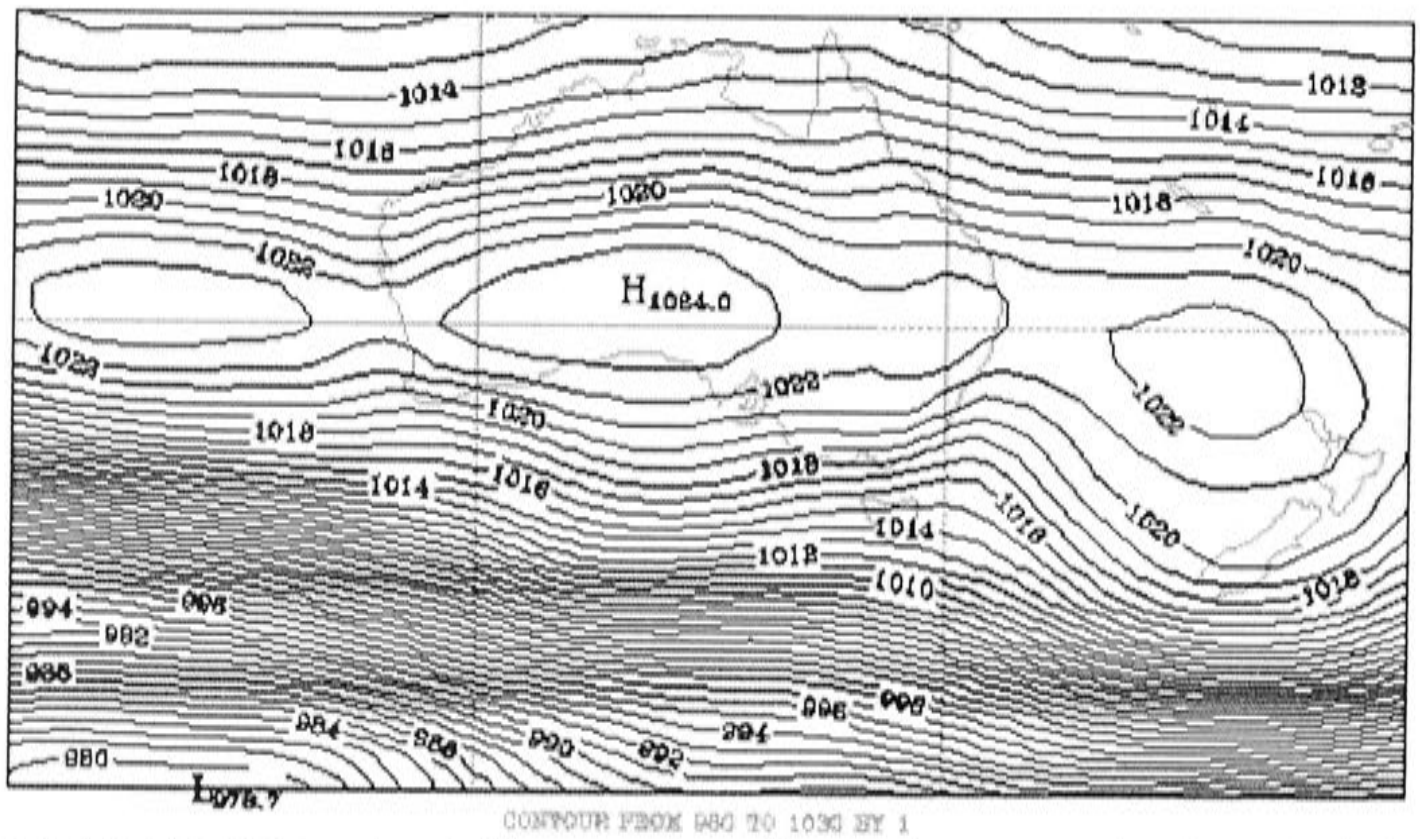

Figure 5.3.6: Case IV constructed by averaging all anomaly events using Reanalysis-2 data.

For the summer months, cases II and V also display contrasting meridional and zonal flow, but the difference results from the positioning of the high pressure systems. For case II, the highs are positioned over the Great Australian Bight and east of New Zealand funnelling southern maritime air northwards to sometimes interact with tropical/sub-tropical moisture (Figure 5.3.7). For case V the highs are positioned further east; one over the Southern Ocean and one in the Tasman, with the Southern Ocean high extending well-eastwards forming a baric ridge over Tasmania (Figure 5.3.8). It is the relative positioning and extent of these highs that dictate the passage of the low pressure

systems which are able to pass near Tasmania in case II but are absent in case V. Again, case II represents the meridional flow pattern and case V the zonal flow pattern.

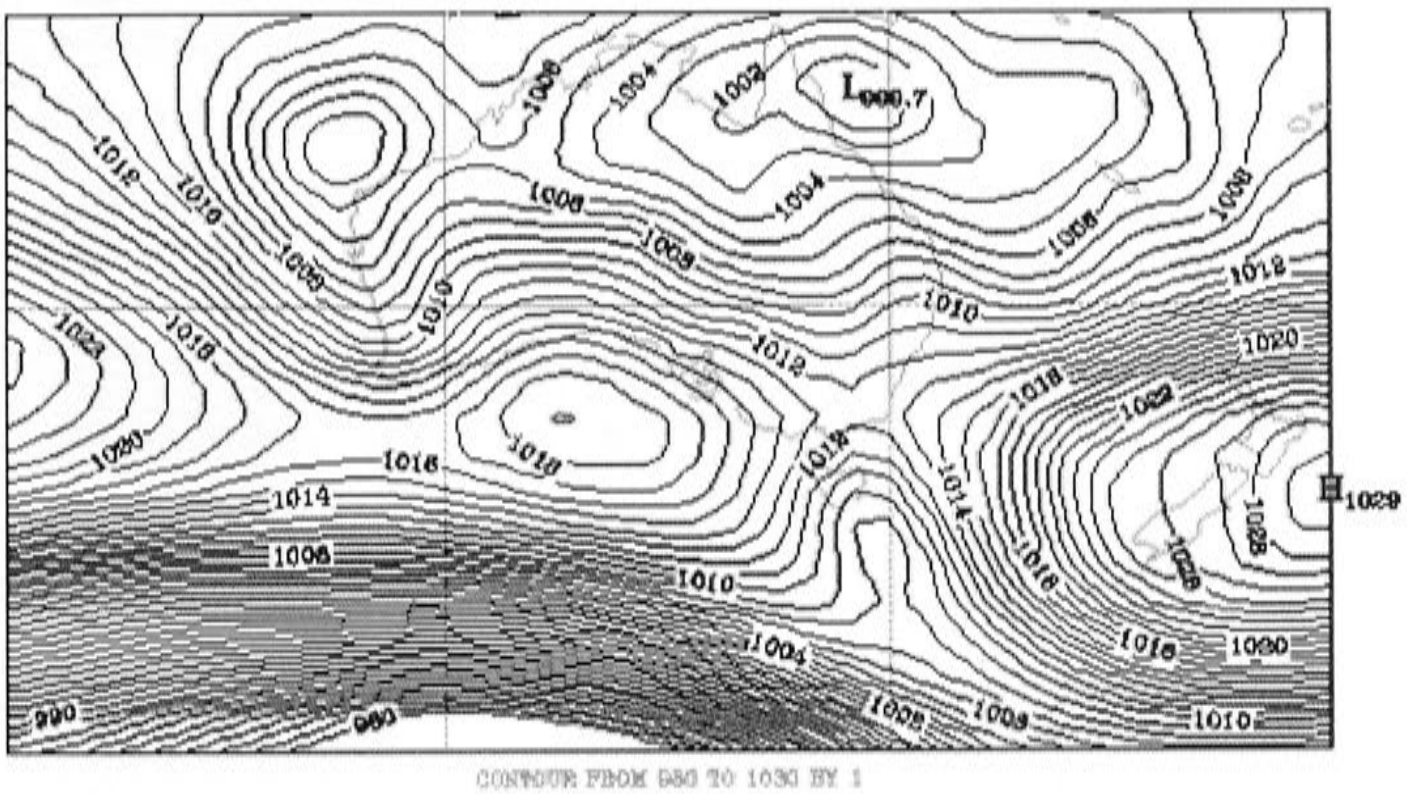

Figure 5.3.7: Case II constructed by averaging all anomaly events using Reanalysis-2 data.

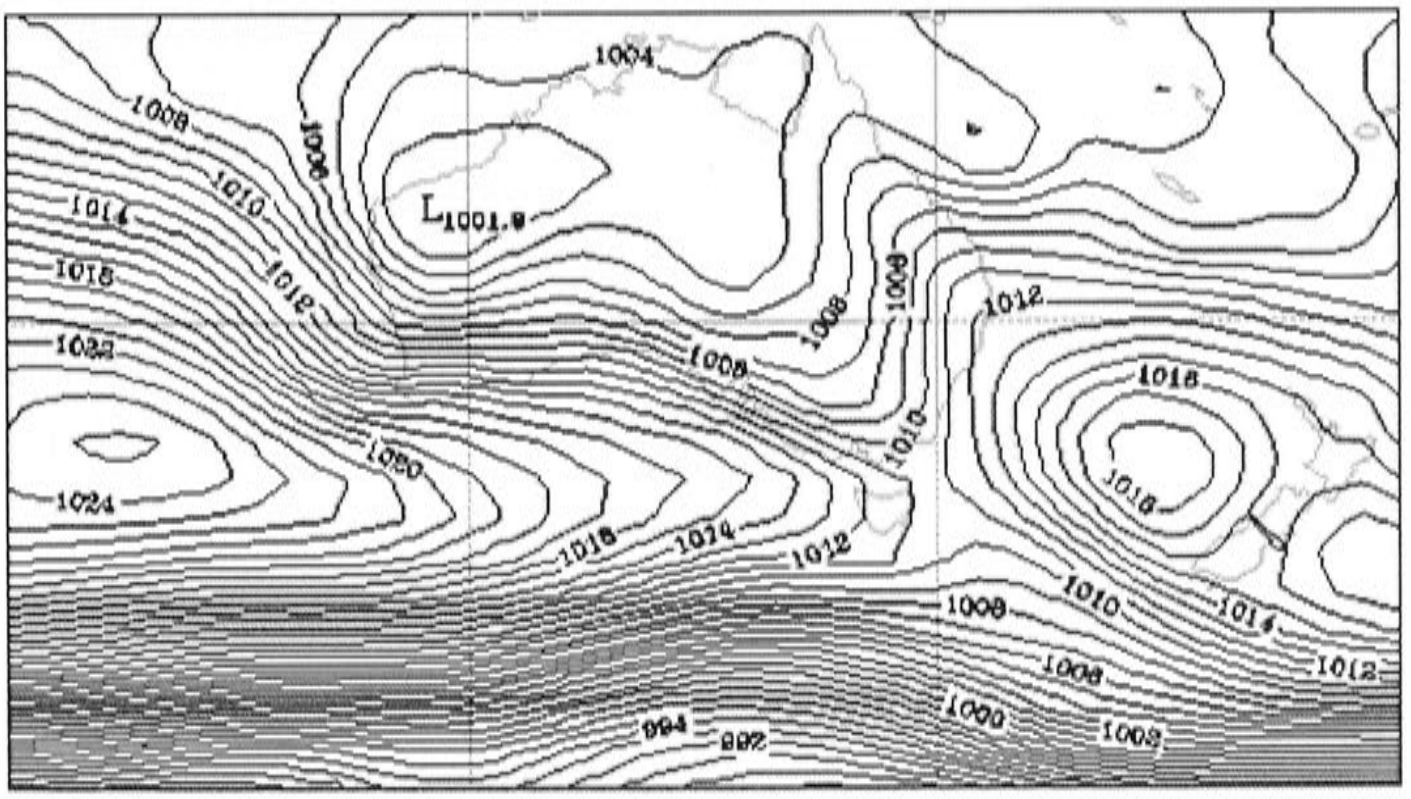

Figure 5.3.8: Case V constructed by averaging all anomaly events using Reanalysis-2 data.

Case III (Figure 5.3.9) is similar in appearance to case I (winter), however, the difference lies in the presence (III) or absence (I) of continental moisture, which will raise the $\delta^{18}O_P$ value.

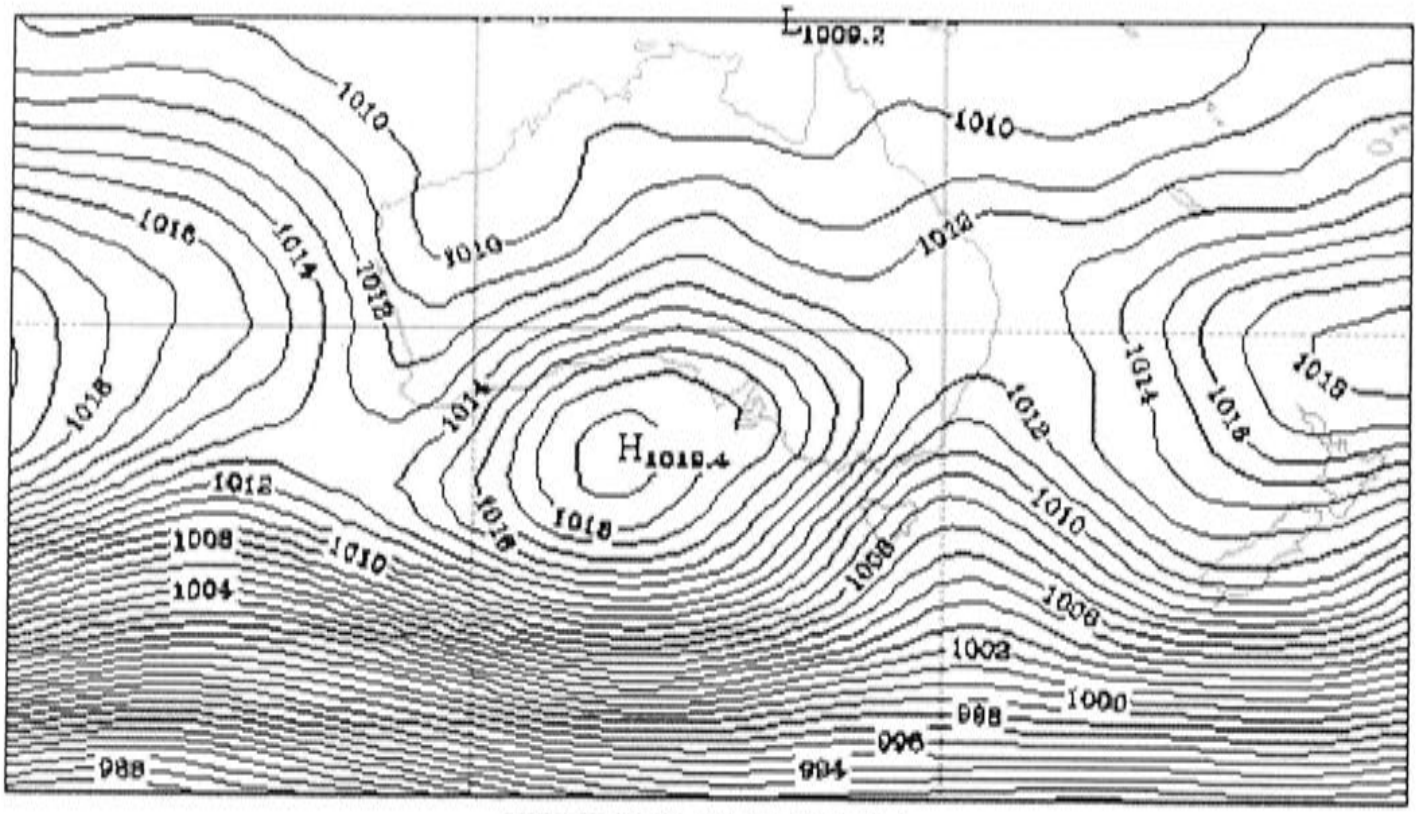

Figure 5.3.9: Case III constructed by averaging all anomaly events using Reanalysis-2 data.

The results of this synoptic analysis show that the rainfall amount and $\delta^{18}O_P$ signal is controlled by the relative positioning of, and hence the interaction between the sub-tropical high pressure systems and the Southern Ocean low pressure systems. The two extremes, most clearly seen in the winter isobars are meridional flow (case I) where there is greatest interaction between these vastly different air masses, causing north-south flow patterns and high rainfall; and zonal flow (case IV) where there is least interaction between these air masses. The interruptions to this two-end member model (case III) are caused by injections of isotopically heavier continental/tropical moisture.

This implies that there should be a relationship between the $\delta^{18}O_P$/rainfall and the proximity of the nearest low pressure system. To examine this, a way of identifying the location of low pressure systems was needed. Low pressure systems are defined as closed isobars with pressure decreasing towards the centre. The Reanalysis-2 data set was re-examined by N. Telcik (Dept. Water Resources and Engineering, The University of Western Australia) who had written an algorithm to identify low pressure systems by checking three by three grid squares in the region 25 to 65°S and 95 to 175°S. If the middle grid value was determined to be a minimum relative to the surrounding values then the grid location was classified as a 'low' and its MSLP and location recorded. This produced a data set listing the latitude, longitude, mslp for every low pressure system in this region for the period 1994-2000.

The data corresponding to the dates required were extracted by this author and several steps of data reduction performed:

1. Removal of superficial lows (lows greater than 1000 hPa).
2. Reduction of the initial grid range to 35 to 65°S and 140 to 157.5°E.
3. Lows occurring equatorwards of 43°S were classified as cut-off lows if they were west of 149°E or east coast lows if they were east of 149°E.
4. East coast lows were verified using Bureau of Meteorology daily MSLP charts (BOM, 1994-2000) (an east coast low is characterised by a trough in isobars cradled between a front and an anticyclone in east (Sturnam and Tapper, 1996 p.191).
5. If multiple lows were identified, the geographically closest low was selected after calculating the distance using the Great Circle Distance formula (http://www.auslig.gov.au/geodesy/datums/distance.htm).
6. Finally, the classification was cross-checked using daily MSLP charts. If tropical moisture was thought to be present in the system *e.g.* isobars suggesting northwest cloud bands or tropical cyclones were present, then the possible contribution of tropical moisture made by these systems was checked against OLR images.

Figure 5.3.10 shows that there is a linear relationship between $\delta^{18}O_P$ and the proximity of the nearest low pressure system, and similarly between rainfall and the proximity of the nearest low pressure system for the Margate 1994 data. The events affected by continental moisture, identified as open symbols stand away from this relationship, having isotopically heavier values for similar rainfall amounts. This supports the observations of the case studies above.

Finally, the last objective of this part of the study was to check whether these relationships held regionally by applying the same analysis to the event-based rainfall collected for this study. As only few reliable data could be obtained for this, it is only checked for Cape Leeuwin using data collected between October 2000 and June 2001 below (Figure 5.3.11A-B), since Cape Leeuwin is furthest from Hobart and at the northernmost latitude.

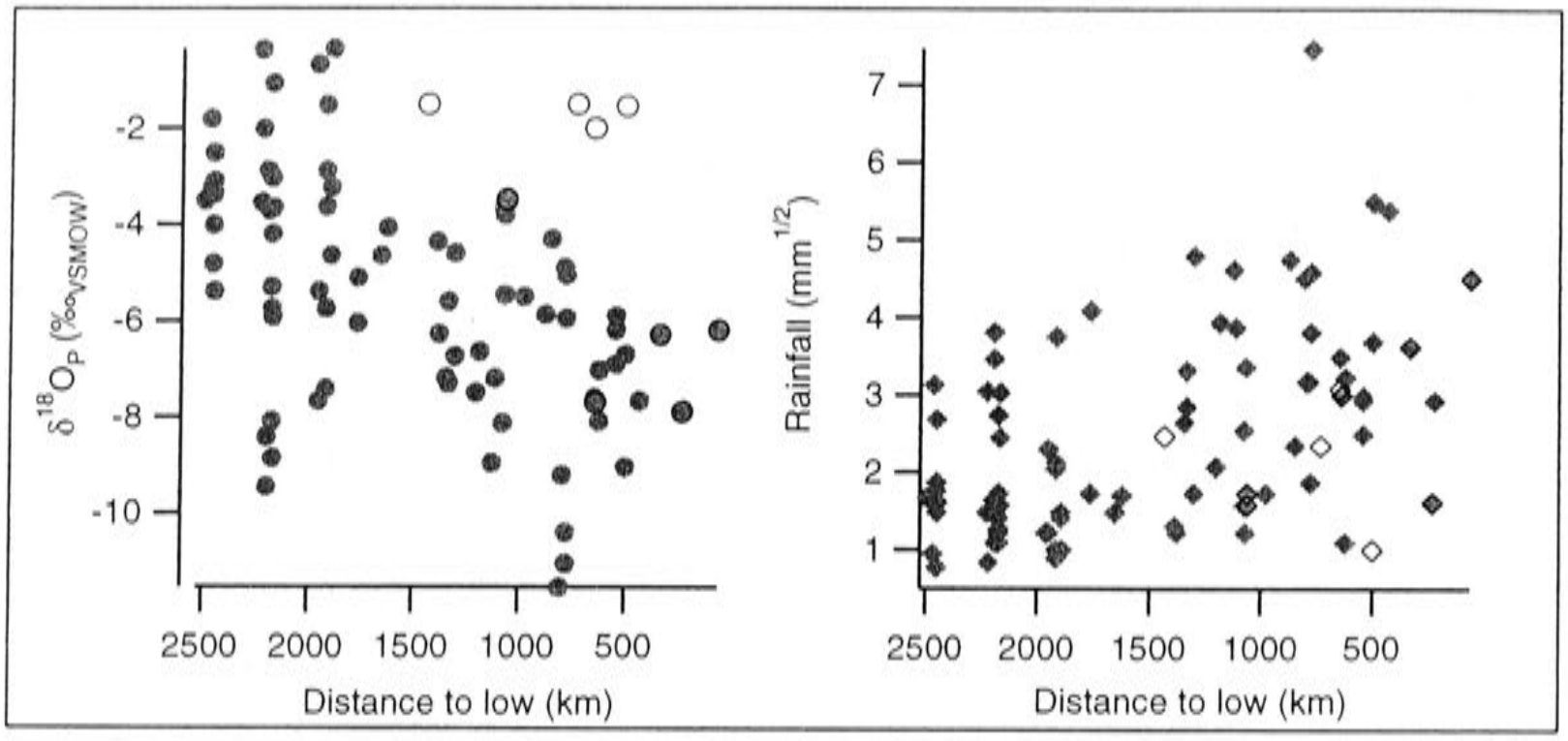

Figure 5.3.10A-B: The relationship between $\delta^{18}O_P$ and the distance to the nearest low pressure system (A), and the relationship between rainfall and the distance to the nearest low pressure system (B), for Margate 1994. (Closed symbols indicate mostly southern maritime or polar air while open symbols indicate where tropical/sub-tropical moisture is present also.)

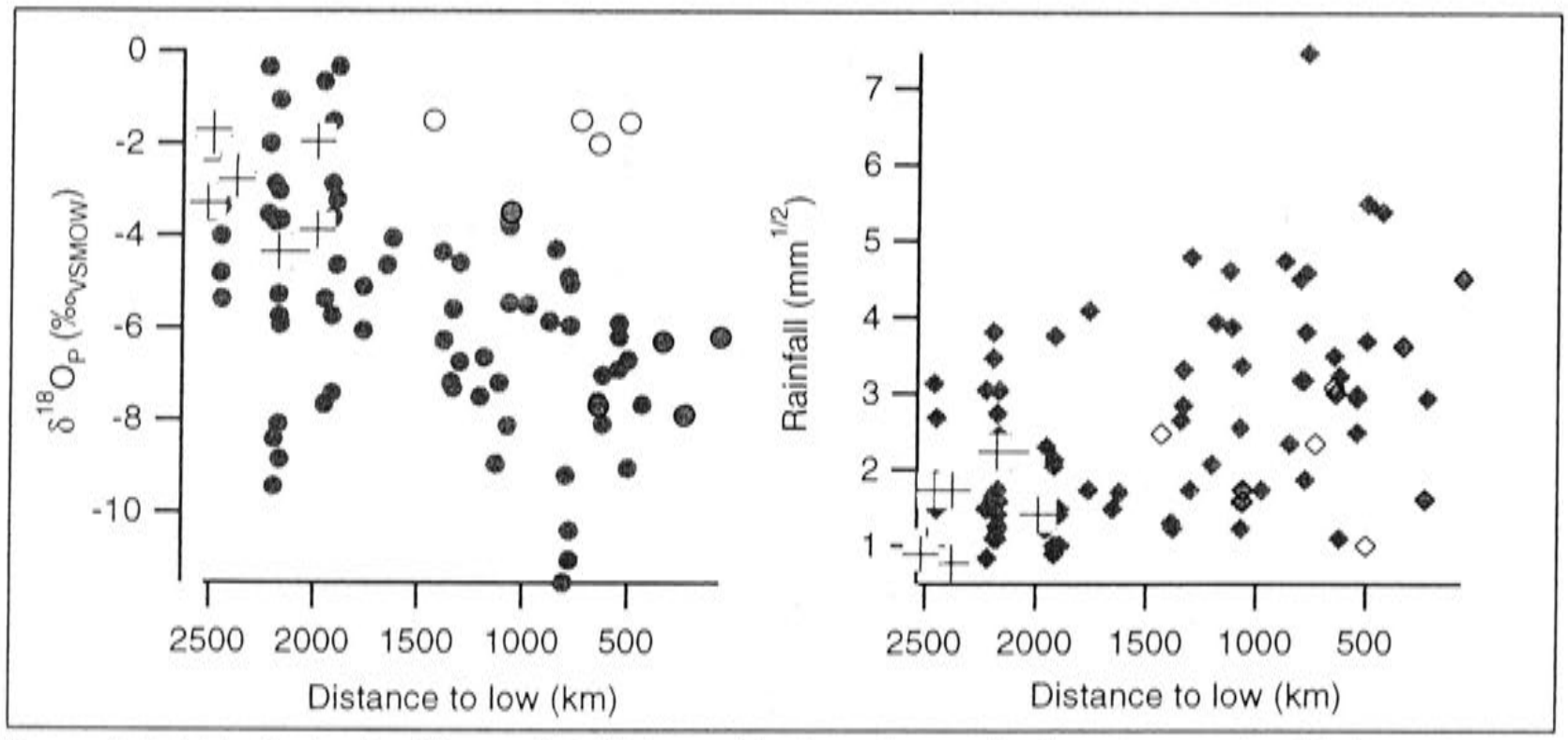

Figure 5.3.11A-B: As for Figure 5.3.10 but with Cape Leeuwin data (crosses) added.

The moderately strong correlation coefficient between $\delta^{18}O_P$ and rainfall for Cape Leeuwin ($r = -0.58$, $p < 0.001$) indicates that the amount affect is present for southwestern Australia. Figure 5.3.11A-B shows that the Cape Leeuwin data fall in the range of variation seen for Margate, but there are too few data analysed ($n = 31$) to be confident that the same relationship holds. However, the Reanalysis-2 maps indicate that the synoptic influence on $\delta^{18}O_P$ is regionally extensive across southern Australia, which strongly supports the inference that these processes would also apply to Cape Leeuwin and the other sites for which the water samples were unable to be analysed.

5.4 DISCUSSION AND SUMMARY

It is unlikely to be a coincidence that studies using event-based rainfall collection from sites in the sub-tropical to mid-latitudes (Lawrence *et al.,* 1982; White and Gedzelman, 1984; Gedzelman *et al.,* 1987; Gedzelman and Lawrence, 1990; Rindsberger *et al.,* 1990; Lawrence *et al.,* 1998; and this study) have found that temperature is not a large or sometimes even a significant driver of $\delta^{18}O_P$. Similar to these other studies, this study finds that $\delta^{18}O_P$ is in some way linked to the extra-tropical low pressure systems, also responsible for the high correlation with rainfall or the 'amount effect'. The results from these studies conflict with those based on IAEA monthly data that conclude that temperature accounts for a large portion of $\delta^{18}O_P$ variation (Dansgaard, 1961; 1964; Yurtsever and Gat, 1981; Rozanski *et al.*, 1993; Araguas-Araguas *et al.*, 2000). However, this study has demonstrated, at least for the Margate site, that strong correlations between temperature and $\delta^{18}O_P$ are biased by the similarity of their annual cycles.

Gedzelman and Arnold (1994) modelled cloud physics with isotope tracers ($\delta^{18}O$ and δD) to show that it is the sublimation (vapour to ice) altitude and subsequent melting (ice to liquid) level, vertical ascending velocity, isotopic exchange with surrounding vapour and moisture recycling that determine rainfall isotope ratios. Gedzelman and Arnold simulated two types of synoptic activity; stratiform and convective precipitation, to show that $\delta^{18}O_P/\delta D_P$ could sometimes be predicted by the synoptic pattern. For stratiform (frontal) systems where vertical velocity is much less than convective, the temperature effect was clearly demonstrated as a poleward gradient in $\delta^{18}O_P/\delta D_P$ ratios in snow along this front *i.e.* exchange with surrounding vapour is minimised in the solid state. For stratiform rains, $\delta^{18}O_P/\delta D_P$ were much higher and the poleward gradient was greatly weakened or lost due to the exchange with heavier vapour isotope ratios as the rain descended.

For convective (cyclonic) events, an amount effect was present due to deeper, more effective cooling and because exchange occurs with isotopically depleted vapour. $\delta^{18}O_P/\delta D_P$ were lightest for events where recycled moisture which is isotopically

depleted owing to prior fractionation, was present. The processes responsible for these trends was highlighted in the $\delta^{18}O_P/\delta D_P$ gradient from the core to the edges of the cyclonic system. $\delta^{18}O_P/\delta D_P$ were lightest around the core where convective lifting and adiabatic cooling were greatest. The descending rain was more likely to consist of recycled vapour recaptured in the core up-draft, and the effects of isotopic exchange were weaker owing to the depleted $\delta^{18}O_P/\delta D_P$ of the surrounding vapour. Moving outwards, where frontal systems begin to dominate as the air mass of the low pressure system interact with contrasting air masses, the $\delta^{18}O_P/\delta D_P$ produced is isotopically heavier for the reasons mentioned above for stratiform precipitation.

The Margate data set, which is lengthy (1994-2000) in comparison to other event-based studies undertaken so far (Lawrence *et al.*, 1982; White and Gedzelman, 1984; Gedzelman *et al.*, 1987; Gedzelman and Lawrence, 1990; Ayalon *et al.*, 1998) has permitted many individual events to be stacked and averaged to identify common causal patterns. This and these other studies, have many implications for palaeoclimate interpretation as they indicate that adopting the Dansgaard spatial and temperature dependent relationship of +0.69‰/°C to palaeoclimate records that preserve the isotopic composition of precipitation is inappropriate. On a pessimistic note, if no simple calibrations exist, then the task of interpreting palaeo-$\delta^{18}O_P$ proxies becomes difficult and the interpretations carry greater uncertainty. For speleothems, the fact that $\delta^{18}O_{SP}$ can not be expressed as two temperature dependent fractionations of meteoric and calcite precipitation (excluding glacial-age cases where ice volume must also be considered), means that at a minimum, multiple proxies such as trace elements (or better still, fluid inclusion analysis) are required to strengthen palaeoclimate interpretations.

For the case of speleothems in the Southern Australian region, this study suggests that changes in atmospheric circulation (meridional versus zonal flow); together with conditions that may favour or exclude tropical/sub-tropical moisture contribution need to be considered. Shifts in zonal and meridional patterns linked to tropospheric wave patterns, may be particularly important over time-scales where the migration of the Hadley cell may be affected by changes in solar insolation receipt (10^3-10^5 years); and, when the migration of these systems may also be influenced by exposure of continental shelves.

CHAPTER SIX

MODERN SPELEOTHEM RESULTS AND DISCUSSION

6.1 RESULTS

6.1.1 High resolution data: LA-ICP-MS data

A modern speleothem from south-west Australia, MND-S1, was chosen to examine the relationships between trace elements, stable isotopes, and annual climate cycles. This sample has the major advantage that its age (A.D.1911-1992) is well-constrained by the date of placement of the boardwalk on which it grew. LA-ICP-MS scans using the 32 μm spot (see Chapter 4, section 4.4) revealed 84 ± 1.3 cycles[1], most clearly evident in Ba concentrations (the full length of a typical scan is shown in Appendix II, and a detailed section is shown in Figure 6.1.1). The number of cycles is in excellent agreement with the number of years (81) that the boardwalk was in the cave, implying that these cycles are annual. These cycles were also evident in Sr, U, P and Mg (Mg is antiphase with the other elements; Figure 6.1.1) suggesting that these elements also express an annual cycle. Na occasionally shows cycles with a similar wavelength to these other elements, however unlike the other elements, its wavelength is variable and thus the Na cycles may not be annual.

The raw LA-ICP-MS were smoothed (twice filtered with a 9 point second-order Savitzsky-Golay filter) and then re-sampled, necessary for lag correlation, by interpolating each annual cycle into 12 points (one point representing one month). A lagged correlation analysis confirmed that the strongest correlations occur at phase lag zero except for Mg (6 months lag *i.e.* antiphase) and Na (discussed later). Table 6.1.1 shows Pearson's correlation coefficients for a typical scan. The strongest correlations are between Ba and Sr ($r = +0.90$, $p<0.001$), Ba and U ($r = +0.82$, $p<0.001$), and Ba and Mg ($r = -0.71$, $p<0.001$). Moderate correlations are found between Sr and Mg ($r = -0.57$,

---

[1] This number was determined by calculating the average and 1 standard error of the number of cycles along 11 adjacent tracks scanned along the length of the sample over a section ~1 mm wide.)

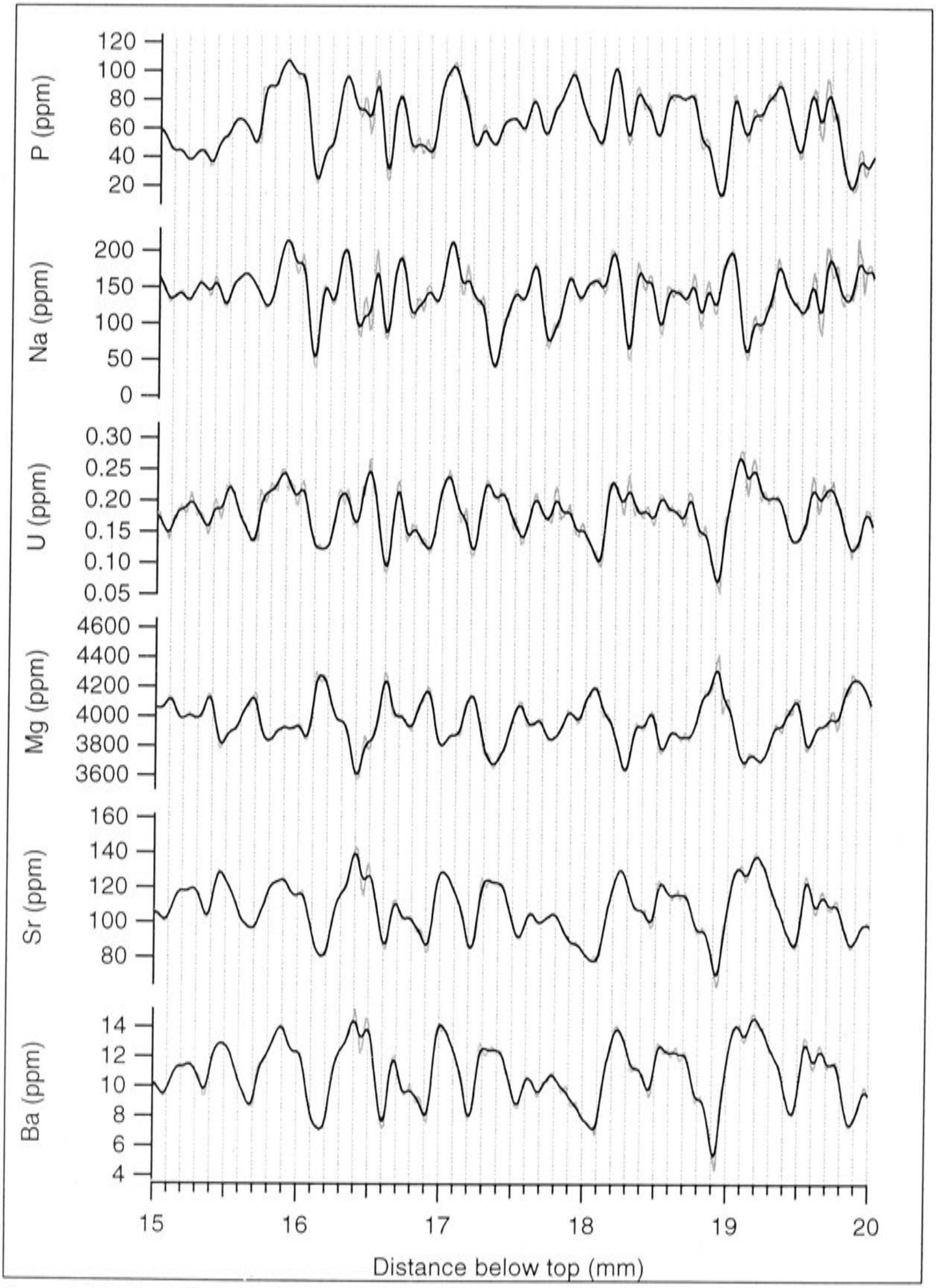

Figure 6.1.1: Typical cycles in P, Na, U, Mg, Sr and Ba for the period A.D. 1968-1961. (Grey line is raw data, solid line is smoothed data; 9 point second-order Savitzsky-Golay filter twice.)

$p<0.001$), Sr and U ($r = +0.63$, $p<0.001$), Mg and U ($r = -0.69$, $p<0.001$), Na and P ($r = +0.44$, $p<0.001$), P and U ($r = +0.49$, $p<0.001$), P and Ba ($r = +0.37$, $p<0.001$) and P and Mg ($r = -0.53$, $p<0.001$). Overall, Na has the weakest correlation coefficients at phase

lag zero, apart from a moderate correlation with P ($r = +0.44$, $p < 0.01$). Correlations between Na and other elements were slightly strengthened for lagged correlations (Figure 6.1.2); for example Ba leads Na by +1, +12, +31, -41 and –52 months, however these lagged correlation coefficients are still low ($r < \pm 0.2$, $p < 0.02$).

Table 6.1.1: Correlation matrix of elements at lag 0 along a typical scan (performed on smoothed data, re-sampled to 12 points per annual cycle). (All values in bold are significant at $p<0.001$. N=2495)

r	Ba	Sr	Mg	U	Na	P
Ba	**1**	**0.90**	**-0.71**	**0.82**	**0.11**	**0.37**
Sr		**1**	**-0.57**	**0.63**	-0.06	0.01
Mg			**1**	**-0.69**	0.18	**-0.53**
U				**1**	**0.14**	**0.49**
Na					**1**	**0.44**
P						**1**

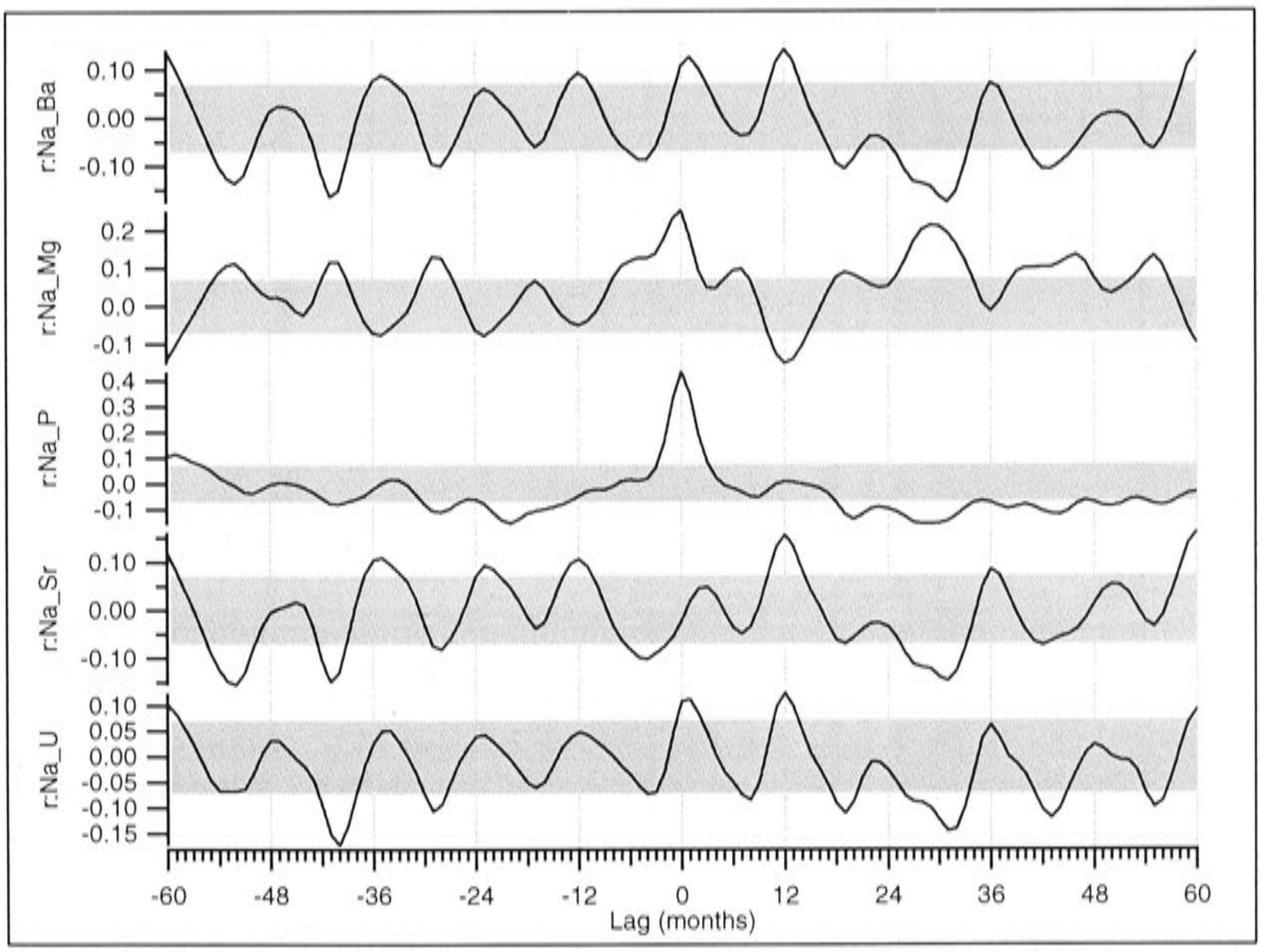

Figure 6.1.2: Lagged correlations between Na with U, Sr, Ba, Mg and P (Na is stationary, other elements are shifted). Grey stippled bar represents correlations outside the 98% confidence interval ($p < 0.02$; $n = 1043$).

Results of a Fourier analysis conducted by first removing high frequency noise using an autocorrelogram, show that the strongest cycle occurs at wave number 87, which

corresponds to a period of 12 months for the following elements, in order of decreasing cycle strength: Ba, Sr, U, Mg and P (n=1043; Figure 6.1.3). P also shows cycles at significant amplitude at periods 36, 70 and 348 months (3, 5.8 and 29 years, respectively). Surprisingly, the Fourier analysis detects no annual cycle for Na. Na displays other cycles at periods 25, 43 and 50 months (2.1, 3.6 and 4.1 years, respectively), however, these are well below the 99% confidence level. Repeating the Fourier analysis on raw Na data (no autocorrelogram) did not change this result.

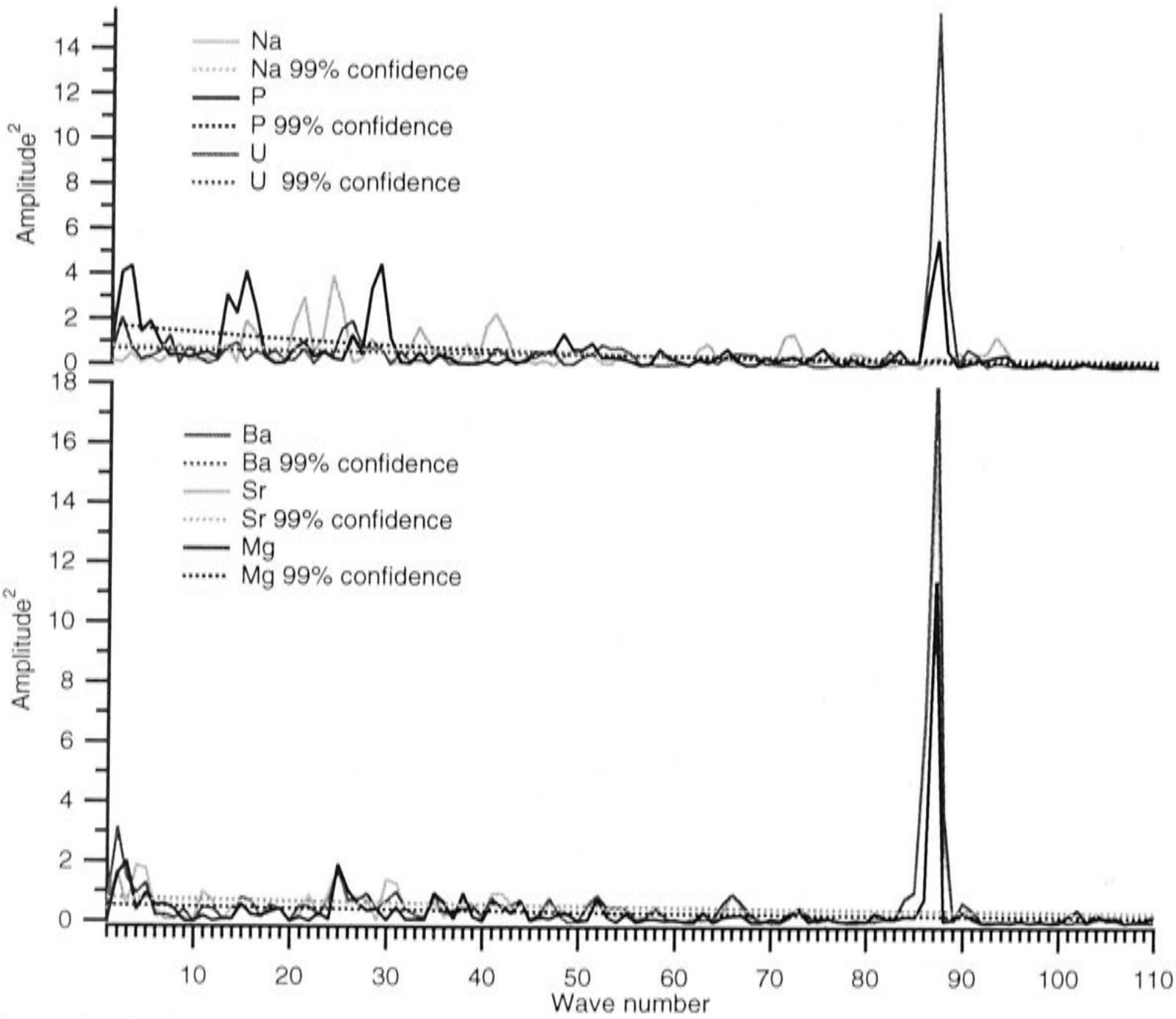

Figure 6.1.3: Results of a Fourier analysis performed on along a typical scan (performed on smoothed data, re-sampled to 12 points per annual cycle). Data only shown to wavelength of 110 (no significant frequencies appear beyond this.)

To consider long-term trends, the filtered data were fitted with cubic polynomials, which demonstrate that mean P concentration has decreased by over 60% and mean Na concentration by 20% since ~A.D.1965, while mean U concentration shows a small but continuous decline throughout the entire period with an overall of 10% (Figure 6.1.4). Mg concentration has increased over the period by ~5%, which is consistent with its

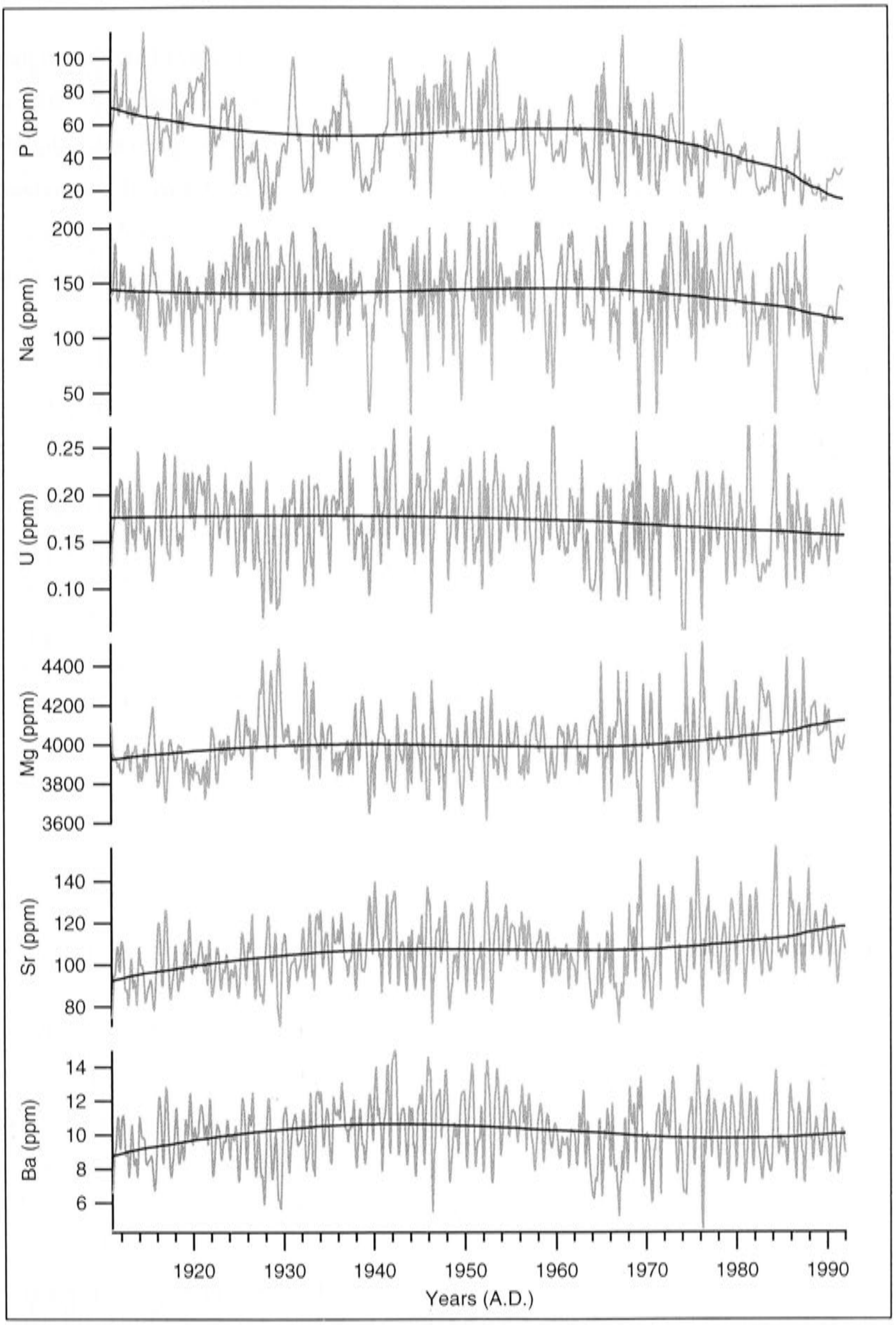

Figure 6.1.4: Annual variations in trace element concentrations re-sampled by interpolation to 12 points (months) per annual cycle and fitted with a cubic polynomial to show overall trend.

antiphase behaviour. Sr and Ba concentrations show the least consistent long-term trends with both elements showing an early increase before a plateau from ~A.D.1935 to ~A.D.1955. After A.D.1955, Sr concentration increased while Ba decreased slightly (Figure 6.1.4). Table 6.1.2 shows that de-trending the data strengthened correlations between Mg and Sr ($r = -0.72$ compared with $r = -0.57$, $p < 0.001$) and P and Sr ($r = +0.22$, $p < 0.001$ compared with $r = +0.01$), while other values were either only slightly weakened or strengthened.

Table 6.1.2: As for 6.1.1 but here data have been interpolated to 12 points per Ba cycle and long-term trends removed.

r	Ba	Sr	Mg	U	Na	P
Ba	**1**	**0.95**	**-0.77**	**0.84**	**0.11**	**0.44**
Sr		**1**	**-0.72**	**0.72**	-0.01	**0.22**
Mg			**1**	**-0.68**	**0.23**	**-0.49**
U				**1**	**0.12**	**0.49**
Na					**1**	**0.41**
P						**1**

To investigate any possible changes in the strength of the inter-annual relationships through the duration of the record, a 12 month moving window correlation was performed on the de-trended data. This exercise (Figure 6.1.5A) reveals that U is predominantly highly correlated on the annual cycle scale with Sr, Ba and Mg ($r > +0.95$, $p < 0.02$) implying that the overall correlation values (Table 6.1.2) are weakened by occasional years when the relationship is weak or even antiphase. Similar behaviour is observed for Mg (Figures 6.1.5B). There is no consistent behaviour in the U or Mg concentrations during these non-correlated episodes, to suggest why this usually strong correlation occasionally breaks down (Figure 6.1.5A and B).

Figure 6.1.6A reveals that P is also often strongly correlated with Ba, Sr, U, Na ($r > +0.90$, $p < 0.02$) and also with Mg ($r < -0.90$, $p < 0.02$). However, there are many years when these correlations are weaker and sometimes antiphase. In the case of P, these later periods appear to coincide with periods when the P cycle is less well defined and lower

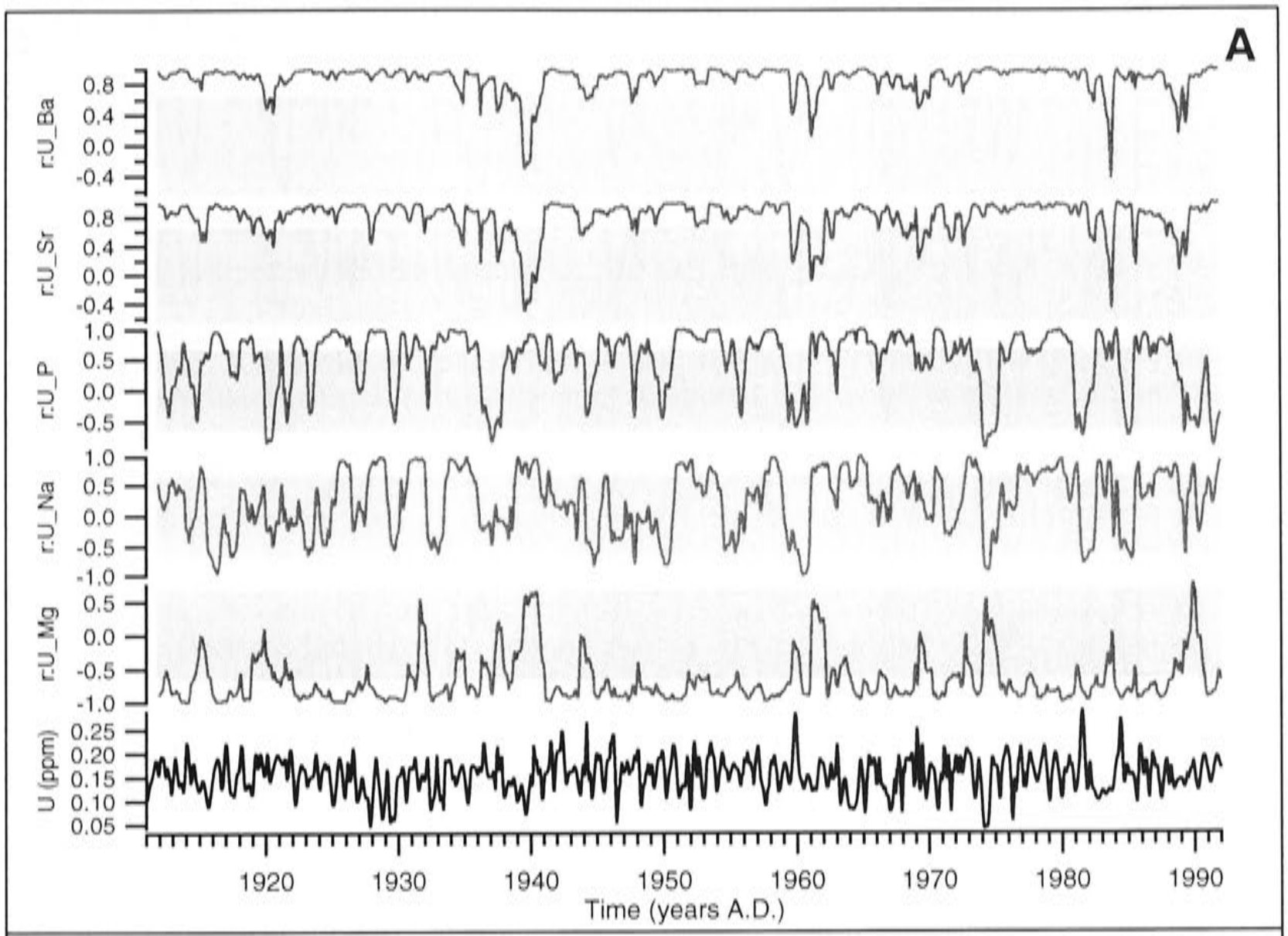

Figure 6.1.5A and B: 12 month moving window correlations for elements against U (A) and Mg (B). U and Mg concentrations are shown for comparison. The grey stippled bar represents correlations outside the 98% confidence interval ($p < 0.02$, $n = 12$).

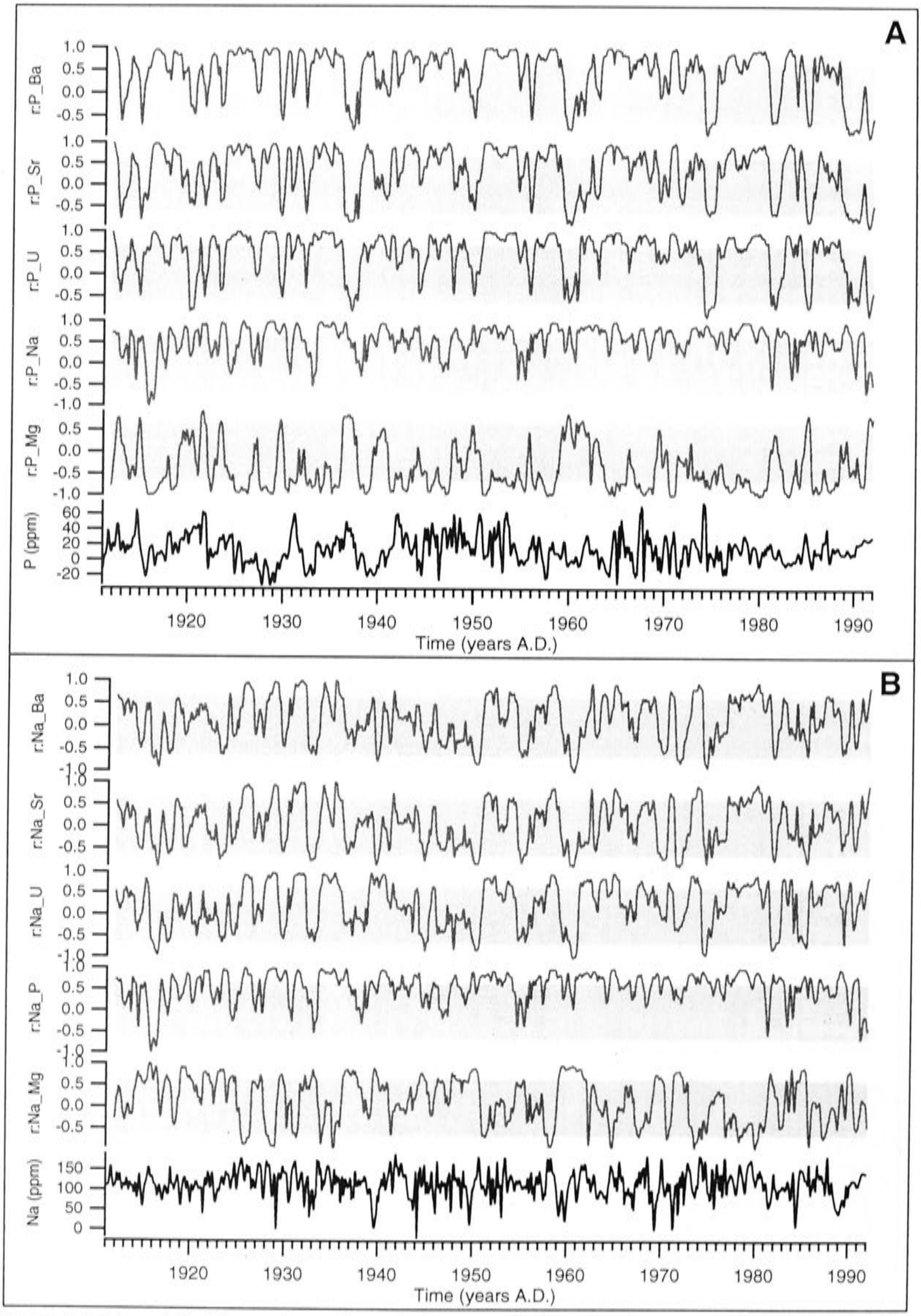

Figure 6.1.6A and B: 12 month moving window correlations for elements against P (A) and Na (B). P and Na concentrations are shown for comparison. The grey stippled bar represents correlations outside the 98% confidence interval ($p < 0.02$, $n = 12$).

in amplitude (Figure 6.1.6A). The correlations between Na with Sr, Ba, U and Mg are highly variable and occasionally are strongly inphase or antiphase (Figure 6.1.6B).

By contrast, the correlation between P and Na is generally strong ($r > +0.80$, $p < 0.02$) and is rarely antiphase. In the case of U, Mg and P (Figures 6.1.5A, 6.1.5B, 6.1.6A) the weakly correlated years appear to be due to missing or poorly defined (generally lower amplitude) cycles in the U, Mg or P concentrations; however Na differs in that weaker correlations appear to be due to periods when there are a greater number of Na cycles compared to the other elements (Figure 6.1.6B). Neither Figures 6.1.5A, 6.1.5B, 6.1.6A or 6.1.6B demonstrate that there are consistent changes in element relationships on the annual scale over the length of the record.

6.1.2 Relationship with calcite fabric

The annual cycles seen in Ba, Sr, Mg and U closely coincide with visible patterns in the speleothem calcite fabric. Troughs in Ba, Sr, U and peaks in Mg closely align with lines of small holes that became apparent after many episodes of polishing and ultra-sonic cleaning in MQ H_2O (Figure 6.1.7).

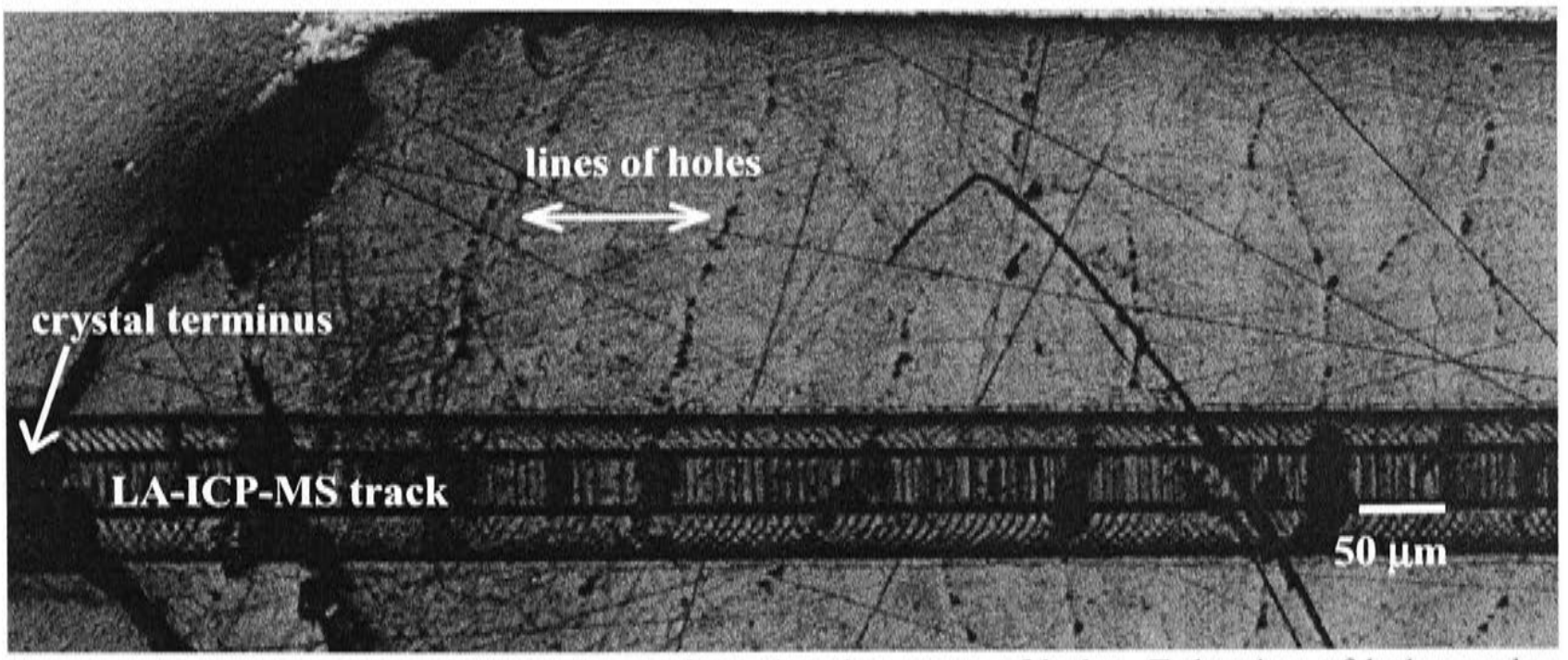

Figure 6.1.7: Photograph of MND-S1 surface showing rows of holes. Enlarging of holes under the LA-ICP-MS track shows further damage caused by the laser pulsing over the surface.

The section shown above was mapped by acquiring LA-ICP-MS measurements (5 x 50 µm slit) along adjacent parallel tracks. The data were gridded, smoothed across the grid

(3 point moving average) and then contoured (Figure 6.1.8). This map is shown overlain with a tracing of the lines of holes shown in Figure 6.1.7, showing that the troughs in Ba concentration coincide with these lines of holes. The relationship between the annual cycles of trace elements and the layered fabric of the calcite implies that these holes are the consequence of seasonal changes in calcite precipitation and/or drip-water chemistry. Thus, diagnosing their origin may resolve the causes of the seasonality of the trace elements. An enlarged view of typical lines of holes is shown in Figure 6.1.9A, (photographed with Au coating under reflected light immediately adjacent to the mapped surface), and SEM images of individual holes are shown in Figure 6.1.9B and C. Appendix II shows an image of MND-S1 with the spatial relationship of all images and data acquired. These holes were not seen in a thin section which was cut from the back of this sample mount, but the material used for the thin section was not repeatedly washed in MQ H_2O, which suggests that these holes were enlarged during etching. Striations in the etched surfaces reveal cleavage planes that would have been initially camouflaged by polishing (Figures 6.1.9A, B and C).

It is likely that these holes, enlarged by etching in MQ H_2O, are voids resulting from the failure of new crystal growth to fully anchor to the previous growth surface following a period of non-deposition. If so, they mark the driest part of the year, which is likely to be during summer, depending on the delay of water depletion in the calcarenite cave roof. The cave managers observed seepage-fed water table response within one month of winter rains, however there may be a 4-10 month delay between peak water table and peak rainfall (S. Eberhard, *pers. comm.*). If the drip-water trace element concentration is a function of residence time, then it may be inferred that MND-S1 Ba, U, P and Sr are highest and Mg is lowest under wetter drip flow conditions, most likely in winter and transitional seasons, and are lowest (Mg highest) during the driest conditions, *i.e.* summer months. However, this model may not hold if the beginning of the trace element cycle does not match with the restoration of drip flow, as the case may be if these elements are dominated by soil, meteoric, or aeolian sources. A full year of drip-water collection is obviously needed to confirm this.

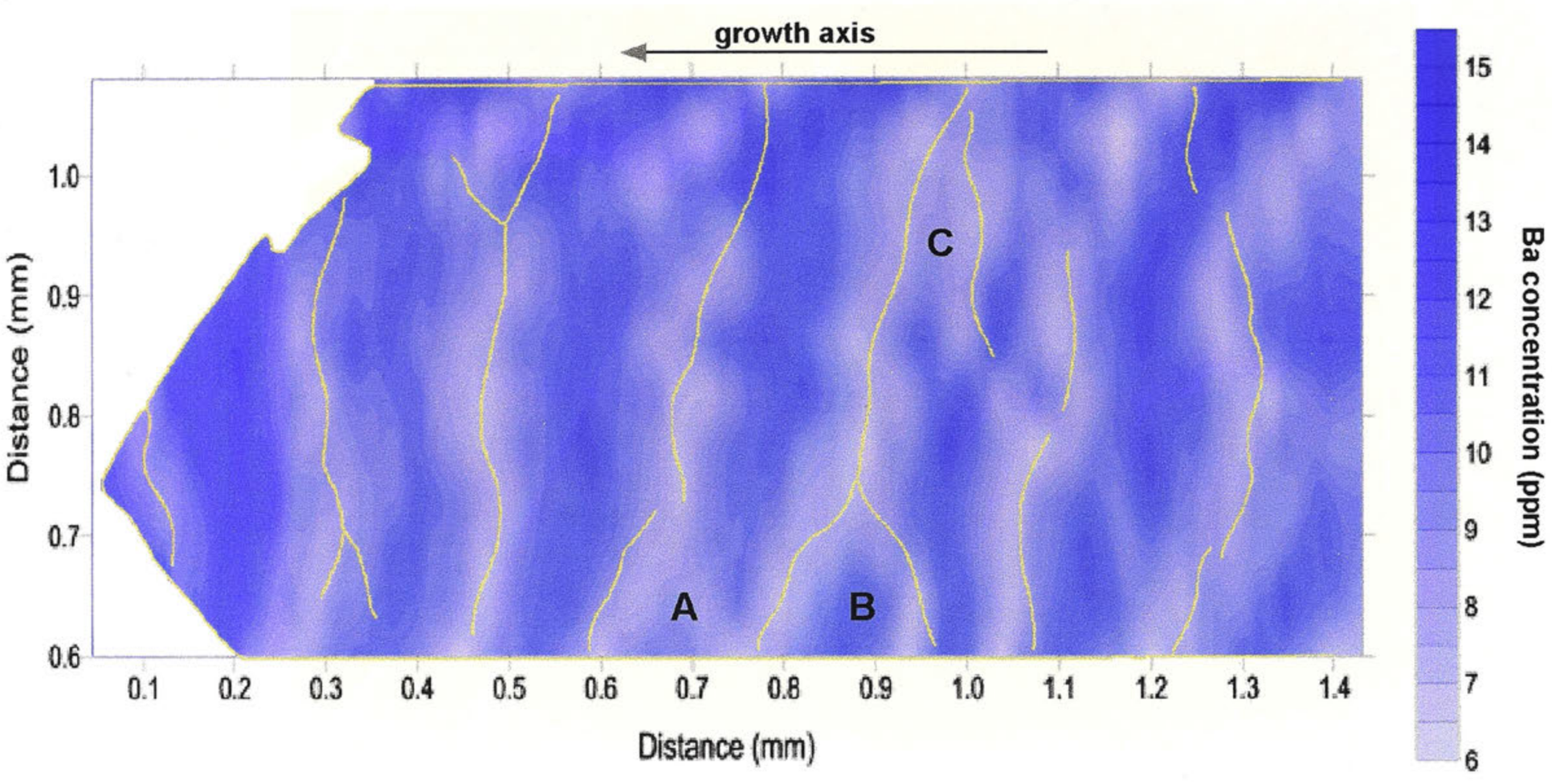

Figure 6.1.8: Ba map with tracing of sample boundary and pattern of holes (yellow). A, B and C mark unconformable features referred to in the text.

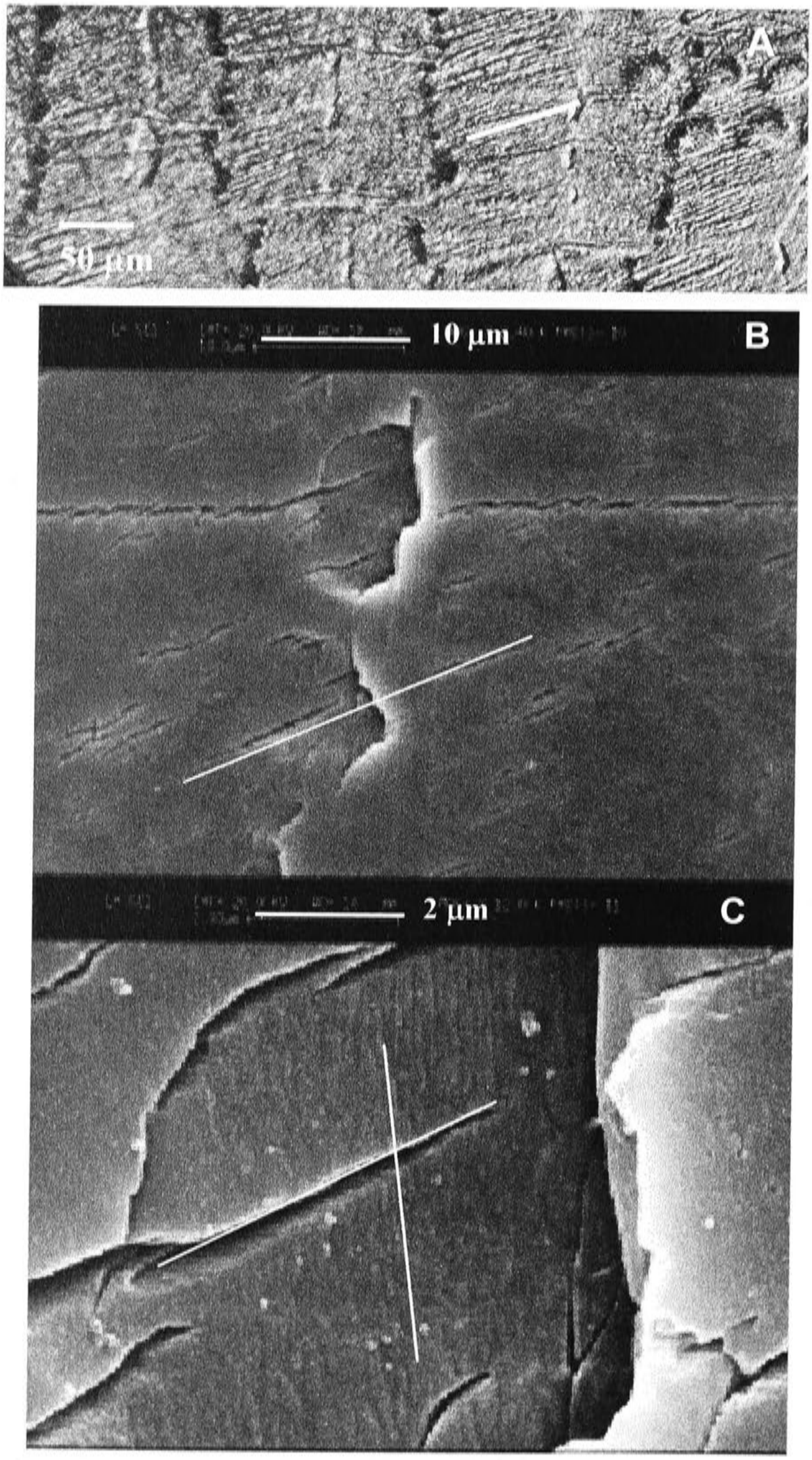

Figure 6.1.9A, B and C: A: Patterns of holes delineate annual growth cycles (circular features are ion microprobe pits (Section 6.3). Photograph taken under reflected light with Au coating on surface.) B: SEM images of holes. C: close-up of upper hole in B. (Striations, marked by white lines in A and C are cleavage planes revealed during etching by MQ H_2O.)

Figure 6.1.8 reveals further information about the incorporation of trace elements in speleothems. Annual Ba layers and the lines of holes are approximately perpendicular to the growth axis but their width varies across the crystal, resulting in pinching and bifurcating layers (marked as A, B and C; Figure 6.1.8). Two possible explanations for this uneven growth pattern are:

1. that the crystal is fed from an unevenly distributed saturated solution across the surface; and/or
2. that the crystal initially grows as a constant thickness across the surface but subsequent erosion removes part of this growth leaving remnants of crystal across the surface (marked A, B and C).

The first model is consistent with speleothem growth from trickling drip-water whose pathway switches as the surface topography of the crystal evolves, or whose pathway may simply be chaotic from splashing drips. However, neomorphism and erosion processes (second model) are indicated by the truncation of Ba bands by the surface of the large crystal rhomb tip at the crystal terminus. That the Ba bands are perpendicular to the growth axis, and not parallel to this final growth surface, suggests that solution and/or neomorphism processes have re-sculpted the crystal(s) into larger rhombs, while the Ba layering is preserved as a primary feature. If neomorphism has occurred, then it may be that the growth sections marked by A, B and C in Figure 6.1.8 also reflect previous recrystallised rhombs following a process suggested by Figure 6.1.10.

Inspection of a thin section cut from the back of the mounted sample used in these trace element analyses reveals that the sample consists of several large crystals (the section under investigation here is part of a single crystal) with no distinguishing features on the scale of the annual trace element cycles. The lack of crystal boundaries on the scale of the Ba bands and the truncation of these bands in Figure 6.1.8 by the formation of the rhomb tip is evidence that neomorphism has occurred.

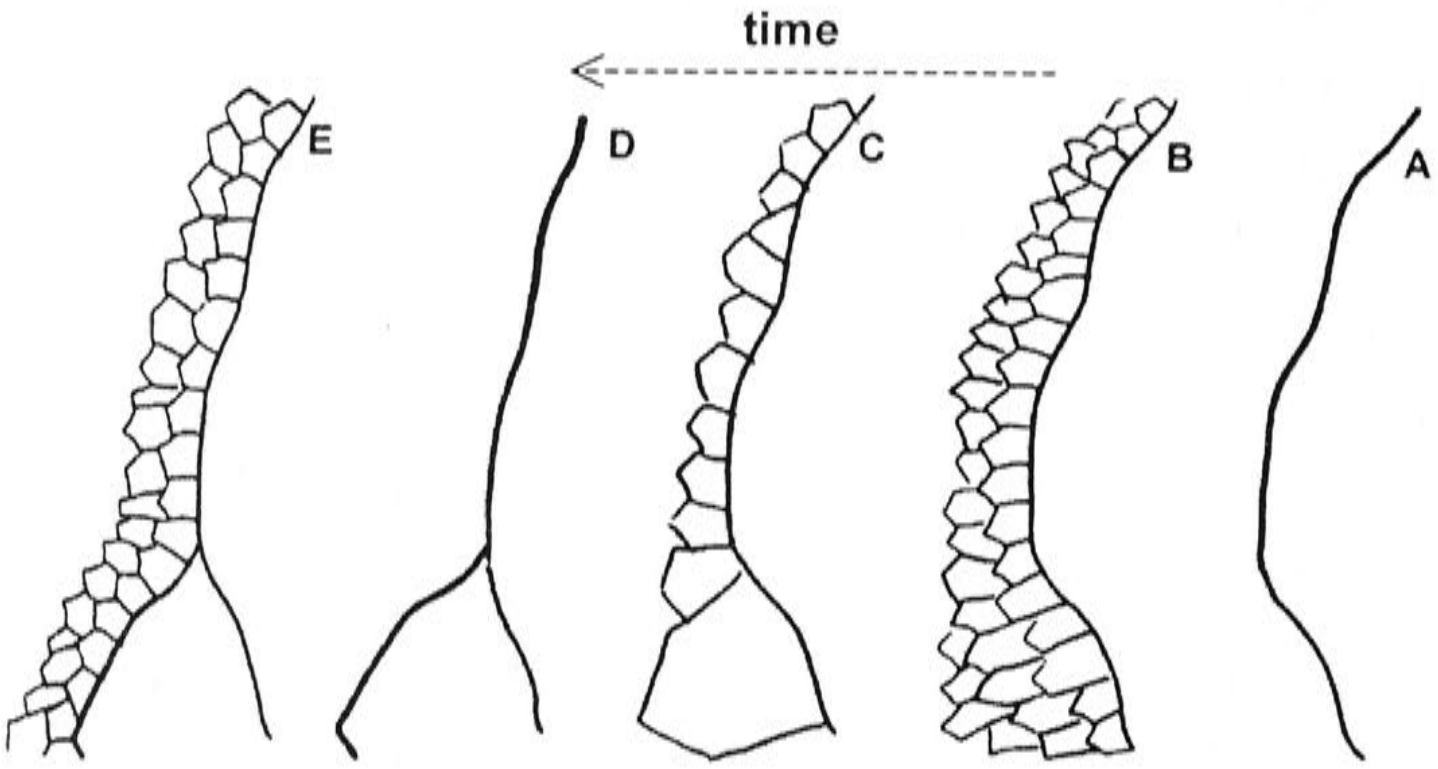

Figure 6.1.10A-E: Schematic illustration of possible Ostwald ripening process producing remnant crystal rhomb "C" on Figure 6.1.8. A is the initial crystal surface, B is the new season precipitation of small crystals, C is the coarsening of these crystals over time, D is the selective erosion of the smaller crystals leaving larger rhomb behind, and E is the subsequent year's growth.

Neomorphism implies that initial crystallisation must have occurred as a less stable intermediate form and is common for carbonates that initially formed as aragonite. This is not the case for MND-S1 as its relatively low Sr content suggests it formed initially as calcite. However, it is common for carbonates to be initially deposited as fine crystals (usually due to the quick precipitation of numerous nuclei from a saturated solution) which over time, tend to coarsen to more thermodynamically stable crystals at the expense of the smaller crystals, a process known as aggrading neomorphism or Ostwald ripening (Folk, 1965; Bathurst, 1975; Morse and Casey, 1988). Ostwald ripening is a two stage process with the initial formation of less stable but faster reaction rate intermediates, which are driven by contrasts in surface tension to recrystallise into thermodynamically more stable, larger crystals. This second step may involve full dissolution of small crystals and transport of the ions through solution to the larger crystal, or grain boundary migration under anhydrous conditions (Morse and Casey, 1988). The absence of continuous banding adjacent to isolated rhomb shapes (marked A, B and C; Figure 6.1.8) may indicate the loss of the smaller crystals during progressive, uninterrupted growth of the coarsened crystals as illustrated in Figure 6.1.10.

If this model is correct, coarsening and possibly erosion may alter the primary trace element patterns, although the congruence of trace element and growth lines in Figure

6.1.8 indicates that this does not significantly affect the final annually layered pattern. However, the model has important implications for palaeoclimate interpretation of speleothem geochemistry, in that it implies that neomorphism may have the potential to affect the integrity of speleothem trace element and stable isotope composition, and that some material is lost to erosion. To examine the problem, maps of other trace elements are shown below and are then compared with instrumental climate data, in Section 6.2 of this Chapter.

6.1.3 Relationships of trace elements and visible banding

The polished section shown in Figure 6.1.8 was re-mapped using the 32 μm laser spot, in order to adequately measure all trace elements including lower abundance metals such as U. Elements Al and Si were also acquired to monitor the presence of sedimentary mineral detritus. Obviously, using a larger spot (32 μm circular as opposed to 5 μm slit) results in lower resolution maps, however, comparing Figures 6.1.11A and B shows that the main features are preserved for Ba, and that similar features are reproduced for Sr and U (Figure 6.1.11C and D). Mg and Na appear noisy (Figure 6.1.11E and F) but relative variability seen in measurements of standards is much lower, suggesting that this is not due to measurement sensitivity; thus the distribution of Mg and Na must be relatively heterogeneous.

Unexpectedly, the map of P (Figure 6.1.11G) shows banding oblique to the Ba, Sr and U layering. The band of highest P concentration appears to coincide with a strong Al band (Figure 6.1.11H), which marks the presence of detritus and thus possibly a hiatus (Figure 6.1.12). Both Al and P bands are parallel to the surface of the recrystallised rhomb tip, which is oblique to the growth axis, described above. It can be eliminated that the P banding is the result of contamination from the epoxy mounting, which is shown as a 'front' of mass 29 moving through the rhomb tip from the top of the page downwards (Figure 6.1.11I). Mass 29 was nominally collected as ^{29}Si but as epoxy is an organic compound, it is unlikely to contain this level of Si (exact epoxy content unknown). Mass 29 must therefore be an isobaric interference probably from an organic C-N-H species in the epoxy, that has seeped into the calcite crystal from the sample top edge.

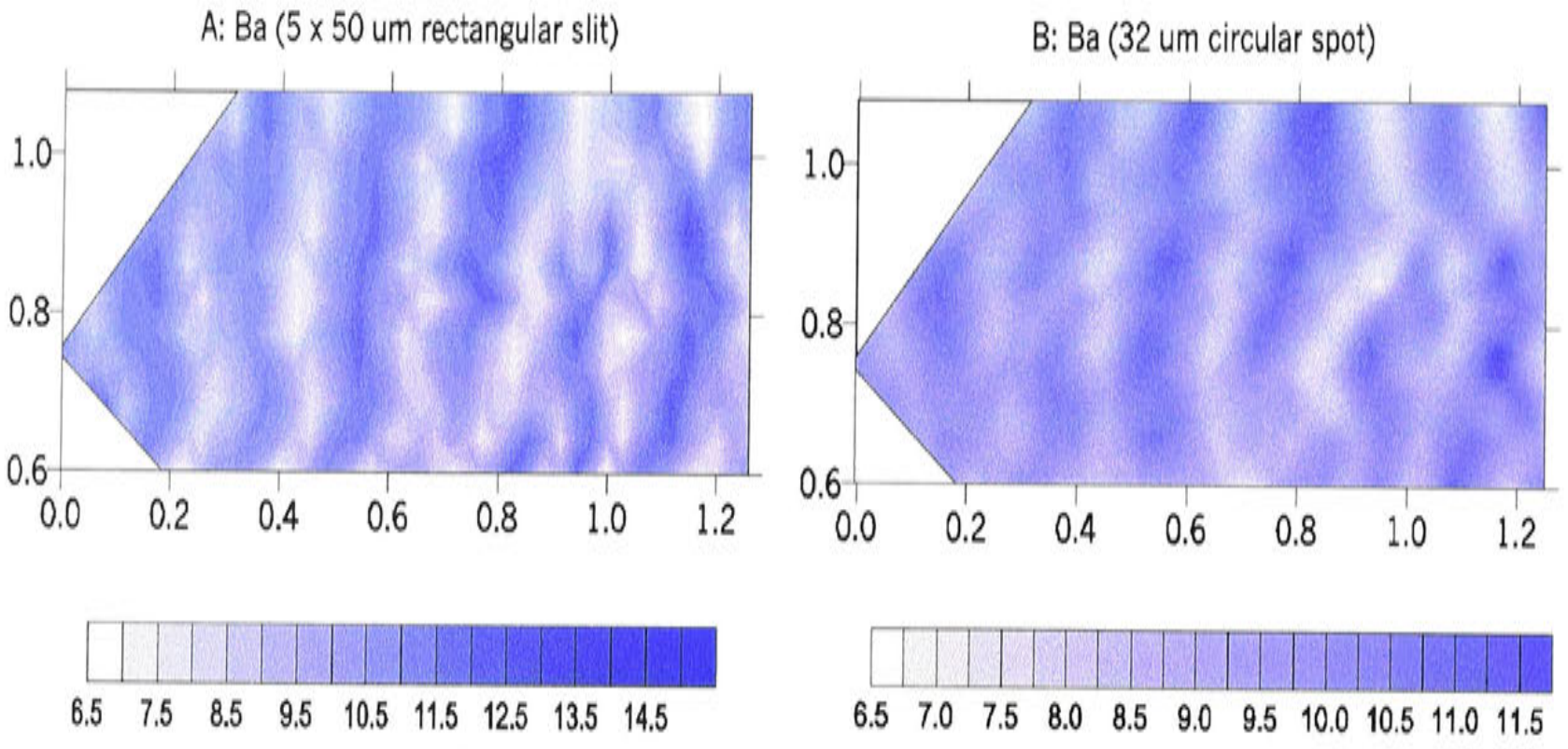

Figures 6.1.11A-D: Ba concentration mapped with the 5x50 μm slit (A), the 32 μm spot (B) and Sr and U concentrations (C and D) mapped with the 32 μm spot. (X and Y axes are in mm and the colour scales are in ppm.)

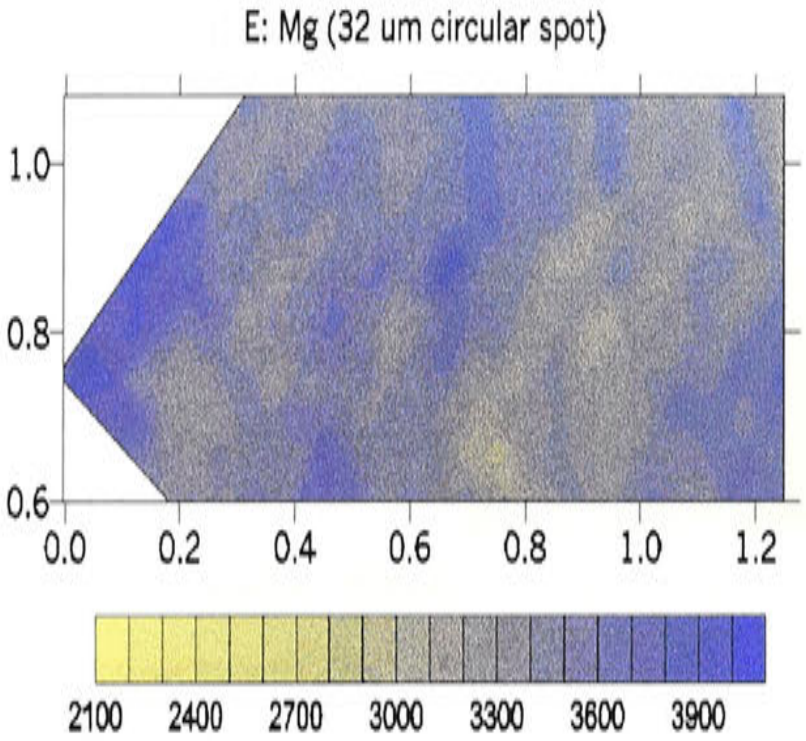

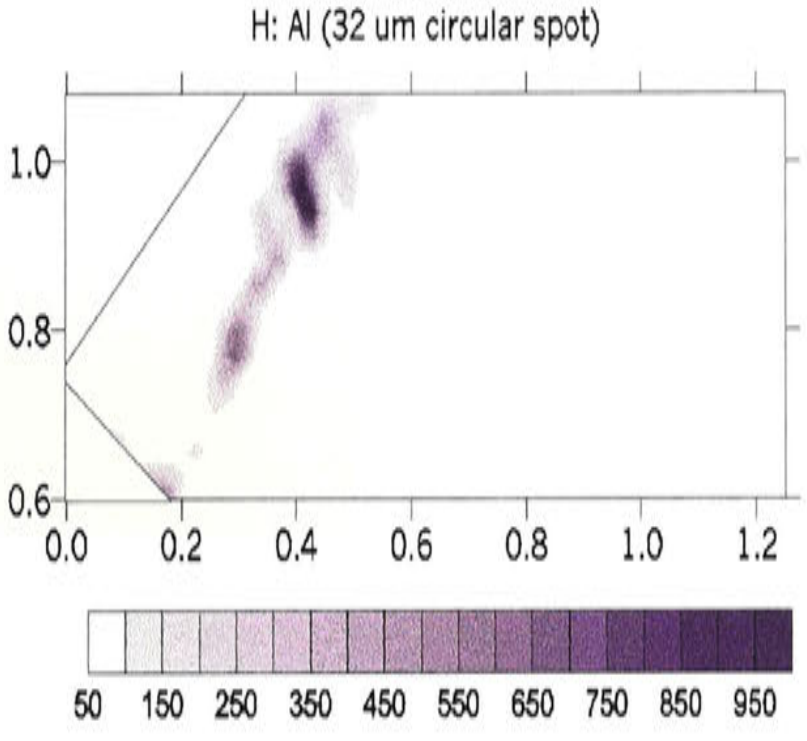

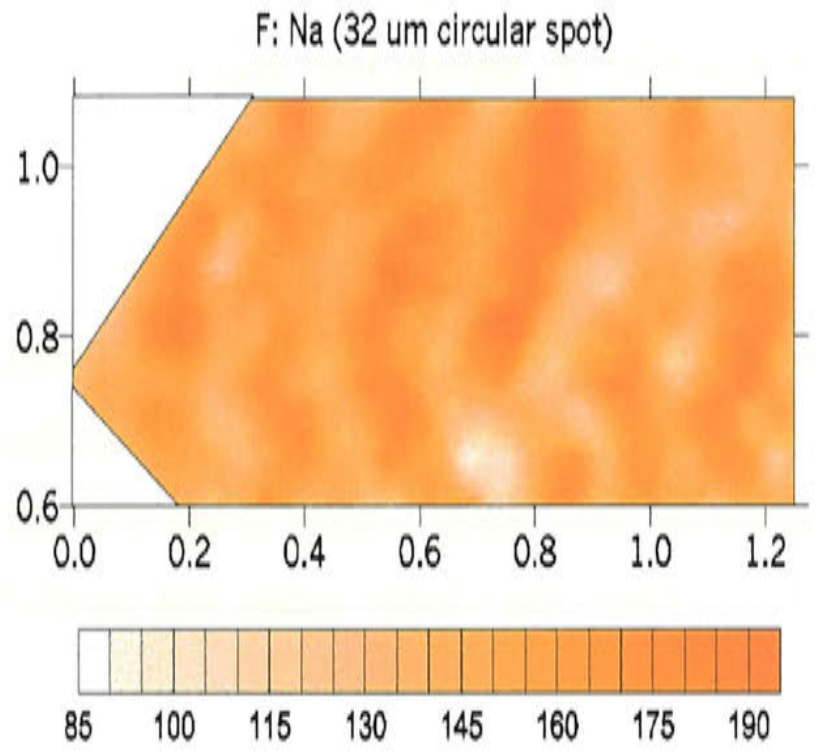

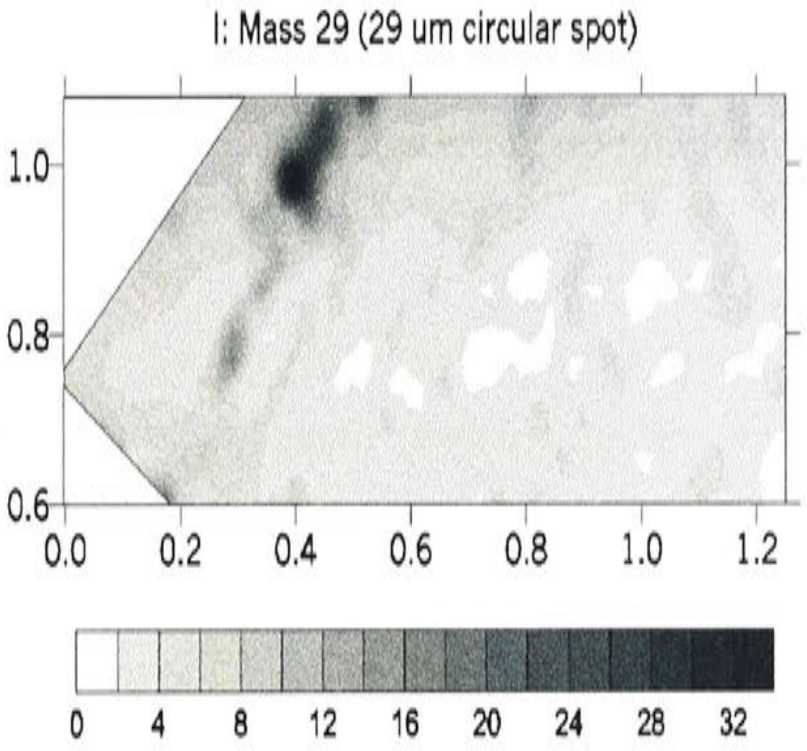

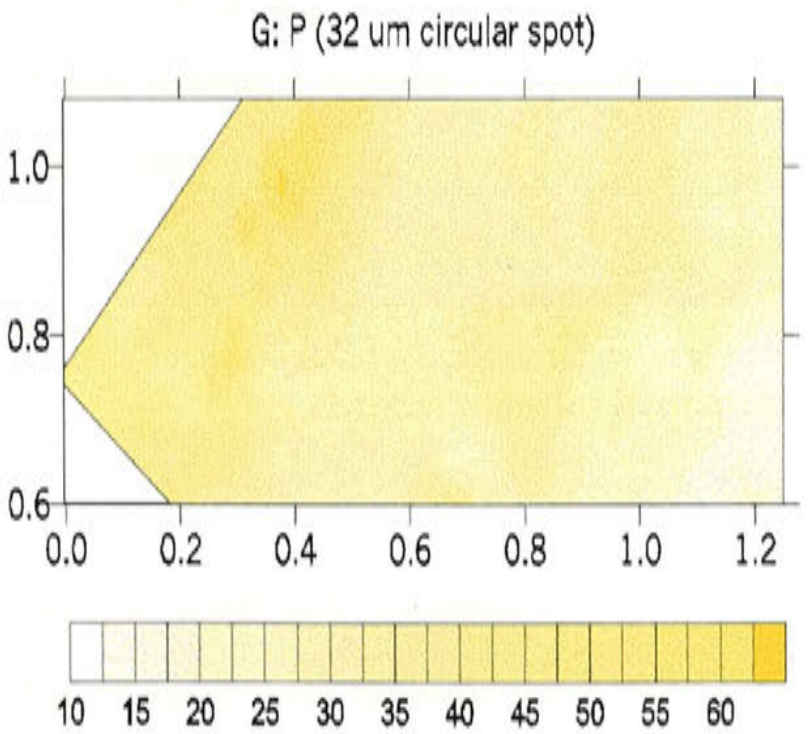

Figures 6.1.11E-I continued: Mg (E), Na (F), P (G), Al (H) and mass 29 (I) concentration mapped with the 5x50 μm slit. (X and Y axes are in mm and the colour scales are in ppm.)

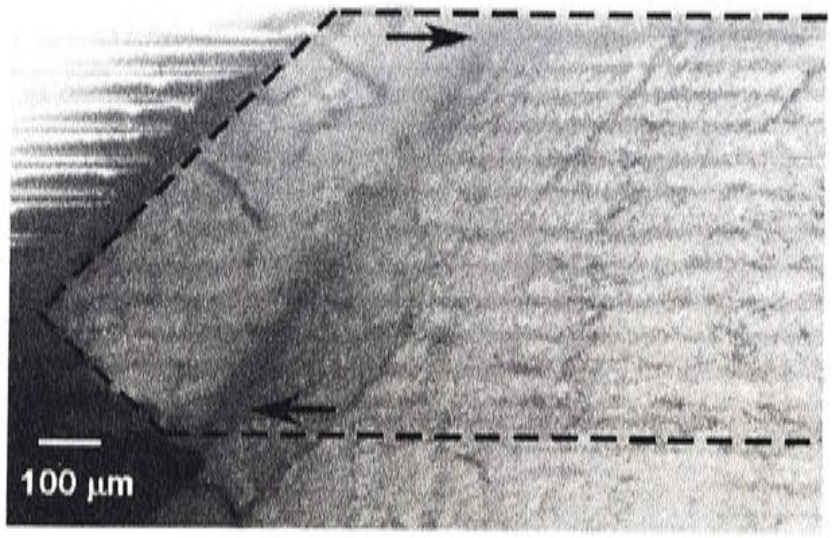

Figure 6.1.12: Detrital band marked by arrows in section mapped (dashed outline) in Figures 6.1.8 and 6.1.11. Left-right orientated ridges are laser ablation tracks.

The fact that the P bands are parallel to the recrystallised surface rather than the Ba bands suggests that P entered the specimen later than Ba and other trace cations, which parallel the annual growth lines and thus are assumed to accumulate during primary precipitation of the calcite.

Further LA-ICP-MS scans on an adjacent section of MND-S1 (where UV and visual banding are clearest; immediately above the section shown in Appendix II) show that large amplitude variations in P concentration coincide with bands visible in the UV and visible spectrum (Figure 6.1.13 and Figure 6.1.14). Here, the visible bands run parallel to the final (Ostwald-ripened) surface (Figure 6.1.14).

The concentration of P parallel to recrystallised surface raises the question as to its origins. It is proposed here that P bands may be the result of Ostwald ripening that has forced P out of its original lattice sites, towards the grain boundaries. Alternatively, P may have been adsorbed on the recrystallised surface by a secondary mechanism. These hypotheses will be left to discussion in Section 6.4 (pages 150-153), following further comparisons of the trace element data with instrumental climate records.

It is worth pointing out here, before moving to climate comparisons, that these mapping exercises have revealed that high resolution speleothem trace element records can not be based on just one analysis track, as has been the case in Secondary Ion Mass Spectrometer (SIMS) studies of speleothems (Roberts *et al.*, 1998; Fairchild *et al.*, 2001 and Huang *et al.*, 2001). LA-ICP-MS has the advantage that many more data can be

acquired, at higher resolution, such that the resolution approaches continuous scanning mode. This allows scans to be acquired and stacked so that variability between adjacent transects is reduced when constructing master records for climate comparison. The exercise described here has revealed the complex morphology of these growth layers, which is clearly revealed in Figure 6.1.15A-C. Figure 6.1.15C illustrates the potential difference between two LA-ICP-MS scans across the speleothem, just 0.5 mm apart. The lower 'scan' shows 7 cycles, while the upper scan of Plot C shows just 5 cycles. This exercise clearly demonstrates that one track, typical of SIMS analyses, could lead to high errors in distinguishing annual cycles and is therefore not sufficient to capture the true variability of speleothem annual growth bands. It appears that although high-resolution studies are steps forward in understanding speleothem element variation, multiple tracks must be taken and stacked to form analyses that are truly representative of this variation.

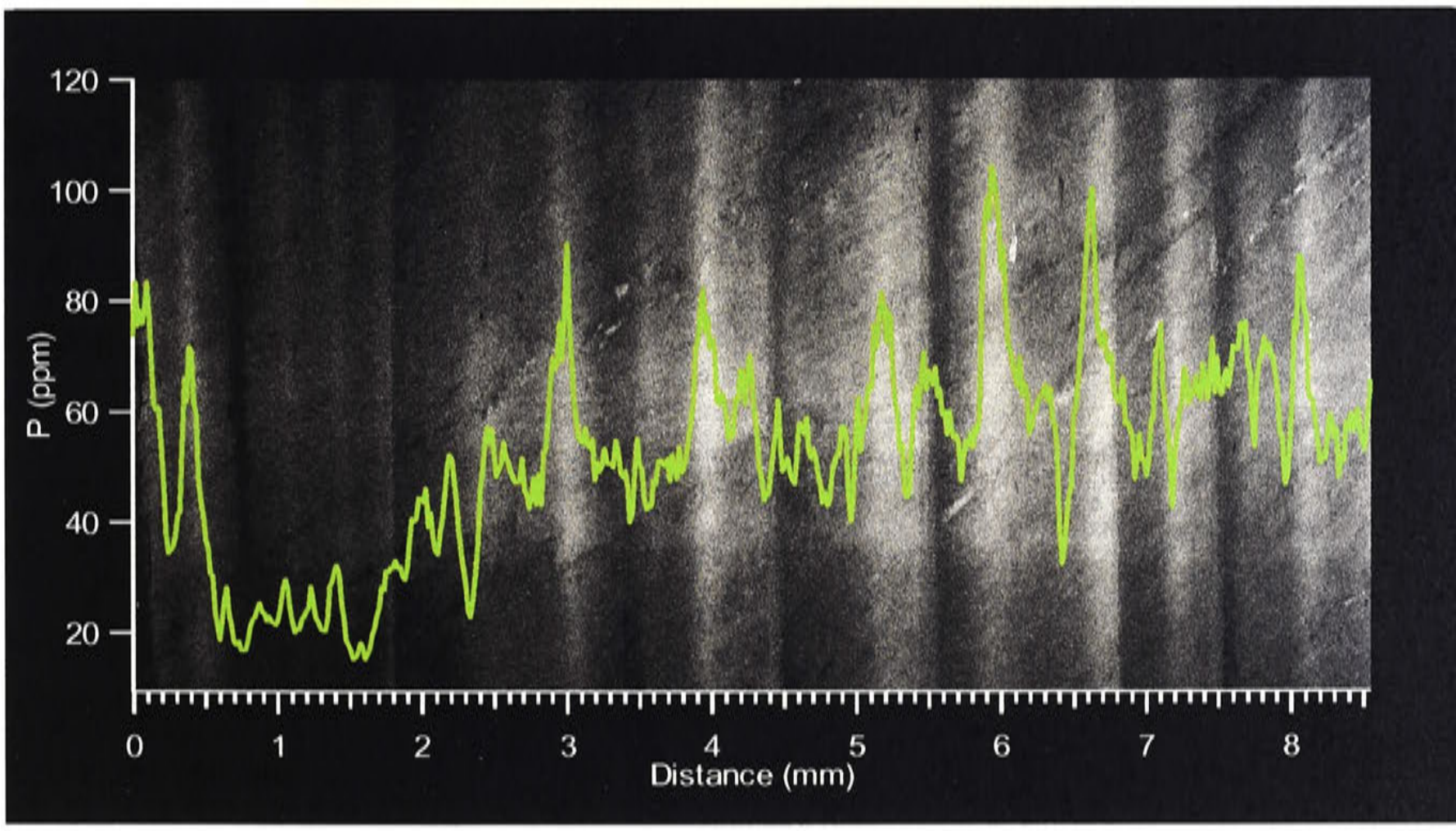

Figure 6.1.13: Highest P concentration coincides with light grey UV bands.

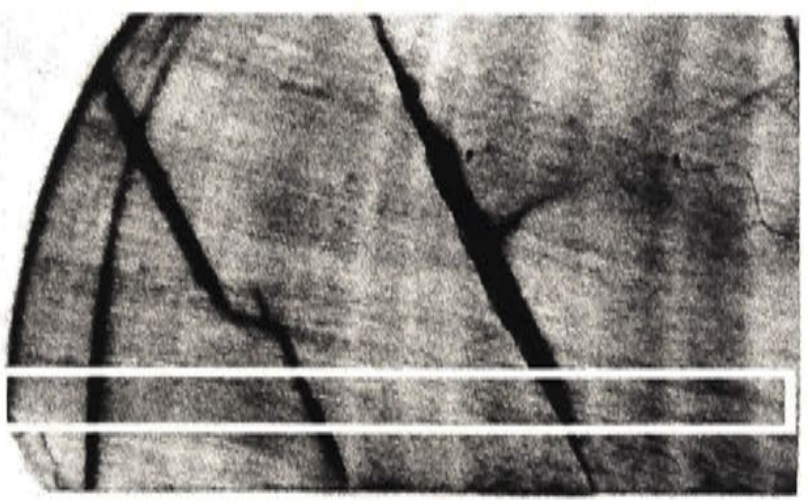

Figure 6.1.14: Section of MND-S1 taken immediately above the main section described here (Appendix III) showing clear visible banding that run parallel to the recrystallised surface. (Box shows section shown in Figure 6.1.13.)

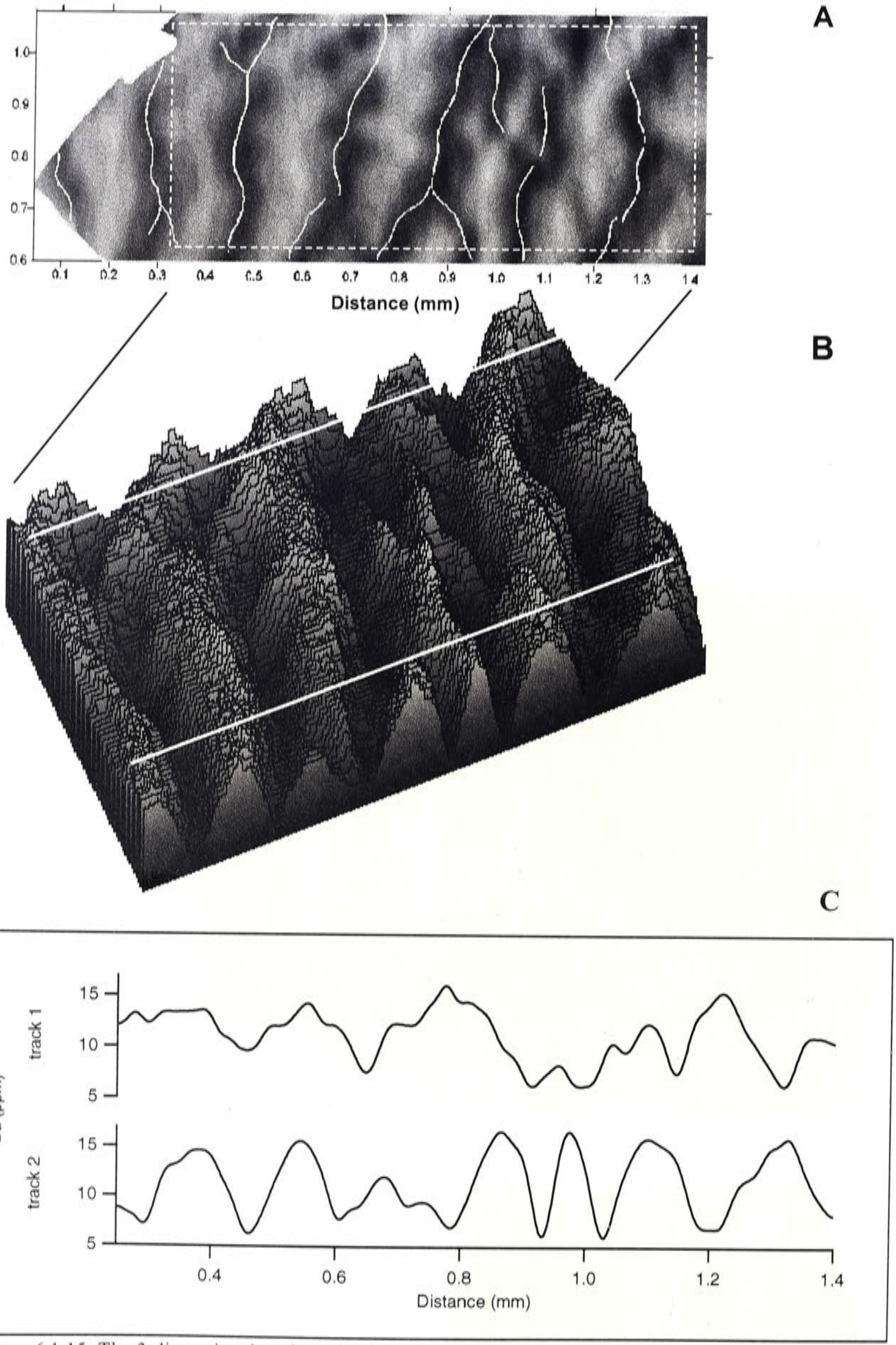

Figure 6.1.15: The 3-dimensional surface plot (B) emphasises the spatial heterogeneity of speleothem Ba concentration (white dashed box in plot A shows the position of this surface plot on the Ba map. Plot C, constructed from B, demonstrates how two tracks that are only ~0.5 mm apart may differ in the appearance and number of cycles. Surface plot made with Scion Image (http://www.scioncorp.com).

6.2 RESULTS OF COMPARISON BETWEEN TRACE ELEMENTS AND CLIMATE RECORD

6.2.1 Trends

To compare MND-S1 trace elements to instrumental climate records, 11 adjacent tracks were stacked to form a master record by first interpolating the cycles as previously described[2] and then taking the average yearly maximum of each element (minimum for Mg) and calculating the standard error for each value. Only the maxima (minima for Mg) were used, as opposed to yearly averages, since the mapping exercises described in Section 6.1 revealed that trace element concentrations are highest (Mg lowest) during the wettest months, and reduction of winter rainfall is the strongest climatic trend over the growth period of MND-S1. Results are plotted in Figure 6.2.1, with the mean of the A.D.1960-1992 period subtracted, so that positive values refer to values higher than the mean for this period. A.D.1960-1992 is characterised by 20% less winter rainfall (Nicholls and Lavery, 1992; Smith *et al.*, 2000).

Trace element and rainfall variations are conveniently compared in four episodes: (i) pre-A.D.1930, (ii) A.D.1931-1956, (iii) A.D.1957-1969 and (iv) A.D.1970-1991. Figure 6.2.1 shows that between themselves, these elements are strongly correlated in the stacked master record (Mg:P $r = -0.73$, Mg:U $r = -0.75$, P:U $r = +0.62$; $p < 0.01$; Table 6.2.1). Mg, P and U in particular, resemble many features of the rainfall record suggesting that Mg, P and U may be useful palaeo-hydrological indicators. Ba, Na and rainfall show similar trends during A.D.1930-1992, with higher values during A.D.1931-1956 (ii), however the trend towards lower values after A.D.1970 (iv) is not as clear as it is for U, P and (higher) Mg. Ba, Na and also Sr show an opposite trend to rainfall prior to A.D.1930 (i), where Ba, Sr and Na are all below the mean and rainfall is above the mean. Overall, Sr shows the least resemblance to the rainfall record.

---

[2] The method used to mark annual cycles was by re-sampling the data at 12 points between the start and finish distance of a Ba cycle (trough to trough), which shows the clearest annual cycle. All other elements were passively re-sampled against the Ba cycles such that the timing of peaks/troughs in Figure 6.2.1 are all relative to Ba. This method preserves the phase relationships between the elements.

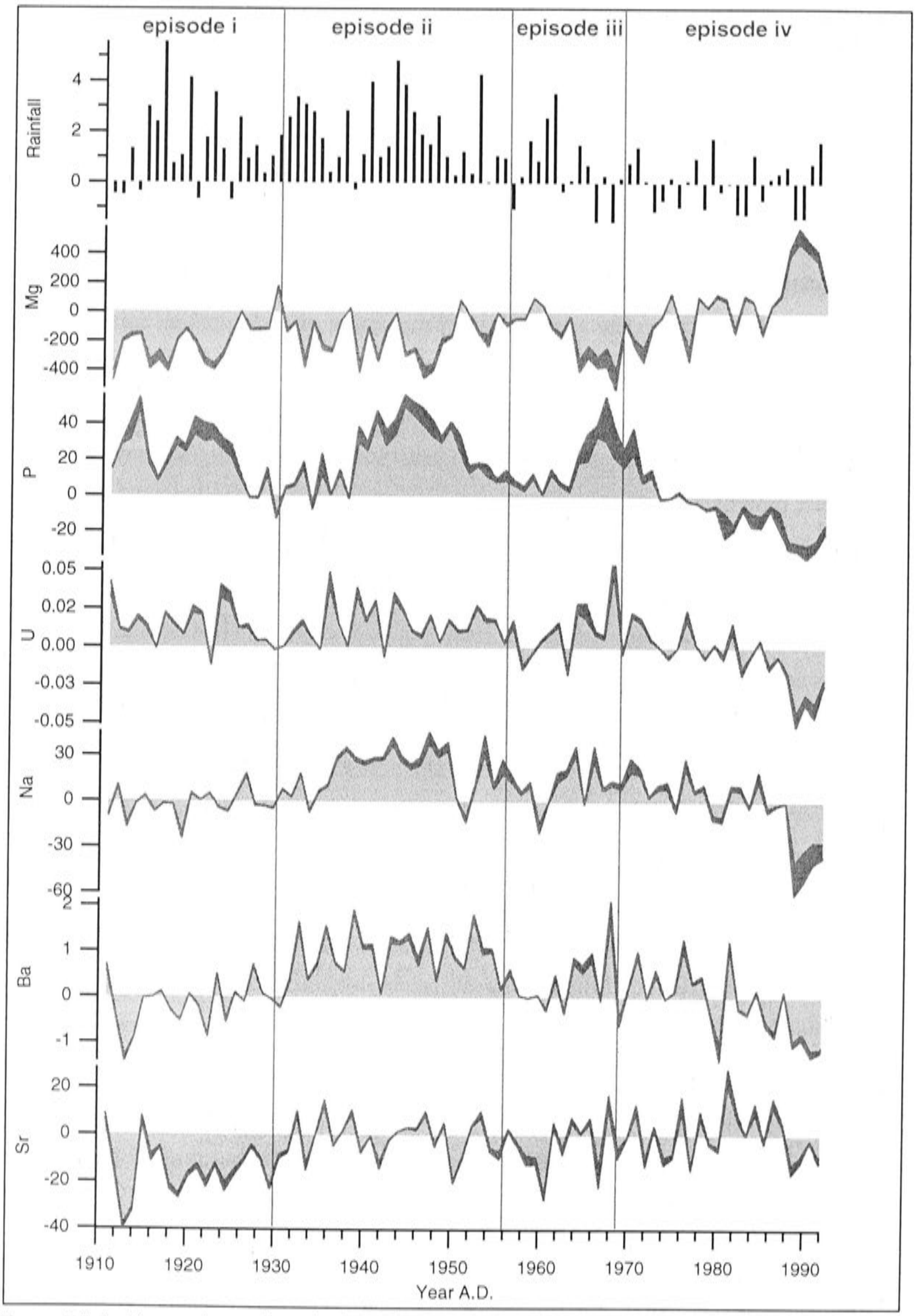

Figure 6.2.1: Comparison of stacked maximum values of Ba, Sr, U, Na and P (and minimum Mg) occurring for each year with the amount of winter rainfall (June-August). All element values have the mean of the period A.D.1961-1992 subtracted while rainfall is standardised (by subtracting the mean and dividing by the standard deviation). Dark grey line represents standard error of stacked master record.

Table 6.2.1: Correlation coefficients for stacked master record (Figure 6.2.1).

r	Ba	Sr	Mg	U	Na	P
Ba	**1**	**0.60**	**-0.51**	**0.67**	**0.67**	**0.37**
Sr		**1**	**-0.20**	**0.21**	**0.43**	-0.19
Mg			**1**	**-0.75**	**-0.54**	**-0.73**
U				**1**	**0.50**	**0.62**
Na					**1**	**0.52**
P						**1**

It is possible that the geochemistry of this earlier part (episode i) of the speleothem record is adversely affected, for example, by increased solution turbulence as the calcite was initially precipitated from drip-water running over a corner of the boardwalk (see Chapter 2 for description). Certainly, the annual cycles in the earliest portion of the record are shorter in length and are more variable within and between analysis tracks, however, if this part of the speleothem record is affected by faster, and therefore possibly kinetically-driven calcite precipitation, it does not appear to have affected the P and Mg signals in the same way (Figure 6.2.1) and thus is probably not significant. A further observation is that the decline in P, U (and rise in Mg) in episode iv appears to lag the decline in rainfall (~5 years). It is possible that the physical delay in cave seepage is responsible for this, although it is also possible that this may be due to the over-counting of cycles earlier in the record.

Finally, while some elements appear to closely mimic rainfall through episodes i-iii, their gradients contrast with the zero gradient rainfall during episode iv. Their behaviour in episode iv is summarised below:

- Mg is increasing;
- P, U, Na and Ba are declining;
- growth rate is declining; and
- $\delta^{18}O_{SP}$ and $\delta^{13}C_{SP}$ (described below, Section 6.2.4) are both increasing.

Thus, while rainfall has shifted to consistently low values, each trace element response, apart from Sr, appears to be smeared and even exaggerated, considering the shift in magnitude of values for the last 5 years of the record (A.D.1987-1992). It is plausible that this response reflects the progressive drying of the soil-calcarenite moisture column which feasibly could take years given that the depth of this column is ~20 m. This will

be discussed further in the following two Sections (6.2.2 and 6.2.3) after the effect of the rainfall decrease on the annual cycle, and the origins of the trace elements have been considered.

6.2.2 Post-A.D.1960 decline

To closely examine the possible effect of the rainfall decline on each element, individual annual cycles for each element were stacked into a single average annual cycle for the period A.D.1911-1960 and compared with a similarly stacked annual cycle for the period A.D.1961-1992 (Figure 6.2.2). The relationship of the time-scale for the elements to the rainfall calendar depends on the seasonal growth rate of the speleothem which is likely to be slower in summer than winter and may cease entirely in late summer.

Comparing the average annual rainfall cycle prior to A.D.1960 to that post-1960, clearly shows a large decrease in the dominant winter rainfall, while summer rainfall, which is light, is unaffected (Figure 6.2.2A). The rainfall pattern is otherwise unchanged *i.e.* both before and after A.D.1960, the peak in winter rainfall is close to mid-winter and also the transition from summer to winter rainfall is steeper than the transition from winter to summer.

The amplitude of the average annual cycle of Ba, U and P (Figure 6.2.2B, D and F) has decreased since A.D.1960, most markedly during winter months, but they differ in their waveforms. Both Ba and U peaks shift from being skewed towards the later part of the year before A.D.1960, to centred mid-way in the speleothem growth cycle (mid-winter) after A.D.1960, while P, which peaks earlier in the annual cycle, shows the same pattern before and after A.D.1960. Surprisingly, the Sr concentration *increased* after A.D.1960 (Figure 6.2.2E), which is unexpected given the strong correlation between Ba and Sr ($r = +0.95$, $p < 0.01$; Table 6.1.1), but is consistent with the trends of annual maxima (Figure 6.2.1). Sr also differs in that its annual cycle changes from being mid-centred to skewed towards the beginning of the year.

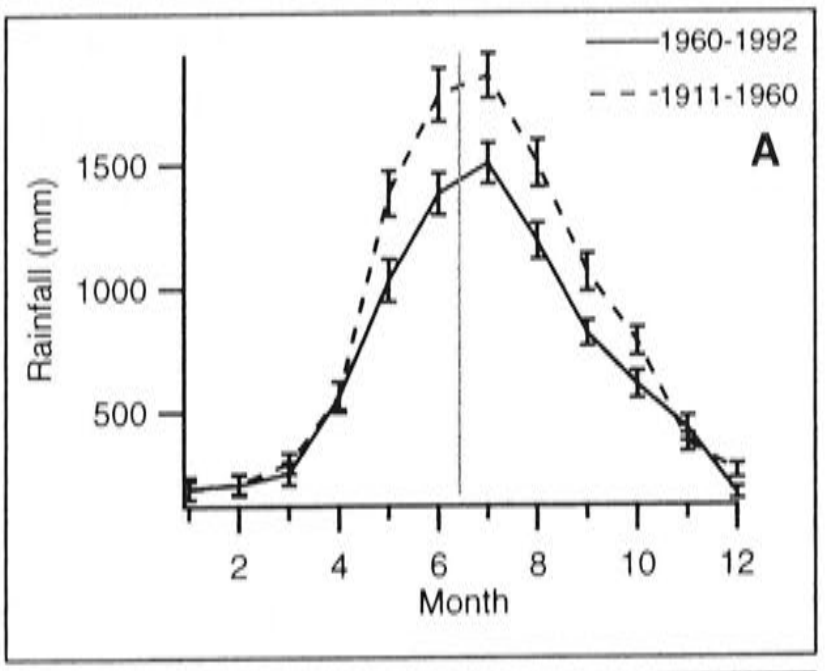

Figures 6.2.2A-G: Stacked average annual cycles for rainfall (A), Ba (B), Mg (C), U (D), Sr (E), P (F) and Na (G) for the period 1911-1960 (dashed line) and 1960-1992 (solid line). Bars indicate one standard error. The x axis shows speleothem growth 'months' where 12, 1 and 2 are inferred summer months; 3, 4 and 5 are inferred autumn months; 6, 7 and 8 are inferred winter months and 9, 10 and 11 are inferred spring months. Grey lines indicate the mid-point of the speleothem annual growth cycle (mid-June), shown to emphasise the timing of the peak of the trace element and rainfall annual cycle.

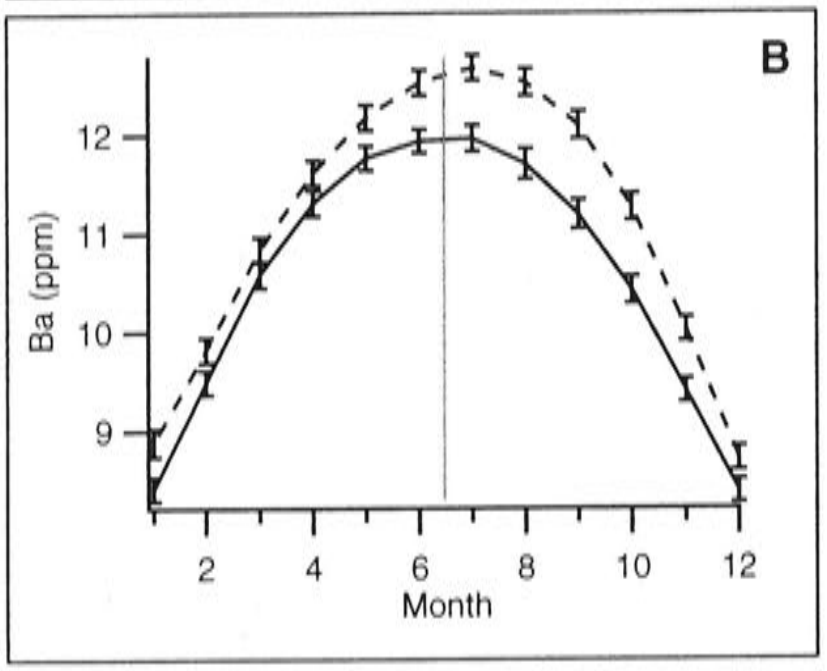

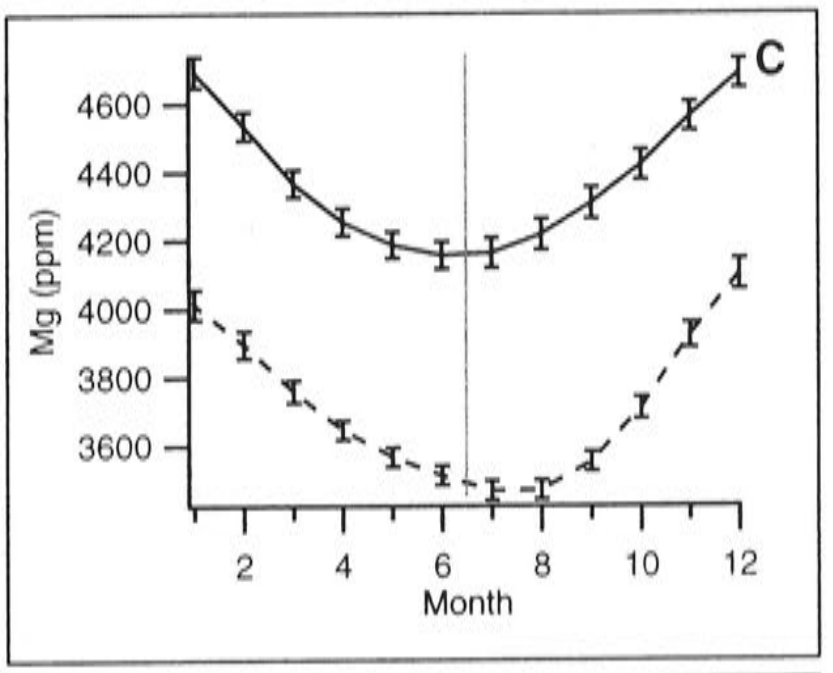

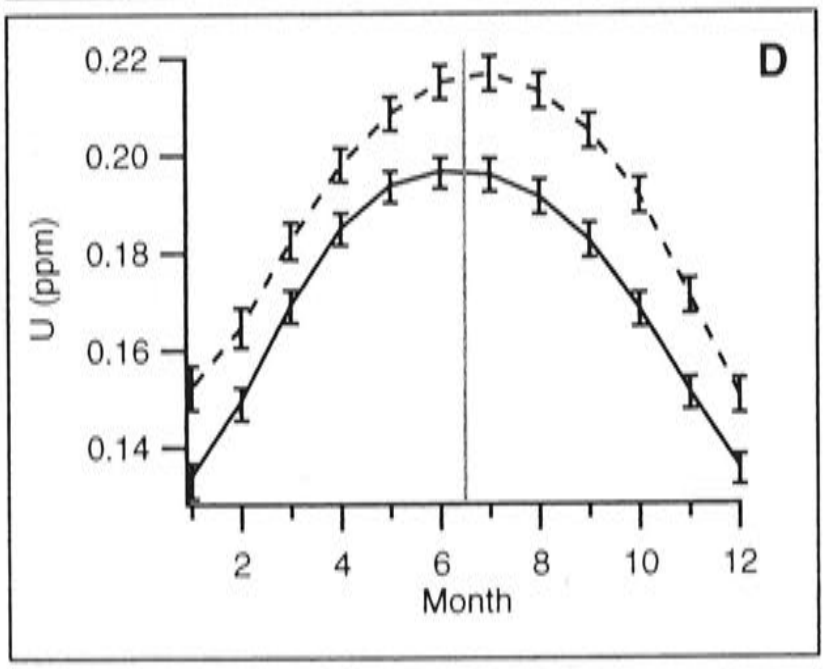

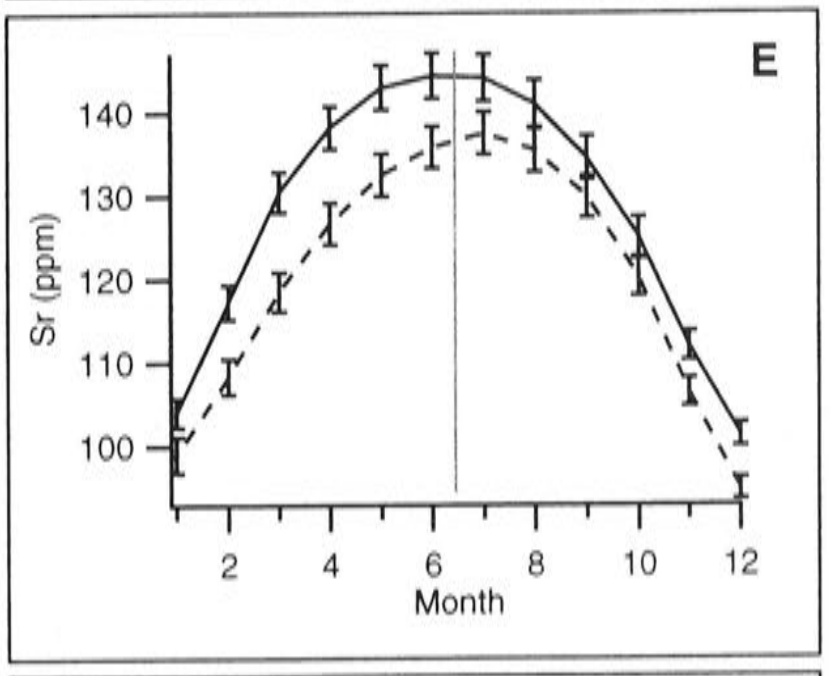

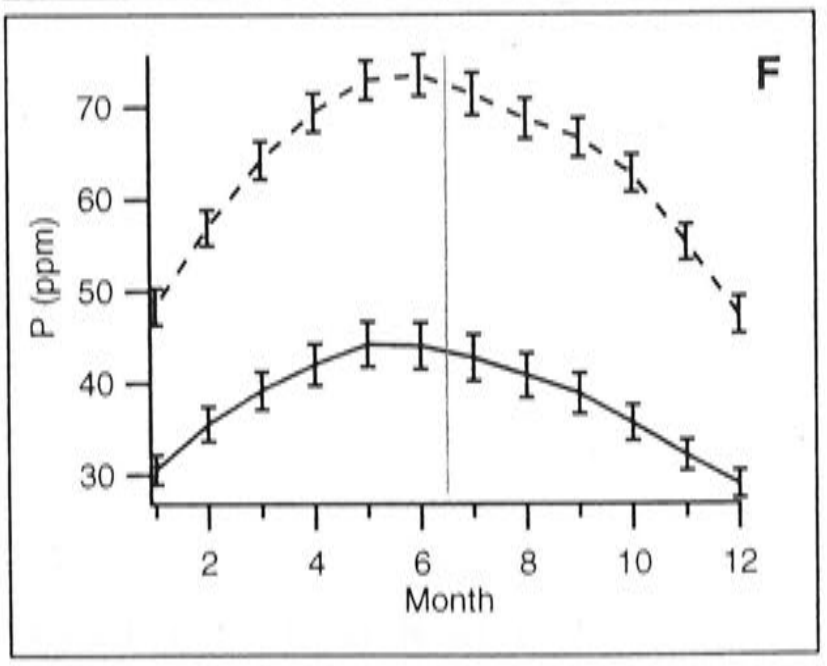

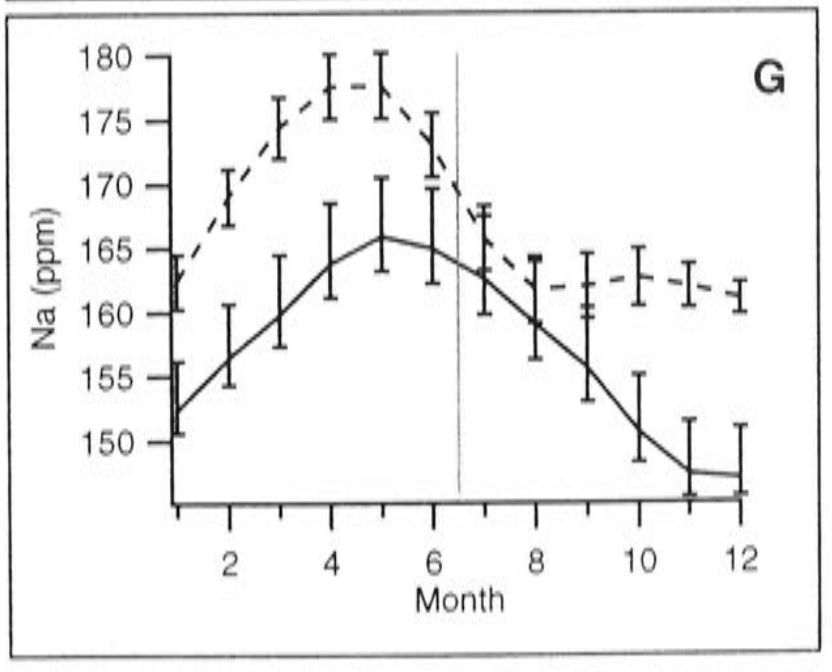

Unlike Ba, U and P, but consistent with the antiphase behaviour of Mg on the intra-annual scale, Mg concentration has increased since A.D.1960 for all months, predominantly for the winter months but also significantly for the summer months (Figure 6.2.2D). Similar to Ba, U and P, the Mg cycle, prior to A.D.1960 was skewed towards the later half of the year and after A.D.1960 is centred at the middle of the year.

Na is the most unusual of the elements, primarily as its pre-A.D.1960 form is highly skewed towards the early half of the year with a rapid return to summer values at the end of winter. Since A.D.1960, Na concentration has reduced and the cycle became broader. The timing of the post-A.D.1960 Na peak is close to that of P, which occurs earlier in the year compared with the other elements in the speleothem annual growth cycle. This early Na peak suggests that Na is relatively mobile through the calcarenite and probably represents flushing.

A final observation is that the elements that appear to be good palaeo-hydrological indicators over the long-term (Mg, P, U; Figure 6.2.1) show a significant change in concentration in the summer months post-A.D.1960, however the rainfall record shows the summer months after A.D.1960 are no drier than those prior to A.D.1960. This may reflect the fact that the annual cycle in drip-water is not likely to directly mimic the surface rainfall pattern, owing to aquifer residence time. The drip-water cycle is more likely to be a suppressed and broadened form of the annual rainfall cycle, a fact that is commonly seen in drip-water studies comparing surface $\delta^{18}O_P$ with $\delta^{18}O_{DRIP}$ (*e.g.* Figure 6.2.3; Goede *et al.*, 1982). To further consider the effect of drip-water through-flow in calcarenite under declining rainfall, a pilot study was conducted to investigate seasonality of oxygen isotopes in MND-S1 (Section 6.3). This effect and other possible climatic drivers for these elements will be fully examined in Section 6.4 after comparisons with intra- and inter-annual stable isotopes are made (Section 6.2.4 and 6.3).

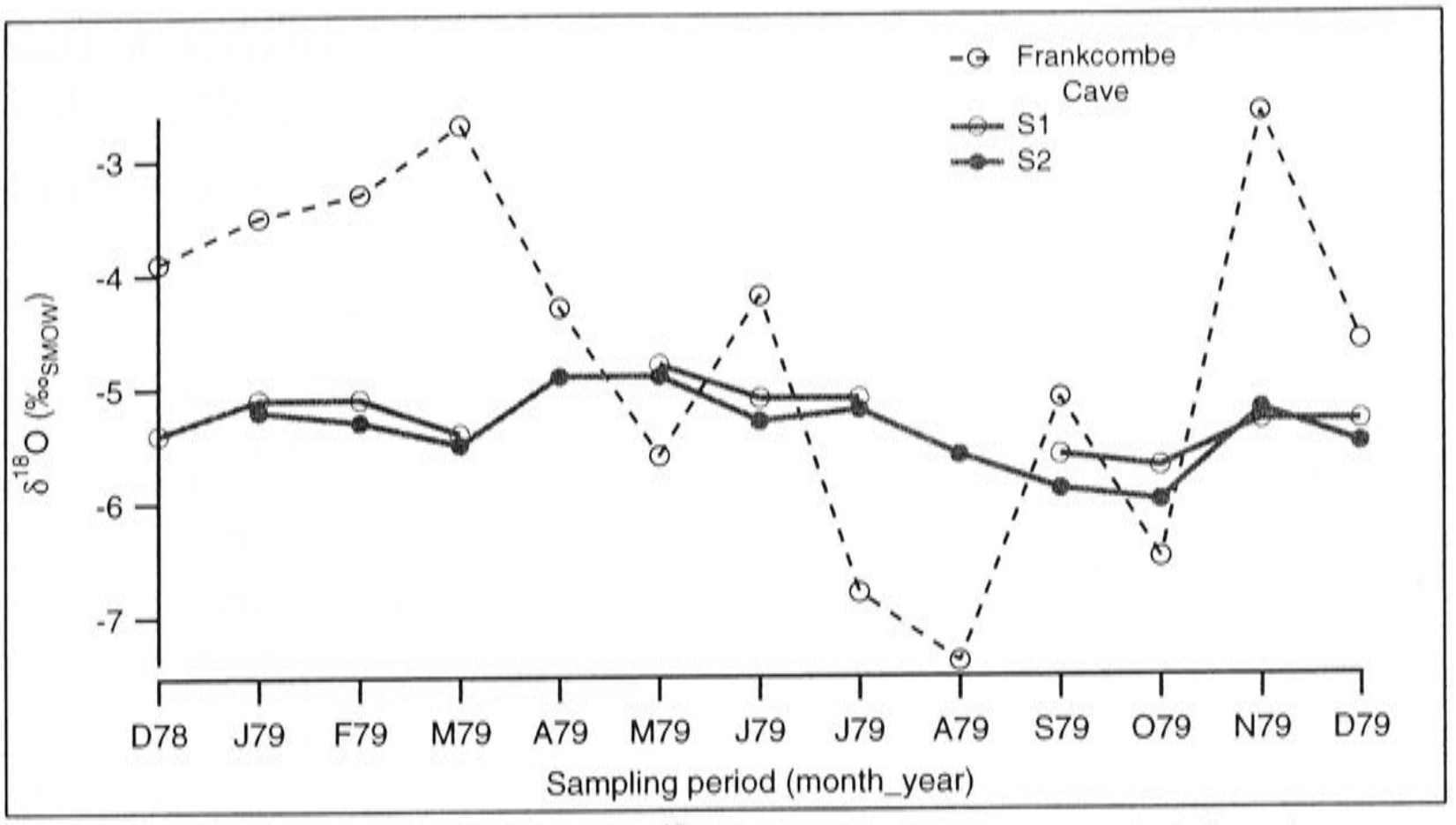

Figure 6.2.3: Comparison of monthly $\delta^{18}O$ measured for surface rainfall and two cave drips at Frankcombe Cave, Tasmania. (From Goede *et al.*, 1982.)

The comparison of trace elements and rainfall, Figures 6.2.1 and 6.2.2, suggests that trace elements in speleothems may be useful palaeoclimate proxies. However, to be confident of this, it is necessary to understand the origin of these trace elements.

6.2.3 Origins of trace element variations

The concentration of Ca, Ba, Sr, Mg, U, P and Na in possible source materials was determined for the dissolvable fraction of the parent calcarenite rock and for one drip-water sample collected from Moondyne Cave during 30/05/02-05/06/02. Analyses were done by an external laboratory (Ecowise, Canberra). Concentrations expressed as the molar ratio with respect to Ca are shown in Table 6.1.3 along with values for rainfall collected at Cape Grim, Tasmania (see Chapter 5). These data are compared to the average molar ratio of MND-S1 for the last ten years of record (A.D.1982-1992). Results show that while Sr/Ca and perhaps U/Ca of the drip-water are less than the calcarenite, Mg/Ca, Ba/Ca and Na/Ca are greater. This suggests that the latter elements may have an external source, possibly rainfall, since Mg and Na are commonly high in rainfall (Table 6.1.3; Ba values at Cape Grim are unknown). A high content of Mg in drip-water has been observed in other cave water studies which was attributed to the relatively high concentration of Mg in rainfall (Baker *et al.*, 2000). However, here the

MND-S1 Mg content may not reflect Mg in rainfall, as the observed antiphase relationship between Mg, Ba and Sr suggests it is lowest whilst being fed by winter rain. Why then is Mg lower and Ba, Sr, U and P highest in winter? The observations of each element will now be weighed against their known characteristics.

Table 6.2.3: Molar ratios (m_{Me}/m_{Ca}) calculated from rain, calcarenite, drip-water and MND-S1 concentrations. Rain concentrations are from Keywood *et al.* (2001). *Last ten years (A.D.1982-1992) used rather than whole record as drip-water ion concentration may have changed significantly since beginning of record. Blank cells indicates data unavailable (rain) or not measured (drip-water).

Molar ratio	**Rain**	**Calcarenite**	**Drip-water**	**MND-S1* (measured)**
Ba/Ca		5.84×10^{-6}	2.76×10^{-5}	7.21×10^{-6}
Sr/Ca		2.22×10^{-3}	9.38×10^{-4}	1.27×10^{-4}
Mg/Ca	3.35	4.69×10^{-2}	2.11×10^{-1}	1.66×10^{-2}
U/Ca		$< 4.80\times10^{-7}$	1.03×10^{-7}	6.78×10^{-8}
P/Ca		8.87×10^{-4}		1.27×10^{-4}
Na/Ca	41.83	8.37×10^{-3}	2.23	5.75×10^{-4}
Total Ca	70.27 µmol/l	873 mmol/g	4.49 mmol/l	10 mmol/g

Sr and Ba

The effect of calcite growth rate on Sr is well documented in empirical studies which find that Sr concentration increases with growth rate (*e.g.* Lorens, 1981; Pingitore and Eastman, 1986; Tesorio and Pankow, 1996; Huang and Fairchild, 2001; Figure 6.2.4). Given the observed correlation between Sr and Ba ($r = +0.90$, $p < 0.001$; Table 6.1.1), growth rate may similarly affect Ba uptake. The effect of inter-annual growth rate on MND-S1 trace element concentration may be examined by comparing average growth rate with the trace element time series (Figure 6.2.5). This exercise shows that growth rate has a strong relationship with Ba concentration, a moderate relationship with the Na concentration and weak to no relationship with other cations. This is unexpected given that the effect of growth rate should be greater for Sr than for Ba (Pingitore and Eastman, 1984, 1985; Tsesorio and Pankow, 1996).

While there is no similar way of testing the effect of growth rate on the intra-annual scale, the difference between winter and summer D_{Sr} (and D_{Ba}) values may be calculated using the drip-water (Table 6.2.3) and MND-S1 winter (peak) and summer (trough) data (Figure 6.2.2). This yields: $D_{Sr} = 0.16$ (winter) and 0.11 (summer); and for Ba, $D_{Ba} =$

0.37 (winter) and 0.21 (summer). Comparing the Sr values with those of Tsesorio and Pankow (1996; Figure 6.2.4) suggests an increase in growth rate from summer to winter by a factor of 2. This value is entirely plausible and supports a growth rate control for Ba. Unfortunately, D_{Ba} could not be compared with the empirical data since the values (0.21-0.37) were beyond the range of values (0-0.06) investigated by Tesoriero and Pankow (1996; Figure 6.2.4). The much higher D_{Ba} values calculated here suggest that the Ba concentration measured for the drip-water sample is in error.

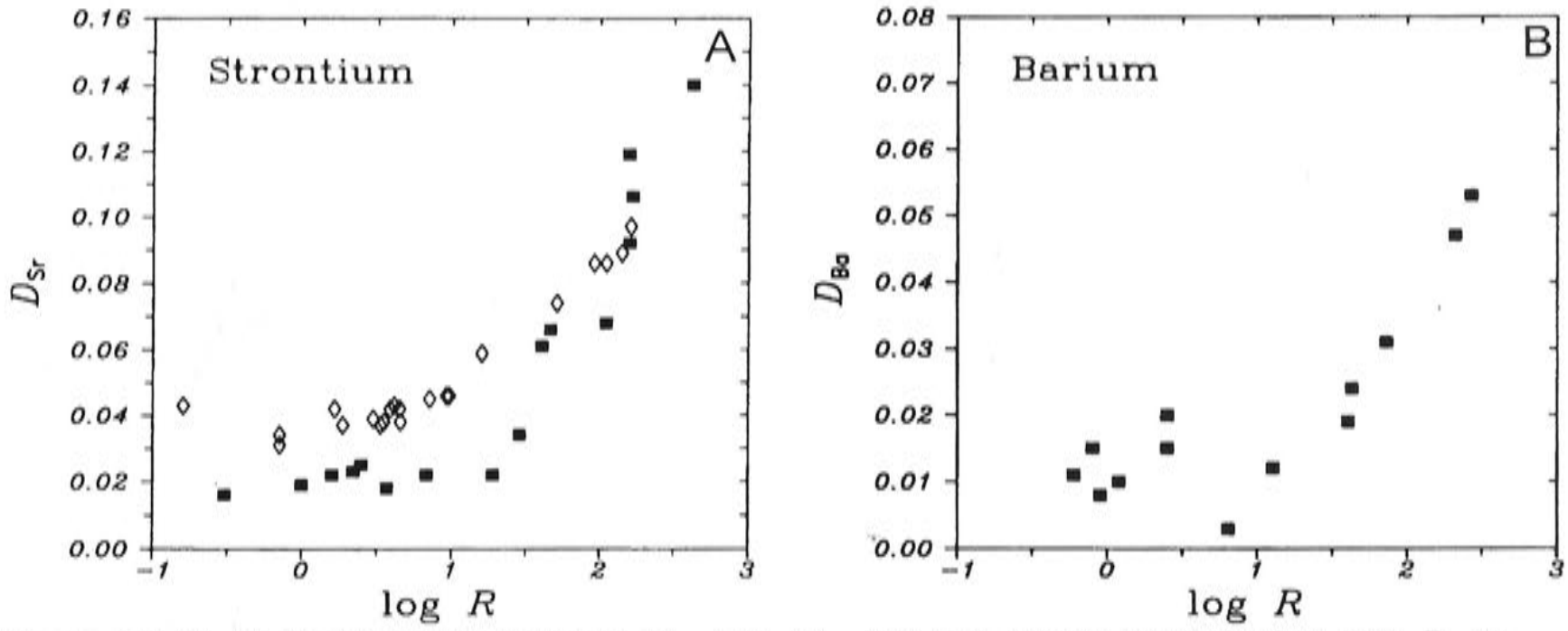

Figure 6.2.4A-B: Relationship between D_{Sr} (A), D_{Ba} (B) and calcite precipitation rate, R, as measured by Tesoriero and Pankow (1996; filled squares) and Lorens (1981; open diamonds). R is nmols/mg.min where mg refers to mass of seed material used.

Na

Interestingly, the strong agreement between Ba and Na on the inter-annual scale (Figure 6.2.5) suggests Na is also growth rate controlled, which agrees with empirical studies (Ishikawa and Ichikuni, 1984. Busenberg and Plummer, 1985). The overall inter-annual scale relationship between growth rate and Ba and Na concentrations is further supported by a change in calcite fabric to a branching needle habit over A.D.1930-1956 (episode ii -see image in Appendix III). This habit, termed dendritic, has been shown to be characteristic of speleothems grown under non-equilibrium conditions by Frisia *et al.* (2000).

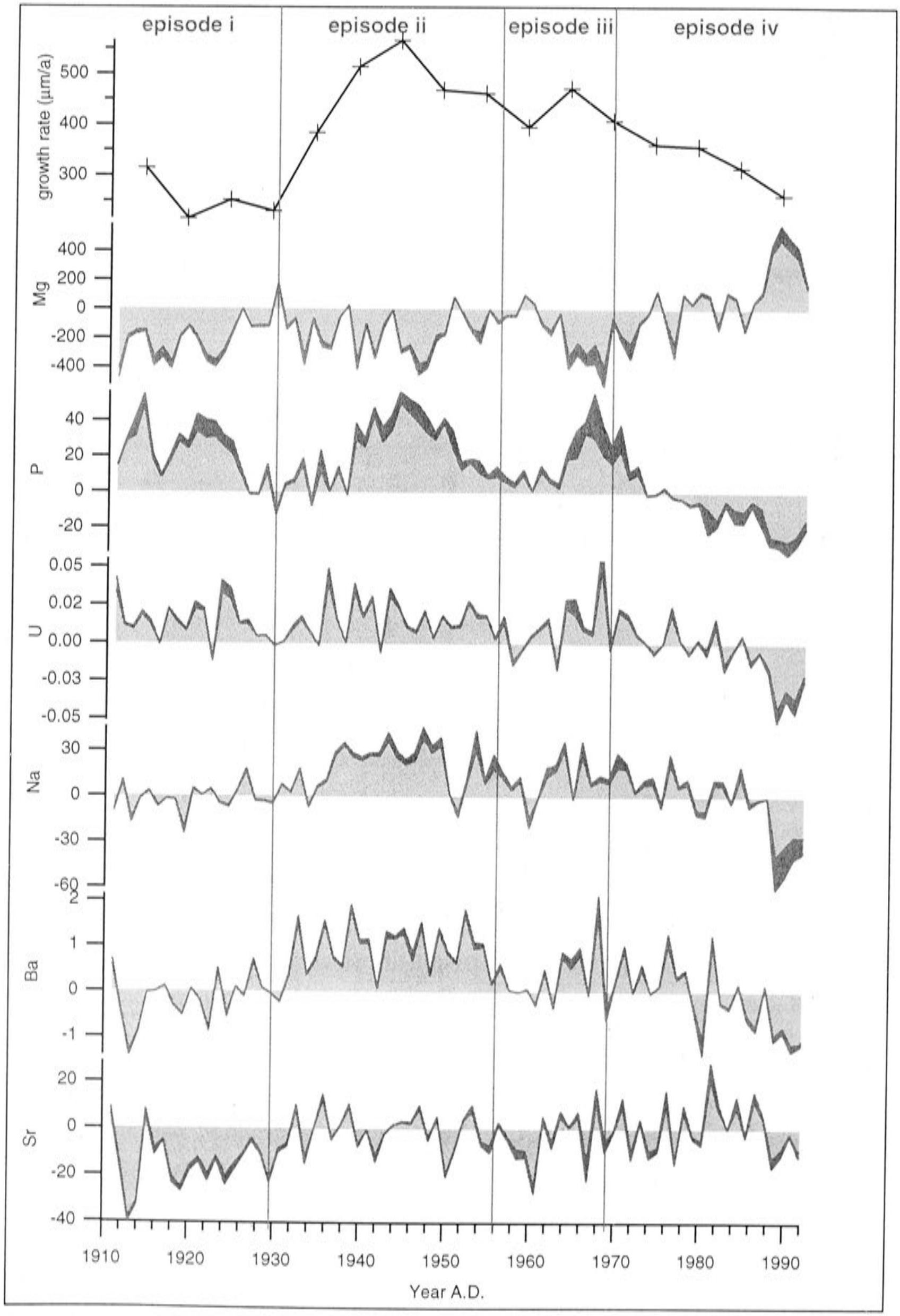

Figure 6.2.5: Relationship between growth rate and trace element concentration. Growth rate is averaged in 5-year bins, based on wavelengths of trace element cycles mapped onto MND-S1 (Appendix I).

However, the above observations are not consistent with Na behaviour on the intra-annual scale (Figure 6.2.2) where Na shows a distinctly different annual waveform cycle from the other elements. Na in calcite is also known to occupy interstitial sites (Ishikawa and Ichikuni, 1984. Busenberg and Plummer, 1985). It is suggested here that while Na incorporation may be affected by growth rate at all scales, this effect on the intra-annual scale, may be dwarfed by the saturation of interstitial sites during flushing of high Na concentration drip-waters (Table 6.2.3).

The remaining elements, P, U and Mg, which most closely resemble the rainfall record (Figure 6.2.1) do not show a strong relationship with growth rate (Figure 6.2.5). This is particularly apparent for episodes i and ii where growth rate has trebled while these elements appear unaffected. Although P has two peaks similar in form to growth rate during episodes ii and iii, these peaks lag the growth rate by 2-3 years, which suggests that P may have a lag response to the factors driving growth rate, but that P uptake into the calcite lattice is not growth rate dependent.

P

P in speleothems is suggested to be derived from biomass breakdown, first forming organic P but quickly mineralised to PO_4^{3-} in the soil (Fairchild *et al.*, 2001). This source results in a seasonal maximum in PO_4^{3-} following dieback of summer vegetation which, in southern Australia, coincides with the onset of autumn rain. Thus the timing of P maxima are likely to remain unchanged while the organic production of P will be influenced by soil moisture, hence rainfall. This mechanism is supported by several observations in this study (Figure 6.2.2F). These are:

- the relatively earlier peak of P concentration, month '5' which is equivalent to autumn, compared to months '6-8' (winter) for the other elements;
- that the timing of this peak is unaltered, while for other elements, it shifts 1-2 months between the wetter (pre-A.D.1960) and drier (post-A.D.1960) conditions; and
- the dramatic decrease of nearly 50% for both winter and summer P concentrations post-A.D.1960.

U

The change in form between pre- and post-A.D.1960 of the average U annual cycle most closely resembles Ba in its decline in winter values and the shift in its peak from late

winter to mid-winter (Figure 6.2.2). However, U more closely resembles P in its decline in summer values. This, and the fact that U and P appear closely related on the inter-annual scale (Figure 6.2.1) may suggest that U is coupled to P by the strong affinity of uranyl ions (UO_2^{2+}) for PO_4^{3-} in groundwater (Langmuir, 1978). The conditions for this are explored and compared with observations from MND-S1 further in Section 6.4.

Mg

Mg uptake in calcite is considered to be controlled primarily by temperature (Mucci, 1987; Oomori *et al.*, 1987), but this factor may be eliminated here since the annual range in MND-S1 Mg concentration is far greater than may be accounted for by the annual cave temperature range of 0.6°C (*cf.* Huang and Fairchild, 2001). Similar to P and U, Mg appears to be affected by the post-A.D.1960 rainfall decrease at all times of the year. However, since Mg is antiphase to these elements and has the lowest values in winter when rainfall is highest, its behaviour is unlikely to be driven by sources related to rainfall, or even the dissolution capacity of drip-water. The question remains, how can Mg be inversely related to rainfall? Because a large number of mechanisms need to be considered here, including suggestions from previous speleothem studies, this question will be further examined in Section 6.4.

The remainder of this Results Section will now focus on stable isotopes, both at inter-annual (Section 6.2.4) and intra-annual (Section 6.3) scales.

6.2.4 Inter-annual comparison between stable isotopes, trace elements and rainfall

The comparison of MND-S1 trace elements and conventionally analysed stable isotopes is potentially hampered by the fact that they could not be sampled from the same part of the stalagmite owing to the large volume of calcite required (200 μg) for conventional stable isotope analysis. To overcome this, LA-ICP-MS Ba concentrations were acquired over the ledge created from milling samples for conventional stable isotope analysis (see Figure 4.2.1, Chapter 4). The Ba cycles were then "wiggle matched" to those acquired for the master trace element record, allowing an age model equivalent to the trace

element chronology, to be constructed for the conventional stable isotopes (Figure 6.2.6).

Considering the stable carbon isotopes, episode by episode as before, Figure 6.2.6 reveals:

- $\delta^{13}C_{SP}$ is stable at ~ -9‰ prior to A.D.1930 (episode i), while rainfall, P and U are high; and Mg, Sr, Ba, Na and growth rate are low.
- $\delta^{13}C_{SP}$ reaches its lowest value at the beginning of episode ii (-10‰) before rising through A.D.1931-1970 (episode ii and iii), during which P, U, Ba, Na and growth rate are high and Mg is low.
- $\delta^{13}C_{SP}$ rises to its highest value in episode iv during which Mg also rises, while P, U, Ba, Na and growth rate decrease. Sr is unchanged but variable and rainfall is constant but lower than the other episodes.

Considering only episodes ii-iv, there is an antiphase relationship between $\delta^{13}C_{SP}$ and rainfall, although $\delta^{13}C_{SP}$ continues to rise through episode iv whilst rainfall is consistently low. Overall, there appears to be a broad positive trend common to $\delta^{13}C_{SP}$ and Mg; and an antiphase trend between $\delta^{13}C_{SP}$ with Ba and Na.

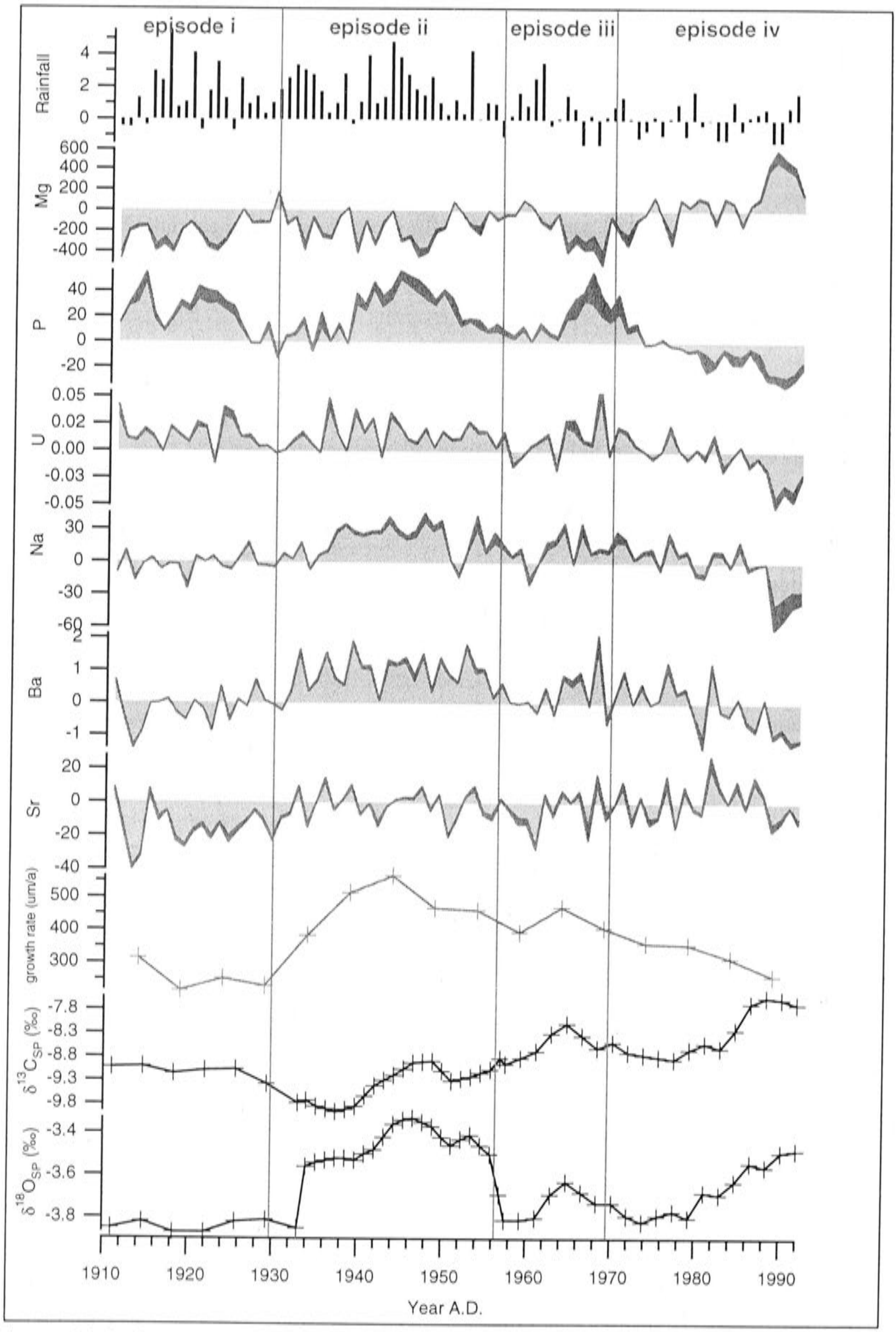

Figure 6.2.6: Comparison between rainfall, trace elements, growth rate and conventionally analysed stable isotopes.

The main factors that are considered to influence $\delta^{13}C_{SP}$ are:

1. disequilibrium between atmospheric and soil CO_2 (Holland *et al.*, 1963, Hendy, 1971; Dreybrodt, 1982);
2. the degree of limestone dissolution (Genty *et al.*, 2001);
3. prior degassing/precipitation of the drip-water (Baker *et al.*, 1997); and/or
4. kinetic precipitation (Hendy, 1971; Frisia *et al.*, 2000).

A considerable range exists between $\delta^{13}C$ of the atmosphere (-8.5 to –6.7‰ over MND-S1 growth period), soil C (~ -25‰) and limestone C (~ 0 to +2‰) (Genty and Massault, 1999; Genty *et al.*, 2001; and references therein). The interplay between these end-members (factors 1 and 2 above), driven by soil cover and vegetation activity, determines the $\delta^{13}C$ of drip-water ($\delta^{13}C_{DRIP}$). $\delta^{13}C_{DRIP}$ will be preserved in $\delta^{13}C_{SP}$ provided the drip-water does not degas significantly prior to reaching the stalagmite surface under lower recharge conditions (factor 3), and that precipitation on the stalagmite is not corrupted by kinetic effects (factor 4). These latter two effects will drive $\delta^{13}C_{SP}$ towards higher values as described in Chapter 1, Section 1.3.4.

The antiphase relationship between $\delta^{13}C_{SP}$ and rainfall for episodes ii-iv, suggests MND-S1 $\delta^{13}C_{SP}$ is sensitive to hydrology. Hydrology, or more specifically, recharge conditions, may influence $\delta^{13}C_{SP}$ indirectly by any or all of factors 1-4. Hypothetically, a change in soil cover and soil CO_2 production under drier conditions may increase the open system behaviour within the calcarenite, that is, continued exchange with atmospheric CO_2 of $\delta^{13}C_{DRIP}$ (factor 1). This exchange or re-equilibration, results in re-acidification of the percolating waters following calcite precipitation in the calcarenite. Progressive cycles of limestone re-dissolution will increase the relative limestone C contribution, and thus shift $\delta^{13}C_{SP}$ towards limestone $\delta^{13}C$ (isotopically heavier) values (factor 2).

It is also possible for $\delta^{13}C_{DRIP}$ to become enriched under closed system conditions by the effects of prior degassing and precipitation of drip-waters (factor 3). This process only differs from the above, by its isolation from gaseous CO_2 once percolating waters leave the soil zone (Hendy, 1971). Thus, evolution of the drip-waters under either open or closed system conditions will raise $\delta^{13}C_{DRIP}$ but less so for closed system conditions as there is less opportunity for re-dissolution of isotopically heavy limestone C.

It is plausible that the 200 mm reduction in rainfall sustained for more than 30 years is sufficient to increase the vadose zone of the calcarenite by lowering the water table, hence increasing the potential for evolution of $\delta^{13}C_{DRIP}$ either under open or closed system conditions. Unfortunately, it is only possible to separate these effects from each other, and also possibly from kinetic precipitation effects, by measuring the relative contribution of limestone C species itself, either by investigating the DCP (radiocarbon dating methods see Chapter 3) and/or Sr isotopes (Chapter 7). Neither of these techniques were attempted in this study, but are priorities for future research. Unfortunately, until these are investigated, the interpretation of MND-S1 $\delta^{13}C_{SP}$ suffers from these uncertainties.

Turning to oxygen isotopes, Figure 6.2.6 shows:

- $\delta^{18}O_{SP}$ is lowest during A.D.1911-1932 (episode i) when rainfall is variable but still above the A.D.1961-1992 mean. Mg, Sr, Ba, Na and growth rate are low and P and U are high.
- $\delta^{18}O_{SP}$ is highest during A.D.1933-1956 (episode ii) when rainfall, Ba, Na, growth rate, P and U are also highest.
- $\delta^{18}O_{SP}$ is increasing through A.D.1957-1992 (episodes iii and iv) whilst rainfall is has decreased markedly, and Mg is rising while P, U, Ba, Na and growth rate are declining.

$\delta^{18}O_{SP}$ shows a less consistent trend with rainfall than does $\delta^{13}C_{SP}$, as high $\delta^{18}O_{SP}$ values occur in episode ii and iv when rainfall is highest and lowest, respectively. However, episode ii coincides with the period when growth rate is also highest. It may be that the faster calcite growth during episode ii is greater than that compatible with isotopic equilibrium. Strangely, apart from the small bump during A.D.1940-1950 which is common to both $\delta^{18}O_{SP}$ and $\delta^{13}C_{SP}$, $\delta^{13}C_{SP}$ does not appear to be similarly affected by possible kinetic precipitation, since $\delta^{13}C_{SP}$ is overall lowest during episode ii. Kinetic precipitation by rapid degassing should, theoretically, drive both $\delta^{18}O_{SP}$ and $\delta^{13}C_{SP}$ isotopically heavier, but the effects should be greater for $\delta^{13}C_{SP}$ than $\delta^{18}O_{SP}$ because the reservoir of C atoms in the drip-water is far less than that of O (Hendy, 1971).

More recently, Frisia *et al.* (2000) have demonstrated that speleothem calcite deposited from fast-dripping, highly saturated solutions, is more likely to be precipitated under kinetic conditions, and may be characterised by dendritic branching crystallites. As previously noted in Section 6.2.3, the calcite corresponding to episode ii exhibits this dendritic-type fabric. Thus, several observations point to kinetic effects on $\delta^{18}O_{SP}$ during episode ii, although it remains puzzling why $\delta^{13}C_{SP}$ is relatively isotopically light during this period.

Considering just episodes i, iii and iv only, where it is assumed growth rate was slow enough for isotopic equilibrium to be maintained; $\delta^{18}O_{SP}$ follows the trend predicted by $\delta^{18}O_P$ results (Chapter 5). That is, in the winter rainfall regime of southern Australia, $\delta^{18}O_P$ is isotopically lighter when rainfall is greater (episodes i) and will be driven isotopically heavier by a reduction in rainfall, which in turn, will drive $\delta^{18}O_{SP}$ isotopically heavier (episodes iii - iv).

6.3 High resolution ion microprobe results

The detection of such clear annual trace element cycles in MND-S1 was sufficiently encouraging to attempt to measure $\delta^{18}O_{SP}$ at high resolution alongside the trace element profiles. As the spatial resolution required to do this (< 50 μm) was less than that attainable by conventional analyses (~500 μm was milled along the growth axis; Chapter 4) and by UV-laser fluorination techniques (200 μm; D. Mattey Royal Holloway, *pers. comm.*), the analyses were conducted using the Cameca ims-1270 ion microprobe at the Department of Earth and Space Sciences, University of California, Los Angeles (UCLA). This work was undertaken in collaboration with Prof T. M. Harrison and Prof K. D. McKeegan with the support of a visiting RSES Fellowship funded by Mervin and Katalin Paterson.

$\delta^{18}O_{SP}$ analyses by ion microprobe typically have an internal error of ~0.2‰ (1 σ) and an external reproducibility of ~0.5‰ (*e.g.* Fayek *et al.*, 2001). It was known that the annual temperature effect at calcite precipitation would be extremely small since a temperature logger placed at the former site of MND-S1 records a yearly temperature

range of 0.6°C for the period June 2001 to May 2002, which could account for no more than 0.15‰ assuming a temperature effect of –0.24‰/°C (McCrea, 1950) but that the rainfall $\delta^{18}O_P$ would be considerably greater (IAEA rainfall $\delta^{18}O_P$ at a similar west coast site experiencing the same winter dominant frontal rainfall; Cape Grim, Tasmania, shows an average annual range of $\delta^{18}O_P$ from –2.2‰ in summer to –5.5‰ in winter; IAEA, 2002).

The understanding of what drives the annual $\delta^{18}O_{SP}$ cycle and its phase relationship with the annual trace element cycle recorded in speleothems is important for two reasons; firstly, speleothem $\delta^{18}O_{SP}$ has been the climate proxy in speleothems that has received the most attention (Hendy and Wilson, 1968, Bar-Mathews *et al.* 1999, McDermott *et al.*, 2001) and yet, as the previous section suggests, its signal is still poorly understood; and secondly, because $\delta^{18}O_{SP}$ is arguably the best tracer of sub-surface water (*e.g.* Coplen *et al.*, 2000) and thus the $\delta^{18}O_{SP}$ signal may give us the best insight into the seasonality, residence time and mixing of the percolating water which will similarly affect the trace element concentrations.

Figure 6.3.1 shows all ion microprobe $\delta^{18}O_{SP}$ data that was acquired in relatively long sequences (Appendix III shows position of tracks on sample). It appears that $\delta^{18}O_{SP}$ data show cycles at similar wavelengths as the adjacent trace elements, which suggests that the $\delta^{18}O_{SP}$ ion microprobe data are also detecting annual cycles. However, there is significant variability. There are a number of known sources of error involved in $\delta^{18}O$ analysis by SIMS primarily arising from instrumental mass fractionation (Valley *et al.*, 1997) and matrix effects (Fayek *et al.*, 2001). Some of these effects were recognised during the analyses, but others were not and therefore some obvious preventative steps were not considered until after the analyses were completed. The various sources of error are considered below.

Firstly, it took several hours for the ion microprobe to achieve stability. This can be seen by comparing tracks that were acquired near to the beginning of a day (tracks 1 and 13) to nearby tracks acquired later in the analysis run. For example tracks 1, 9 and 20 show similar features but track 1 has an overall 2‰ range of variation as opposed to 1‰ for tracks 9 and 20. Tracks 1 and 13 thus are not used in the analysis described below, nor

are tracks 9, 10 and 12, which contain too few data points. Hence, only tracks 16, 17, 18, 19, 20 and 21 are considered further.

Figure 6.3.2 shows that the cycles seen in adjacent tracks (19 and 20) of the $\delta^{18}O_{SP}$ ion microprobe measurements were reasonably reproducible (top section) although there is obviously random error affecting the point-to-point reproducibility. The smoothed trends[3] through the ion microprobe measurements have the same direction as that seen in conventional $\delta^{18}O_{SP}$ measurements, although the average shift from start to finish of the ion microprobe session is much larger (~1‰ compared to ~0.2‰). Furthermore, the disagreement between the gradients of the smoothed trends of tracks 19 and 20, further suggests that there is a systematic error present, which cannot be due to temporal analytical drift as tracks 19 and 20 were acquired in opposite directions.

A possible explanation is that the ion microprobe data were affected by drift induced by geometric effects, which differs from temporal drift. Geometric effects caused by topography of the sample surface are a consideration for ion microprobes that use an electron flood gun to compensate for the charge created by the primary Cs^+ beam impacting the sample surface. Topography may affect the angle at which the electrons are deflected which may interfere with the trajectory of the O ions, and thus the measured beam intensities. Tracks 19 and 20 were conducted between 6 and 9 mm from the edge of the sample mount where the mount should not suffer topographic effects (such as rounding due to polishing) and furthermore track 16, ~850 μm away, does not seem to be similarly affected. However, the only way to fully eliminate such geometric interferences would be to re-mount this section of the sample into the centre of the mount at a different orientation (K. D. McKeegan, pers. comm.). This is not a feasible goal for this PhD study.

---

[3] The smoothed trend was created by averaging 10 ion microprobe measurements which is approximately equivalent to the spatial averaging of a conventional analysis.

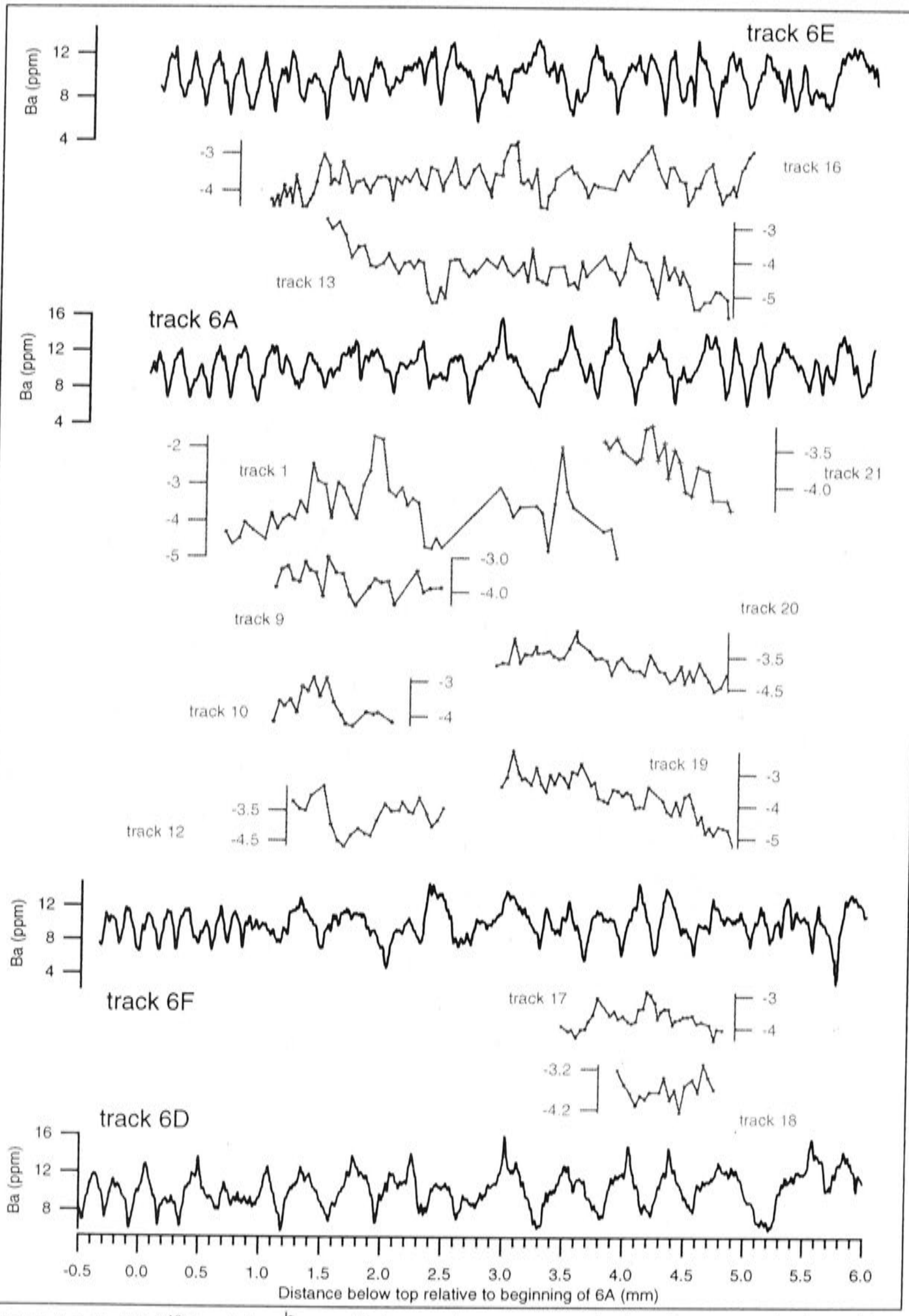

Figure 6.3.1: All $\delta^{18}O_{SP}$ data were sufficient points were acquired to form a track alongside a LA-ICP-MS (5x50 μm slit data) track. The positioning of tracks are shown representative to their positions relative to LA-ICP-MS track 6A. (Tracks 2-8 were performed elsewhere on the sample but not sufficiently close together for comparison. Tracks 11, 14 and 15 are not shown as they are short (<10 points).

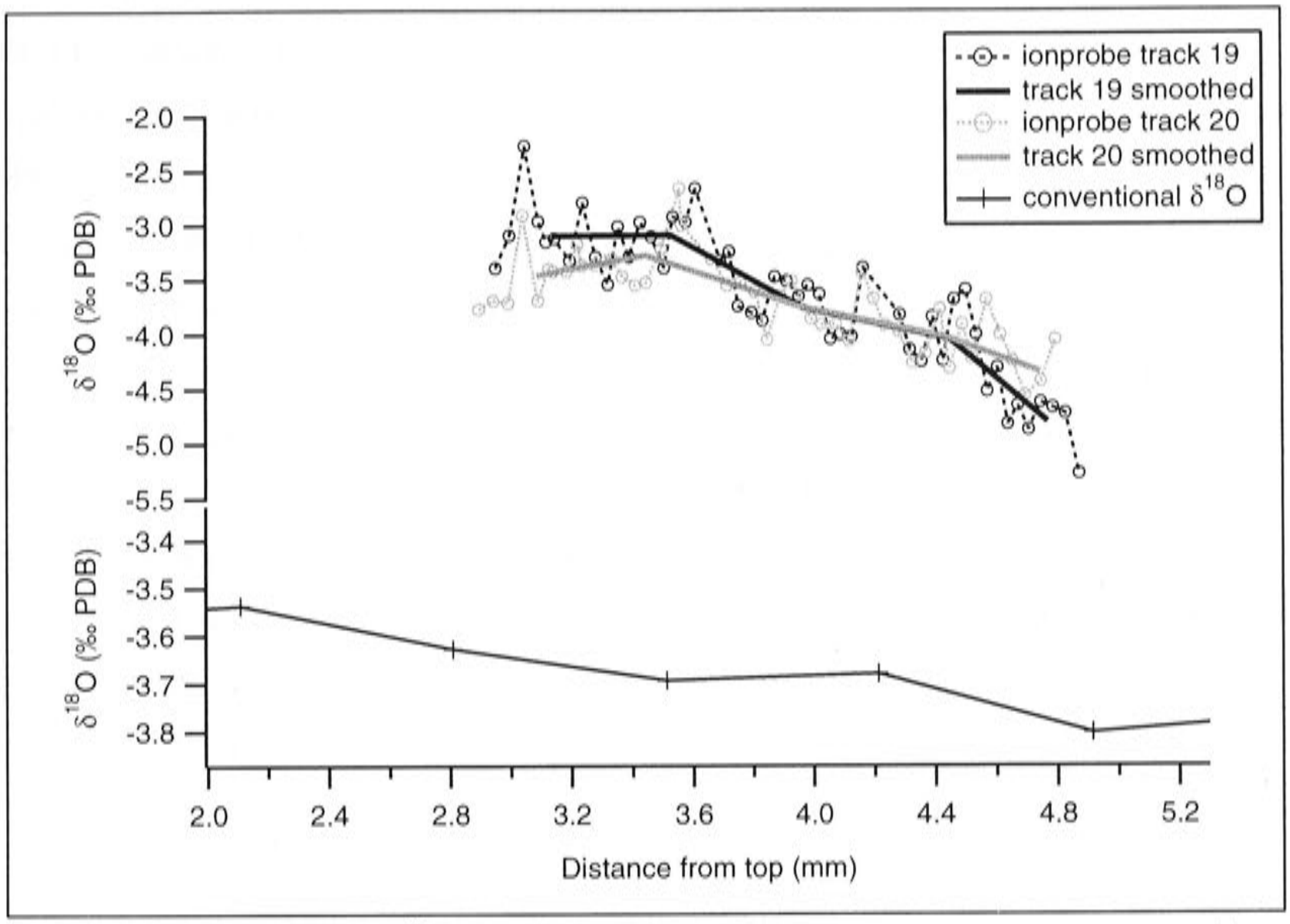

Figure 6.3.2: Ion microprobe $\delta^{18}O_{SP}$ data were reproducible for adjacent tracks and agree with the overall trend seen in conventional $\delta^{18}O$ analyses. The smoothed trend was created by averaging 10 ion microprobe measurements which is approximately equivalent to the spatial averaging of a conventional analysis. (Note: vertical axes have different scales.)

A final possibility for the larger average variation in ion microprobe $\delta^{18}O_{SP}$ analyses is that the "per mil scale" set on the mass spectrometer for conventional analyses is not comparable to that set for the ion microprobe analyses. In conventional analyses work, standards are typically included with unknowns to meet the following two objectives:

1. to place the unknown on either the PDB or SMOW scale; and
2. check the range of the per mil scale as set on the mass spectrometer.

From the point of view of conventional analysts, there is additional internal standardisation, for example on the RSES Finnigan MAT 251, the measurements of sample CO_2 gas are alternated with that of a known reference gas for 4 cycles during the measurement block, to minimise random error and mass bias. This is achieved by dividing by the isotopic ratio of the unknown by that of the reference gas when δ is calculated (Equation 1.3.2 reproduced below):

$$\delta_{sample} = \left(\frac{R_{sample}}{R_{reference}} - 1 \right) \qquad (1.3.2)$$

The isotopic composition of the unknown is then reported relative to the PDB or SMOW scale (objective 1) by correcting the measured δ values of the standard to the internationally accepted value, and then applying the same correction to the unknowns. The δ scaling relative to the reference gas (Equation 6.3.1) is checked and corrected by comparing the spread between two isotopically distinct standards included in the run, with the difference between their internationally accepted values (objective 2).

For ion microprobe measurements, elimination of random errors and mass bias by internal standards measured within an analysis block cannot be done as standards can only be run between the measurements of unknowns. Unfortunately, if only one standard is measured between unknowns, then it can only serve to correct for systematic errors (geometric or temporal drift). However, if two isotopically distinct standards are measured between unknowns, then the instrumental mass fractionation effects may be checked, which fulfils objective 2.

In this study, objective 1 was met by correcting the ion microprobe δ measurements to the known δ value determined from conventional analyses, which is equivalent to including one standard between unknowns. Obviously, for the future analysis of speleothem stable isotopes, where the greatest possible precision is required, the inclusion of two isotopically distinct standards must be done to fulfil objective 2.

An added complication, specific to this study where measurements were conducted over fine growth laminae is the uncertainty at which coeval material is being sampled. All tracks were analysed parallel to the growth direction but as the trace element maps reveal, the growth layers vary considerably in thickness over small scales, so that adjacent tracks may not be sampling coeval material. This uncertainty will be further compounded by the method of spatial sampling discussed in Chapter 4, section 4.4.2 and illustrated in Figure 6.3.3 for tracks 19 and 20 (*i.e.* successive ion microprobe pits are laterally offset). Thus, to attain the best comparison between trace element and $\delta^{18}O_{SP}$ cycles, the trace element data were re-acquired by running LA-ICP-MS scans directly over the $\delta^{18}O_{SP}$ ion microprobe tracks. This produced considerably better agreement between trace element and $\delta^{18}O_{SP}$ cycles, as shown in Figures 6.3.4 and 6.3.5 (tracks 19 and 20 are shown as de-trended $\delta^{18}O_{SP}$ values to eliminate possible geometric matrix

effects). Tracks 16, 19 and 20 show that $\delta^{18}O_{SP}$ most closely agrees with the timing and shape of Mg cycles however, the timing is not closely related for tracks 17 and 18, but as they are short, there can be less confidence between the registration of these tracks. There appears to be an inverse relationship between $\delta^{18}O_{SP}$ with U and Ba, and only poor agreement with Na and P (Sr is not shown as it is identical in form and phase to Ba over these short intervals).

Assuming that the seasonal timing based on Ba is correct, then the relationships between $\delta^{18}O_{SP}$ and trace elements suggest that $\delta^{18}O_{SP}$ is highest in summer, which is consistent with expectations since winter rainfall is isotopically light while summer rainfall is isotopically heavier (Chapter 5). The measured range of annual $\delta^{18}O_{SP}$ is also consistent with the range in annual cave drips in Frankcombe Cave, Tasmania (Goede *et al.*, 1983; Figure 6.2.3), which receives the same westerly rainfall. A final comment, considering the results of Chapter 5 showed that $\delta^{18}O_P$ displays both an annual cycle but also strong inter-annual variability governed by large event-based variations and, that while the percolating water is likely to be an integration of successive events, the annual $\delta^{18}O_{SP}$ cycle is likely to record this inter-annual variability and thus is expected to be inherently more noisy than the trace elements that are dominated by the range of the seasonal rainfall cycle.

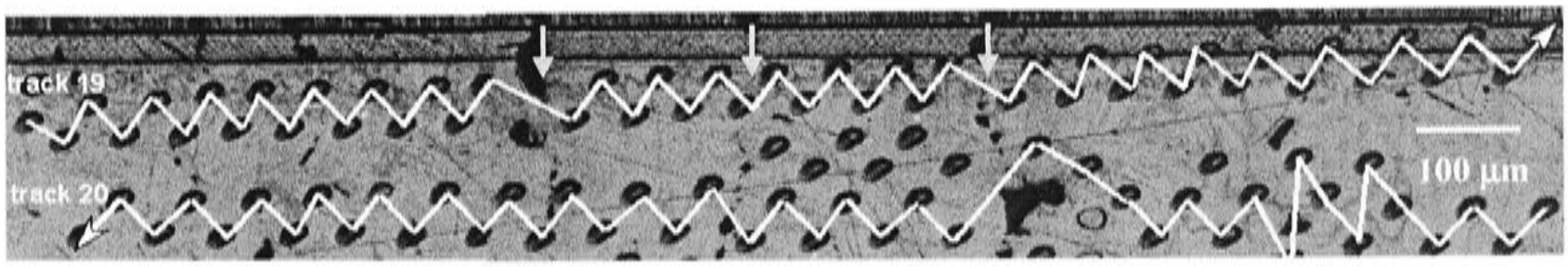

Figure 6.3.3: Positions of sequential ion microprobe $\delta^{18}O_{SP}$ analyses along tracks 19 and 20. White arrow heads indicate direction of measurement. Grey arrows indicate lines of holes argued to represent annual hiatuses.

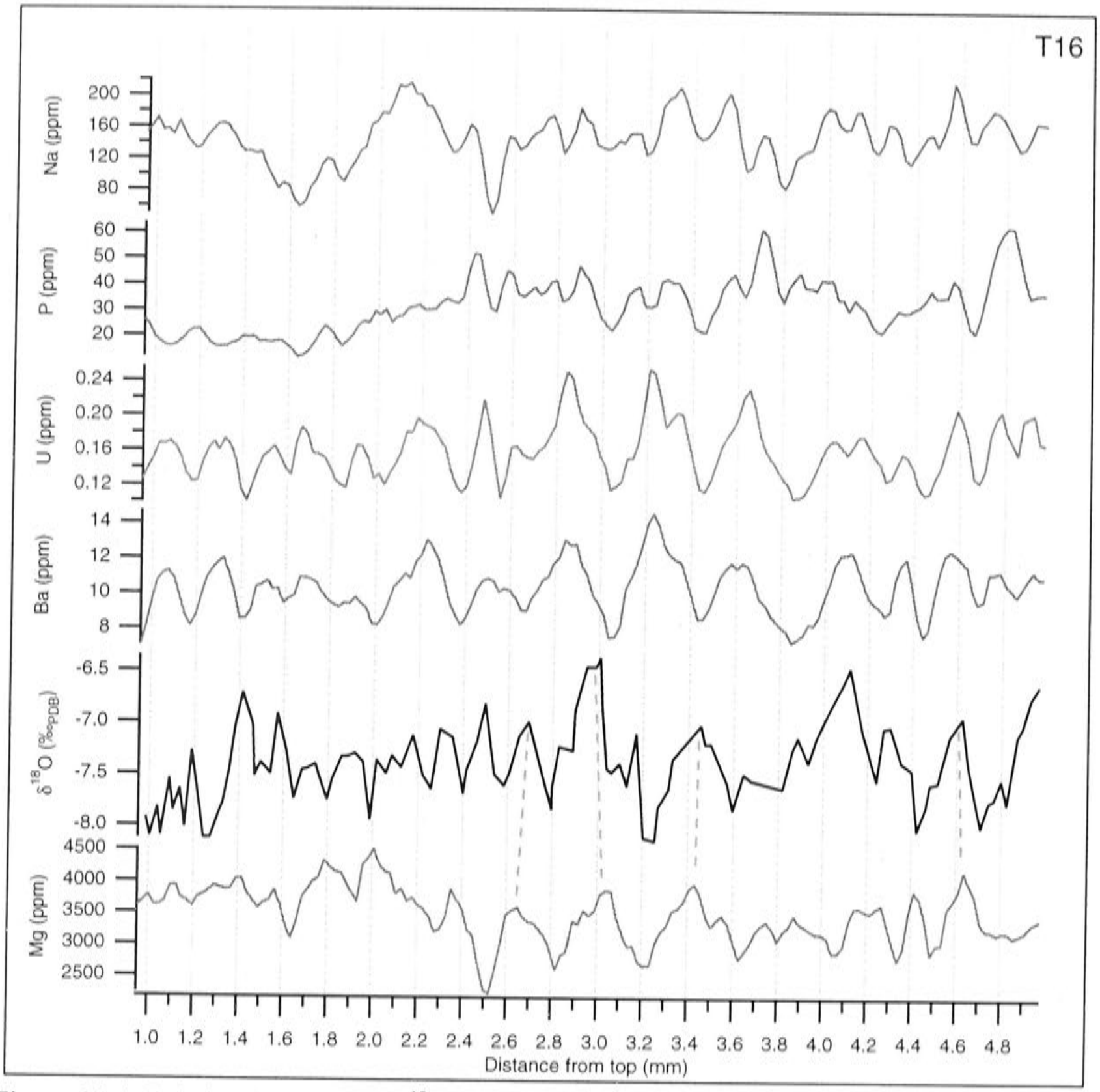

Figure 6.3.4: Relationship between $\delta^{18}O_{SP}$ and trace element annual cycles for track 16 (T16).

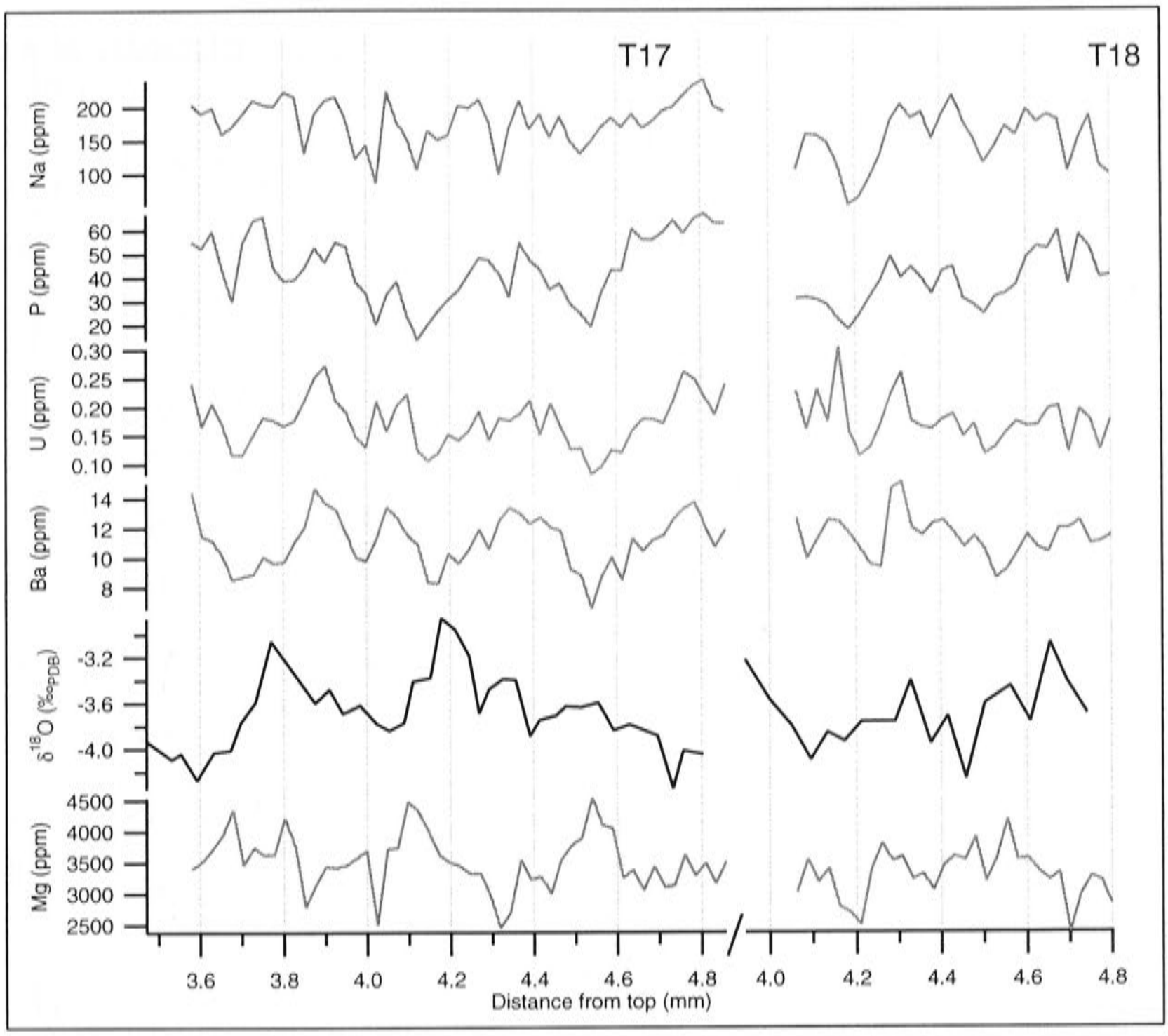

Figure 6.3.5: As for Figure 6.3.4 but for tracks 17 (T17) and 18 (T18).

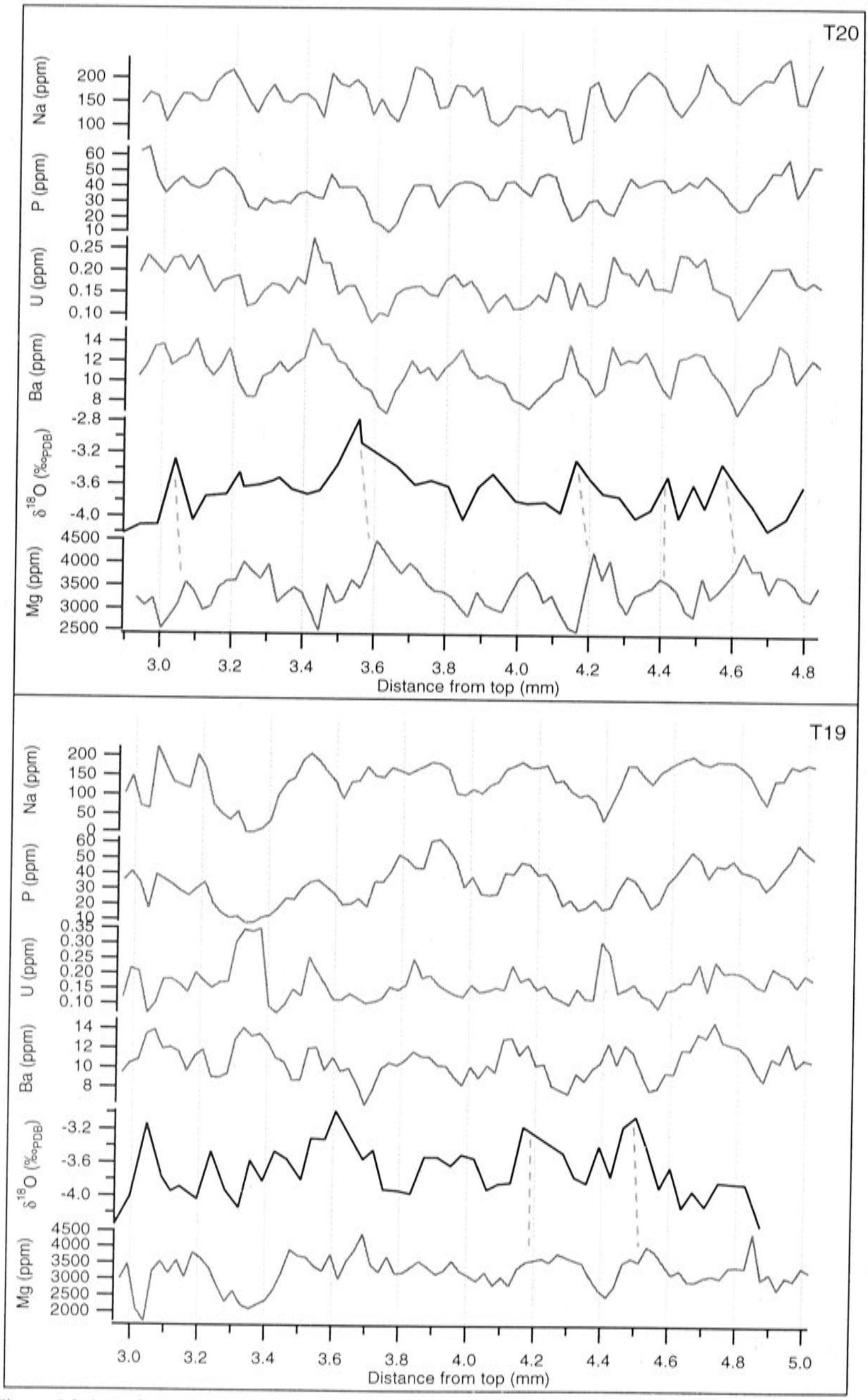

Figure 6.3.6: As for 6.3.4 but for tracks 19 (top) and 20 (bottom).

6.4 MND-S1 DISCUSSION

The following four features of the data presented in Sections 6.1-6.3 warrant further discussion:

- The excellent agreement between the number of cycles in trace elements with the age constrained by the boardwalk.
- The definite relationship between trace element cycles and crystal growth patterns.
- The geochemical signatures that mimic the rainfall record (Mg, P and U), and may be useful rainfall proxies.
- $\delta^{18}O_{SP}$ cycles corresponding to trace element cycles.

An important step in validating palaeoclimate research is to obtain modern samples and directly compare their geochemical records with instrumental climate records. MND-S1 shows 84 ± 1.3 cycles counted in Ba, that are also present in Sr, Mg, U and P, which is consistent with the length of time that the boardwalk, on which it grew, was in the cave (A.D.1911-1992). Annual cycles in trace elements have been observed by other authors but the chronology of these studies, derived from UV luminescence banding and extension rates from U-series chronologies (Roberts *et al.*, 1998; Fairchild *et al.*, 2001; Huang *et al.*, 2001) and estimated annual growth rate (Desmarchelier, 1999), are substantially less certain than that for MND-S1. No extensive comparisons with instrumental climate records have previously been made.

In this study, the multiple scans of MND-S1 made with a LA-ICP-MS led to the discovery of the coincidence of annual calcite fabric patterns and Ba concentration, which provides information about the seasonal variation in trace element uptake during a speleothem annual growth cycle. To summarise, Ba, Sr, U and P concentrations are higher in the wetter months (winter) and lower in drier months (summer, or near to summer if growth ceased during the driest time of the year), while Mg concentrations are lower in winter and higher in the summer or drier months. A similar seasonal pattern is seen in ion microprobe measurements of $\delta^{18}O_{SP,}$ with $\delta^{18}O_{SP}$ about 1‰ higher in summer

than in winter, which is consistent with the known annual rainfall cycle for Southern Australia (Chapter 5). These relationships between trace elements and climate are now compared with findings from other studies where annual trace element cycles were found.

Sr, Ba and Mg

Annual cycles of Sr, Ba and Mg have been measured in previous speleothem studies (Roberts *et al.*, 1998; Desmarchelier, 1999; Fairchild *et al.*, 2001; Huang *et al.*, 2001). The most striking feature of these three metals observed in this and previous studies is the strong correlation between Sr and Ba (here $r = +0.90$, $p < 0.01$) and the antiphase relationship between Mg and the other elements. The strong correlation between Sr and Ba is commonly observed in low-temperature natural inorganic calcites and although the geochemical behaviour of Ba is not well-studied, Pingitore and Eastman (1984; 1985) confirmed that Sr and Ba substitute for Ca, by demonstrating that their partition coefficients under equilibrium conditions are almost identical, the lower concentration of Ba owing to its larger cation size ($r = 1.44$ Å compared with Sr, $r = 1.21$ Å and Ca, $r = 1.08$ Å).

The antiphase relationship between Mg and the other elements is not readily explained by simple lattice geometry as co-precipitation of Mg in calcite (smaller cation than Ca) tends to linearly increase the uptake of ions larger than Ca, by deforming the lattice to allow larger ions to be more easily accommodated in neighbouring Ca sites (*e.g.* Sr; Mucci and Morse, 1983). Moreover, the only common mechanism that would discriminate against Mg while favouring Sr and Ba is co-precipitation of aragonite and calcite, since the larger cations (Sr, Ba) are favoured in the orthorhombic structure of aragonite while the smaller Mg cation is favoured in the trigonal structure of calcite (Wenk *et al.*, 1983). However, aragonite/calcite combinations may be eliminated as the overall relatively high Mg content of MND-S1 indicates that it was originally precipitated as calcite.

Roberts *et al.* (1998; 1999), Fairchild *et al.* (2001), Huang and Fairchild (2001) and Huang *et al.* (2001) attribute the antiphase relationship between Sr (Ba) and Mg to a

model first proposed by Roberts *et al.* (1998; 1999), which suggests the trace element behaviour in the speleothem is controlled by seasonal fluctuations in the drip-waters, owing to the differential dissolution of Sr (Ba) rich; (but Mg poor) calcite and Sr (Ba) poor; (but Mg rich) dolomite. Roberts *et al.* (1998; 1999) suggested that in seasons of shorter residence time (wetter months) the percolating waters have only sufficient time to dissolve the most soluble calcitic component of limestone in fast conduit flows above the cave. They argue that this contrasts with the lower flow conditions of the drier months, where they propose that the waters remain for much longer periods in the diffuse channels where they are able to quickly reach $CaCO_3$ saturation and thus begin to precipitate $CaCO_3$. However, as they have not yet reached saturation with respect to $CaMg(CO_3)_2$, they are able to continue dissolving Mg from the dolomite fraction of the aquifer after it has begun to precipitate $CaCO_3$. These authors propose that it may be the simultaneous precipitation, thus loss, of Sr (Ba) from the calcium carbonate saturated waters, with the concurrent dissolution of Mg-rich dolomite, that may result in an antiphase relationship between Sr (Ba) with Mg in the speleothem. This model follows the principles of trace element partitioning of aquifer waters in sedimentary carbonates described by Veizer (1983b). This model however, only adequately describes the development of opposite trace element gradients when elements with $D_{Me/Ca_{CALCITE}} >> 1$ and $D_{Me/Ca_{CALCITE}} << 1$ are both present. Since D_{Sr}, D_{Ba}, D_{Mg} are all less than unity (Pingitore and Eastman, 1984; Oomori *et al.*, 1987, Tersorio and Pankow, 1996, Huang and Fairchild, 2001) the evolved solution will be enriched in all three, and it is thus difficult to imagine how this accounts for the antiphase behaviour of Sr (Ba) and Mg.

There is a second argument against the applicability of Robert's model in this study. The calcarenite of the Leeuwin-Naturalist ridge is composed of chemically relatively homogeneous fragments of low-Mg calcareous sand and shell matter. While the amount of Mg dissolved may still be influenced by residence time, clearly, no models involving periodic contact with distinct localised Mg-rich end-members can be invoked to explain the antipathetic behaviour of Sr (Ba) and Mg in speleothems. Furthermore, in an empirical experiment to precipitate speleothem calcite under similar cave and (constant) solution conditions Huang and Fairchild (2001) also observed this same antiphase relationship, which they attribute to intra-sectional zoning on non-equivalent vicinal faces described by Paquette and Reeder (1990; 1995). However, this same mechanism

can rarely be invoked to explain antiphase behaviour in natural carbonates, as their changing solution composition usually prevents preservation of zoned faces large enough to be detected (Paquette et al. 2002).

A further process for consideration is the effect of prior calcite precipitation (Fairchild *et al.*, 2000). Here, the cumulative effect of preferentially removing Ca from the solution will be to enrich the solution in Mg as $D_{Sr} > D_{Mg}$ (Huang and Fairchild, 2001). This also does not explain the antiphase behaviour since D_{Sr} and $D_{Mg} < 1$ and they therefore evolve in the same direction.

Evidence that Mg is driven by environmental rather than kinetic process comes from its strong inter-annual relationship with rainfall (Figure 6.2.1). Mg concentration in MND-S1 increased since the 1960s while rainfall has decreased (Figure 6.2.2). An increase in drip water m_{Mg}/m_{Ca} during lower recharge is consistent with the prior calcite precipitation model (Fairchild *et al.*, 2001; Huang and Fairchild, 2001). The antiphase relationship between Ba and Mg may be accounted for by the faster growth rate (higher Ba) during greater drip-water through-flow with less residence time; and thus lower drip-water Mg/Ca, hence speleothem, Mg/Ca ratio. This suggests that MND-S1 Mg concentration is an effective palaeo-rainfall proxy because prior calcite precipitation is sensitive to residence time hence recharge, which confirms the suggestions and observations by Fairchild *et al.* (2001) and Huang *et al.* (2001).

P and U

P and U are considered here together because of their resemblance to the rainfall record and because of their broad agreement in the long-term ($r = +0.62$; Figure 6.2.1) which may be explained by U's strong affinity for PO_4^{3-} ($UO_2(HPO_4)_2^{2-}$). Langmuir (1978) summarises the main factors affecting U in groundwater as:

- source rock content or proximity to U minerals and their leachability;
- seasonal climatic effects (affecting oxidation and leaching);
- pH and oxidation state of water;

- presence of U complexing carbonates, phosphates, sulphates and other species;

The transport of U (uranyl, UO_2^{2+}) is greatly enhanced by its affinity for forming complexes with CO_3^{2-}, OH^-, PO_4^{3-}, F^- and SO_4^{2-}; which greatly increases its solubility and mobility (the actual ligand formed is a function of pH (Langmuir, 1978; Figure 6.4.1)). $UO_2(HPO_4)_2^{2-}$ is particularly stable and dominates natural waters of pH 4-7.5, since cave drip waters are effective buffer solutions with near-neutral pH (*e.g.* 7.0-8.2; Holland *et al.*, 1963; Baker *et al.*, 2000), any U is likely to be scavenged and transported as $UO_2(HPO_4)_2^{2-}$. This mechanism likely explains the close agreement between U and P seen in Figure 6.2.1.

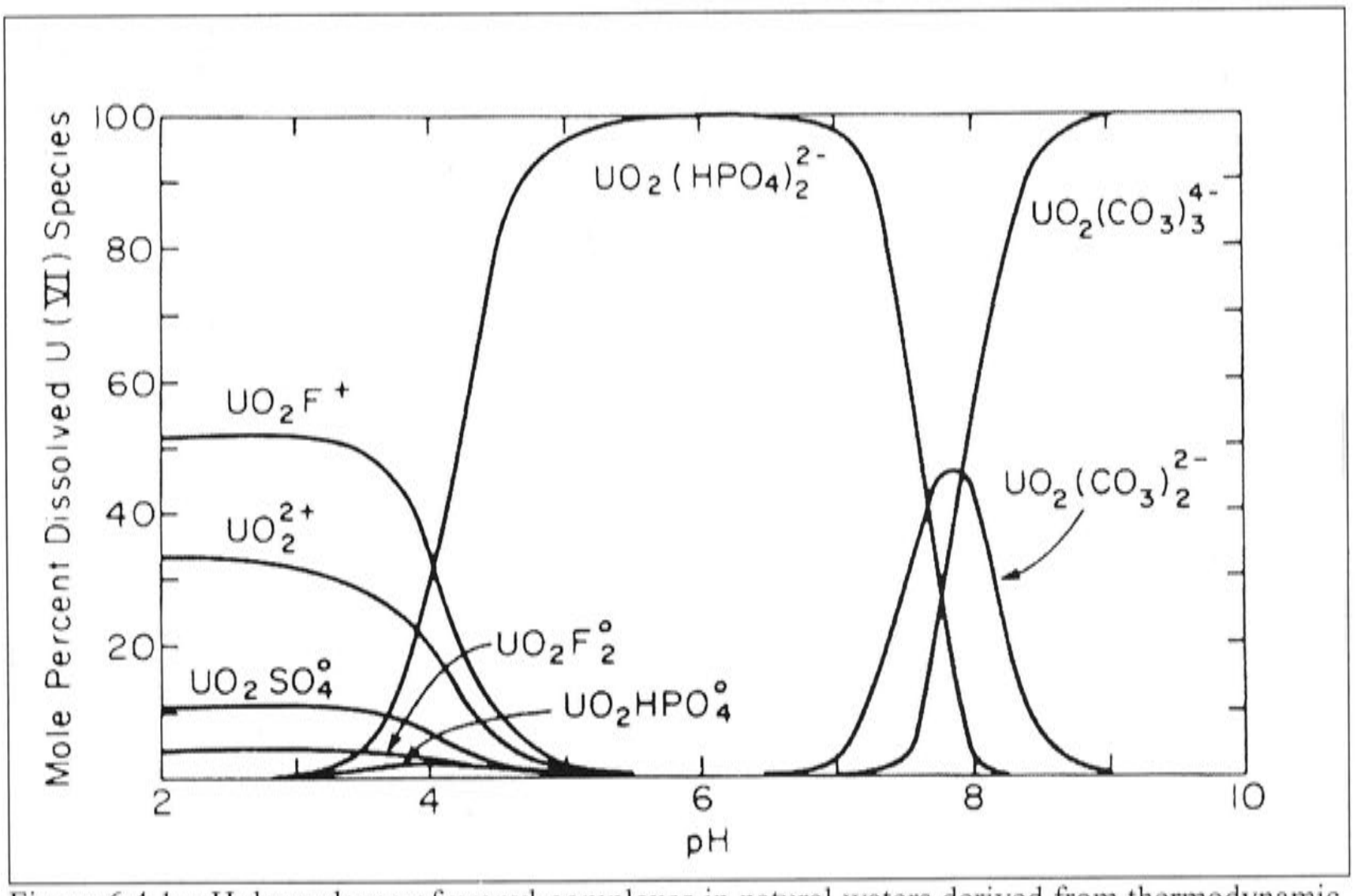

Figure 6.4.1: pH dependence of uranyl-complexes in natural waters derived from thermodynamic calculations. (From Langmuir, 1978.)

The obvious sources of P are:

- fertilisers;
- decomposition of vegetation which use P as a nutrient (organic P); and
- PO_4^{3-} content of the calcarenite.

Since MND-S1 is located in a non-agricultural catchment fertilisers may be ruled out, which is fortunate as MND-S1 thus provides an example of a natural catchment system untainted by anthropogenic processes, which is important for calibrating climate proxies. It has been argued that organic P released from biomass would quickly convert to PO_4^{3-} in the soil zone thus providing a seasonally available excess of PO_4^{3-} over that derived from calcarenite (Fairchild *et al.*, 2001). Of the previous speleothem studies that investigated P, Huang *et al.* (2001) and Baldini *et al.* (2002) found P to be antiphase with Sr for an Italian and Irish speleothem while Fairchild *et al.* (2001) report another Irish speleothem for which P varies in its phase relationship with Sr. It appears that P may be the least consistent of elements, displaying the most variability in phase and also concentration over climatically diverse environments, which may in itself argue that it is a climatically driven proxy. Here it has been shown to be strongly correlated with rainfall, however this study has raised a point of potential concern, that P banding is not aligned with the other elements in the crystal matrix and may thus be affected by recrystallisation or its origin may be secondary.

One consistency between speleothem studies of P in which an explanation for this anomaly may lie is the common observation that P peaks tend to coincide with laminae features such as fluid inclusions (Huang *et al.*, 2001) and colouration interpreted as seasonal hiatuses (Fairchild *et al.*, 2001). In these previous studies, some of these layers are reported to be visible in the UV spectrum leading to the interpretation that the P and UV source are delivered by high infiltration events, possibly the arrival of autumn rains flushing the soil organic load through to the cave (Huang *et al.*, 2001; Fairchild *et al.*, 2001). In this study, a strong coincidence of P with UV banding is also observed (Figure 6.1.11), however the disconcordance of P bands with annual bands of Ba, Sr, Mg and U the offers an alternative hypothesis:

that the concentration of P banding along the UV laminae is a result of a secondary process possibly associated with the coarsening of calcite crystals by Ostwald ripening.

The effects of neomorphism (Ostwald ripening) on trace element diffusion has not yet been discussed but has important implications for palaeoclimate interpretation of speleothems, that is, to what extent are foreign ions re-organised, thus corrupting the

relationship of the ions, as the crystal lattice attempts to stabilise itself when it undergoes coarsening? This process may include:

1. P migration by lattice exclusion; or
2. Secondary processes along the re-sculpted crystal surface, such as adsorption and entrapment or movement along grain boundaries.

No literature was found for lattice diffusion in low-temperature carbonates, however, it is known from empirical experiments of diagenetic processes under simulated metamorphic conditions, that the degree of foreign ion diffusion in calcite depends on:

- occupation site (ion diffusion via Ca sites is slow while diffusion via interstitial sites is fast (Cherniak, 1998); and
- ionic size and covalent bonding strength (Cherniak, 1997).

Comparing activation energies of foreign ions relative to that for self-diffusion of Ca in calcite (Farver and Yund, 1996) suggests Mg can diffuse faster than Ca (Fisler and Cygen, 1999) while Sr is slower than Ca (Cherniak, 1997) and rare earth elements are even slower (Cherniak, 1998). The validity of extrapolating these results to predict diffusion under Ostwald ripening is highly questionable, given that these experiments consider only solid state migration within a single crystal, and diffusion rates across crystal boundaries would be significantly greater in the presence of a solution; however, the experimental data suggest that it would take on the order of millions of years at temperatures ~500°C for these elements to diffuse the length of one of these annual band widths (~300 μm). One further argument against P diffusion under neomorphism is that PO_4^{3-} bonds strongly to calcite, as discussed below.

A possible mechanism that applies to elements with a high adsorbing capacity to calcite is trace element incorporation by surface enrichment, described by Watson (1996). This mechanism describes the entrapment of elements that are not necessarily highly compatible with lattice sites but strongly adsorb onto calcite, and thus are included in the crystal if crystal growth is sufficiently fast that it out-competes the diffusion of lattice compatible ions to the crystal boundary (Watson, 1996). P strongly adsorbs to calcite surfaces as $Ca_3(PO_4)_2$ (de Kanel and Morse, 1978; Millero *et al.*, 2001) and its

occupation has been shown to be enhanced at defect sites (Berner and Morse, 1974). Thus the adsorption of ions is likely to be concentrated along crystal boundaries where defect sites are exposed (Watson, 1996).

It is proposed here that the UV bands are actually characterised by the increased number of defect sites along the recrystallised surface that provide adsorption sites resulting in concentrated bands of P. An obvious question is how does the P get there if it is unlikely to have diffused from its original lattice position? And how much does this corrupt the speleothem P record?

The first question remains difficult to address as SEM imaging of MND-S1 revealed no distinguishable fabric features characterising the UV bands. Even at the hiatus, where there is a P band (Figure 6.1.11), there were few distinguishing features apart from some isolated, perhaps detrital inclusions (marked by arrows; Figure 6.4.2), but certainly no secondary recrystallisation. The lack of evidence for secondary crystallisation concentrated along these sites suggests that the P banding results from P adsorption to the high concentration of defects and subsequent entrapment on this re-sculpted surface. It may be that this recrystallisation process occurs during the annual break in deposition and subsequent percolation of autumn rains carry sufficient PO_4^{3-} to saturate the many defect sites on the re-sculpted surface however, without further field investigations (water sampling) the vehicle for transporting the P to these sites remains unknown.

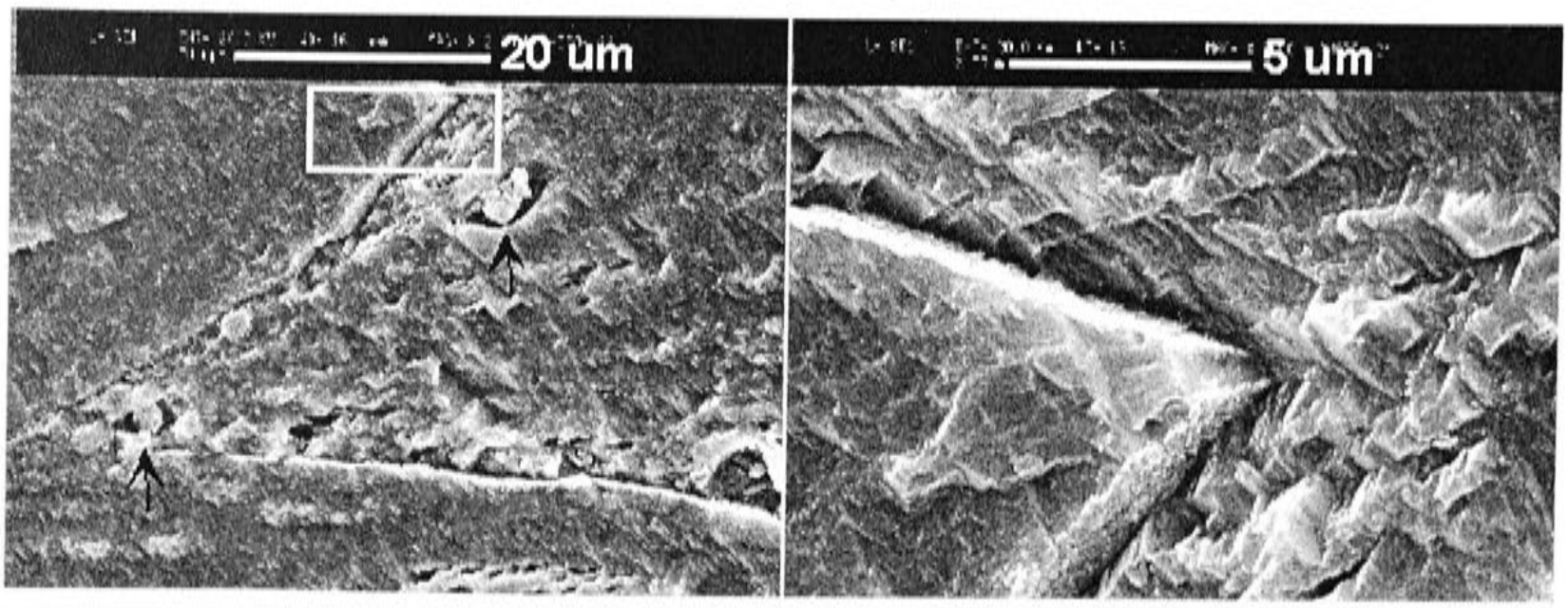

Figure 6.4.2: SEM images of UV visible hiatus showing possible detrital fragments (marked by arrows, left) but no evidence of secondary recrystallisation along the hiatus (right). The right-hand image is a close-up of the area marked by a white box in the left-hand image (Surface above the hiatus shows cleavage planes revealed by etching.)

The non-concordant P bands do not appear to corrupt the master record (P and rainfall are well-correlated). This may be due to the fact that the P spikes are more subdued in range over the crystal area ablated for the master record (which is consistent with the less distinct UV banding) compared to the area shown in Figure 6.1.11, but possibly also due to the fortuitous fact that creating the master record was done by passively stacking P cycles according to the positioning of Ba troughs. Since the Ba and P records are oblique and thus misaligned, this may have also helped to minimise their contribution to the master record.

Further evidence that post-depositional coarsening (neomorphism) has not greatly affected the P and general geochemical integrity of MND-S1 lies in the clearly resolvable annual cycles that show a definite response with rainfall changes (Figure 6.2.2), which are also consistent with the long-term rainfall trend. However, the disconcordance of P banding with the other elements may indicate a secondary process and is thus disturbing. This discovery may serve as a caution towards using UV bands as chronological indicators.

Inter-annual stable isotopes

Comparison of conventionally analysed $\delta^{18}O_{SP}$ and $\delta^{13}C_{SP}$ with rainfall and trace elements revealed that both $\delta^{18}O_{SP}$ and $\delta^{13}C_{SP}$ display an antiphase relationship with rainfall trend; although for $\delta^{18}O_{SP}$, this relationship is weakened during episode ii (A.D.1930-1956), which was argued earlier to be corrupted by kinetic precipitation effects. While both $\delta^{18}O_{SP}$ and $\delta^{13}C_{SP}$ appear to be related to rainfall, it is only $\delta^{18}O_{SP}$, that directly reflects the isotopic composition of rainfall (Chapter 1, Section 1.3), while $\delta^{13}C_{SP}$ is indirectly driven by the effects of recharge on the water table and hence vadose zone above the cave.

As argued in Chapter 5, the isotopic composition of rainfall, $\delta^{18}O_P$, for southern Australia is driven by the proximity of a site to the low pressure systems of the mid-latitudes. It is the vigorous recycling, and greatest vertical uplift near the centre of these systems, which results in isotopically lightest precipitation. Thus the isotopic composition of rainfall at

any site in southern Australia is driven by its proximity to these systems. A report on the marked reduction in winter rainfall in southwestern Australia (IOCI, 1999) states that this phenomenon is characterised by a decline in the number of rain days and the amount of rain received in extreme events. The 'extreme events' occur when these low pressure systems pass close to the south-western Australia coast. From the results of Chapter 5, it is argued that a reduction in these events will result in a reduction in isotopically lighter rain, the effects of which may further be exacerbated by evaporation in the soil zone if the relative humidity and soil moisture is reduced as a consequence of the reduction in the number of wet days. If episode ii is excluded, based on possible corrupting effects of kinetic precipitation (Section 6.2.4), then MND-S1 $\delta^{18}O_{SP}$ appears to record this precipitation effect on $\delta^{18}O_P$ as it trends towards heavier $\delta^{18}O_{SP}$ whilst rainfall is declines.

$\delta^{13}C_{SP}$ also becomes heavier as rainfall declines from episode iii to iv. This may reflect an increase in prior-degassing and precipitation, under either closed or open system conditions. It was hypothesised in Section 6.2.4 that this may be induced by an increase in the size of the vadose zone of the calcarenite, by lowering of the water table due to lowered recharge. A lowering of the water table over this time period is supported by observations of cave lake levels by tourism managers (S. Eberhard, *pers. comm.*). This shift towards greater prior-degassing and precipitation as response to reduced rainfall, is supported by the agreement between $\delta^{13}C_{SP}$ and Mg (Figure 6.2.6). It was argued earlier in this discussion that these effects were the only plausible explanation for the Mg behaviour in MND-S1.

A relationship between $\delta^{13}C_{SP}$ and Mg has been found for other speleothem studies (Hellstrom and McCulloch, 2000; Verheyden *et al.*, 2000), however, in these studies, it was argued that the increase in Mg during lower recharge conditions was a consequence of dissolution of dolomitic phases following Roberts *et al.* (1998; 1999). As discussed earlier, this study shows that the existence of dolomite is not necessary to explain the effects of lowered recharge on Mg, and that evolution of the waters by prior-degassing/precipitation in the karst vadose zone appears adequate to explain this behaviour.

The study of Hellstrom and McCulloch (2000) observed an antiphase relationship between $\delta^{13}C_{SP}$ and Ba, which is seen here also, which was interpreted in terms of greater leaching of Ba from the soil/limestone by higher concentrations of carbonic acid (greater soil CO_2 production; Hellstrom and McCulloch, 2000). In the present study, Ba has been strongly linked with growth rate, and Figure 6.2.5 shows that Ba and growth rate are antiphase with $\delta^{13}C_{SP}$. As soil CO_2 production and speleothem growth rate are inevitably linked, these observations likely reflect common mechanisms.

Intra-annual stable isotopes

To a degree, the matching of $\delta^{18}O_{SP}$ cycles has helped circumvent the lack of a full year of trace element and stable isotope data from drip water, a major deficiency of this study. The phase relationship of the $\delta^{18}O_{SP}$ cycles is consistent with the seasonality of the trace elements, which was inferred from the coincidence of the trace element cycles with the lines of holes representing annual breaks in deposition. The positive co-variation between $\delta^{18}O_{SP}$ and Mg also supports that MND-S1 Mg concentration may be driven by seasonal fluctuations in prior calcite precipitation since isotopically heavier $\delta^{18}O_{SP}$ (summer) coincides with high Mg concentrations. The coincidence of lighter $\delta^{18}O_{SP}$ (winter) with higher concentrations of Ba further supports that the uptake of Ba is driven by growth rate. Thus measuring the $\delta^{18}O_{SP}$ cycles has been instructive in revealing that $\delta^{18}O_{SP}$ is driven by rainfall $\delta^{18}O_P$ on the annual cycle, and has also contributed to understanding the kinetic and equilibrium effects on the lessor understood speleothem trace elements.

Despite some of the teething problems outlined in Section 6.3, the measurement of stable isotopes using SIMS appears worth pursuing. Plans for future work are to collect enough data to compare stacked cycles from prior to A.D.1960 with those collected here (post-A.D.1960) and also to similarly acquire $\delta^{13}C_{SP}$ annual cycles, which will likely be useful as $\delta^{13}C_{SP}$ will likely be sensitive to prior calcite precipitation effects and changes to vegetation and soil zone dynamics.

6.5 CONCLUSIONS

To summarise, the most surprising findings of the MND-S1 trace element record are the complex growth patterns of the annual bands involving crystal coarsening and possible erosion. The major implication is that single scans along the growth axis are unlikely to be truly representative of the trace element variation. The two dimensional mapping performed here is clearly necessary to fully appreciate the trace element distribution in speleothems and specific to this study, was needed to register the ion microprobe $\delta^{18}O_{SP}$ data and investigate secondary processes.

This is the first multi-proxy study conducted at sub-annual resolution on a speleothem whose well-constrained chronology allows for a confident comparison between the instrumental climate record and these geochemical climate proxies. This exercise has revealed that $\delta^{18}O_{SP}$ is primarily driven by rainfall $\delta^{18}O_P$ at the intra-annual scale which makes it a useful tracer of hydrological processes and trace elements when the phase relationships between these proxies can be confidently determined. Ba and Na appear to be sensitive to growth rate on intra-annual and inter-decadal scales. By contrast, the inter-decadal behaviour of Sr differs from Ba over the longer-term, where the effects of prior calcite precipitation on Sr appear to be important.

Mg, P and U appear to be the most effective palaeohydrological indicators although they differ in their mechanisms; Mg is sensitive to residence time (recharge conditions) while P and U are related because of the stability of $UO_2(HPO_4)_2^{2-}$, and reflect more the climatic effects on the rate of bio-production of P and perhaps also the rate of dissolution of PO_4^{3-} and U from the calcarenite.

CHAPTER SEVEN

HOLOCENE SPELEOTHEM RESULTS AND DISCUSSION

7.1 PREVIOUS WORK AND CURRENT OBJECTIVES

A Holocene stalagmite, FC-S3, from Frankcombe Cave, south-central Tasmania (see Chapter 2, Section 2.2.1 for description) was the subject of this author's Honours thesis (Treble, 1998). Two U-series age measurements (top = 0.23 ± 0.08 ka and base = 3.67 ± 0.21 ka; Chapter 3, Section 3.4), and 43 conventional stable isotope analyses, sampled with a 0.8 mm drill bit every 1.2 mm; were performed for this previous work producing the low resolution 1.2 to 0 ka isotope record shown in Figure 7.1.1 below.

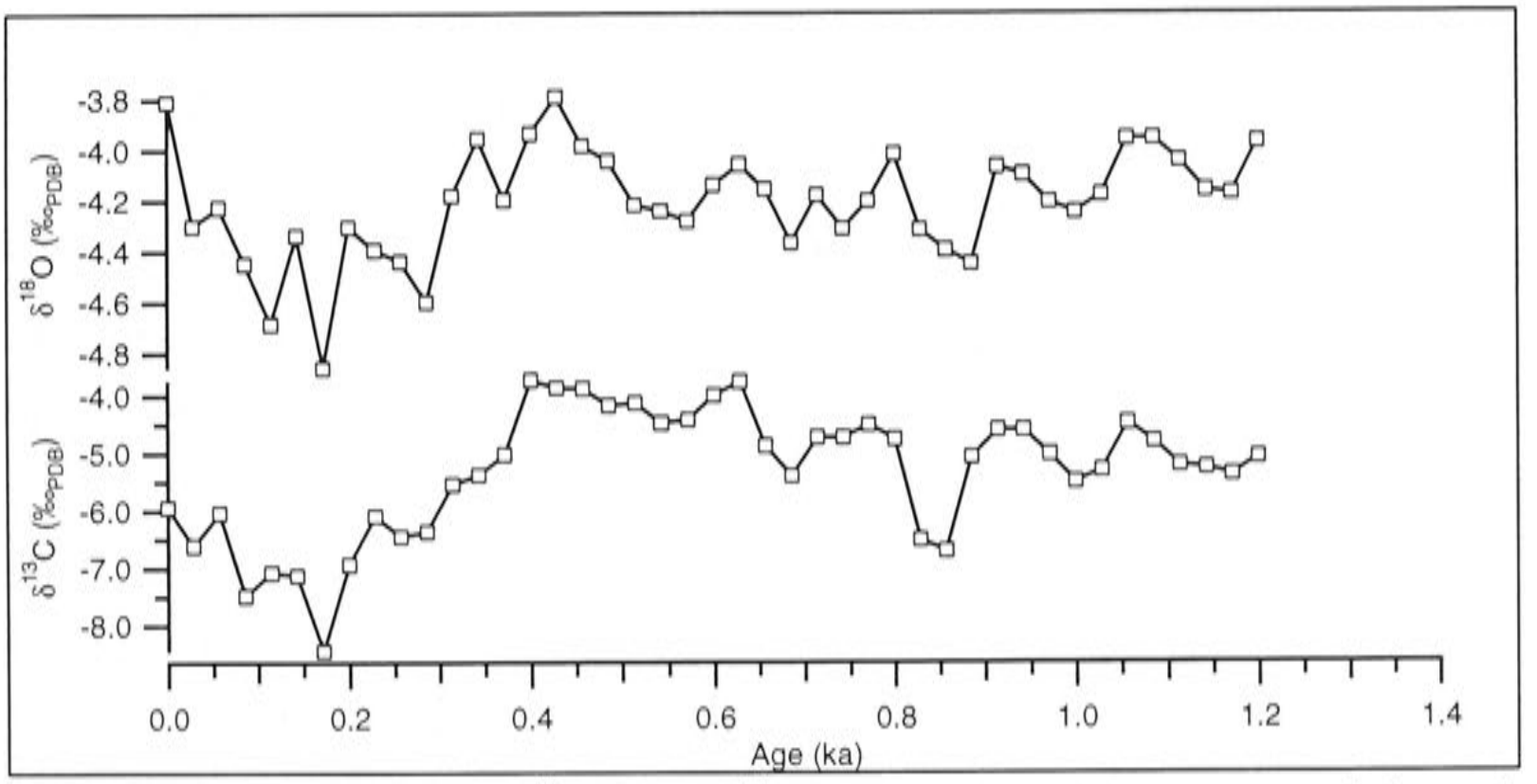

Figure 7.1.1: Low-resolution $\delta^{18}O_{SP}$ and $\delta^{13}C_{SP}$ record for FC-S3 constructed for author's Honours thesis (Treble, 1998).

The major findings of this previous research were:

1. That the range of $\delta^{18}O_{SP}$ for the FC-S3 record (1.2-0 ka) was greater than that expected from temperature effects alone. This was shown by converting the range of FC-S3 $\delta^{18}O_{SP}$ values (1‰) to temperature, yielding 4.2°C, which is two-thirds of that estimated for the LGM-Holocene transition (Colhoun *et al.*, 1996) and thus unlikely for the last ~0.5 ka. The improbability of such a temperature shift is supported by the well-established Tasmanian tree-ring reconstructions (Cook *et al.*, 1992) which show

no significant change in temperature for this period. Following arguments outlined for Chapter 1, Section 1.3; that $\delta^{18}O_{SP}$ is driven by cave temperature and meteoric precipitation effects, implies that the isotopic composition of rainfall, $\delta^{18}O_P$, must have changed in a manner not attributable to mean surface temperature effects over this time. This led to the inference

2. that the ~1‰ depression in $\delta^{18}O_{SP}$ between 0.4 to 0 ka may represent the Little Ice Age (LIA), broadly defined to be a period of cooler temperatures from A.D.1550-1800 (Lamb, 1977) or A.D.1600 to 1850 (Grove, 1988) based predominantly on Northern Hemisphere records. To date, no evidence for the LIA has been recognised for Tasmania, nor southern Australia. However, as the chronology at this stage of research was uncertain (see discussion of U-series age measurements in Chapter 3, Section 3.4), the timing of this depression was likewise uncertain. Moreover, if the chronology were biased to older ages, it is possible that this depression represents European activities above Frankcombe Cave, which was affected by logging and associated fires and regrowth during the 19th and 20th centuries (Eberhard, 1996).

This leaves two questions to be investigated for FC-S3: Does the depression in both $\delta^{18}O_{SP}$ and $\delta^{13}C_{SP}$ represent a climate shift or anthropogenic catchment disturbance? And if it is climatic, does it reflect a change in rainfall or temperature? To investigate these two questions, the following work was carried out as part of this PhD research:

- FC-S3 was re-sampled for stable isotope analyses using micro-milling techniques described in Chapter 4, Section 4; increasing the resolution from > 1 mm to 0.5 mm intervals, and also extending the record further back in time to 2.4 ka.
- 9 radiocarbon $A^{14}C_{SP}$ measurements were performed for the top 45 mm of FC-S3, to check for bomb spike C (> 100 PMC; Chapter 3, Section 3.7). These results showed that the top of FC-S3 ceased growing post-A.D.1956, and the modelling exercise may constrain this to A.D.1980 ± 15 years.
- Trace elements were analysed by LA-ICP-MS (5x50 µm slit and 32 µm spot), and also TIMS Sr isotope measurements were conducted on aliquots of the samples milled for conventional stable isotope analyses. It was hoped that including proxies that are potentially sensitive to soil dynamics (Holmgren *et al.*, 1999; Hellstrom and McCulloch, 2000; Fairchild *et al.*, 2001) would separate the effects of natural and post-European settlement on the stable isotopes.

- An attempt at reproducing the FC-S3 record was made using a second stalagmite, FC-S8, from the same cave. The age measurements for FC-S8 appear in Chapter 3, Table 3.4.1, and the conventional stable isotope record constructed is compared with the newly sampled FC-S3 record below.

7.2 RESULTS

7.2.1 Reproducing and extending the FC-S3 record

Figure 7.2.1A shows that the general trend of the previous coarsely sampled stable isotope data is reproduced in the higher resolution data sampled for this research. This newer record reveals greater detail, such as the trough at 28 mm which is not seen in the old coarsely sampled data. This trough marks the end of a series of concurrent cycles in $\delta^{18}O_{SP}$ (amplitude ~0.5‰) and $\delta^{13}C_{SP}$ (amplitude ~2‰) that occur every 5-10 mm from 110 to 28 mm along the extended record (Figure 7.2.1B). This 110 mm record is the maximum extent of FC-S3 that could be sampled, as the basal 50 mm of the growth axis was riddled with voids. Adopting for now, the basal U-series date (3.67 ± 0.21 ka) and the top radiocarbon date (post-A.D.1956 or 0 ka), shows that the wavelength of these cycles is approximately 100-200 years (Figure 7.2.1C), although this wavelength may be less if the basal age estimate of FC-S3 is too old as suggested by low $^{230}Th/^{232}Th$ measurements (~2; Chapter 3, Section 3.4).

In terms of this chronology, between 0.6-0.3 ka the mean $\delta^{18}O_{SP}$ and $\delta^{13}C_{SP}$ shift by 0.5‰ and 2‰, respectively, towards isotopically heavier values before returning to the previous values. For $\delta^{18}O_{SP}$, it also appears that the 100-200 year cycles persist through this 0.6-0.3 ka period, superimposed over this larger isotopic shift. Between 0.3-0 ka, $\delta^{18}O_{SP}$ repeats one further cycle before moving towards isotopically heavier values again. By contrast, $\delta^{13}C_{SP}$ reaches a plateau between 0.6-0.4 before returning to isotopically lighter values between 0.4-0 ka, and no longer resembles the $\delta^{18}O_{SP}$ trend, as it did prior to 0.6 ka.

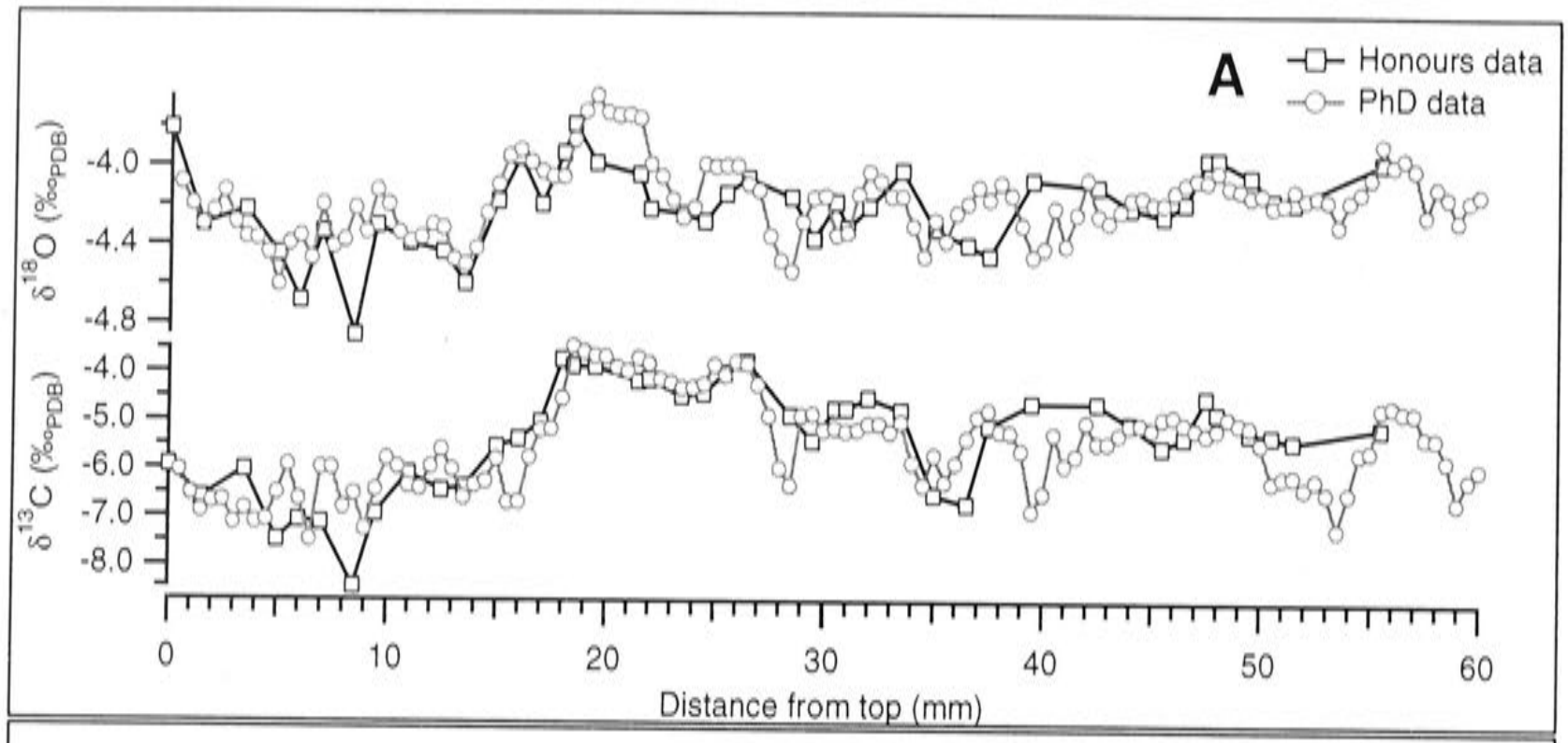

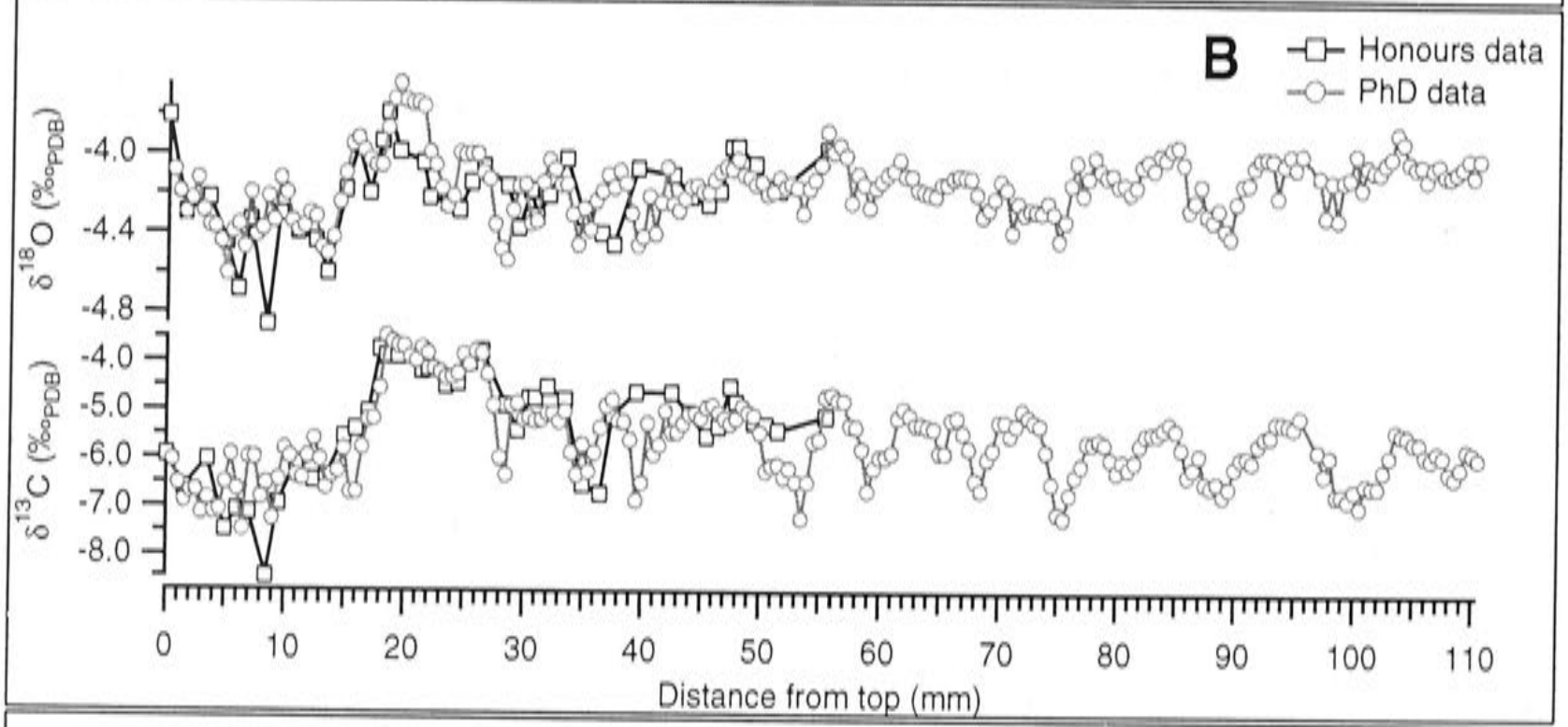

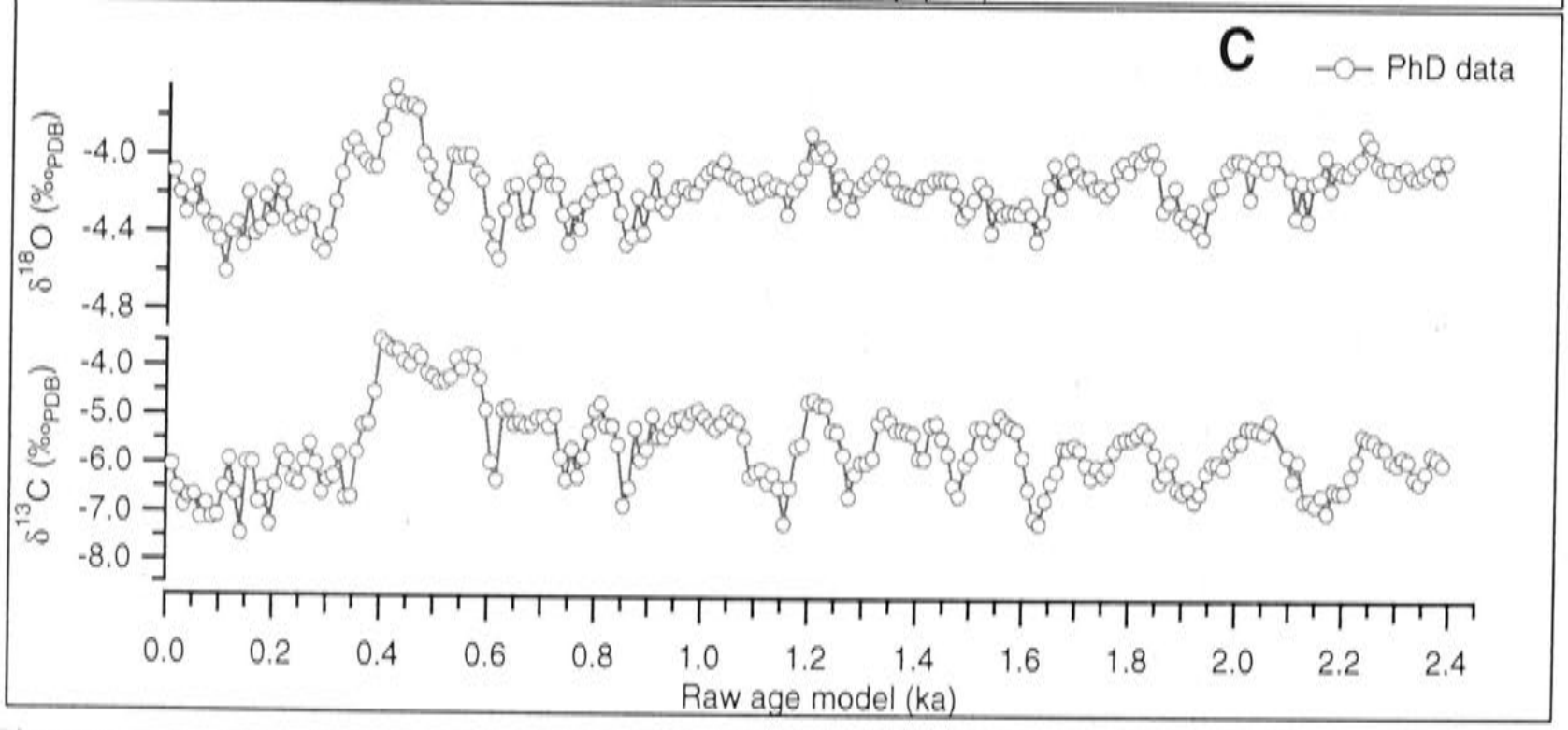

Figures 7.2.1A-C shows the re-sampled conventional stable isotope results overlying the previous results (Honours research); topmost 60 mm (A), extended re-sampled 110 mm record (B), and this new data on the age-scale (C).

Re-sampling and extending the FC-S3 record, has revealed further characteristics which necessitate a re-interpretation of the results. Whereas previously, the depression of

isotopically lighter values between 0.4-0 ka stood out (Figure 7.1.1), it now appears that these values more closely resemble the extended record between 2.4 to 0.6 ka, and it is the shift to isotopically heavier values between 0.6-0.4 ka that appears anomalous for the past 2.4 ka (Figure 7.2.1C).

The high resolution and extended record allows other features to also be closely scrutinised. FC-S3 $\delta^{18}O_{SP}$ and $\delta^{13}C_{SP}$ are highly correlated throughout the entire record ($r = +0.60$, $p < 0.01$). A high correlation along the growth axis of a speleothem may indicate kinetic fractionation (Hendy and Wilson, 1968; see Chapter 1, Section 1.3.4 for discussion); however, environment conditions can also produce correlated $\delta^{18}O_{SP}$ and $\delta^{13}C_{SP}$ (*e.g.* Hellstrom *et al.*, 1998), when rainfall, vegetation activity and limestone dissolution are coupled and thus co-vary. Because the investigation of such factors may be strengthened by trace element and Sr isotope measurements, they will be discussed after these measurements have been introduced (Section 7.3). The reproducibility of the FC-S3 stable isotope record is first examined below.

7.2.2 Comparison of FC-S3 and FC-S8 stable isotope records

To test reproducibility, a second stalagmite, FC-S8, was collected from Frankcombe Cave. FC-S8 was removed whilst actively growing on a ledge near to the streamway where FC-S3 was found (see Chapter 2, Section 2.2.1 for description). A U-series age measurement from the base of FC-S8 shows it to be of similar age (2.99 ± 0.17 ka) to FC-S3 (3.67 ± 0.21 ka, Chapter 3, Section 3.4). However, FC-S8 is more than twice the height (410 mm) of FC-S3 (160 mm) and thus grew faster. The results of conventional stable isotopes, also sampled at 0.5 mm increments, on FC-S8 are shown in Figure 7.2.2 alongside those of FC-S3, which shows that the fine-scale isotopic variability in FC-S8 is greater than that observed for FC-S3. The faster growth rate of FC-S8, coupled with the same sampling interval of FC-S3, may account for the difference in results, as FC-S3 has fewer samples per unit of time and thus its true variability may be more smoothed than FC-S8. With respect to the lower order variability, FC-S8 does appear to show $\delta^{18}O_{SP}$ and $\delta^{13}C_{SP}$ cycles with wavelength of 100-200 years and similar amplitude

(~0.5‰ and ~2‰, respectively) to FC-S3, although their presence is obscured by the fine-scale variability.

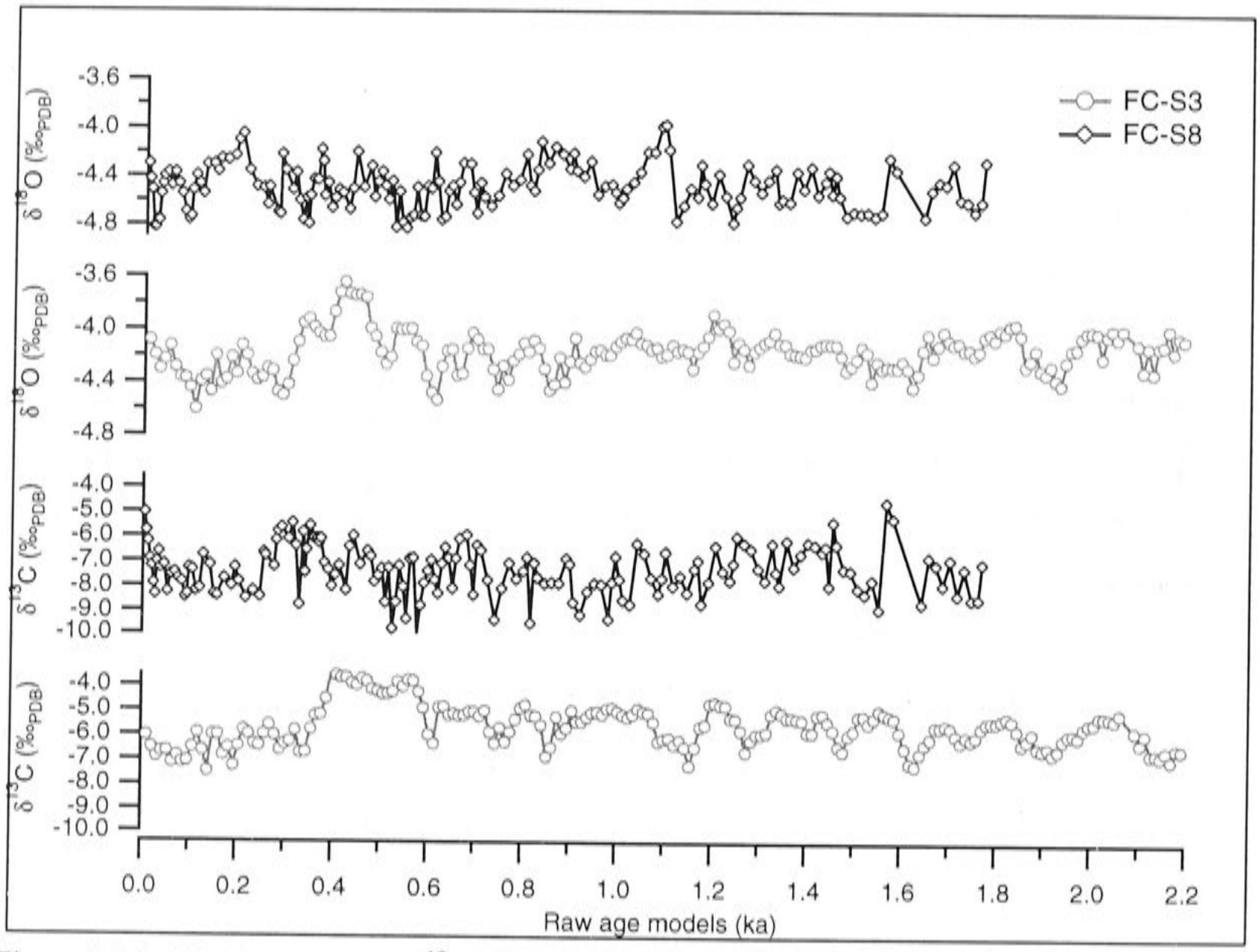

Figure 7.2.2: FC-S8 and FC-S3 $\delta^{18}O_{SP}$ (upper half) and $\delta^{13}C_{SP}$ (lower half).

The fact that fine-scale variability in FC-S8 differs in amplitude and pattern from FC-S3, is disconcerting. There are two possible mechanisms which may account for this:

1. that the stalagmites are fed by drip-water with different mixing time in the limestone, and thus respond to different integrations of rainfall events; and/or
2. that the cave atmosphere around the stalagmites is unstable, fluctuating perhaps in its temperature, humidity and P_{CO_2}, causing carbonate precipitation under different conditions at the two sites.

The first mechanism appears unlikely for two reasons. Firstly, the FC-S8 record shows sample-to-sample variability of up to ~0.5‰ in $\delta^{18}O_{SP}$ and ~3‰ in $\delta^{13}C_{SP}$, with each sample representing ~10 years of growth. This range is greater than the response seen in MND-S1 to a dramatic 20% (200 mm) decrease in rainfall persisting for 30 years (Chapter 6, Section 6.2) which suggests that the variability of FC-S8 is unlikely to reflect interplay between climate shifts and mixing time in the limestone. Secondly, the overall range of $\delta^{18}O_{SP}$ values is greater for FC-S3 (~1‰) than it is for FC-S8 (~0.8‰),

which is the opposite of what would be expected if FC-S3 was a smoothed version of FC-S8. Moreover, this is too large a discrepancy between stalagmites from the same cave for both to be judged as records of environmental conditions. Thus the first mechanism, that the variability may reflect changing drip-water isotopic composition induced by climatic processes, is unlikely.

A second possible mechanism for the large fine-scale variability in FC-S8 is that it is caused by variation in localised carbonate precipitation conditions. FC-S8 grew on a small ledge just above the streamway. While this stream is recorded as being only perennially active (Eberhard, 1996 p.96), and on the four trips made by this author in different seasons there was never more than several cm's of standing water; if the stream was active in the past, flowing water may have caused significant air movement. Air currents may contribute to kinetic precipitation effects by increasing degassing and evaporation rates (Hendy, 1971). However, this cannot explain the discrepancy between FC-S3 and FC-S8 values, as FC-S8 values are isotopically lighter, not heavier (Figure 7.2.2) as would be the case under precipitation conditions driven by rapid degassing and greater evaporation.

Evidence does exist that FC-S3 and FC-S8 were precipitated under different conditions, in the striking visual differences between their crystal structure. FC-S8 consists of frosty-white, inclusion-rich calcite at its core, changing to translucent pale-yellow to grey, inclusion-poor, well-banded calcite on its flanks (Figure 7.2.3A). By contrast, FC-S3 (Figure 7.2.3B) resembles almost entirely the flanks of FC-S8 (translucent yellow to grey distinct bands), with only the core of the basal 80 mm interrupted by sections of opaque calcite that dominates the entire core of FC-S8. Speleothem calcite fabrics may reveal information about their precipitation conditions, as they have been found to consistently differ in their isotopic composition for modern calcites collected from the same cave (Frisia *et al.*, 2000).

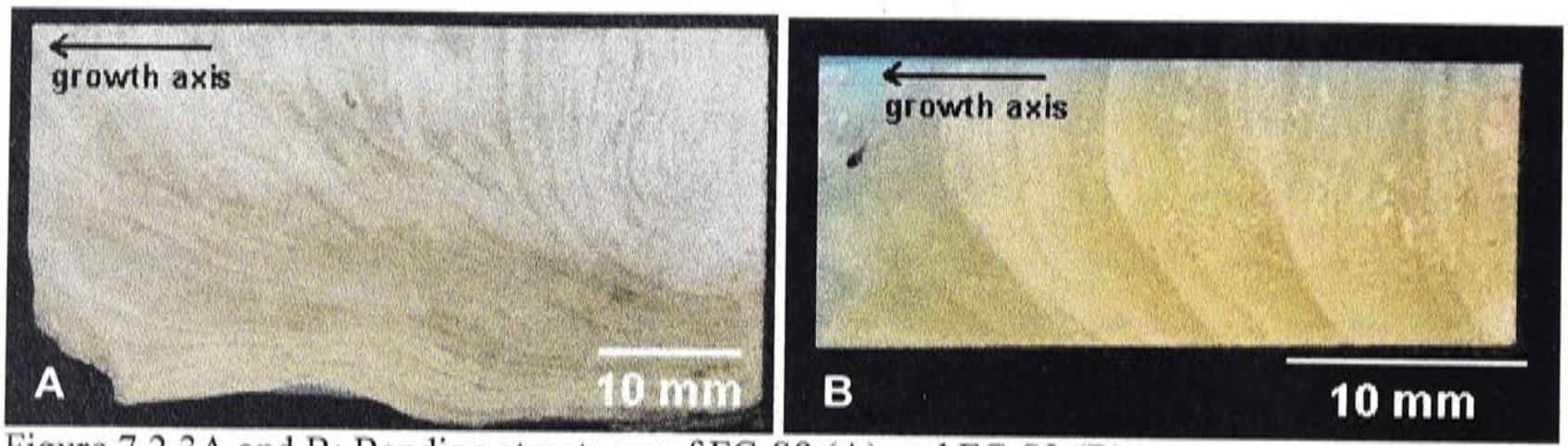

Figure 7.2.3A and B: Banding structures of FC-S8 (A) and FC-S3 (B).

Thin section analysis of FC-S3 and FC-S8 confirmed that the fabric of FC-S8's core consisted predominantly of poorly banded, inclusion-rich calcite where the composite crystals (crystallites) may only be defined by voids between them (Figure 7.2.4A). Moving from the core to its flanks, FC-S8 shows clearer banding, but again only distinguishable by the density of small voids (Figure 7.2.4B). FC-S8 flanks also consist of large crystals (cm's long) radiating out from the centre of the stalagmite. The boundaries of these are clearly seen by their non-uniform extinction under polarised light (Figure 7.2.4B). These distinct, large radiating crystals indicate competitive growth (Frisia *et al.*, 2000).

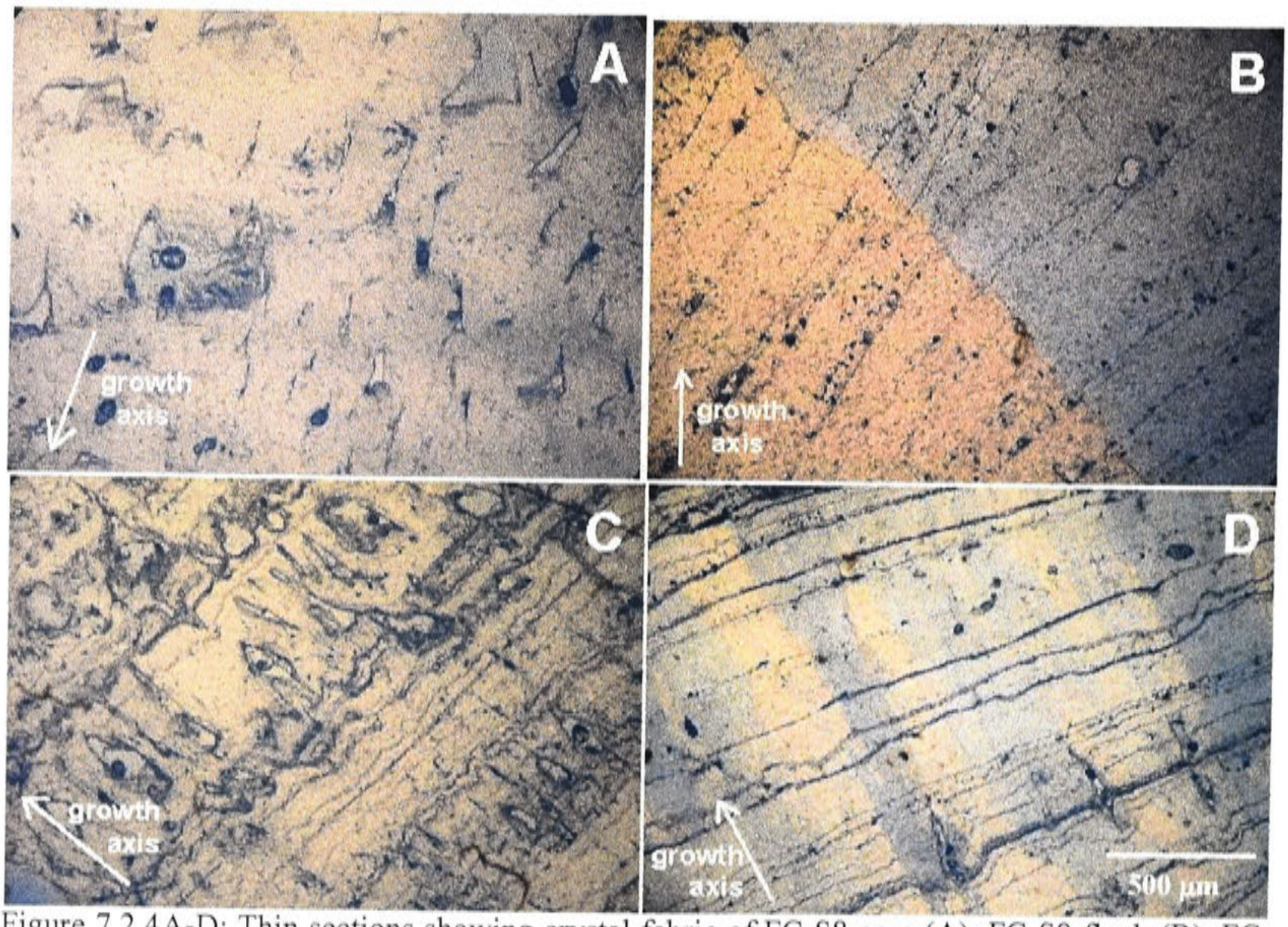

Figure 7.2.4A-D: Thin sections showing crystal fabric of FC-S8 core (A), FC-S8 flank (B), FC-S3 basal core (C) and FC-S3 flank (D).

A thin section which spans the transition from the well-banded translucent calcite to the milky small crystals at the core of the basal section of FC-S3 was made to compare with FC-S8. Figure 7.2.4C shows that the basal core of FC-S3 is rich in voids between crystallites, and the calcite has uniform extinction similar to the core of FC-S8 (Figure 7.2.4A). This contrasts greatly with the fabric above this transition (where most of the stable isotope samples come from) and also on the flanks where composite crystallites with near-uniform extinction, can be seen crossing the growth laminae parallel to the growth axis (Figure 7.2.4D).

Following the descriptions of Frisia *et al.* (2000) FC-S3 fabric, except for its basal core section, may be classified as columnar because of its lower density of voids and lack of competitive growth in the crystallites. The flanks of FC-S8 may be similarly classified as columnar, but its core is microcrystalline based on the density of small crystallites and voids, and the non-uniform extinction due to orientation of composite crystals perpendicular to the local growth surface rather than parallel with the stalagmite growth axis.

From the small population of fabrics studied by Frisia *et al.* (2000), microcrystalline speleothem calcite was found to have slightly lighter $\delta^{18}O_{SP}$ and $\delta^{13}C_{SP}$ values, than the columnar fabrics (Figure 7.2.5). The difference was attributed to the difference in super-saturation state. While both fabrics formed from solutions whose mean super-saturation state was low, the drip-discharge feeding microcrystalline fabric was much more variable and super-saturation similarly fluctuated (Frisia *et al.*, 2000). It was shown by drip-water monitoring that the variation in discharge may be caused by drips feeding through faster flow paths rather than seepage by capillary flow (Frisia *et al.*, 2000). Frisia *et al.* (2000) also suggested that a major factor leading to the formation of microcrystalline fabrics was probably the presence of growth inhibitors, which were present in higher concentrations in these faster through-flow waters. $^{230}Th/^{232}Th$ measurements (Chapter 3, Table 3.4.1) show FC-S8 and FC-S3 have similar allogenic content. However, impurities may also be organic, or simply molecules with a high adsorption affinity for calcite which obscure the crystalline substrate, affecting the continuity of crystal growth (*e.g.* Lebron and Suarez, 1998; Davis *et al.*, 2000; Millero *et al.*, 2001).

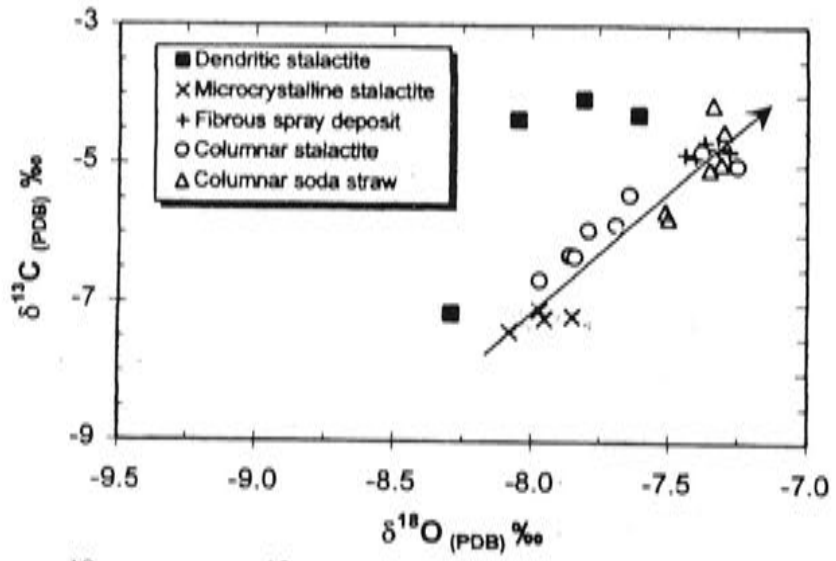

Figure 7.2.5: Variations in $\delta^{18}O_{SP}$ and $\delta^{13}C_{SP}$ for different fabrics of active speleothems from the same Italian Alps Cave. (From Frisia *et al.*, 2000).

It is also suggested here that higher super-saturation waters may precipitate microcrystalline fabric since precipitation will be more rapid, resulting in spontaneous formation of numerous nuclei. These nuclei may coarsen over time (Ostwald ripening; Morse and Casey, 1988 and Chapter 6) resulting in competitive crystal growth rather than slow crystal growth extending the existing crystal face parallel to the growth axis.

Lighter $\delta^{18}O_{SP}$ and $\delta^{13}C_{SP}$ values for kinetically-precipitated calcite compared with equilibrium-precipitated calcite appears non-intuitive. However, it is suggested here that the dominant fractionation is between calcite and bicarbonate ($\alpha_{calcite\text{-}HCO_3^-}$) rather than between bicarbonate and CO_2 ($\alpha_{CO_{2(g)}\text{-}HCO_3^-}$) which occurs under rapid degassing resulting in isotopically heavier HCO_3^-, hence $\delta^{13}C_{SP}$. Kim and O'Neil (1997) have demonstrated that an oxygen fractionation between calcite and bicarbonate under isotopic equilibrium conditions is smaller than under kinetic precipitation resulting in relatively isotopically lighter calcite for kinetic fractionation. The same was found for C (Turner, 1982) but was conte. ed (Romanek *et al.*, 1992). For speleothems, because the C reservoir is much smaller than the O reservoir, then these non-equilibrium effects should be greater for C than for O, as observed in this study. However, since no super-saturation measurements were taken for this study from the former sites of FC-S3 and FC-S8, speculations such as these cannot be resolved. It may be significant, however, that the growth rate of FC-S8 is more than twice that of FC-S3 implying that the precipitation of FC-S8 may be further from equilibrium conditions.

It was intended to further compare FC-S3 and FC-S8 by examining their trace element records, which may have constrained the likely prospect that FC-S8 is affected by

kinetic precipitation. However, several problems were encountered trying to obtain reliable trace element data from FC-S8. The first of these was simply because cutting FC-S8 into small pieces, necessary for mounting, resulted in a greatly fractured (crazed) sample. Epoxy readily seeped into these cracks, easily detected by having stained the epoxy blue. This made the objective of obtaining LA-ICP-MS data of any significant length for FC-S8, very difficult. The small amount of data collected were noisy and no further attempts were made as it was clear that data required to compare with that of FC-S3 could not be obtained. The trace element record of FC-S3 alone will be examined in Section 7.3.

7.3 FC-S3 TRACE ELEMENTS

7.3.1 Results

Trace elements were acquired by LA-ICP-MS using the 5x50 µm slit (Ba, Sr, U, Mg) and the 32 µm spot (Ba, Sr, U, Mg, P, Na). The primary objective of obtaining trace element data here was to examine their behaviour over time, and their relationship with the centennial-scale cycles seen in $\delta^{18}O_{SP}$ and $\delta^{13}C_{SP}$ records. As no attempt was made to closely examine annual cycles, only two parallel tracks were acquired, spaced ~500 µm apart. The purpose of using two tracks was to substitute the data from the second track if the first was affected by mass bias from large fluctuations in Ca counts (this problem is discussed in Chapter 4, Section 4.3.2). Having stated this, annual cycles were detectable in the 5x50 µm data. However, they will only be referred to here as chronological markers, as for year-to-year variability to be confidently examined as for MND-S1, would require many more tracks to be acquired and stacked into a master record. The method used here (2 tracks) was considered sufficient for the questions being investigated.

As indicated above, two laser spot sizes were used to collect trace element data. The twice-smoothed data (18-point Savitsky-Golay) in Figure 7.3.1 shows that the 5x50 µm slit was more suitable for detecting small-scale features *e.g.* the short-lived troughs, which are reduced in range by the averaging effects of the larger spot size for the 32 µm

data. For this reason, much of the analysis focuses on the 5x50 µm data, except where P (32 µm data) is briefly considered.

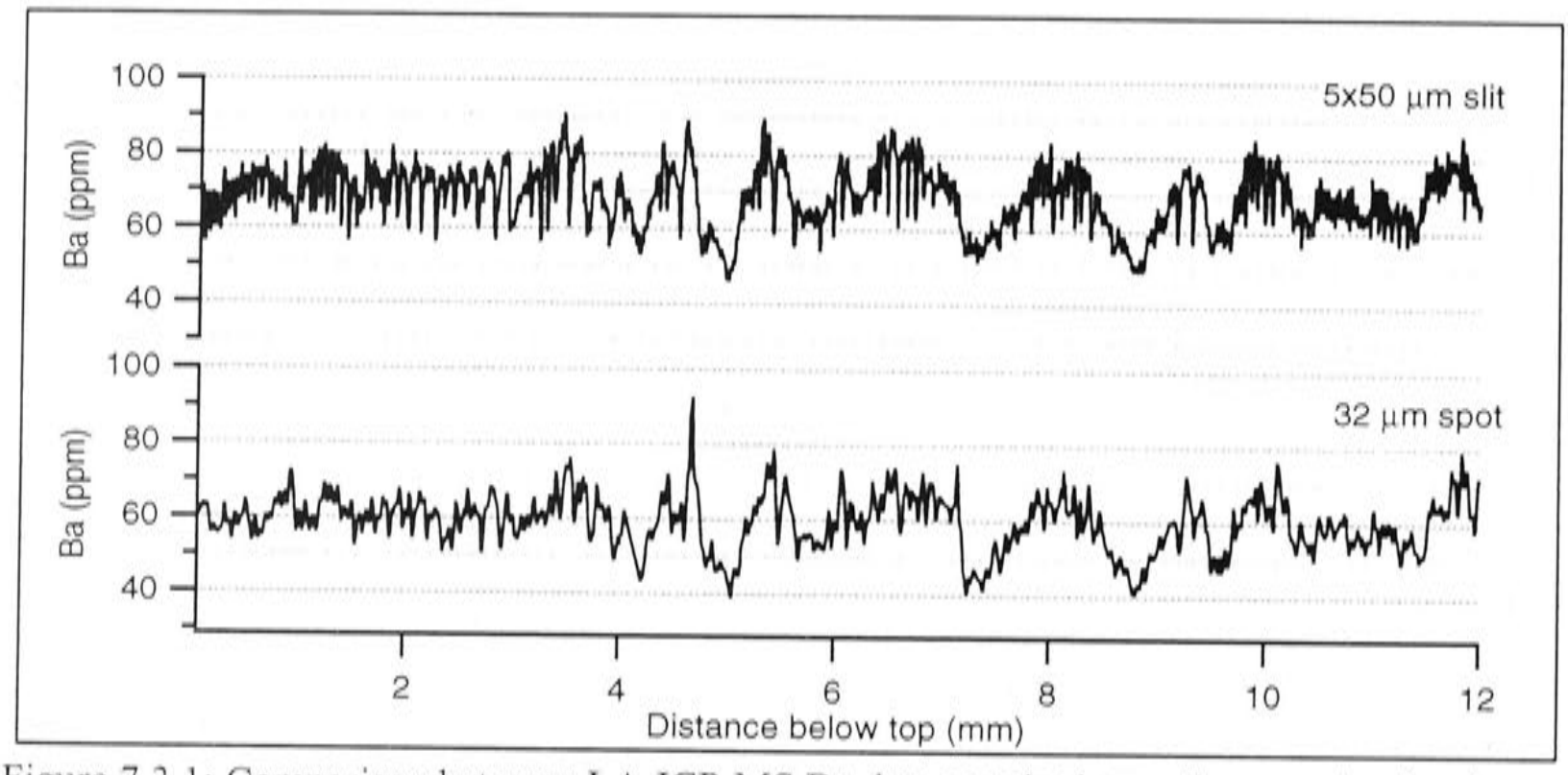

Figure 7.3.1: Comparison between LA-ICP-MS Ba data acquired over the same track using the 5x50 µm slit (top) and the 32 µm spot (bottom).

The LA-ICP-MS data shows clearly resolvable, inphase cycles with wavelengths ranging from ~50 to 150 µm in Ba and Sr (Figure 7.3.2). These cycles are also present for Mg and U but are less clearly resolvable. In the case of U this is due to the relatively low concentration of U in FC-S3 (0.5 ppm). Mg variability is not due to machine sensitivity as Mg concentration in FC-S3 is far above measurement limits, and thus Mg concentration is inherently more variable than other trace elements in FC-S3, as was the case for MND-S1.

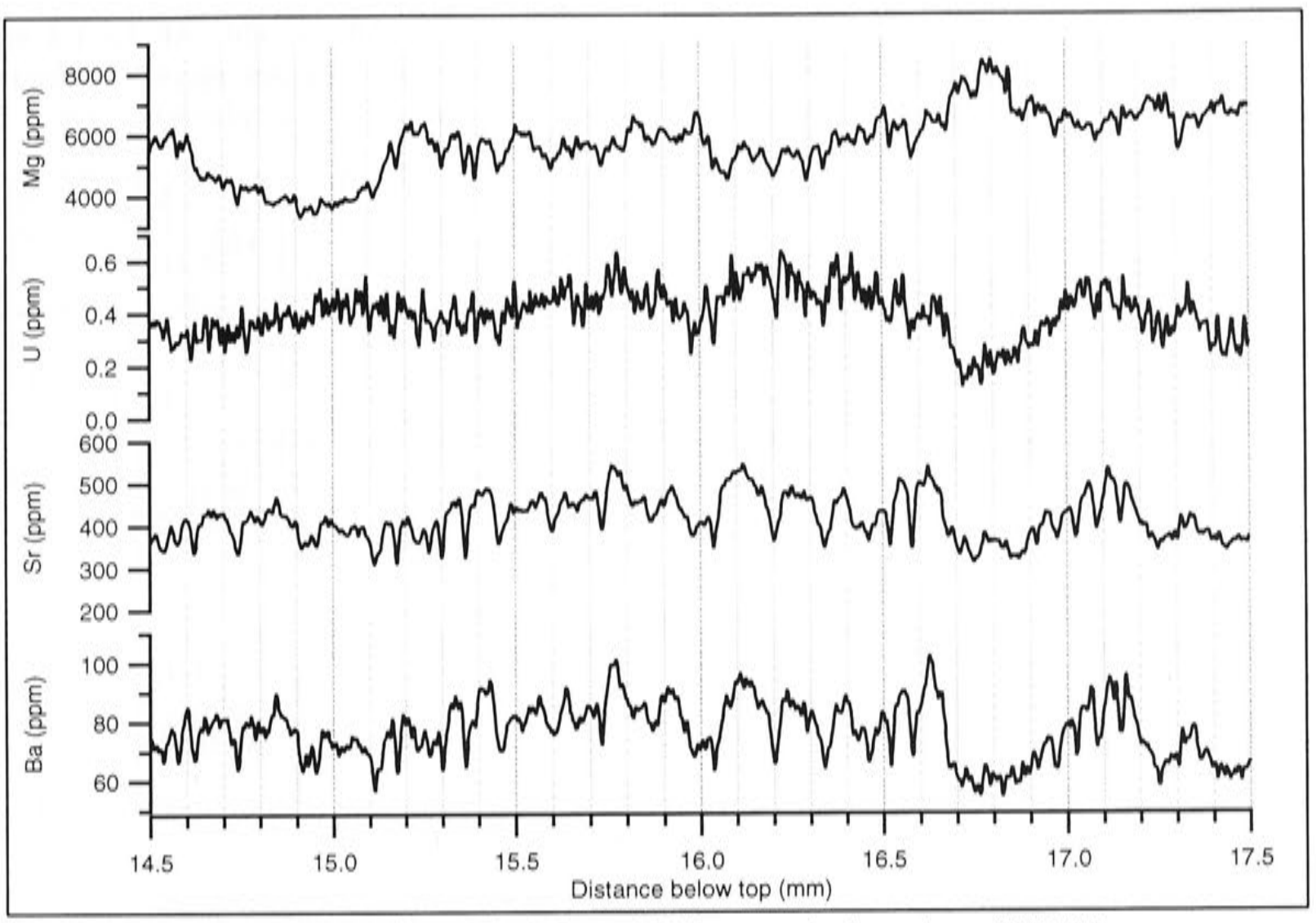

Figure 7.3.2: Annual cycles in Ba, Sr, Mg and U for a typical portion of FC-S3.

Counting Ba cycles on one track reveals 1730 cycles in the topmost 87.5 mm, which represents approximately 1900 years according to the raw U-series chronology. Hence, the trace element data suggest that the basal U-series age may be reasonably accurate, although trace element data below 87.5 mm was not measured to count the cycles over the entire length of the growth axis. This level of agreement, suggests that the Ba cycles and, by inference from the strong correlation of Ba with Sr ($r = +0.69$, $p < 0.001$; Table 7.3.1), the Sr cycles, are annual.

Correlations between Ba with U and Mg are much weaker, $r = +0.30$ and $r = +0.25$, respectively (Table 7.3.1); but stronger between Sr with U and with Mg, $r = +0.58$ and $+0.32$ ($p < 0.01$), respectively. The correlation between Mg and U is moderate, $r = +0.51$ (Table 7.3.1). Figure 7.3.2 shows that Mg may vary from inphase to antiphase with Ba and Sr, both for the smallest resolvable cycles (~50-100 μm) and for higher order trends. The noisier signal of U makes it difficult to examine its phase relationship with the other elements at the sub-annual scale. However, in some parts of the record on the inter-annual scale, U appears to follow the longer-term trends of Ba and Sr rather than Mg (Figure 7.3.2).

Table 7.3.1: Correlations between elements acquired with the 5x50 µm slit. All values are significant ($p < 0.001$, $n = 49063$). Data used are the re-sampled master record produced primarily using one track but substituting data from the adjacent track (see above) where it is affected by low Ca counts.

r	Ba	Sr	U	Mg
Ba	1	+0.69	+0.30	+0.25
Sr		1	+0.58	+0.32
U			1	+0.51
Mg				1

No attempt is made here to perform spectral analysis as was done for MND-S1 as the task of re-interpolating each Ba cycle into 12-points (converting to time domain) is not warranted for the primary objective of examining the broad trends of trace elements, and comparing these with the stable isotopes in FC-S3 (below).

7.3.2 Comparison of long-term trends in trace elements and stable isotopes

Because the trace elements and stable isotopes were taken from adjacent but different sections of the growth axis, there are small variations in the depths at which coeval calcite bands occur. To place the stable isotope and trace elements on a comparable distance, hence age scale, the clearly distinguishable visual bands from the calcite section from which stable isotopes were milled were matched to bands on the trace element mounts. This has shifted the depth, or age scale of some of the stable isotope features slightly, notably the plateau of isotopically heavier $\delta^{18}O_{SP}$ and $\delta^{13}C_{SP}$ from 0.6-0.4 ka to 0.7-0.3 ka. The beginning of this period (0.7 ka) coincides with the prominent trough in Mg, U, Ba and Sr, and a peak in P (Figure 7.3.3).

Broadly, Figure 7.3.3 shows Ba and Sr trends are inphase and strongly correlated ($r = +0.69$, $p < 0.001$; Table 7.3.1). Ba and Sr are inphase with U and Mg, although more strongly resemble U. One difference is Ba concentration is highest between 0.7 and 0 ka, while Sr and U are higher prior to 0.7 ka. Highest Mg concentration occurs between 1.4-0.7 ka, although rise again to a plateau between 0.7 to 0.3 ka. P concentrations (32 µm

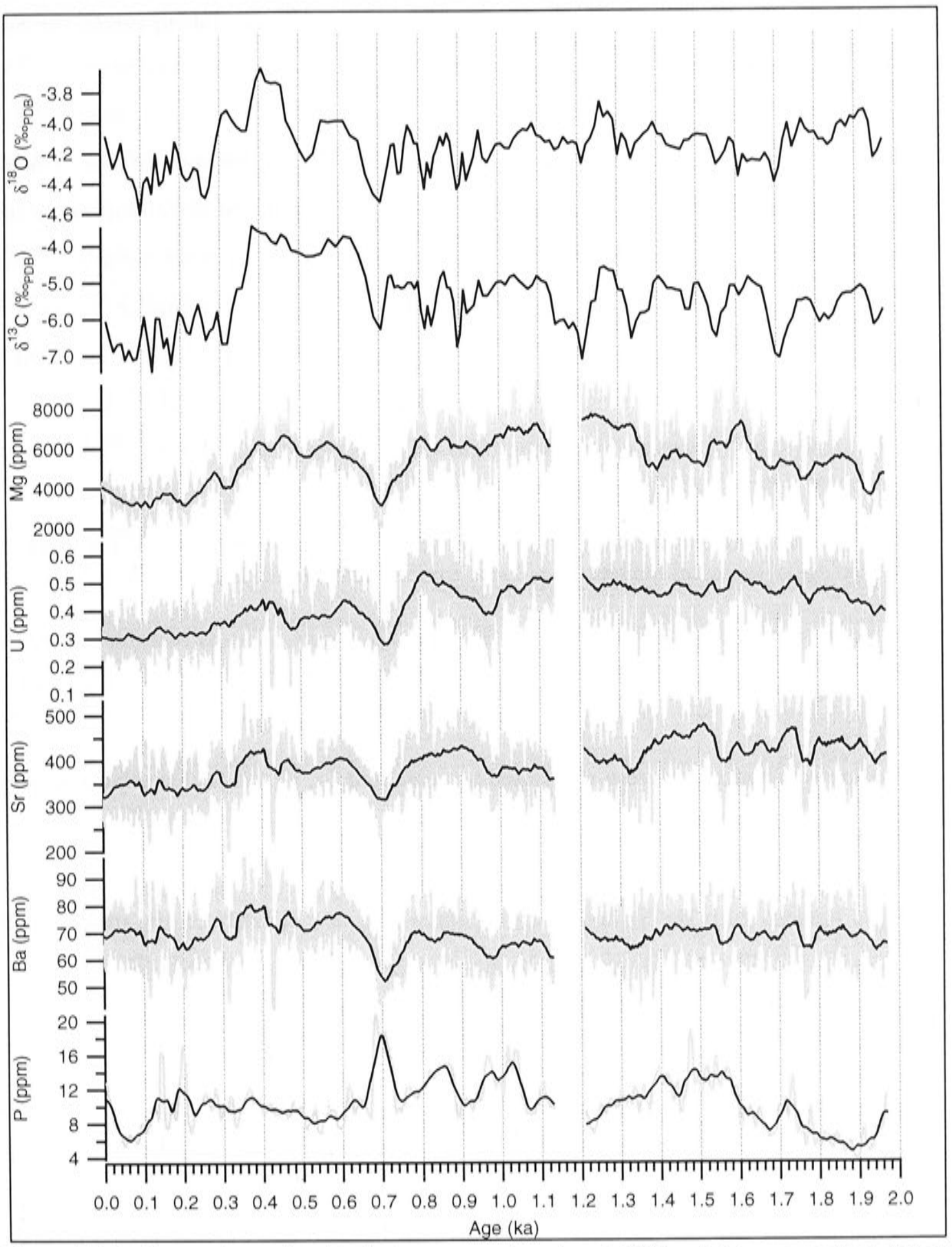

Figure 7.3.3: Comparison of stable isotopes, raw (grey) and 1000-point box-smoothed (black) Mg, U, Sr, Ba (5x50 μm) and P (32 μm) data. (The same box filter was used for P after it had been interpolated to contain the same number of data as the other elements.)

data) are low (average 10 ppm), although the mid-portion of the record, 1.6-0.8 ka is relatively higher and there is a prominent peak at 0.7 ka, which was reproduced in the adjacent track, and coincides with a trough in the other elements and stable isotopes.

Overall correlation coefficients for P are close to zero and not significant, except for Mg which is very weak ($r = +0.13$, $p < 0.001$).

Mg shows the strongest resemblance to $\delta^{18}O_{SP}$ and $\delta^{13}C_{SP}$, because of the similar excursion between 0.7-0.3 ka, which is not as apparent in the other trace elements except for Ba. Ba appears to show some cycling on the order of 100-200 years similar to $\delta^{18}O_{SP}$ and $\delta^{13}C_{SP}$, although the timing of these differs. Mg, U and Sr show a similar depression in mean concentration coincident with the depression in $\delta^{18}O_{SP}$ and $\delta^{13}C_{SP}$ values during 0.3-0 ka. Common to all variables, is the prominent trough (peak for P) at 0.7 ka. Mg, U, Ba and Sr also show suppressed variation following this trough (0.7-0.6 ka).

FC-S3 trace elements display both similar and different trends from those of the modern stalagmite, MND -S1. The common trends are:

- A strong correlation between Ba and Sr, although for FC-S3 this relationship holds for both intra- and inter-annual scales while it was weaker on inter-annual scales for MND-S1.
- U is inphase and moderately correlated with Ba and Sr, although this relationship is weakened occasionally.

The contrasting trends are:

- Mg is inphase with Ba, Sr and U on the inter- and occasionally on the intra-annual scales for FC-S3, while it was antiphase with these elements for MND-S1.
- The lack of any consistent relationship between P and the other elements.

Ba and Sr, determined to be kinetically controlled for MND-S1, are similarly correlated in FC-S3. This suggests that Ba and Sr may also be kinetically controlled here which will be investigated by examining growth rate below. The elements determined to be environmentally driven for MND-S1; Mg, U and P, show distinctly different behaviour for FC-S3. This may in itself support that they are also environmentally controlled for FC-S3 and possible environmental controls will be investigated following the examination of growth rate.

FC-S3 growth rate

FC-S3 growth rate was determined as for MND-S1 by measuring the extension along the growth axis in 5-year intervals (5 Ba cycles). Element variability is shown by, *e.g.* "Ba st.dev.", which is a moving standard deviation window, 300-points wide corresponding to ~5 year window, performed on unsmoothed data, giving a measure of change in the peak-trough range of annual cycles. Figure 7.3.4 shows that mean growth rate is higher, and variable from 0.5-0 ka where Ba is also relatively high and variable. Similarly, Ba is lowest and least variable between 0.8-0.6 ka where growth rate is also low. However, there is no increase in Ba concentration or variability early in the record (2-1.8 ka) where growth rate is high.

Sr also shows strong variability (Sr st.dev.) between 0.5-0 ka coincident with higher and variable growth rate, however, while there is some agreement between Sr variability and growth rate, Sr concentration does not appear to be strongly related to growth rate *e.g.* Sr concentration is relatively low between 0.5-0 ka. Thus similar to MND-S1, growth rate and Ba show a relatively strong trend, and while Sr shows a weaker trend with growth rate, suggesting Ba may also be kinetically controlled for FC-S3, but Sr less so.

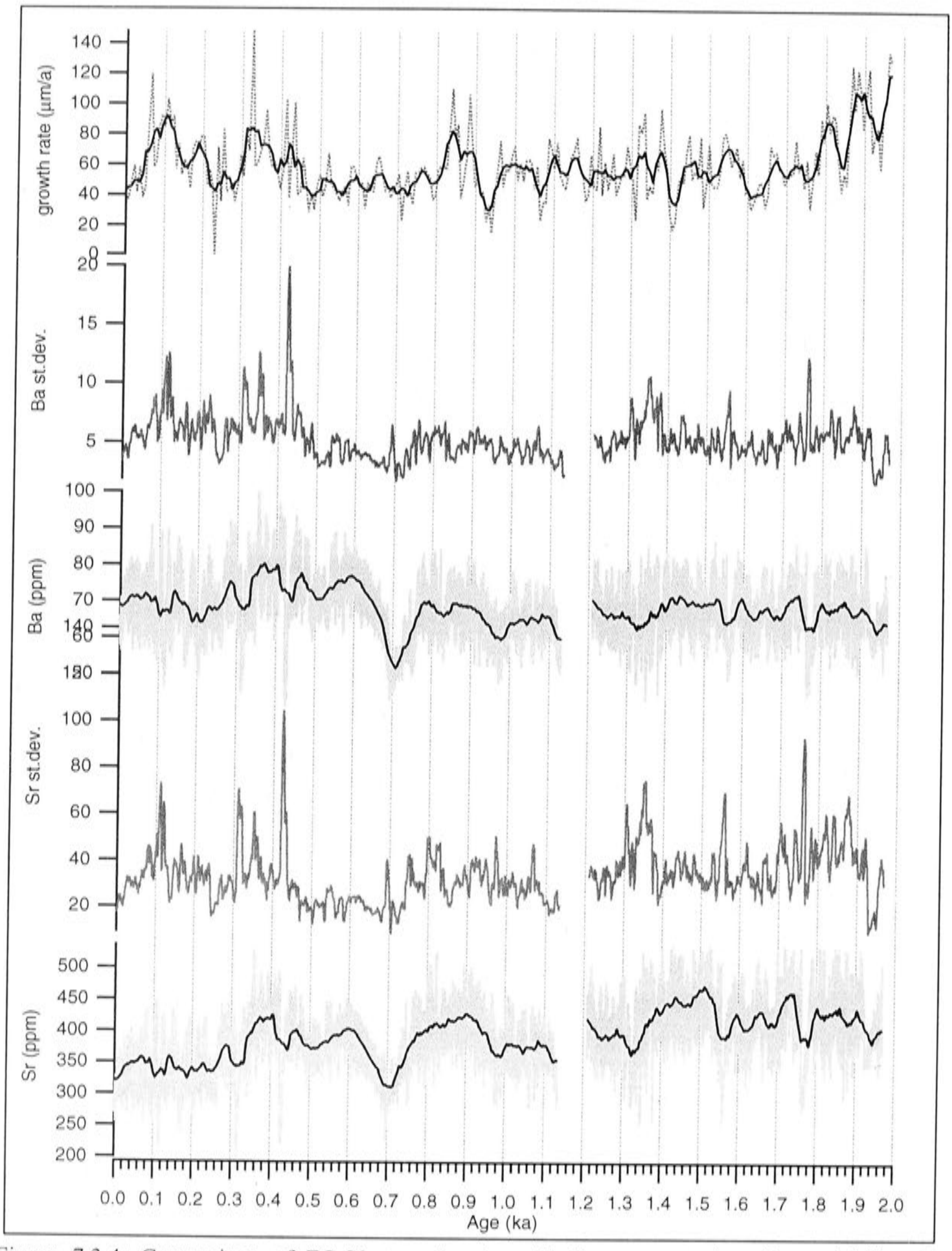

Figure 7.3.4: Comparison of FC-S3 growth rate with Ba concentration, Ba variability, Sr concentration and Sr variability. (Variability, "st.dev.", is expressed as a 300-point moving standard deviation window. Grey lines are raw data, black are 1000-point box smoothed data for concentrations.)

The relationship between trace elements and visual banding pattern also was investigated. FC-S3 contains clear, distinct visual laminae ~200 to over 1000 µm wide, which are characterised by colour changes from translucent yellow to smokey-grey, and occasional opaque cream bands (Figure 7.2.3B). The number of bands was counted and their band width measured using a dendrochronometer at the NWG Macintosh Centre for Quaternary Dating at the University of Sydney as part of this author's Honours thesis (Treble, 1998). The visual bands were determined not to be annual, as the number counted, 435, was far fewer than the age of FC-S3 suggested by U-series age measurements (3.67 ± 0.21 ka, see Chapter 3, Table 3.4.1).

These measurements, shown in Figure 7.3.5 below, do show that the visual bands have increased in width episodically through time. The most distinct of these are the episodes between 2.5-1.5 ka, 1.5-0.9 ka and also 0.9-0 ka, where mean band widths increased from 209, 347 and 464 µm, respectively; which are greater than the mean width in the earliest section 3.7-2.5 ka (130 µm). The section 0.6-0 ka consists of highly variable visual laminae width, which corresponds with the episode of highest variability in Ba (peak-trough) variation and growth rate (Figure 7.3.4), although there is no correspondence between Ba wavelength and visual banding.

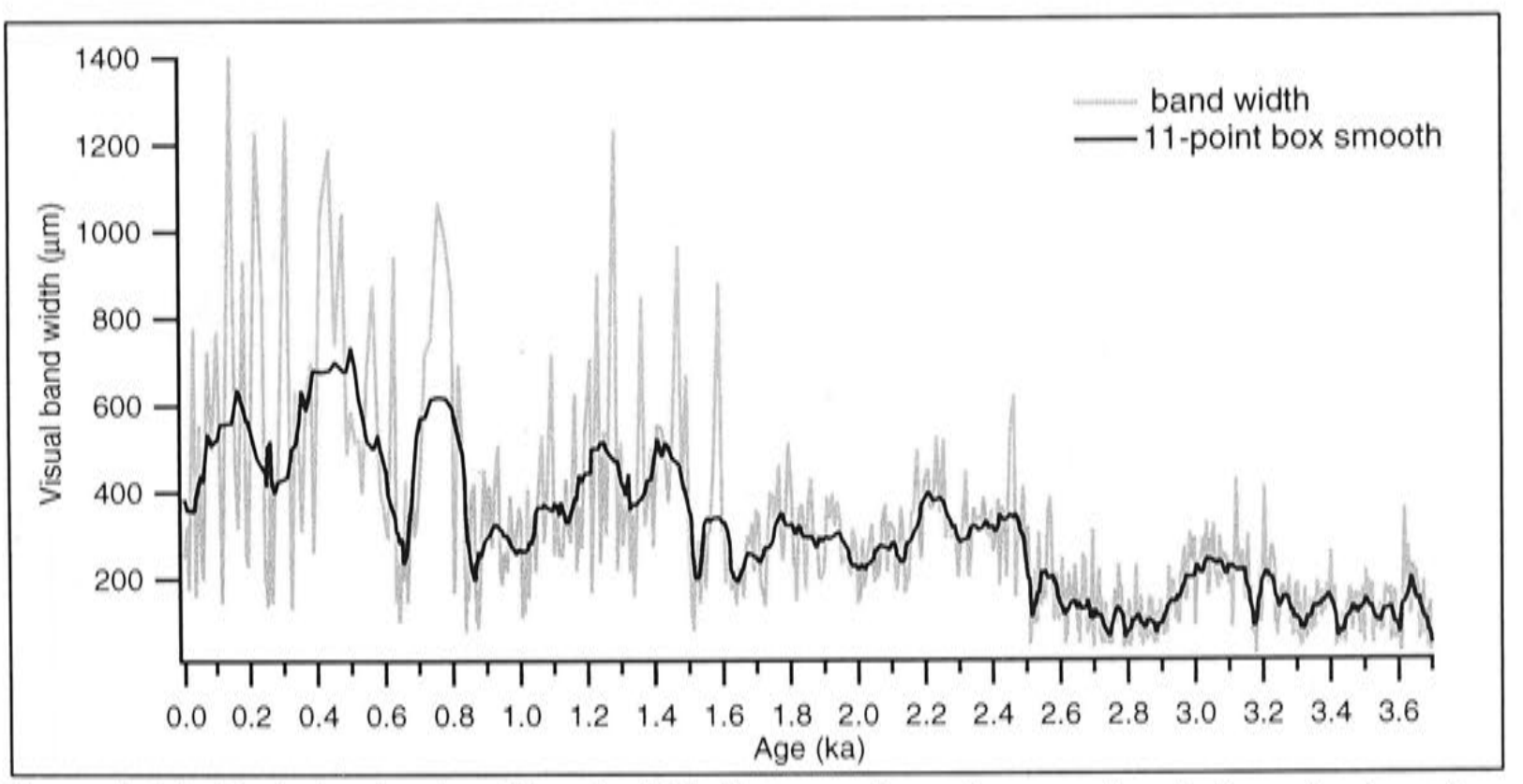

Figure 7.3.5: Variation in visual band width distance along the growth axis from the top of FC-S3.

Mg, U, P and stable isotopes

The annual Ba cycles were used to re-adjust the chronology to allow the age of the excursion in stable isotopes and trace elements to be more confidently determined. Tightening the chronology allows suspected environmental variables, $\delta^{18}O_{SP}$, $\delta^{13}C_{SP}$, Mg, U and P to be examined in a historical context. The section containing the $\delta^{18}O_{SP}$ and $\delta^{13}C_{SP}$ excursion (youngest 600 years or formerly 0.8 ka) was concentrated on, as it is the only part of the record where all proxies appear to be commonly affected.

Comparing the annual Ba cycles with the radiocarbon results gives the opportunity to investigate the accuracy of radiocarbon age modelling, which had placed the top of FC-S3 at A.D.1980 ± 15 years A.D. (Chapter 3, Section 3.5). Figure 7.3.6 shows that there are approximately 40 Ba cycles between the period of inferred catchment disturbance and the cessation of FC-S3 growth. This eliminates A.D.1976 as the beginning of the disturbance event as FC-S3 was collected in A.D.1996, and leaves A.D.1934 or 1948 (bushfires) as the remaining possibilities, which implies that FC-S3 ceased growing in either ~A.D.1974 or 1988, both which are within the upper constraint of post-A.D.1956 and agree with the modelled estimate of A.D.1980 ± 15 years. These dates are close to the time when all vegetation above Frankcombe Cave was cleared, and soil cover greatly disturbed by logging and regeneration fires (A.D.1976-1978) suggesting this may have caused FC-S3 to cease growing.

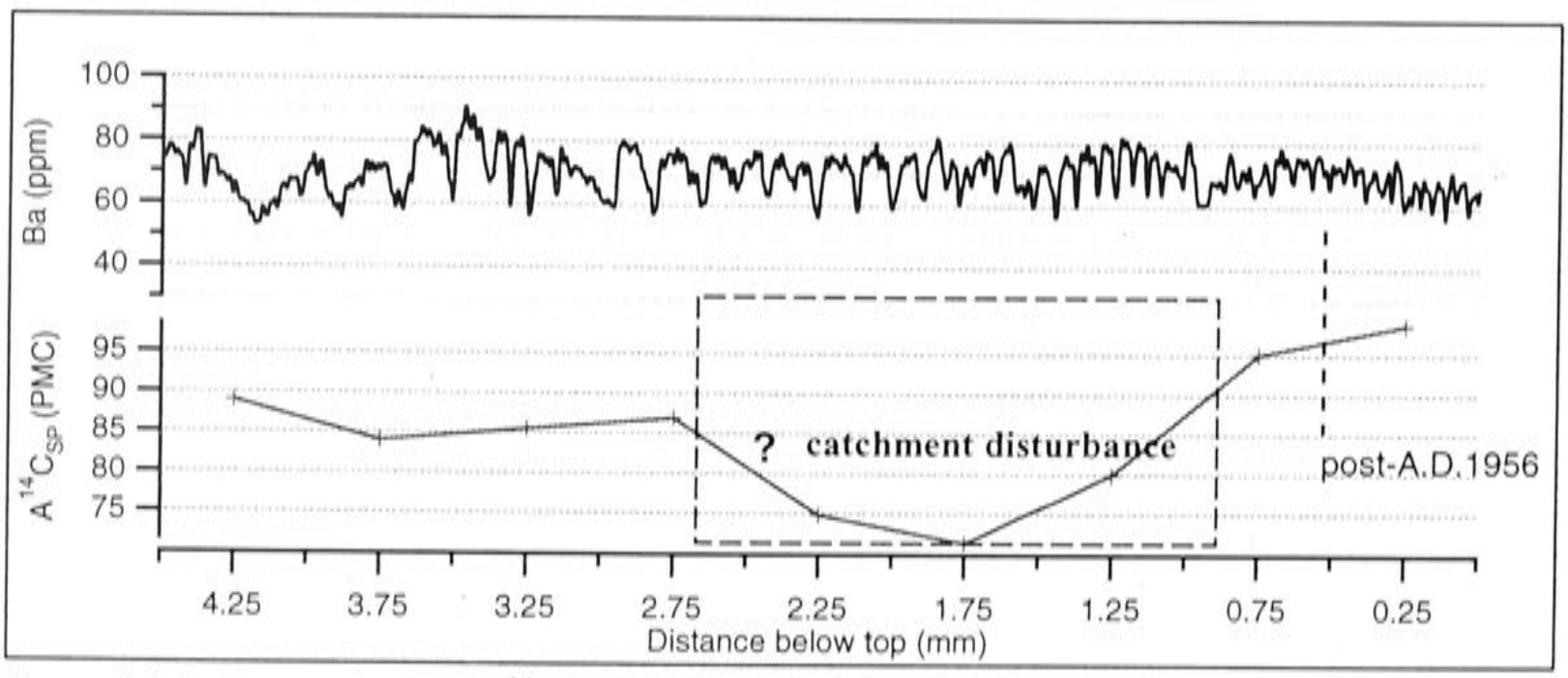

Figure 7.3.6: Comparison of $A^{14}C_{SP}$ measurements with Ba annual cycles.

Figure 7.3.7 shows the stable isotope and trace element data on the newly adjusted age-scale. This places the excursion in $\delta^{18}O_{SP}$, $\delta^{13}C_{SP}$, Mg and U at A.D.1450-1770 for

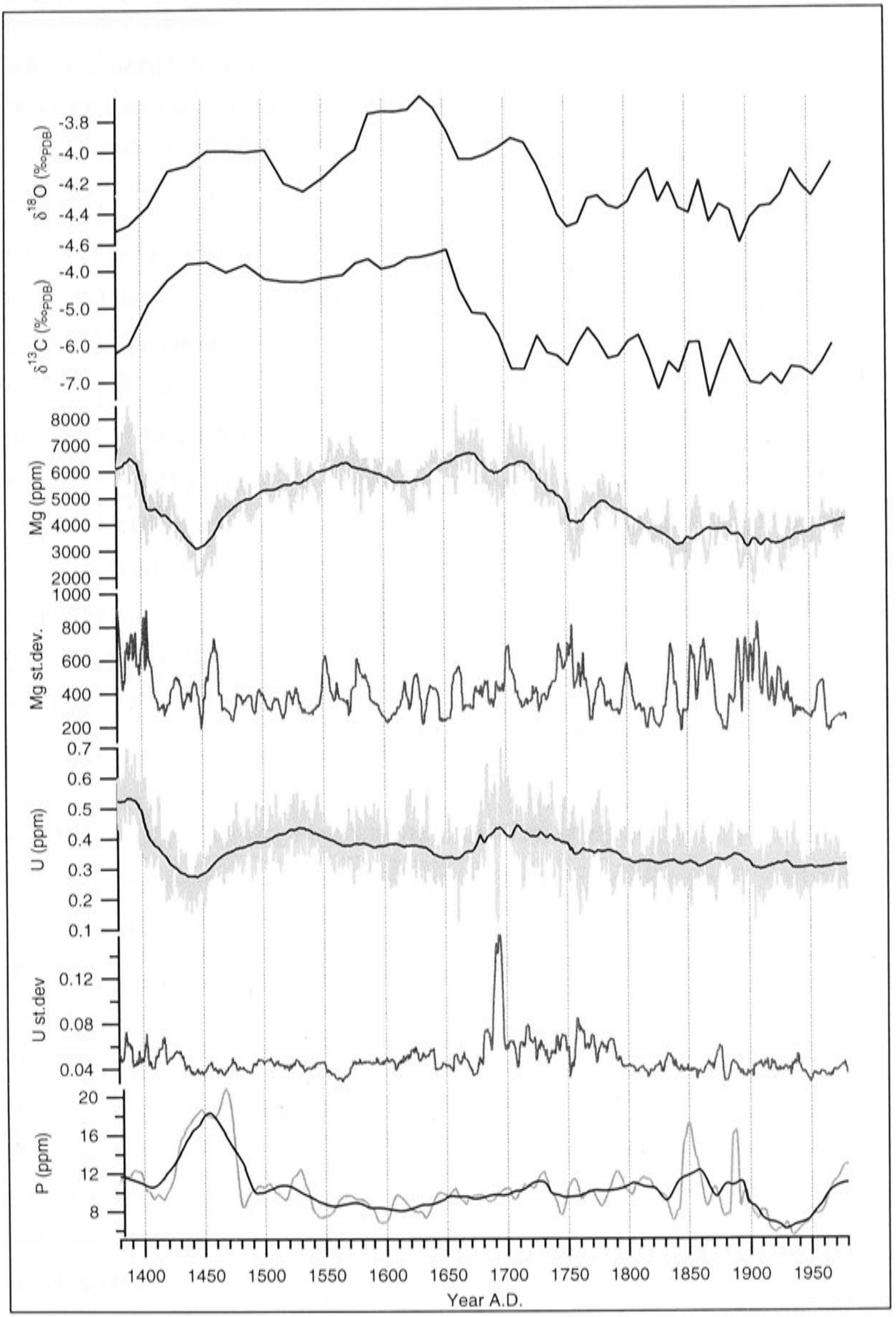

Figure 7.3.7: $\delta^{18}O_{SP}$, $\delta^{13}C_{SP}$, Mg, Mg variability, U, U variability and P shown on new age scale determined by annual Ba band counting. (Grey indicate raw, black indicate 1000-point box smoothed element concentrations. Variability is 300-point moving standard deviation window.)

$\delta^{13}C_{SP}$, Mg and U and A.D.1450-1790 for $\delta^{18}O_{SP}$, both prior to European settlement in Australia, and of a long enough duration, that short-term catchment disturbances such as fires may be ruled out. It is thus likely that this period must be due to a shift in the climate regime lasting around 350 years.

The $\delta^{18}O_{SP}$ excursion between A.D.1450 and 1790 to isotopically heavier values is too great to be temperature (~1‰ = 4.2°C) and thus most likely reflects a rainfall signal. Following the arguments of Chapter 5, an increase in $\delta^{18}O_{SP}$ may reflect a shift to lower rainfall as the isotopic signature of rainfall, $\delta^{18}O_P$, in southern Australia is negatively correlated with rainfall amount, driven by proximity to the passage of low pressure systems. This interpretation is consistent with higher $\delta^{13}C_{SP}$ and Mg if these variables represent residence time of drip-water in the limestone as argued for MND-S1 (Chapter 6). This possibility is supported by a reduction in Mg variability (Figure 7.3.7). A reduction in the annual range of Mg in drip-water is consistent with a reduction in the annual range of rainfall, most likely a decrease in winter rainfall as suggested by isotopically heavier $\delta^{18}O_{SP}$ values. Drier conditions are also supported by the broad reduction in FC-S3 growth rate over this period (Figure 7.3.4).

The cause of the $\delta^{13}C_{SP}$ excursion was further investigated by Sr isotope analysis, to test whether the $\delta^{13}C_{SP}$ signal was moving between seawater and limestone end-members, as these have distinct $^{87}Sr/^{86}Sr$ values, 0.70913 and 0.70860, respectively (Banner *et al.*, 1996). Sr isotopes measurements by TIMS (Chapter 4, Section 4.5) were performed on aliquots of the samples milled for stable isotope analysis. Figure 7.3.8 shows that the $^{87}Sr/^{86}Sr$ track very closely with $\delta^{13}C_{SP}$ between 2-0 ka, including the 0.7-0.3 ka excursion, however, there are exceptions to this trend, marked by black rings on the data points. For the 1.2-0 ka period, $^{87}Sr/^{86}Sr$ measurements closely track $\delta^{13}C_{SP}$ although two are slightly heavier. Nonetheless, these values indicate that more limestone was dissolved during the $\delta^{13}C_{SP}$ excursion. This supports that rainfall recharge was lower between A.D.1450-1790 allowing cycles of limestone re-dissolution following prior-calcite precipitation.

The behaviour of U and Mg differ from MND-S1 as they were negatively correlated for MND-S1, while they are positively correlated for FC-S3 (Figures 7.3.3 and 7.3.7). The

explanation for this may simply lie in the low P concentration of FC-S3 (Figures 7.3.3 and 7.3.7). A scarcity of P may reduce the importance of uranyl scavenging by phosphate ions and thus may not dominated the U trend in FC-S3. This may leave U to be controlled by other mechanisms, possibly prior-calcite precipitation, which is consistent with U's resemblance to Sr and Mg (Figure 7.3.3).

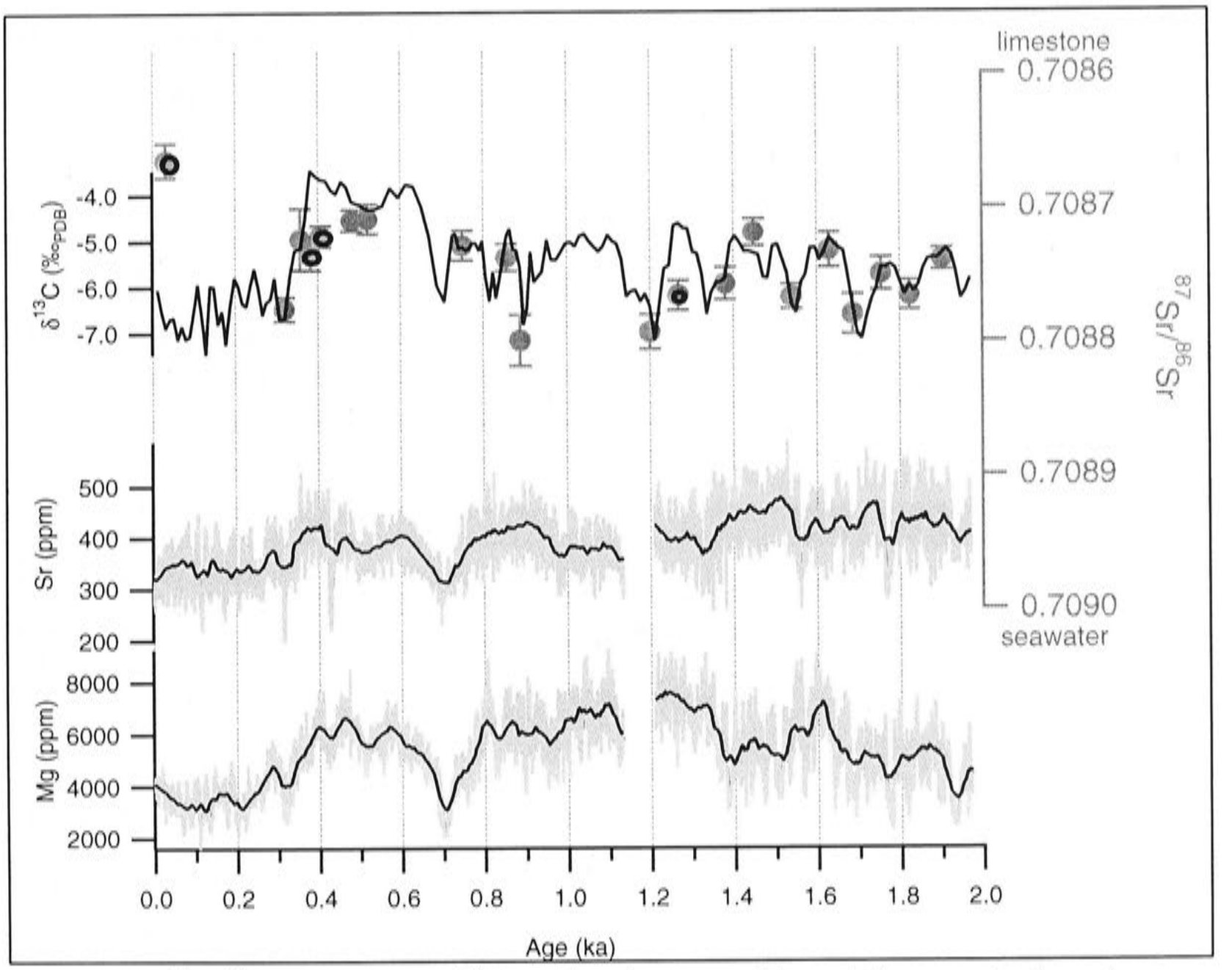

Figure 7.3.8: $^{87}Sr/^{86}Sr$ plotted over $\delta^{13}C_{SP}$. Also shown are Mg and Sr concentration where grey is raw and black is 1000-point box smoothed data. Black rings indicate poorer agreement between $^{87}Sr/^{86}Sr$ and $\delta^{13}C_{SP}$.

The most harmonious interpretation between trace elements and stable isotopes is that the period A.D.1450-1790 was drier. While there is no instrumental or historical records to confirm this (Tasmania was settled after A.D.1788), this period is close in age to the Little Ice Age (LIA), a period clearly documented for the Northern Hemisphere, but beginning ~100 years later than the FC-S3 excursion (A.D.1550-1850; Lamb, 1977; A.D.1600-1850; Grove, 1988), but more sparsely recorded in the Southern Hemisphere (Thompson *et al.*, 1986; Gellatly *et al.*, 1988; Kreutz *et al.*, 1997; Morgan and van Ommen, 1997; Holgren *et al.*, 1999; Hendy *et al.*, 2001).

7.4 DISCUSSION

The most interesting feature of the FC-S3 record is the excursion to higher values of $\delta^{18}O_{SP}$, $\delta^{13}C_{SP}$, Mg and low growth rate, argued above to represent drier conditions between A.D.1450 and 1790, which begins earlier but overlaps with New Zealand glacier advance and the Northern Hemisphere constrained LIA. A LIA period in south-central Tasmania characterised by drier and possibly cooler conditions is unexpected, since records from elsewhere in the mid to high southern latitudes suggest either no change or possibly wetter conditions. These are:

- No marked changes during this period in Tasmanian tree-ring reconstructions (Cook *et al.*, 1992; 2000);
- Advanced New Zealand glaciers indicating a possibly wetter climate (Grove, 1988; Gellatly *et al.*, 1988).

The Tasmanian tree-ring reconstructions come from the relatively long-lived Huon Pine species in the Mt Read area, 107 km northwest of Frankcombe Cave. Warm-season temperatures have been reconstructed back to 1600B.C. from ring-width measurements (Figure 7.4.1; Cook *et al.*, 1992; 2000). The record accounts for 47% of the growing season (November-April) temperature variability and has been used in Southern Hemisphere temperature reconstructions (Mann *et al.*, 1998; Jones *et al.*, 1998; 2001). The record indicates approximately 1°C variation, largely on decadal scales, for the past 1.1 ka but evidence for the LIA is lacking. One possible indication of an LIA signal, is the suppression of decadal variability during A.D.1500-1900, which succeeds a persistent warm period from A.D.900-1500, although Cook *et al.* do not draw attention to this as a possible LIA signal. The FC-S3 record shows that the variability in Mg and possibly in U are much greater for 2.0 ka to A.D.1450 (Figure 7.3.7) and relatively suppressed after A.D.1450 which may indicate a signal common with the tree record.

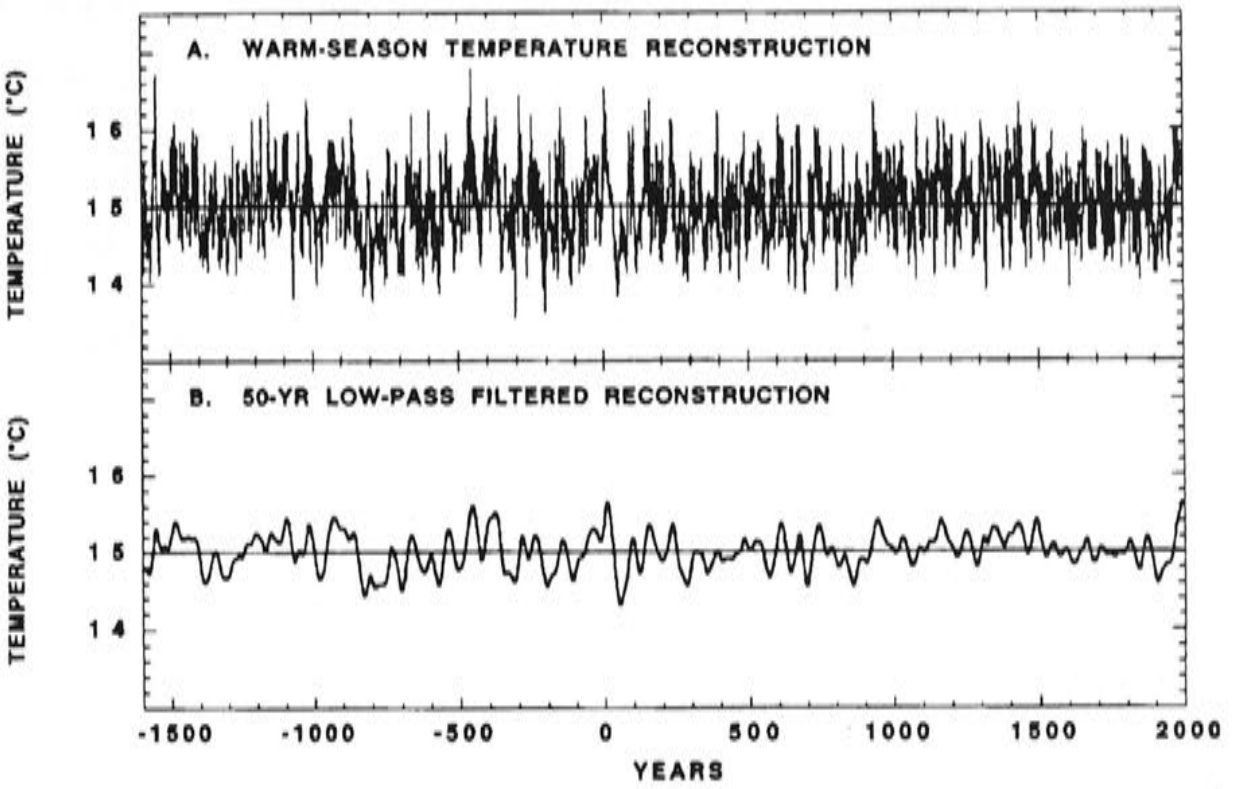

Figure 7.4.1: Warm-season temperature reconstructed from Mt Read tree ring record. (From Cook *et al.*, 2000.)

One would not necessarily expect a close agreement between Tasmanian dendroclimatic records and FC-S3, because they are summer and winter biased, respectively; and a stronger winter expression of the LIA signal has been argued for east Antarctic ice cores (Morgan and van Ommen, 1997). It is also reasonable to expect FC-S3 may be more sensitive to LIA conditions, particularly a reduction in winter rainfall, as Frankcombe Cave (260 m asl) in the lee or rain-shadow side, of Mt Read on the West Coast Range.

Comparing evidence across the Tasman Sea, a drier LIA scenario in Tasmania appears inconsistent with the extended west coast glaciers of New Zealand (Grove, 1988; Gellately *et al.*, 1988). Considerable debate existed over whether this glacier advance was precipitation or temperature dominated (Hessell, 1983; Gellately et al. 1988 ~~and Norton~~, 1988). However, later interpretations appear to have resolved this, concluding that cooler temperatures both in summer and winter, induced by changes in the atmospheric circulation are primarily responsible (Fitzharris *et al.*, 1992; 1999). One interesting feature in the investigation of Fitzharris *et al.* is the atmospheric circulation patterns shown for the analogous, but smaller advance of the Franz-Josef glacier during the A.D.1980s. These circulation conditions were a stronger than normal high-pressure cell extending over Australia and into the Tasman Sea, that enhanced southwesterly flow over South Island New Zealand (Figure 7.4.2A-B). This strengthened southwesterly flow reduced summer ablation rates by cooler temperatures and/or greater cloudiness.

Interestingly, the winter circulation pattern that dominated the Franz Josef glacial advance in the A.D.1980s, and argued by analogy to have predominated during the LIA (Fitzharris *et al.*, 1992), is characterised by zonal flow (Figure 7.4.2), which, in this study (Chapter 5), has been shown by rainfall $\delta^{18}O_P$ event analysis to deliver rainfall that is lower and isotopically heavier than average, hence produce heavier speleothem $\delta^{18}O_{SP}$ consistent with the observations of FC-S3.

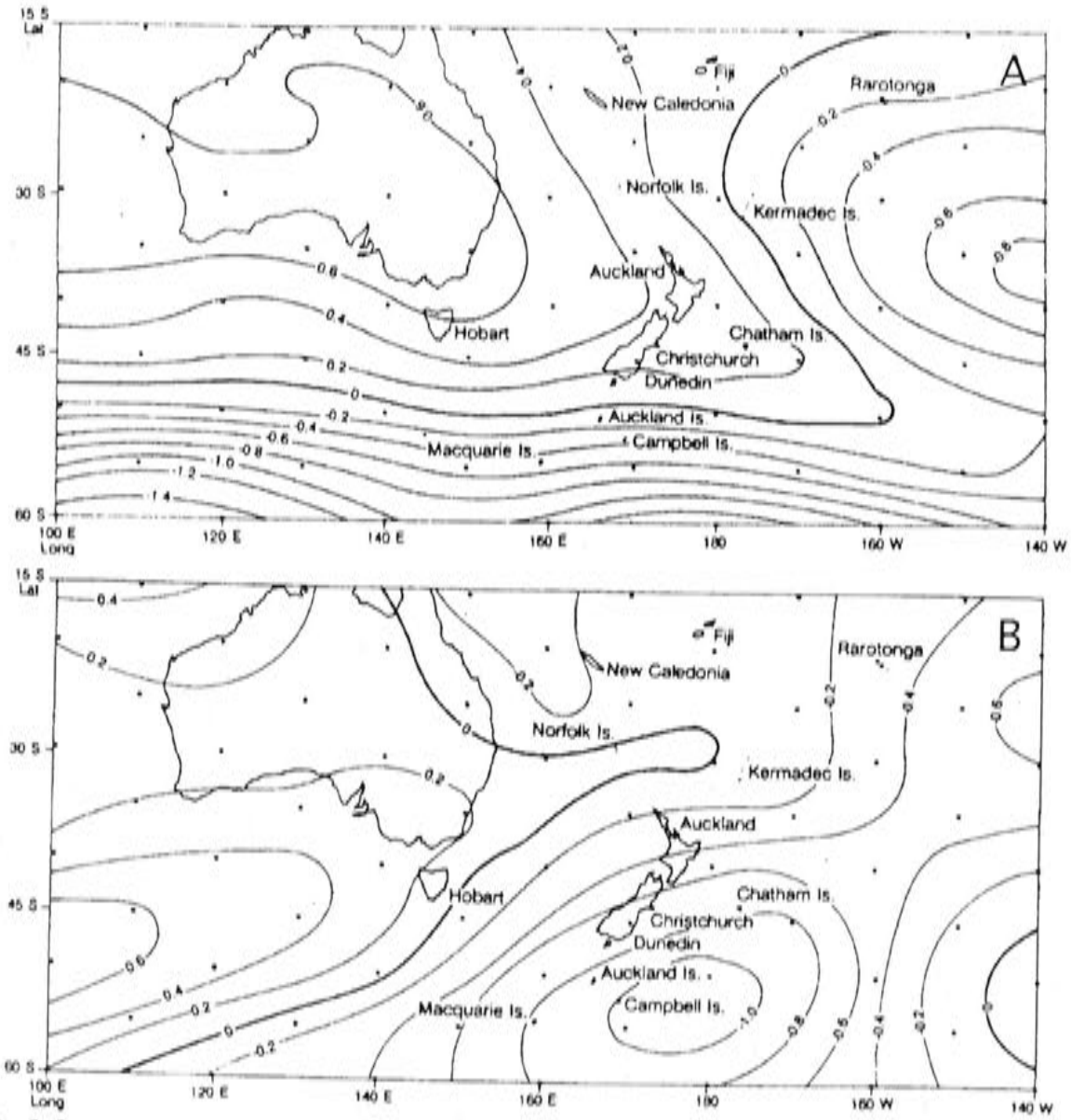

Figure 7.4.2A-B: Mean synoptic patterns for winter (A) and summer (B) for 1980-1989 during an extension of the Franz-Josef glacier. (From Fitzharris *et al.*, 1992.)

Thus, comparing these reconstructions suggests a synoptic pattern that could produce drier conditions in Tasmania, while favouring glacier advance in South Island, New Zealand. The consistency of this comparison further support that the mid-latitudes of the Southern Hemisphere were dominated by zonal flow conditions during the LIA.

Evidence for drier conditions elsewhere in Australia during the LIA comes from lower latitudes at the Great Barrier Reef (Hendy *et al.*, 2002). Here, a 420-year multi-proxy record constructed from corals show warmer regional sea-surface temperatures during A.D.1565-1700 and higher sea-surface salinity from A.D.1565-1870. Hendy *et al.*,

propose that the higher salinity results from greater evaporation, suggested to be from strengthened trade wind circulation. However, as these periods begin and end nearly 100 years after the excursion seen in FC-S3, which is well-outside the age uncertainty of either record, may not share common climate mechanisms. It is nonetheless encouraging that both records suggest that drier conditions predominate in Australia within the wider bracketing age span of the northern Hemisphere LIA.

7.5 SUMMARY

The FC-S3 2.4 ka speleothem stable isotope and 2.0 ka trace element record indicates a shift to drier conditions between A.D.1450-1790, a period beginning and ending earlier than, but overlapping the LIA recorded in Great Barrier Reef corals, New Zealand glacier advance, east Antarctic ice cores and many sites globally. This record was unable to be reproduced with the coeval FC-S8 record from the same cave, as the FC-S8 record appears to be affected by non-equilibrium precipitation conditions.

The conflict between the LIA expression in Tasmania and the absence of any signal in the well-established tree-ring records suggest the LIA in Tasmania is restricted to lower winter rainfall. A LIA suggested to represent lower winter rainfall is supported by a synoptic study over the period of glacier advance in the 1980s, which shows that the enhanced zonal flow through this region would be able to produce concurrent meteorological conditions that were drier in Tasmania, but favoured glacial advance in New Zealand. It is proposed here that the LIA in the mid-latitudes of this Southern Hemisphere region, experienced a similar period of enhanced zonal flow, reducing rainfall on the west coast of Tasmania while permitting glacier advance across the South Island of New Zealand.

CHAPTER EIGHT

PLEISTOCENE SPELEOTHEM RESULTS AND DISCUSSION

8.1 INTRODUCTION

Oxygen has been the key element for palaeoclimate reconstruction from speleothems. Its isotopic composition in speleothem calcite ($\delta^{18}O_{SP}$) is dependent on the isotopic composition of its meteoric rainfall ($\delta^{18}O_P$) and also the cave temperature (Chapters 2, 6 and 7). Thus, speleothems are potentially a record of both temperature and rainfall variations, which may be expressed in a simple equation as follows:

$$\Delta\delta^{18}O_{SP} = {}^{1}\Delta\delta^{18}O_{cave\text{-}temperature} + \Delta\delta^{18}O_P \; {}^{2}[+ \Delta\delta^{18}O_{ice\text{-}volume}] \qquad (8.1.1)$$

[1]May be calculated using the known fractionation factor for inorganic precipitated calcite (-0.24‰/°C; McCrea, 1950). [2]The isotopic shift in sea-water due to continental glacier building, $\Delta\delta^{18}O_{ice\text{-}volume}$, is an additional parameter for glacial periods (~1.1‰, see Shrag *et al.*, 1996).

In the earliest speleothem study, Hendy and Wilson (1968) created a palaeotemperature record from a $\delta^{18}O_{SP}$ record (Figure 8.1.1A-B) using Equation 8.1.1 and a key assumption; that the $\delta^{18}O_P$ at their site obeyed a simple global relationship between $\delta^{18}O_P$ and site temperature (+0.69‰/°C; Dansgaard, 1964) and that this relationship was constant for the growth period of the speleothem. Consequently, $\delta^{18}O_{SP}$ is considered to be driven by two competing temperature effects, a meteoric dew-point temperature effect which is positive (+0.69‰/°C) and the cave temperature effect, which is negative (-0.24‰/°C). As the two effects are opposite in sign, the net effect on $\delta^{18}O_{SP}$ may be positive, negative or neutral depending on the magnitude of the temperature changes (Chapters 1 and 2, Sections 1.3 and 2.1). Schwarcz (1996) defined this net behaviour of $\delta^{18}O_{SP}$ as speleothem γ where $\gamma = d\delta^{18}O_{SP}/dT$, to indicate whether the meteoric rainfall (positive γ) or cave temperature effect (negative γ) was dominant.

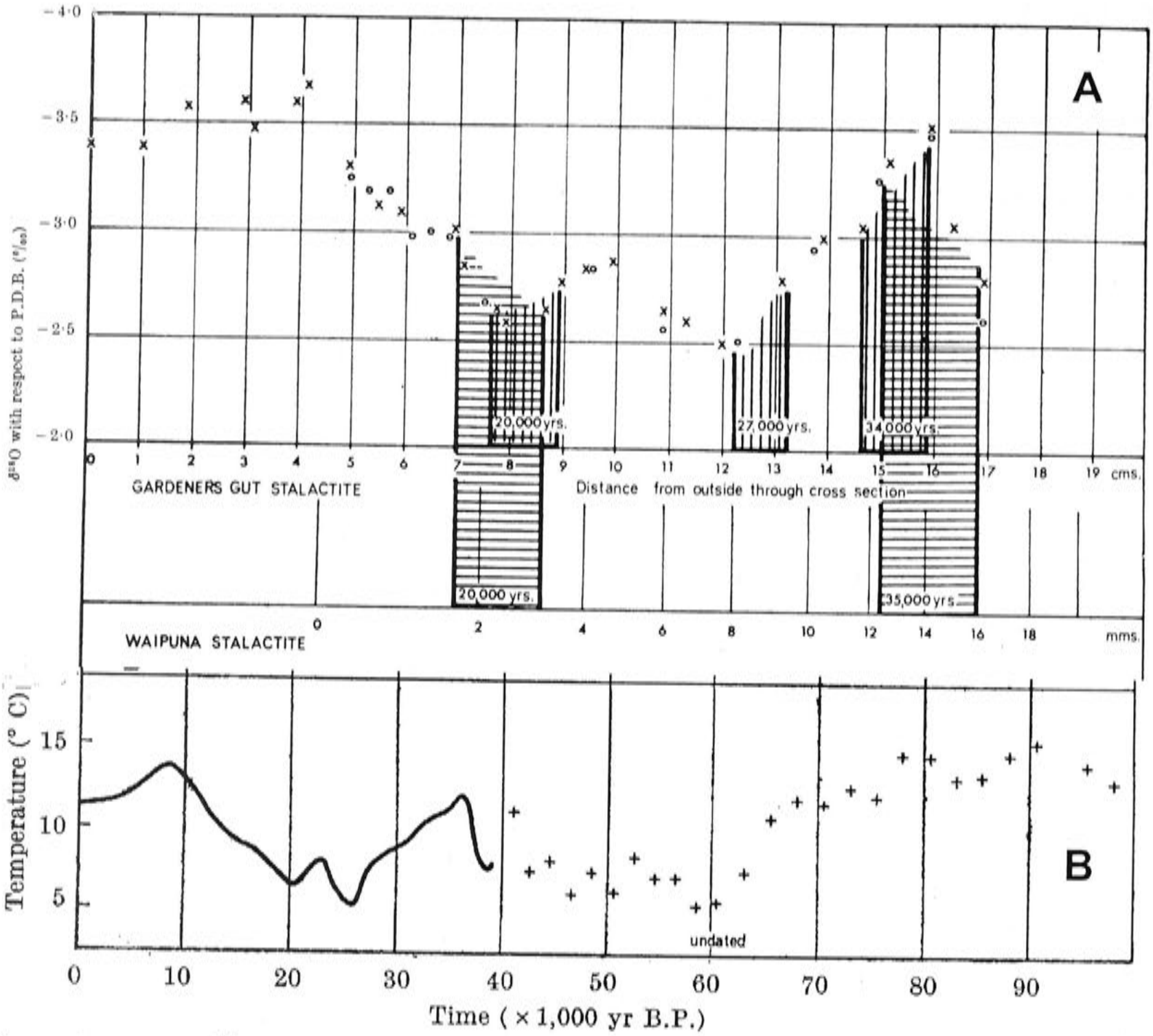

Figure 8.1.1A-B: $\delta^{18}O_{SP}$ record (A) converted to palaeotemperature (B) for North Island, New Zealand. (From Hendy and Wilson, 1968.)

The assumption that Dansgaard's relationship, +0.69‰/°C holds true at any one site either for today or at any time in the past is controversial (*e.g.* Cole *et al.*, 1999). Specific to this study, it was shown in Chapter 5 that the isotopic composition of rainfall in the rain-bearing low pressure systems and fronts is controlled primarily by the intensity and water source area of these systems, which is governed, under current climate patterns, by meridional versus zonal flow. At a given site, the relationship between $\delta^{18}O_P$ and the intensity of these systems may be approximated by the linear distance between the sites and the nearest low pressure centre. Thus, for southern Australia, a simple approximation such as Dansgaard's is not appropriate.

The classification of $\delta^{18}O_{SP}$ in terms of Schwarcz's γ carries large consequences for the interpretation of $\delta^{18}O_{SP}$ records as being predominantly temperature or rainfall records.

The γ parameter over-simplifies the meteoric factors in play, highlighted by the conflicting $\delta^{18}O_{SP}$ records from the physiographic and climatically similar sites of New Zealand and Tasmania. Data from New Zealand (Hendy and Wilson, 1968: Figure 8.1.1A; Hellstrom *et al.*, 1998) show that $\delta^{18}O_{SP}$ was isotopically heavier during the last glacial period compared with modern calcite, while data from Tasmania (Goede, 1994; Desmarchelier and Goede, 1996; Goede, 1998) indicate that $\delta^{18}O_{SP}$ was isotopically lighter during the last glacial period compared with modern calcite. These data imply that $\delta^{18}O_{SP}$ moves negative with temperature in New Zealand (negative γ) but positive with temperature in Tasmania (positive γ); or, that the cave temperature effect dominates in New Zealand, while rainfall signals dominate in Tasmania. Given their essential similarity, both now and at the LGM, this is unexpected.

Ideally, other proxies would be used to deconvolve the competing cave temperature and meteoric rainfall signals. In theory, this may be done by fluid inclusion analysis of $\delta^{18}O$ and δD (Schwarcz and Younge, 1983; Dennis *et al.*, 2001) which involves direct isotopic analysis of the trapped water (fluid inclusions) in the speleothem calcite. This technique can provide an independent record of rainfall isotopes which are not affected by cave temperature. Unfortunately, fluid inclusion analysis, which began in the mid-1980s (Schwarcz and Yonge, 1983; Yonge *et al.*, 1985) remains problematic (McGarry *et al.*, 2002; Serefiddin *et al.*, 2002). Few speleothems contain sufficient fluid inclusions for analysis, and if enough water can be liberated, reproducibility is often poor because of fractionation during extraction (Goede *et al.*, 1986; Dennis *et al.*, 2001) and because water also is adsorbed to allogenic clays in speleothem calcite (McGarry *et al.*, 2002).

As no technique is routinely accessible for deconvolving rainfall from cave temperature signals, the key question is: how well can $\delta^{18}O_{SP}$ records be interpreted as palaeoclimate recorders based on the net behaviour of $\delta^{18}O_{SP}$ alone? The conflicting records of Tasmania and New Zealand $\delta^{18}O_{SP}$ are thus a critical case study, since these two physiographic and climatically similar sites, have $\delta^{18}O_{SP}$ records that move in opposite directions over the LGM-Holocene transition. The strength of this comparison hinges on knowledge of temperature variation over the period of the existing $\delta^{18}O_{SP}$ records. For the New Zealand records, this is reasonably well-known since the records span the LGM-Holocene post-glacial warming (~4.5°C; Porter 1975a,b; Soons, 1979). However,

none of the existing Tasmanian $\delta^{18}O_{SP}$ records span this period but, rather, they cover earlier parts of the last glacial period (125-55 ka), where independent temperature estimates for the region are limited to the Vostok deuterium record of Jouzel *et al.* (1987) (Figure 8.1.2). While it can be seen that the average Pleistocene $\delta^{18}O_{SP}$ is lighter than modern calcite (Figure 8.1.2), implying that γ is positive, a speleothem record spanning the LGM period is required to confidently determine that γ is indeed positive for Tasmania.

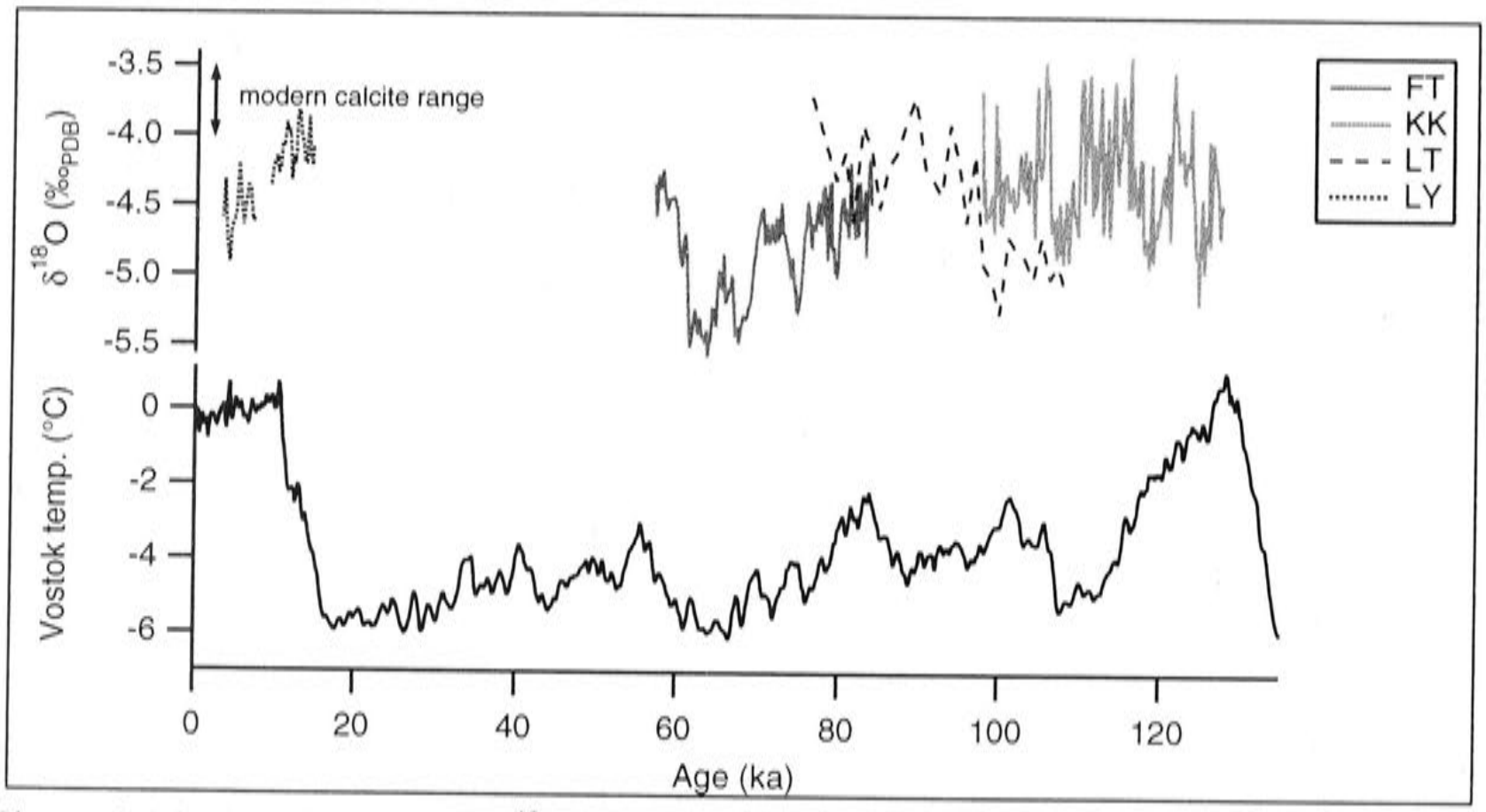

Figure 8.1.2: Trends between $\delta^{18}O_{SP}$ (Goede, 1998) and Vostok temperature derived from deuterium isotopes (Jouzel *et al.*, 1987). (Legend refers to speleothem identification codes given by Goede; details of FT appear in Goede (1994), LT in Desmarchelier and Goede (1996) and LY in Goede and Hitchman (1984). "Modern calcite" is the range of $\delta^{18}O_{SP}$ values reported for calcites collected whilst active at several Tasmanian sites and reported in Goede (1998) and references therein.

The uncertainty of speleothem γ in Tasmania is further compounded by the LY record (Goede and Hitchman, 1984; Figure 8.1.2) which shows a large decrease in $\delta^{18}O_{SP}$ after deglaciation (14-3 ka), which is opposite to the expected trend, if γ for Tasmanian speleothems is positive. The chronology of the LY speleothem was checked by TIMS U-series age measurements in Chapter 3, Table 3.4.1 and is discussed in Section 3.4 and 8.2.

To eliminate the possibility that the $\delta^{18}O_{SP}$ glacial-age records were affected by non- or indirect climatic factors, *e.g.* the proximity to the Tasmanian ice cap, or increased

continentality of mainland Australia when large areas of Bass Strait were exposed by a LGM sea-level lowering of ~120 m (Lambeck and Chappell, 2001), a third site in southwestern Australia was included in this investigation. This region is both upwind of mainland Australia in the westerly wind-flow and was unglaciated at the LGM.

To explore the primary question concerning the apparent contrast between Tasmania and New Zealand $\delta^{18}O_{SP}$ records, the following goals were set:

1. Obtain a $\delta^{18}O_{SP}$ record from a Tasmanian flowstone covering the period from prior to the LGM to the present, to test whether speleothem γ is positive for Tasmania.
2. Obtain a $\delta^{18}O_{SP}$ record spanning the same period for southwestern Australia where γ would be unaffected by glaciation and the increased continentality of mainland Australian at the LGM.
3. To compare Tasmanian and southwestern Australian $\delta^{18}O_{SP}$ records to the New Zealand $\delta^{18}O_{SP}$ record of Hellstrom (1998) and Hellstrom *et al.* (1998), hereafter referred to as MD3.

The strength of the hypothesis that $\delta^{18}O_{SP}$ should be similar for Tasmania and New Zealand relies on evidence that both sites were climatically comparable at the LGM. Since this evidence comes from palaeoclimate proxies, it will be reviewed below.

8.2 TASMANIAN AND NEW ZEALAND PALAEOCLIMATE AT THE LGM

Climatic conditions across mainland southern Australia at the LGM are generally thought to be cooler and drier. The most reliably constrained temperature estimates from geomorphic evidence (moraines) of glacier altitude limits, termed the Equilibrium Line Altitude (ELA), in the Snowy Mountains indicate a cooling of 6°C (Barrows *et al.*, 2001). Amino-acid racemisation measurements on AMS radiocarbon dated fossil eggshells from the interior of southern Australia indicate cooling of 9°C (Miller *et al.*, 1997).

Whether it was drier or wetter at the LGM is more contentious. In southeastern Australia in the Willandra region, lake levels were at their highest between ~30-25 ka radiocarbon

years BP, however the building of source-bordering dunes (lunettes) on the eastern shores (down-wind side) after ~25 ka radiocarbon years BP is interpreted to represent declining lake levels experiencing episodic deflation (Bowler, 1976). Closer to the source of mainland glaciation on the Riverine Plain, it is estimated that lake levels were higher than today, but it is suggested that these high levels were sustained only by the delivery of melt-water from the Snowy Mountain Highlands, possibly enhanced by greater run-off over a less vegetated landscape (Bowler, 1978). In both cases, it is suggested these lakes bear the mark of higher aridity to the west indicated by the presence of pelletised clays blown into lunettes from the deserts (Bowler, 1976; 1978). At Lake George, consideration of the effect of colder conditions reducing evaporation and run-off led Galloway (1965) to conclude that higher lake levels at about the LGM, could be sustained with less rainfall than today. Palynological evidence supports drier conditions at Lake George with woodland taxa suppressed during 25-15 ka radiocarbon years BP (Singh *et al.*, 1981).

Compared with mainland Australia, Tasmania was much more intensively and extensively glaciated region at the LGM, with large areas of the West Coast Range and Central Plateau under ice cover (Colhoun *et al.*, 1996 *cf.* Barrows *et al.*, 2002). Here, LGM temperatures have been constrained by mapping ELA of moraines and dating organic material trapped within these features (Colhoun *et al.*, 1996) which has been revised by Barrows *et al.* (2002) using exposure dating of the moraines themselves. For Tasmania, an estimated 6°C cooling relative to present day mean annual temperature (MAT) was calculated (Colhoun *et al.*, 1996 and references therein). Furthermore, cooler temperatures at the LGM are broadly supported by the expansion of alpine herbaceous taxa to lower altitude at numerous sites surrounding the glaciated region (Tullabardine Dam: Colhoun and van de Geer, 1986; Newall Creek: van de Geer *et al.*, 1989; Lake Selina: Colhoun *et al.*, 1999). Below the high altitude ranges, the radiocarbon dated sedimentary record of Pulbeena Swamp in northwest Tasmania (Colhoun *et al.*, 1982) shows a transition from freshwater marls to sandy sediment between ~25 ka and 11 ka radiocarbon years BP. These marl sediments, precipitated from a local freshwater spring, are interpreted as a proxy for hydrological conditions. The sandy sediments are suggested to reflect drier conditions from ~25 ka and 11 ka radiocarbon years BP, with the lowering of the groundwater table that coincides with a rise in herbaceous taxa, interpreted to represent cooler, drier conditions.

Across the Tasman Sea, in New Zealand, geomorphic evidence of the last glacial period, termed the Otira glaciation, is widely expressed in the South Island and is best exposed at central Westland (northwest South Island). Here, the Otira is identified as three advances, known as the Kumera 1, 2 and 3 (Suggart 1965, 1990), which have been dated by radiocarbon on trapped organic material (summarised in Suggart, 1990). The culmination of these phases occurs at 18 ka radiocarbon years BP. There are several other accounts of Late Pleistocene glaciation elsewhere on the North and South Islands (Gellately, 1988; Pillans, 1991; Williams, 1996), but which of these correspond to the Kumera advances is vague due to the uncertainty of the dating methods. Overall, these findings have not changed the early interpretations of Porter (1975a,b) and Soons (1979) who estimated ELA's at central Westland required a 4.5°C lowering of MAT at the LGM.

8.3 RESULTS

8.3.1 Comments on sample quality

The Late Quaternary flowstone core, MK-F1, obtained from Marakoopa Cave near Mole Creek in Tasmania was earlier described as being significantly contaminated with allogenic material (Chapter 2, Section 2.2.1). This observation was confirmed by high ^{232}Th measurements (Chapter 3, Section 3.4.1). Such contamination prohibits U-series dating, including methods adopting numerical correction techniques, since multiple coeval samples could not be analysed owing to low U concentrations and hence the large sample volume required. As an alternative, Section 3.5 details the construction of a conventional radiocarbon chronology, which is sufficient for comparing the overall trends of New Zealand and Tasmanian $\delta^{18}O_{SP}$ records. The flowstone sequence, ES-F1, was able to be dated by U-series methods, although the base and top date are significantly contaminated by allogenics, indicated by low $^{230}Th/^{232}Th$ (~2, Chapter 3, Table 3.4.1), and thus may be younger than the measured ages of 25.5 ± 2.4 ka and 2.3 ± 0.5 ka.

8.3.2 $\delta^{18}O_{SP}$ RECORDS OF NEW ZEALAND, TASMANIA AND SOUTHWESTERN AUSTRALIA.

The MD3 $\delta^{18}O_{SP}$ record of Hellstrom (1998) and Hellstrom *et al.* (1998) comes from Nettlebed Cave near Mt. Arthur which lies in the northwestern part of the South Island. MD3 $\delta^{18}O_{SP}$ is compared with the Tasmanian (MK-F1) and southwestern Australia (ES-F1) $\delta^{18}O_{SP}$ records constructed for this study. Figure 8.3.1 shows that over the LGM-Holocene warming transition, MK-F1 $\delta^{18}O_{SP}$ increases from –5.5 to –4.0‰, MD3 decreases from –4.1 to –6.0‰ and ES-F1 decreases from –2.3 to –4.6‰. These shifts are summarised in Table 8.3.1. This indicates that MK-F1 (Tasmania) moves positively with temperature, while ES-F1 (southwestern Australia) and MD3 (New Zealand) move negatively with temperature. That is, speleothem γ is positive for Tasmania but is negative for New Zealand and southwestern Australia. This result agrees with the early interpretations of Goede *et al.* (1986; 1990) and Goede (1994).

Using Equation 8.1.1 to subtract the temperature and ice-volume signals from the LGM-Holocene $\delta^{18}O_{SP}$ shift (Table 8.3.1) suggests there must have been a shift in $\delta^{18}O_P$ of ~4‰ for Tasmania, while $\delta^{18}O_P$ in New Zealand has only shifted by a mere 0.3‰. This discrepancy between $\delta^{18}O_P$ for Tasmania and New Zealand cannot be accounted for by the difference in glacier ELA temperatures, or uncertainty of the ELA temperatures because the cave temperature effect is small (-0.24‰/°C). Thus, some additional process is driving $\delta^{18}O_P$ in Tasmania towards anomalously light values.

Table 8.3.1: Rainfall $\delta^{18}O_P$ shift calculated from subtracting the temperature and ice-volume signals from $\delta^{18}O_{SP}$. ([1]Porter 1975a,b and Soons, 1979; [2]Barrows *et al.*, 2002; [3]McCrea, 1950; [4]Schrag *et al.*, 1996; [5]Equation 8.1.1.)

Site	Speleothem	$\delta^{18}O_{SP}$ shift (‰)	Temperature shift (°C)[1,2]	Temperature signal (‰)[3]	Ice-volume signal (‰)[4]	Calculated $\delta^{18}O_P$ shift (‰)[5]
New Zealand	MD3	-1.9	+4.5	-1.1	-1.1	+0.3
Tasmania	MK-F1	+1.5	+6	-1.4	-1.1	+4.0
Southwestern Australia	ES-F1	-2.3	-			

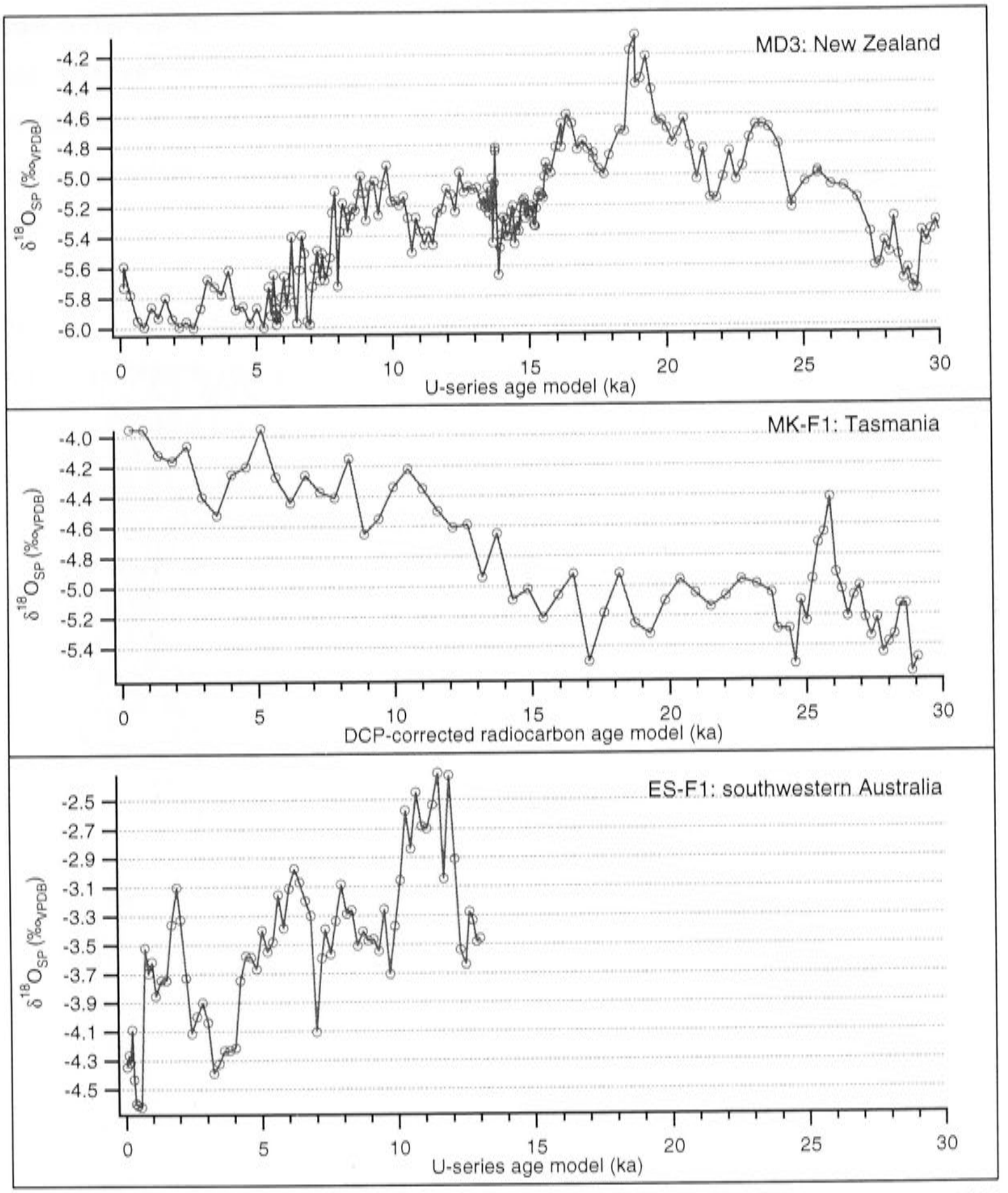

Figure 8.3.1: $\delta^{18}O_{SP}$ records from Tasmania (this study), New Zealand (Hellstrom, 1998; Hellstrom *et al.*, 1998) and southwestern Australia (this study).

Positive γ for Tasmania implies that rainfall effects are dominating here, since only the cave temperature effect is negative. Chapter 5 has shown that $\delta^{18}O_P$ in the southern Australian region is sensitive to the vigour and proximity of the mid-latitude low-pressure systems. The results of the event-based $\delta^{18}O_P$ rainfall analysis imply that it is possible to shift $\delta^{18}O_P$ to isotopically lighter values if low pressure systems were tracking closer to Tasmania at the LGM than they are today. However, a 4‰ shift is large and implies that intense low pressure systems would be needed to produce this

shift. However, it would be expected that such systems would also deliver greater rainfall. Independent evidence (summarised in Section 8.2) suggests Tasmania and southern Australia in general were drier at the LGM, compared to today, which suggests the required $\delta^{18}O_P$ shift was not due to intense low pressure systems tracking closer to Tasmania.

It appears that the only plausible reason for the large shift in the $\delta^{18}O_P$ Tasmania, is that MK-F1 is fed by a localised, isotopically light source of $\delta^{18}O_P$. An examination of the hydrology of the Mole Creek karst region revealed by water tracing using fluorescein dyes (Kiernan, 1989), indicate that water percolating through Marakoopa Cave is sourced from the Western Tiers region (Figure 8.3.2). As this region was glaciated during the LGM (Hannan and Colhoun, 1987; 1991; Colhoun *et al.*, 1996; Figure 8.3.3

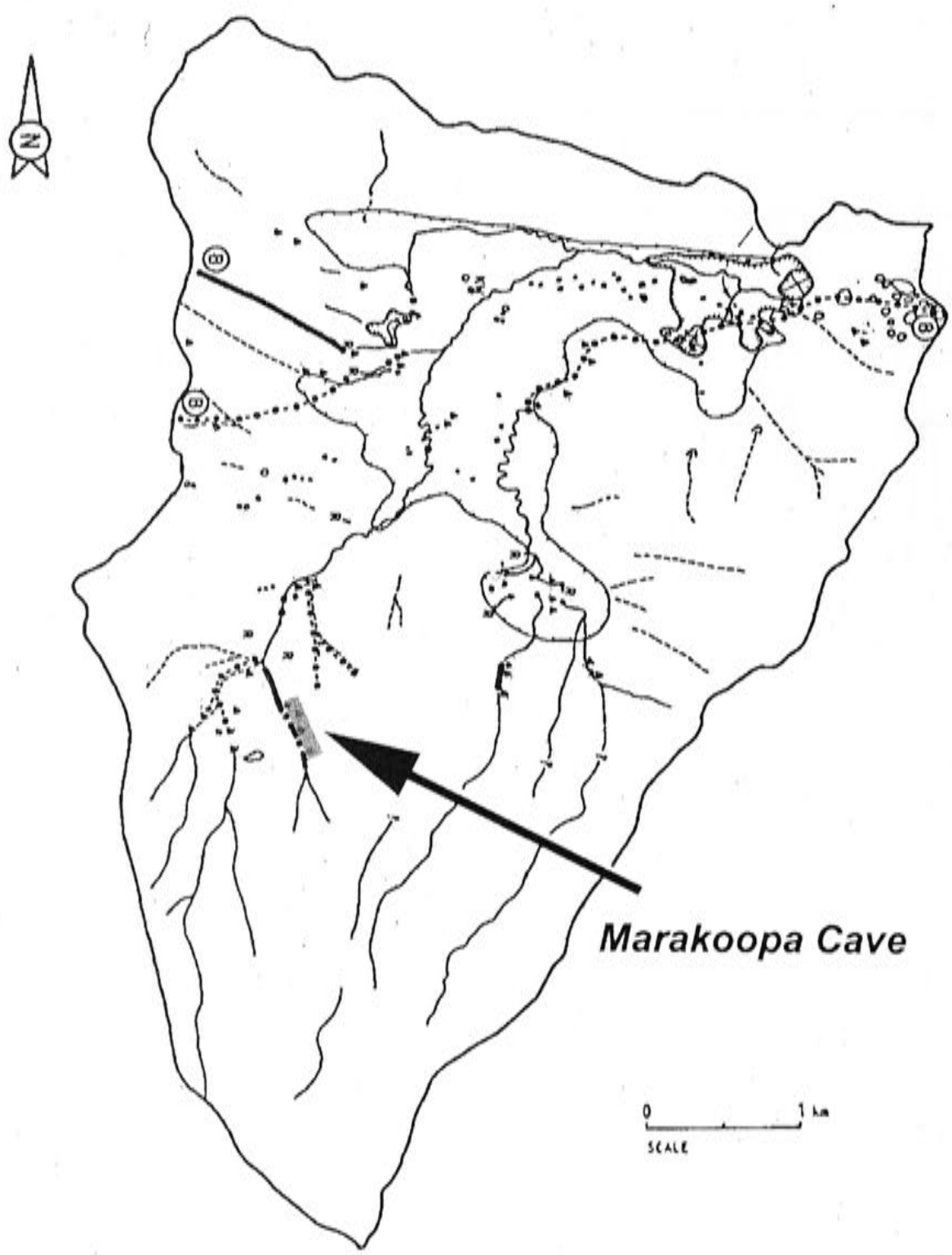

Figure 8.3.2: Surface watershed of the Mayberry area. Location of Marakoopa Cave is shown as broad grey line. Boundary of Western Tiers plateau is along the bottommost boundary line. (From Kiernan, 1989.)

shows extent of glaciers estimated from ELA mapping), it is possible than that the 4‰ decrease in $\delta^{18}O_P$ at the LGM was due to the delivery of melt-water. For example, $\delta^{18}O$ of Takaka and Manuherikia Rivers receiving seasonal snow-melt from the high altitude regions of South Island New Zealand, show that river-water $\delta^{18}O$ is 2.5-3.5‰ lower during the peak of spring snow melting (Stewart *et al.*, 1983). A lowering of atmospheric dew-point at the LGM would further deplete $\delta^{18}O_P$.

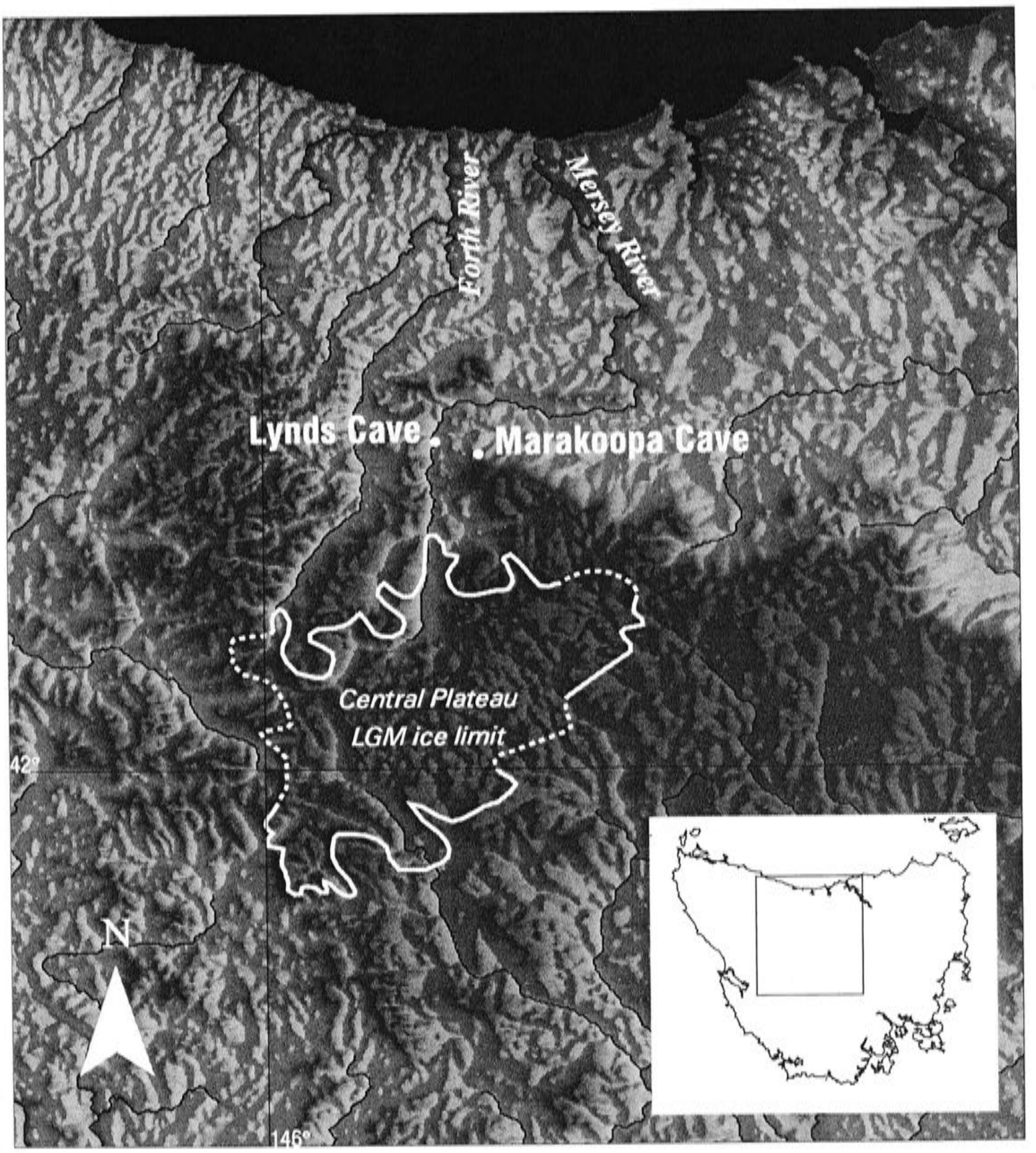

Figure 8.3.3: Topography of north-central Tasmania showing estimates of LGM ice extent. (From Colhoun *et al.* (1996), however the geomorphic features used for this outline have since been re-dated by Barrows *et al.* (2002) who found that some of these features are older than LGM, and thus the true extent of ice cover may be less than shown here, but does not affect the interpretation of this study.)

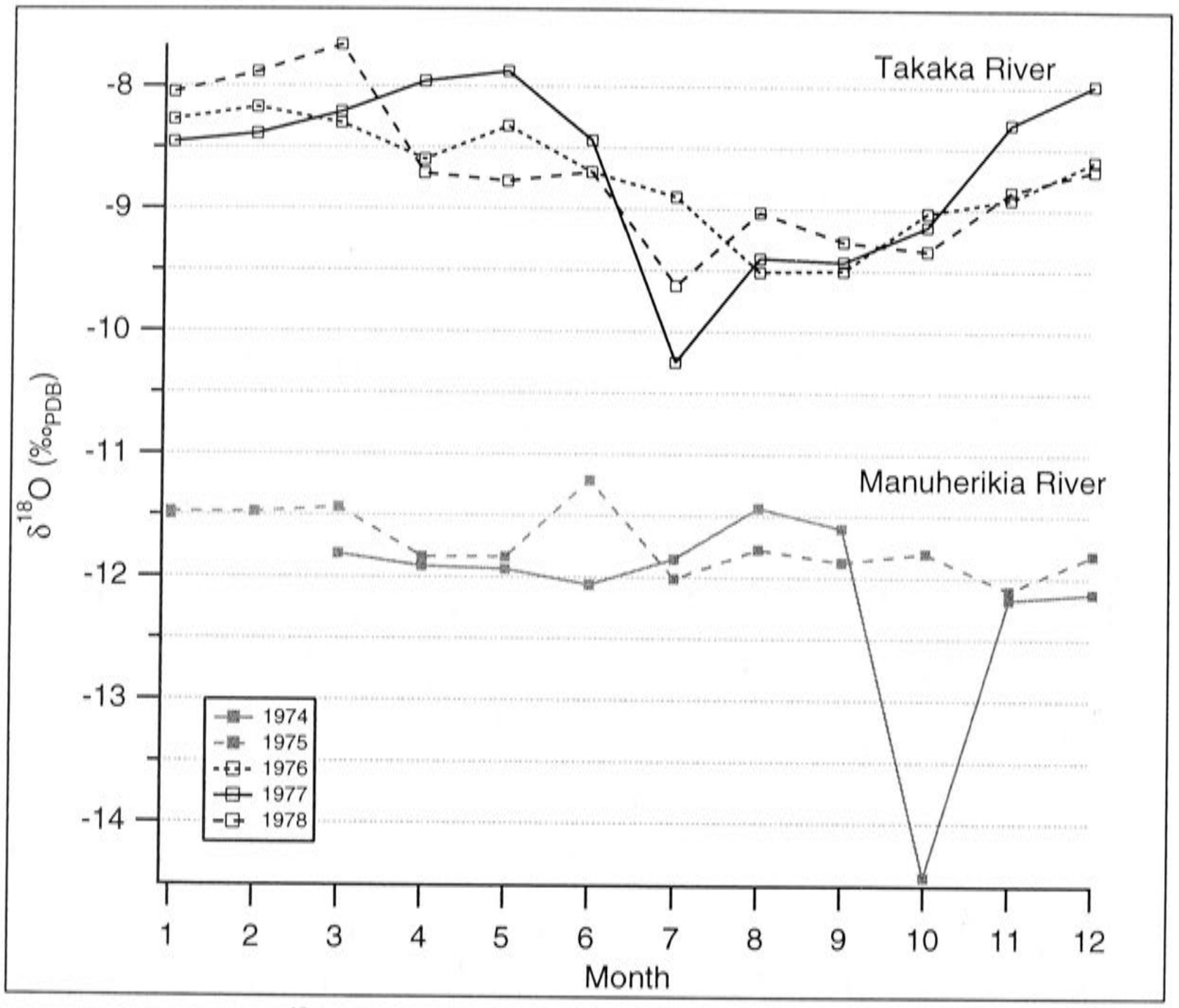

Figure 8.3.4: Monthly $\delta^{18}O$ at Takaka and Manuherikia Rivers in the Takaka Valley and Clutha Rivers catchments of South Island, New Zealand. The Takaka River receives water from the high altitudes of the Mt Arthur region, while the Manuherikia River receives water from the high altitudes of southern South Island. (Data from Stewart *et al.*, 1983.)

This explanation has been elusive, since the $\delta^{13}C_{SP}$ values are relatively unchanged between LGM and modern times (Figure 8.3.5) suggesting that C dynamics (soil organic matter, % of limestone C, degree of degassing) have changed little between glacial and non-glacial periods, which would be unlikely if the cave was underneath a snow cover for much of the year. However, it is now apparent from the results of the water tracing study that a significant snow cover directly over the cave is not required for the cave to receive melt-water through its streamways, and it is suggested here that this isotopically lighter water may be a source for cave drip-water also.

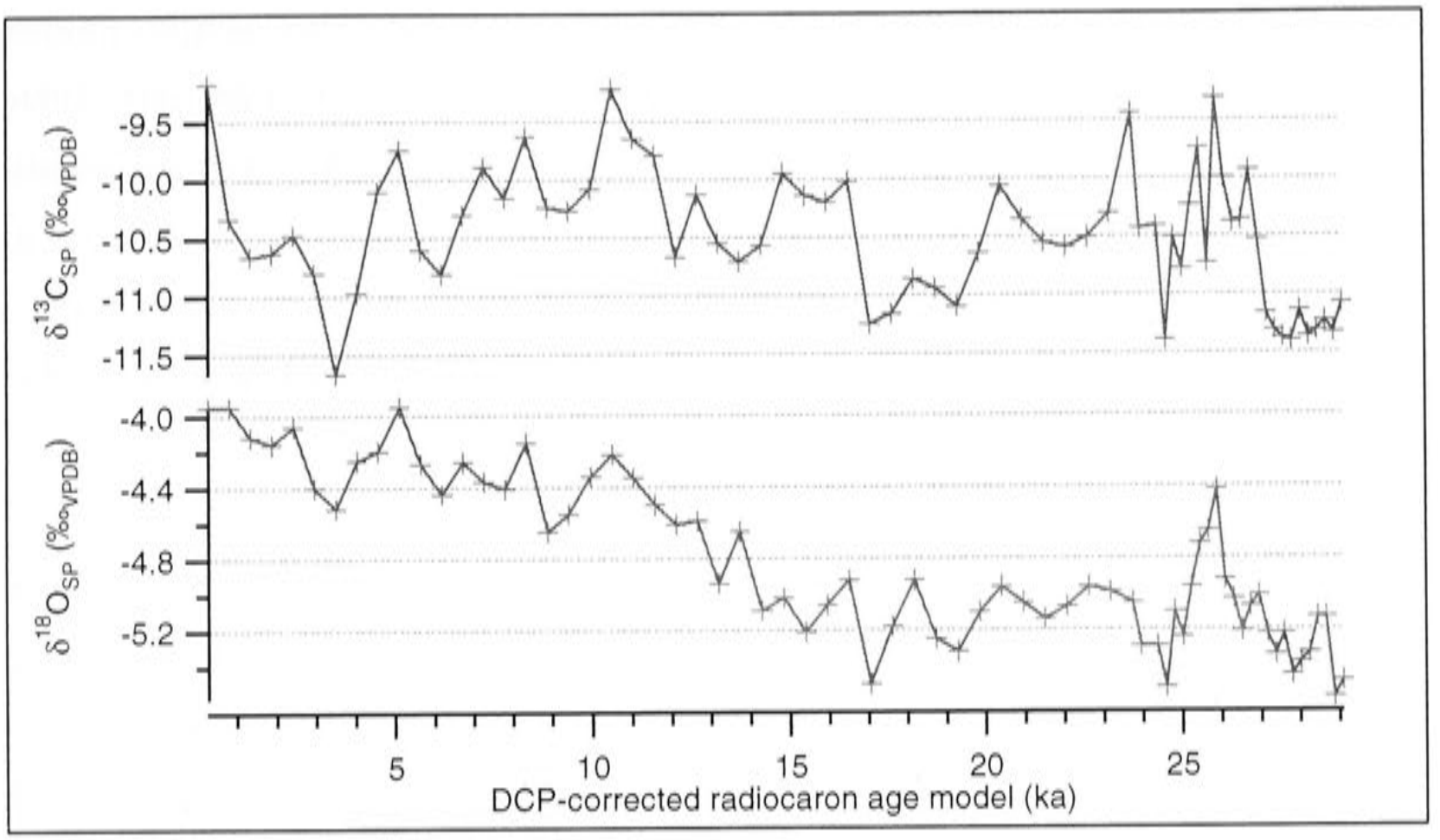

Figure 8.3.5: $\delta^{13}C_{SP}$ and $\delta^{18}O_{SP}$ record of MK-F1 core.

The potential of complex hydrology to affect $\delta^{18}O_{SP}$ records of the region is further highlighted by the opposite trend of another $\delta^{18}O_{SP}$ record from a stalagmite, LY, also from the Mole Creek karst. LY was analysed by Dr A. Goede from Lynds Cave, a mere 5 km northwest of Marakoopa Cave, and the stable isotope record appears in Goede and Hitchman (1984) who adopted a chronology based on radiocarbon age measurements corrected for dead carbon using a model based on electron spin resonance (ESR) techniques. This chronology was revised in Goede (1998) using updated radiocarbon calibration tables. The range (top and basal age) of this speleothem was re-investigated by TIMS U-series age measurements conducted by this author (Chapter 3, Section 3.4): results confirm the adjusted radiocarbon basal age of 14.63 ka (U-series: 14.54 ± 1.13 ka), whereas the top age measurement, 6.47 ± 0.76 ka, is significantly older than the adjusted radiocarbon age of 2.97 ka (uncorrected age is 5.25 ± 0.70 ka; Pta-2979) proposed by Goede (1998). As argued in Chapter 3, Section 3.4 both age measurements are flawed, and the true age probably lies between these estimates. For this comparison study where accurate chronologies are not necessary, an estimate of ~4.7 ka for the youngest calcite is assumed.

The LY $\delta^{18}O_{SP}$ record reported by Goede and Hitchman (1984) was later re-sampled and is shown in Goede (1998; Figure 8.3.6) who interpret the decrease in $\delta^{18}O_{SP}$ from –3.8 to

–4.9‰ as a temperature *cooling* from ~15 to 3 ka of ~4.5°C. This interpretation is surprising, and conflicts with evidence more recent (Colhoun and van de Geer, 1986; van de Geer *et al.*, 1989; van de Geer *et al.*, 1994; Colhoun *et al.*, 1999) than the original publication of the LY record (Goede and Hitchman, 1984). These palynological records indicate a transition from alpine to temperate conditions at around 13-11 ka *i.e.* that this period is *warming* in Tasmania. However, Goede's interpretation is based on the fact that γ appears to be positive for all other Tasmanian speleothems.

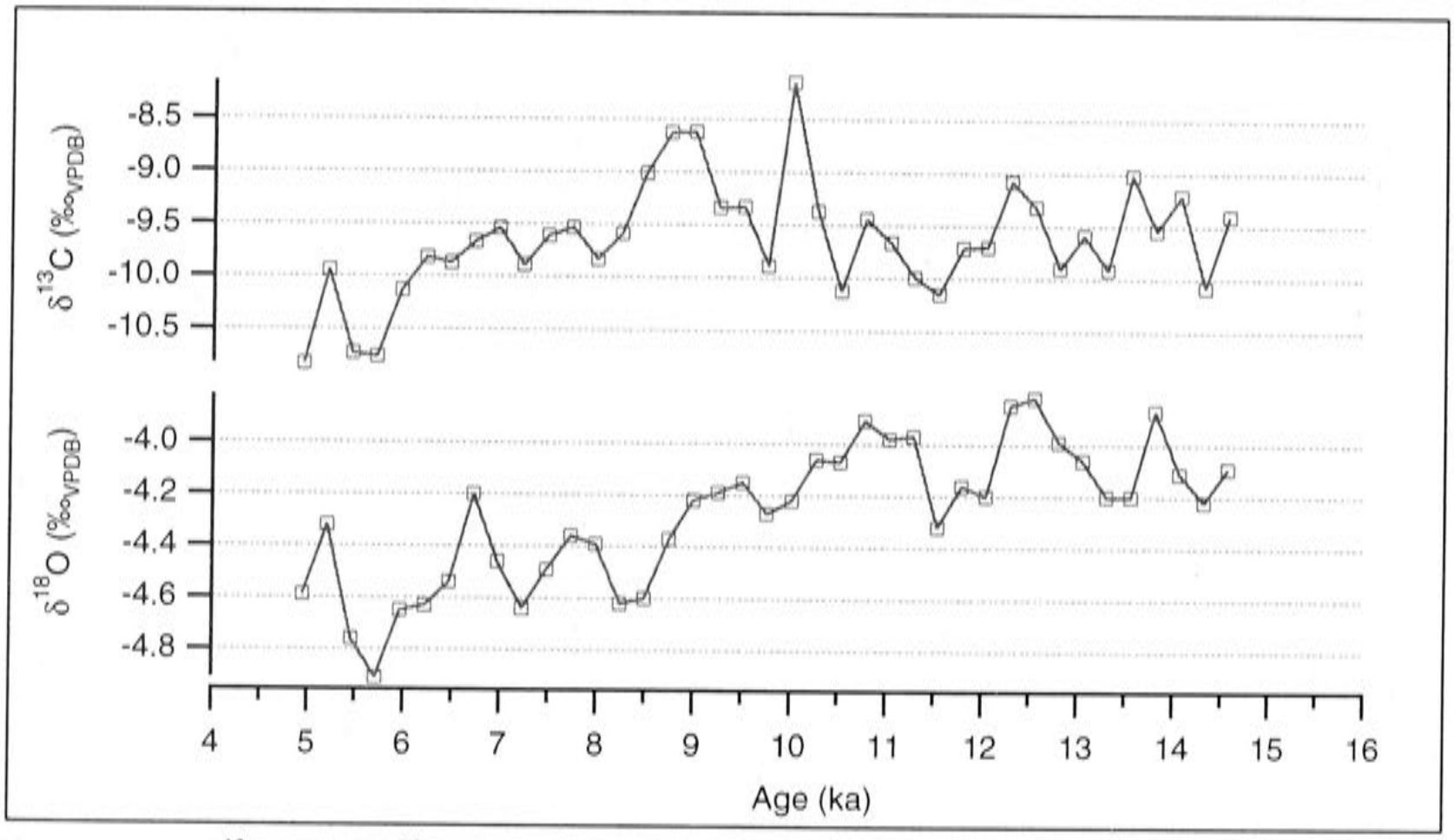

Figure 8.3.6: $\delta^{13}C_{SP}$ and $\delta^{18}O_{SP}$ record of LY stalagmite. The chronology of this stalagmite is based on a basal U-series date (by this author, 14.5 ± 1.1 ka) and an estimate of the youngest age lying between the (allogenic contaminated, 6.5 ± 0.8 ka) U-series date and corrected radiocarbon age estimate (2.9 ka; Goede, 1998). The uncertainty of this chronology is further hampered by the unknown length of a missing portion reported when the stalagmite was found in Lynds cave by Dr A. Goede.

Examining overall isotopic shifts over the period 15 to 5 ka, the MK-F1 $\delta^{18}O_{SP}$ record is moving in the opposite direction to LY (Figures 8.3.1 and 8.3.6) with MK-F1 rising by ~ +0.8‰ (~ -5.2 to -4.0‰) and LY falling by ~ –0.8‰ (~ -3.8 to -4.9‰). The $\delta^{18}O_{SP}$ shift in the LY record is similar to, and in the same direction as MD3 (-0.8‰; Figure 8.3.1) in New Zealand. This author notes that the hydrology of the Lynds Cave system is not linked to the Western Tiers melt-water source. Although the source of the stream in Lynds Cave can breach the topographic divide between Lynds and Marakoopa Cave under high-flow conditions (Kiernan, 1989), the source for overhead seepage flow (drip-water) is likely to lie to the north-west (Mersey River side) of this divide *i.e.* local rather

than from the Western Tiers. It is thus proposed here that LY is dominated by the cave temperature effect (negative speleothem γ), which is not overridden by input of isotopically light melt-water from the Western Tiers during the last glacial advance.

Higher frequency variation

Consideration of higher frequency variation in the MK-F1, ES-F1 and LY are possible but not reliably constrained by the current chronologies. However, one feature may be worth noting. The MK-F1 record indicates three intervals where $\delta^{18}O_{SP}$ attains it lowest values (~ -5.4‰ at 29, 25 and 17 ka; Figures 8.3.1 and 8.3.5). Low $\delta^{18}O_{SP}$ indicate, from the above argument, higher melt-water input and thus presumably, cooler conditions. This contrasts with Barrows *et al.* (2002) who argues for only one phase of glacier advance during this period in the Tasmanian highlands region based on the statistical grouping of cosmogenic ^{36}Cl and ^{10}Be age measurements between 17-20 ka, although the range of ages recorded for terminal moraines in this phase is 16.0 ± 1.5 ka (Poets Hill, West Coast Range) to 27.4 ± 1.6 ka (Ben Lomond Plateau, northeastern Tasmania).

8.4 DISCUSSION

The isotope balance on MK-F1 at the LGM and the hydrology of the Mole Creek karst system, suggest that certain Tasmanian speleothem $\delta^{18}O_{SP}$ records have positive γ because their drip-waters were at least partially fed by melt-water. The contrasting LY and MK-F1 $\delta^{18}O_{SP}$ records illustrates that it is possible that not all caves lying close to glaciated areas will receive melt-water. This appears to explain the contrasting behaviour of some Tasmanian and New Zealand speleothem records over the LGM-Holocene transition. However, it is recognised that the only way to fully resolve the conflicting γ problem of the Tasmania and New Zealand speleothems, *i.e.* independently determining $\delta^{18}O_P$ for each site, would be by fluid inclusion analysis. As stated previously, this technique has the potential to provide an independent record of $\delta^{18}O_P$ which is not affected by cave temperature. The application of this method to this study was discussed with Prof. Henry Schwarcz (McMasters University, Canada), but not pursued since it was doubtful that MK-F1 contained sufficient fluid inclusions (speleothems rich in inclusions usually have a frosty appearance: Prof H. Schwarcz, *pers. comm.*; MK-F1 is

opaque in appearance). Furthermore, MK-F1 contains allogenic clays, which can affect liberated water because of their adsorption properties (McGarry *et al.*, 2002). Moreover, the effort required to do this on the MK-F1 record whose interpretation is limited by its poor chronology, was questionable.

Nonetheless, the limited interpretation of this study still has important implications for interpreting Tasmanian $\delta^{18}O_{SP}$ records. A speleothem that is fed by glacial melt-water, potentially offers important palaeoclimate information, as it may provide a high resolution, continuous record of glacier activity that may be less problematic than the interpretation and dating of geomorphic evidence such as moraines. More specifically, a record of short-lived, rapid changes in glacier activity could contribute significantly to our understanding of phenomena such as Dansgaard-Oeschger events (Dansgaard *et al.*, 1993; Spotl and Mangini, 2002) on the Southern Hemisphere.

8.5 CONCLUSIONS

The Tasmanian MK-F1 $\delta^{18}O_{SP}$ record moves positive with temperature over the LGM-Holocene post-glacial warming period. It appears that this phenomenon is most likely to be attributed to the input of melt-water from the Western Tiers during glacial conditions. This mechanism appears to be highly localised, shown by the contrasting trends of LY and MK-F1 $\delta^{18}O_{SP}$ records during the later stage of deglaciation and in the Holocene. Further studies in this region may exploit this finding to construct potentially important records of glacier activity, if speleothems uncontaminated by allogenic material can be found. However, for now, this study serves as a caution to overly simple interpretations of speleothems owing to the possibility that $\delta^{18}O_{SP}$ records respond to highly localised phenomena.

CHAPTER NINE

CONCLUDING REMARKS AND PROPOSED FUTURE WORK

This research demonstrated that the event-to-event variability in rainfall $\delta^{18}O_P$ and rainfall amount of southern Australia, was controlled by synoptic-scale variables. These are the intensity of the low-pressure systems and the source area of the atmospheric moisture mass. Because the influence of system intensity on rainfall amount and $\delta^{18}O_P$ decreases with distance to its centre, $\delta^{18}O_P$ and rainfall amount showed a positive and negative relationship, respectively, with the linear distance between the site and the low-pressure centre. This relationship is weakened by the mixing of isotopically heavy water vapour from sub-tropical latitudes.

In the context of climate change, the average $\delta^{18}O_P$ and rainfall amount at a site in southern Australia may be controlled by the proximity of the low-pressure storm tracks. On the inter-annual scale, it was identified that this may be governed by patterns of meridional flow producing greater amounts of isotopically lighter rainfall, versus zonal flow producing lesser amounts of isotopically heavy rainfall. On time-scales longer than 10^2-10^4 years, it is recognised that mechanisms that may shift the mean latitudinal position of the westerly wind-flow (*e.g.* long-term changes in solar insolation) need to be considered also.

The rainfall component of this research was important for investigating the dominant controls on speleothem $\delta^{18}O_{SP}$ in Tasmania, as they were previously interpreted as driven primarily by rainfall signals, but these signals were poorly understood. In this study, 100-200 year cyclical variations in the Late Holocene $\delta^{18}O_{SP}$ record, FC-S3, from Frankcombe Cave in south-central Tasmania, were interpreted as a record of shifting atmospheric meridional flow (wetter conditions) and zonal flow (drier conditions). This interpretation is supported by concurrent oscillations in $\delta^{13}C_{SP}$ in the interval from 2.4 ka to the present, and Sr isotope measurements from 1.2 to 0 ka whose values reflect the degree of limestone weathering, hence residence time of percolating drip-water. Heavier $\delta^{18}O_{SP}$ and $\delta^{13}C_{SP}$ are suggested to indicate drier conditions (zonal flow), while

conversely, lighter values indicate wetter conditions (meridional flow). The behaviour of FC-S3 trace elements, Mg, Sr and Ba, was less clear; but an increase in these elements between A.D.1450-1790, likely to reflect increased limestone weathering under extended drip-water residence time, coincides with a $\delta^{18}O_{SP}$ and $\delta^{13}C_{SP}$ and Sr isotope excursion, and is consistent with drier and possibly cooler conditions during the period of the Little Ice Age. This is the first evidence of the Little Ice Age signal in southern Australia, which may be restricted to cool seasons in this region, as it has not been reported in warm season tree-ring records.

The behaviour of speleothem $\delta^{18}O_{SP}$ was also examined for the Pleistocene-Holocene transition using MK-F1, a flowstone core from Marakoopa Cave in north-central Tasmania. Similarly, this 30-0 ka record is driven by rainfall effects, however, in this case, a dramatic shift in source water is suggested by a large isotope shift over the post-glacial warming period. The shift is plausibly explained by an input of highly localised, isotopically light, melt-water from the glaciated Western Tiers during the Late Pleistocene times. This interpretation serves as a caution that localised indirect climate factors potentially affect $\delta^{18}O_{SP}$. Such factors preclude $\delta^{18}O_{SP}$ from being interpreted as simply a rainfall or temperature record.

High resolution trace element analyses of a modern speleothem, MND-S1, from Moondyne Cave in southwestern Australia, which grew over a period (A.D.1911-1992) covered by instrumental rainfall records, revealed that Mg, U and P were correlated with mean annual rainfall. The inverse relationship between Mg and rainfall was interpreted as the effect of hydrological residence time on Mg, with lower rainfall extending the residence time and leading to cycles of calcite precipitation and limestone re-dissolution. By contrast, the trends between U, P and rainfall, are suggested to be linked to the capacity of P bio-production, which is dependent on vegetation activity, hence rainfall. It is suggested that the high affinity between uranyl ions and phosphate, following mineralisation of bio-produced P, is responsible for the agreement between these variables. This later trend will be weakened if P concentrations are low, which may explain its absence for the Holocene FC-S3 record.

Sr, Ba and Na were positively related to growth rate for MND-S1, although the relatively weaker trend between Sr and growth rate, suggests other mechanisms such as

prior-calcite precipitation are also important. Similar trends between Ba, Sr and growth rate (Na not measured) were observed for FC-S3. These trends suggest these elements are susceptible to precipitation kinetics and thus are not suitable climate proxies for MND-S1 and FC-S3.

The relatively fast growth rate of MND-S1 permitted the first sub-annual investigation of $\delta^{18}O_{SP}$. Annual $\delta^{18}O_{SP}$ moves synchronously with the other element cycles but more closely, and in-phase, with Mg. The annual range of $\delta^{18}O_{SP}$, ~1‰, is too large to be driven by temperature effects, but is comparable with the annual drip-water range observed in Tasmania and confirms that the rainfall signal is an important driver of $\delta^{18}O_{SP}$ in southern Australia. The annual expression of $\delta^{18}O_{SP}$ may be explained by the seasonal displacement of the low-pressure systems relative to the southwestern Australian coast. The consistent interpretation of the annual $\delta^{18}O_{SP}$ cycle and the annual Mg cycle, and their inferred seasonal timing, support the interpretation of these two proxies as effective hydrological indicators.

Finally, two-dimensional mapping of MND-S1 trace elements reveals growth patterns more complex than previously thought, with post-depositional crystal ripening and erosion indicating surface alteration, cautioning that information may be lost in this process. This ripening process may also prove responsible for UV banding in speleothems, rather than horizons of humic and fulvic acids deposited from seasonal flushing as often has been supposed.

Of the research explored in this thesis, two features warrant further investigation: these are the concurrent investigation of stable isotope and trace element annual cycles by ion microprobe and LA-ICP-MS, respectively. With respect to existing samples, further analysis of $\delta^{18}O_{SP}$ of MND-S1 using appropriate methods for standardisation is required. It is anticipated that extending this analysis to $\delta^{13}C_{SP}$, will also prove promising and may further constrain the interpretation of the trace element cycles and their relationship to soil zone versus limestone weathering processes, as $\delta^{13}C_{SP}$ is similarly a product of these processes.

Annually resolvable stable isotope and trace element speleothem records have the potential to assist in the investigation of the marked reduction in rainfall for this region. Investigating the palaeoclimate record is the only way of extending our knowledge of rainfall trends beyond the one hundred years, or so, of available instrumental data for this region. To do this, will require future speleothem sampling. Furthermore, an obvious limitation of this MND-S1 study was the lack of monitoring and collection of present day cave drip-waters. Ideally, any future work should include such a program.

A final comment regards the processing of collected water samples. These samples will be analysed and used to expand the regional record of event-based rainfall $\delta^{18}O_P$ samples, should adequate resources become available.

REFERENCES

Ansell, T. J., Reason, C. J. C., Smith, I. N. and Keay, K. (2000). Evidence for decadal variability in southern Australian rainfall and relationships with regional pressure and sea surface temperature. *International Journal of Climatology* 20: 1113-1129.

Araguas-Araguas, L., Froehlich, K. and Rozanski, K. (2000). Deuterium and oxygen-18 isotope composition of precipitation and atmospheric moisture. *Hydrological Processes* 14: 1341-1355.

Aristarain, A., Jouzel, J. and Pourchet, M. (1986). Past Antarctic Peninsula climate (1850-1980) deduced from an ice core isotope record. *Climatic Change* 8: 69-89.

Ayalon, A., Bar-Mathews, M. and Sass, E. (1998). Rainfall-recharge relationships within a karstic terrain within the Eastern Mediterranean semi-arid region, Israel: $\delta^{18}O$ and δD characteristics. *Journal of Hydrology* 207: 18-30.

Ayalon, A., Bar-Matthews, M. and Kaufman, A. (1999). Petrography, strontium, barium and uranium concentrations, and strontium and uranium isotope ratios in speleothems as palaeoclimatic proxies; Soreq Cave, Israel. *The Holocene* 9: 715-722.

Ayliffe, L. K., Marianelli, P. C., McCulloch, M. T., Mortimeter, G. E., Hellstrom, J. C., Moriarty, K. C. and Wells, R. T. (1998). 500 ka precipitation record from southeastern Australia: Evidence for interglacial relative activity. *Geology* 26: 147-150.

Baker, A., Smart, P. and Ford, D. (1993a). Northwest European palaeoclimate as indicated by growth frequency variations of secondary calcite deposits. *Palaeogeography, Palaeoclimatology, Palaeoecology* 100: 291-301.

Baker, A., Smart, P. L., Edwards, R. L. and Richards, D. A. (1993b). Annual growth banding in a cave stalagmite. *Nature* 364: 518-520.

Baker, A., Ito, E., Smart, P. and McEwan, R. (1997). Elevated and variable values of ^{13}C in speleothems in a British cave system. *Chemical Geology* 136: 263-270.

Baker, A., Genty, D., Dreybrodt, W., Barnes, W., Mockler, N. and Grapes, J. (1998). Testing theoretically predicted stalagmite growth rate with Recent annually laminated samples: Implications for past stalagmite deposition. *Geochimica et Cosmochimica Acta* 62: 393-404.

Baker, A., Genty, D. and Fairchild, I. J. (2000). Hydrological characterisation of stalagmite drip waters at grotte de Villars, Dordogne, by the analysis of inorganic species and luminescent organic matter. *Hydrology and Earth System Science* 4: 439-450.

Baldini, J. U. L., McDermott, F. and Fairchild, I. J. (2002). Structure of the 8200 year cold event revealed by a speleothem trace element record. *Science* 296: 2203-2206.

Banner, J. L., Musgrove, M., Asmerom, Y., Edwards, R. L. and Hoff, J. A. (1996). High-resolution temporal record of Holocene ground-water chemistry: Tracing links between climate and hydrology. *Geology* 24: 1049-1053.

Bar-Matthews, M., Ayalon, A., Kaufman, A. and Wasserburg, G. J. (1999). The Eastern Mediterranean paleoclimate as a reflection of regional events: Soreq cave, Israel. *Earth and Planetary Science Letters* 166: 85-95.

Barrows, T., Stone, J. O., Fifield, L. K. and Cresswell, R. G. (2002). The timing of the Last Glacial Maximum in Australia. *Quaternary Science Reviews* 21: 159-173.

Barrows, T., Stone, J., Fifield, L. and Cresswell, R. (2001). Late Pleistocene glaciation of the Kosciuszko Massif, Snowy Mountains, Australia. *Quaternary Research* 55, 179-189.

Bathurst, R. G. C. (1975). Carbonate sediments and their diagenesis. New York, Elsevier.

Beck, J. W., Richards, D. A., Edwards, R. L., Silverman, B. W., Smart, P. L., Donahue, D. J., Hererra-Osterheld, S., Burr, G. S., Calsoyas, L., Jull, A. J. T. and Biddulph, D. (2001). Extremely large variations of atmospheric ^{14}C concentration during the last glacial period. *Science* 292: 2453-2458.

Berner, R. A. and Morse, J. W. (1974). Dissolution kinetics of calcium carbonate in sea water IV. Theory of calcite dissolution. American Journal of *Science* 274: 108-134.

Bird, M. I., Ayliffe, L. K., Fifield, L. K., Turney, C. S. M., Cresswell, R. G., Barrows, T. T. and David, B. (1999). Radiocarbon dating of "old" charcoal using a wet oxidation, stepped-combustion procedure. *Radiocarbon* 41: 127-140.

Bischoff, J. L. and Fitzpatrick, J. A. (1991). Uranium series dating of impure carbonates: an isochron technique using total sample dissolution. *Geochimica et Cosmochimica Acta* 55: 543-555.

BOM (1994-2000). Monthly Weather Review: New South Wales. (January 1994-June 2000). Melbourne: Bureau of Meteorology Press.

BOM (2002). Climate averages, Australian Bureau of Meteorology. Retrieved from the World Wide Web: http://www.bom.gov.au/climate/averages.html.

Bond, G., Heinrich, H., Broecker, W., Labeyrie, L., McManus, J., Andrews, J., Huon, S., Jantschik, R., Clasen, S., Simet, C., Tedesco, K., Klas, M., Bonani, G. and Ivy, S. (1992). Evidence for massive discharges of icebergs into the North Atlantic ocean during the last glacial period. *Nature* 360: 245-249.

Bowler, J. M. (1976). Aridity in Australia: age, origins and expression in aeolian landforms and sediments. *Earth Science Reviews* 12: 279-3 10.

Bowler, J. M. (1978). Quaternary climate and tectonics in the evolution of the Riverine Plain, southeastern Australia. In: Davies, J. L., and Williams M. A. J. (Eds.) Landform evolution in Australia (pp. 70-112). Canberra: Australian National University Press.

Broecker, W. S. (2000). Abrupt climate change: causal constraints provided by the palaeoclimate record. *Earth Science Reviews* 51: 137-154.

Broccoli, A. J. and Manabe, S. (1987). The influence of continental ice, atmospheric CO_2 and land albedo on the climate of the last glacial maximum. *Climate Dynamics* 1: 87-99.

Broecker, W. S. and Denton, G. H. (1989). The role of ocean-atmosphere reorganisations in glacial cycles. *Geochimica et Cosmochimica Acta* 53: 2465-2501.

Busenberg, E. and Plummer, L. N. (1985). Kinetic and thermodynamic factors controlling the distribution of SO_4^{2-} and Na^+ in calcites and selected aragonites. *Geochimica et Cosmochimica Acta* 49: 713-725.

Cerling, T. (1984). The stable isotope composition of modern soil carbonate and its relationship to climate. *Earth and Planetary Science Letters* 71: 229-240.

Charles, C. D., Rind, D., Jouzel, J., Koster, R. D. and Fairbanks, R. G. (1994). Glacial-interglacial changes in moisture sources for Greenland: Influences on the ice core record of climate. *Science* 263: 508-511.

Charles, C. D., Rind, D., Jouzel, J., Koster, R. D. and Fairbanks, R. G. (1995). Seasonal precipitation timing and ice core records. *Science* 269: 247-248.

Cherniak, D. J. (1997). An experimental study of strontium and lead diffusion in calcite, and implications for carbonate diagenesis and metamorphism. *Geochimica et Cosmochimica Acta* 61: 4173-4179.

Cherniak, D. J. (1998). REE diffusion in calcite. *Earth and Planetary Science Letters* 160: 273-287.

Cole, J. E., Rind, D., Webb, R. S., Jouzel, J. and Healy, R. (1999). Climatic controls on interannual variability of precipitation $\delta^{18}O$: Simulated influence of temperature, precipitation amount, and vapour source region. *Journal of Geophysical Research* 104(D12): 14223-14235.

Colhoun, E., van de Geer, G. and Mook, W. (1982). Stratigraphy, pollen analysis, and palaeoclimatic interpretation of Pulbeena Swamp, northwestern Tasmania. *Quaternary Research* 18: 108-126.

Colhoun, E. A. and van de Geer, G. (1986). Holocene to Middle Last Glaciation vegetation history at Tullabardine Dam, western Tasmania, Australia. *Proceedings of the Royal Society of London* B29: 177-207.

Colhoun, E. A., Hannan, D. and Kiernan, K. (1996). Late Wisconsin glaciation of Tasmania. *Papers and Proceedings of the Royal Society of Tasmania* 130: 33-45.

Colhoun, E. A., Pola, J. S., Barton, C. E. and Heijnis, H. (1999). Late Pleistocene vegetation and climate history of Lake Selina, western Tasmania. *Quaternary International* 57/58: 5-23.

Cook, E., Bird, T., Peterson, M., Barbetti, M., Buckley, B., D'Arrigo, R. and Francey, R. (1992). *Climatic Change* over the last millennium in Tasmania reconstructed from tree-rings. *The Holocene* 2-3: 205-217.

Cook, E. R., Buckley, B. M., D'Arrigo, R. D. and Peterson, M. J. (2000). Warm-season temperatures since 1600BC reconstructed from Tasmanian tree rings and their relationship to large-scale sea surface temperature anomalies. *Climate Dynamics* 16: 79-91.

Coplen, T. B. (1994). The reporting of stable isotope data. *Pure and Applied Chemistry* 66: 273-276.

Coplen, T. B., Herczeg, A. L. and Barnes, C. (2000). Isotope engineering-using stable isotopes of the water molecule to solve practical problems. In: P. Cook and A.L. Herczeg (Eds.). Environmental tracers in subsurface hydrology. Boston: Kluwer Academic Publishers.

Corbett, K. and Banks, M. (1974). Ordovician stratigraphy of the Florentine synclinorium, southwest Tasmania. *Papers and Proceedings of the Royal Society of Tasmania* 107: 207-231.

Cuffey, K. M. and Vimeux, F. (2001). Covariation of carbon dioxide and temperature from the Vostok ice core after deuterium-excess correction. *Nature* 412: 523-525.

Dansgaard, W. (1953). The abundance of O^{18} in atmospheric water and water vapour. *Tellus* 5: 461-469.

Dansgaard, W. (1961). The isotopic composition of natural waters. *Meddelelser om Gronland.* Copenhagen. 165.

Dansgaard, W. (1964). Stable isotopes in precipitation. *Tellus* 4: 436-468.

Dansgaard, W., Johnson, S. J., Clausen, H. B., Dahl-Jensen, D., Gundestrup, N. S., Hammer, C. U., Hvidberg, C. S., Steffensen, J. P., Sveinbjornsdottr, A. E., Jouzel, J. and Bond, G. (1993). Evidence for general instability of past climate from a 250-kyr ice-core record. *Nature* 364: 218-220.

Davis, K. J., Dove, P. M. and Yoreo, J. J. D. (2000). The role of Mg^{2+} as an impurity in calcite growth. *Science* 290: 1134-1137.

de Deckker, P. (1982). Non-marine ostracods from two Quaternary profiles at Pulbeena and Mowbray Swamps, Tasmania. *Alcheringa* 6: 249-274.

de Kanel, J. and Morse, J. W. (1978). The chemistry of orthophosphate uptake from seawater on to calcite and aragonite. *Geochimica et Cosmochimica Acta* 42: 1335-1340.

De La Rocha, C. L. and DePaolo, D. J. (2000). Isotopic evidence for variations in the marine calcium cycle over the Cenozoic. *Science* 289: 1176-1178.

Dennis, P. F., Rowe, P. J. and Atkinson, T. C. (2001). The recovery and isotopic measurement of water from fluid inclusions in speleothems. *Geochimica et Cosmochimica* 65: 871-884.

Desmarchelier, J. M. (1999). High-resolution palaeoenvironmental information from speleothems. Unpublished doctoral dissertation, University of Tasmania, Hobart.

Desmarchelier, J. and Goede, A. (1996). High resolution stable isotope analysis of a Tasmanian speleothem. *Papers and Proceedings of the Royal Society of Tasmania* 130: 7-13.

Desmarchelier, J. M., Goede, A., Ayliffe, L. K., McCulloch, M. T. and Moriarty, K. (2000). Stable isotope record and its palaeoenvironmental interpretation for a late Middle Pleistocene speleothem from Victoria Fossil Cave, Naracoote, South Australia. *Quaternary Science Reviews* 19: 763-774.

Dorale, J., Gonzalez, L., Reagan, M., Pickett, D., Murrell, M. and Baker, R. (1992). A high-resolution record of Holocene climate change in speleothem calcite from Cold Water Cave, northeast Iowa. *Science* 258: 1626-1630.

Dorr, H. and Munnich, K. (1986). Annual variations of the ^{14}C content of soil CO_2. *Radiocarbon* 28: 338-345.

Dreybrodt, W. (1980). Deposition of calcite from thin films of natural calcareous solutions and the growth of speleothems. *Chemical Geology* 29: 89-105.

Dreybrodt, W. (1982). A possible mechanism for growth of calcite speleothems without participation of biogenic carbon dioxide. *Earth and Planetary Science Letters* 58: 293-299.

Eberhard, R. (1996). Inventory and management of the Florentine Valley, Tasmania. Hobart: Forestry Tasmania.

Eisenhauer, A., Gussone, N., Dietzel, M., Heuser, A., Bock, B., Bohm, F., Spero, H. J., Lea, D. W., Buma, J., Zeebe, R. and Nagler, T. F. (2002). Kinetic effects on calcium isotopes ($\delta^{44}Ca$) fractionation on calcium carbonate. Goldschmidt conference abstract, Davos, Switerland, *Geochimica et Cosmochimica Acta* 66 (15A): A211-A211 Suppl. 1 August 2002.

Epstein, S. (1956). Variations of the O^{18}/O^{16} ratios of fresh H_2O and ice (pp. 20-28). (Nuclear Science Series report no. 19). American National Academy of Science.
Fairchild, I. J., Borsato, A., Tooth, A. F., Frisia, S., Hawkesworth, C. J., Huang, Y., McDermott, F. and Spiro, B. (2000). Controls on trace element (Sr-Mg) compositions of carbonate cave waters: implications for speleothem climatic records. *Chemical Geology* 166: 255-269.
Fairchild, I. J., Baker, A., Borsato, A., Frisia, S., Hinton, R. W., McDermott, F. and Tooth, A. F. (2001). Annual to sub-annual resolution of multiple trace-element trends in speleothems. *Journal of the Geological Society, London* 158: 831-841.
Farquhar, G. D., Henry, B. K. and Styles, J. M. (1997). A rapid on-line technique for determination of oxygen isotope composition of nitrogen-containing organic matter and water. *Rapid communications in mass spectrometry* 11: 1554-1560.
Farver, J. R. and Yund, R. A. (1996). Volume and grain boundary diffusion of calcium in natural and hot-pressed calcite aggregates. *Contributions to Mineralogy and Petrology* 123: 77-91.
Faure, G. (1986). Principles of Isotope Geology. New York: John Wiley and Sons.
Fayek, M., Harrison, T. M., Grove, M., McKeegan, K. D., Coath, C. D. and Boles, J. R. (2001). In situ stable isotopic evidence for protracted and complex carbonate cementation in a petroleum reservoir, North Coles Levee, San Joaquin Basin California, USA. *Journal of Sedimentary Research* 71: 444-458.
Fisler, D. K. and Cygan, R. T. (1999). Diffusion of Ca and Mg in calcite. *American Mineralogist* 84: 1392-1399.
Fitzharris, B. (1999). Research on glaciers and snow in New Zealand. *Progress in Physical Geography* 23: 469-500.
Fitzharris, B., Hay, J. and Jones, P. (1992). Behaviour of New Zealand glaciers and atmospheric circulation changes over the past 130 years. *The Holocene* 2: 97-105.
Folk, R. L. (1965). Petrology of sedimentary rocks. Austin: Hemphill.
Friedman, I. and O'Neil, J. (1977). Compilation of stable isotope fractionation factors of geochemical interest. US Geological Survey Professional Paper 440-KK.
Frisia, S., Borsato, A., fairchild, I. J. and McDermott, F. (2000). Calcite fabrics, growth mechanisms and environments of formation in speleothems (Italian Alps and SW Ireland). *Journal of Sedimentary Research* 70: 1183-1196.
Fritts, H. C. (1976). Tree rings and climate. London: Academic Press.
Gagan, M. K., Chivas, A. R. and Isdale, P. J. (1994). High-resolution isotopic records from corals using ocean temperature and mass-spawning chronometers. *Earth and Planetary Science Letters* 121: 549-558.
Galloway, R. W. (1965). Late Quaternary climates in Australia. *The Journal of Geology* 73: 603-618.
Galy, A., Bar-Matthews, M., Halicz, L. and O'Nions, R. K. (2002). Mg isotopic composition of carbonate: insight from speleothem formation. *Earth and Planetary Science Letters* 201: 105-115.
Gascoyne, M. (1982). Geochemistry of the Actinides and their daughters. In: M. Ivanovich, and R. S. Harmon (Eds.). Uranium series disequilibria applications to environmental problems. Oxford: Claredon Press.
Gascoyne, M. (1983). Trace-element partition coefficients in the calcite-water system and their paleoclimatic significance in cave studies. *Journal of Hydrology* 61: 213-222.
Gascoyne, M. (1992). Palaeoclimate determination from cave calcite deposits. *Quaternary Science Reviews* 11: 609-632.
Gascoyne, M. and Schwarcz, H. P. (1982). Carbonate and sulphate precipitates. In: M. Ivanovich, and R. S. Harmon (Eds.). Uranium series disequilibria applications to environmental problems. Oxford: Claredon Press.
Gascoyne, M., Schwarcz, H. P. and Ford, D. C. (1978). Uranium series dating and stable isotope studies of speleothems. *Transactions of the British Cave Research Association* 5: 91-111.

Gat, J. R. (1981a). Properties of the isotopic species of water: the 'isotope effect'. In: J. R. Gat, and R. Gonfiantini (Eds.). Stable isotope hydrology. Vienna: International Atomic Energy Agency.
Gat, J. R. (1981b). Isotopic fractionation. In: J. R. Gat, and R. Gonfiantini (Eds.). Stable isotope hydrology. Vienna: International Atomic Energy Agency.
Gat, J. R. and Matsui, E. (1991). Atmospheric water balance in the Amazon Basin: An isotopic evapotranspiration model. *Journal of Geophysical Research* 96(D7): 13179-13188.
Gat, J. R., Bowser, C. D. and Kendall, C. (1994). The contribution of evaporation from the Great Lakes to the continental atmosphere: Estimates based on stable isotope data. *Geophysical Research Letters* 21: 557-560.
Gedzelman, S. D. and Arnold, R. (1994). Modeling the isotopic composition of precipitation. *Journal of Geophysical Research* 99(D5): 10455-10471.
Gedzelman, S. D. and Lawrence, J. R. (1990). The isotopic composition of precipitation from two extratropical cyclones. *Monthly Weather Review* 118: 495-509.
Gedzelman, S. E., Lawrence, J. R., White, J. W. C. and Smiley, D. (1987). The isotopic composition of precipitation at Mohonk Lake, New York: the amount effect. *Journal of Geophysical Research* 92(D1): 1033-1040.
Gellatly, A., Chinn, T. and Rothlisberger, F. (1988). Holocene glacier variations in New Zealand: A review. *Quaternary Science Reviews* 7: 227-242.
Genty, D. and Massault, M. (1997). Bomb ^{14}C recorded in laminated speleothems: calculation of dead carbon proportion. *Radiocarbon* 39: 33-48.
Genty, D. and Massault, M. (1999). Carbon transfer dynamics from bomb-^{14}C and $\delta^{13}C$ time series of a laminated stalagmite from SW France-modelling and comparison with other stalagmite records. *Geochimica et Cosmochimica Acta* 63: 1537-1548.
Genty, D., Vokal, B., Obelic, B. and Massault, M. (1998). Bomb ^{14}C time history recorded in two modern stalagmites-importance for soil organic matter dynamics and bomb ^{14}C distribution over continents. *Earth and Planetary Science Letters* 160: 795-809.
Genty, D., Baker, A., Massault, M., Proctor, C., Gilmour, M., Pons-Branchu, E. and Hamelin, B. (2001). Dead carbon in stalagmites: Carbonate bedrock paleodissolution vs. ageing of soil organic matter. Implications for ^{13}C variations in speleothems. *Geochimica et Cosmochimica Acta* 65: 3443-3457.
Gilbert, J. M. (1958). Forest succession in the Florentine Valley, Tasmania. *Papers and Proceedings of the Royal Society of Tasmania* 93: 129-151.
Godwin, H. (1962). Half-life of Radiocarbon. *Nature* 195: 984.
Goede, A. (1994). Continuous early last glacial palaeoenvironmental record from a Tasmanian speleothem based on stable isotope and minor element variations. *Quaternary Science Reviews* 13: 283-291.
Goede, A. (1998). Quaternary Studies of Caves and Coasts. Unpublished doctoral dissertation, University of Tasmania, Hobart.
Goede, A. and Hitchman, M. A. (1984). Late Quaternary climatic change: Evidence from a Tasmanian speleothem. In: J. C. Vogel (Ed.). Late Cainozoic palaeoclimates of the Southern Hemisphere (pp. 221-232). Rotterdam: Balkema.
Goede, A. and Vogel, J. C. (1991). Trace element variations and dating of a Late Pleistocene Tasmanian speleothem. *Palaeogeography, Palaeoclimatology, Palaeoecology* 88: 121-131.
Goede, A., Green, D. C. and Harmon, R. S. (1982). Isotopic composition of precipitation, cave drips and actively forming speleothems at three Tasmanian cave sites. *Helictite* 19: 57-67.
Goede, A., Green, D. C. and Harmon, R. S. (1986). Late Pleistocene palaeotemperature record from a Tasmanian speleothem. *Australian Journal of Earth Sciences* 33: 333-342.
Goede, A., Veeh, H. and Ayliffe, L. (1990). Late Quaternary palaeotemperature records for two Tasmanian speleothems. Australian Journal of Earth *Sciences* 37: 267-278.
Goede, A., McDermott, F., Hawesworth, C., Webb, J. and Finlayson, B. (1996). Evidence of Younger Dryas and Neoglacial cooling in a Late Quaternary palaeotemperature record from a speleothem in eastern Victoria, Australia. *Journal of Quaternary Science* 11: 1-7.

Goede, A., McCulloch, M., McDermott, F. and Hawkesworth, C. (1998). Aeolian contribution to strontium and strontium isotope variations in a Tasmanian speleothem. *Chemical Geology* 149: 37-50.
Grove, J. M. (1988). The Little Ice Age. New York: Methuen and Co.
Gupta, S. K. and Polach, H. A. (1985). Radiocarbon dating practises at the Australian National University. Canberra: National Library of Australia Publishing.
Harmon, R., Thompson, P., Schwarcz, H. and Ford, D. (1978a). Pleistocene paleoclimates of North America as inferred from stable isotope studies of speleothems. *Quaternary Research* 9: 54-70.
Harmon, R., Schwarcz, H. and Ford, D. (1978b). Stable isotope geochemistry of speleothems and cave waters from the Flint Ridge-Mammoth Cave system, Kentucky: implications for terrestrial climate change during the period 230,000 to 100,000 years BP. *Journal of Geology* 86: 373-384.
Harmon, R., Schwarcz, H., Ford, D. and Koch, D. (1979). An isotopic paleotemperature record for late Wisconsinan time in northeast Iowa. *Geology* 7: 430-433.
Hatcher, L. M. (1995). Moondyne (Coronation) Cave (Caveworks report no. 3).
Hellstrom, J. C. (1998). Palaeoenvironmental records from the geochemistry of speleothems. Unpublished doctoral dissertation, Australian National University, Canberra.
Hellstrom, J. C. and McCulloch, M. T. (2000). Multi-proxy constraints on the climatic significance of trace element records from a New Zealand speleothem. *Earth and Planetary Science Letters* 179: 287-297.
Hellstrom, J., McCulloch, M. and Stone, J. (1998). A detailed 31,000 year record of climate and vegetation change, from the isotopic geochemistry of two New Zealand speleothems. *Quaternary Research* 50: 167-178.
Henderson, G. M. (2002). Seawater (U-234/U-238) during the last 800 thousand years. *Earth and Planetary Science Letters* 199: 97-110.
Hendy, C. (1971). The isotope geochemistry of speleothems-I. The calculation of the effects of different modes of formation on the isotopic composition of speleothems and their applicability as palaeoclimatic indicators. *Geochimica et Cosmochimica Acta* 35: 802-824.
Hendy, C. and Wilson, A. (1968). Palaeoclimatic data from speleothems. ***Nature*** 219: 48-51.
Hendy, E. J., Gagan, M. K., Alibert, C. A., McCulloch, M. T., Lough, J. M. and Isdale, P. J. (2002). Abrupt decrease in tropical Pacific Sea surface salinity at end of Little Ice Age. *Science* 295: 1511-1514.
Hessell, J. W. D. (1983). Climatic effects on the recession of the Franz Josef Glacier. *New Zealand Journal of Science* 26: 315-320.
Holden, N. E., Ed. (1991). Table of the isotopes. CRC Handbook of chemistry and physics, CRC Press Ltd.
Holland, H., Kirsipu, T., Huebner, J. and Oxburgh, U. (1963). On some aspects of the chemical evolution of cave waters. *Journal of Geology* 72: 36-67.
Holmgren, K., Karlin, W., Lauritzen, S. E. and more (1999). A 3000 year high resolution stalagmite-based record of palaeoclimate for northeastern South Africa. *The Holocene* 9(3): 295-309.
Huang, Y. and Fairchild, I. J. (2001). Partitioning of Sr^{2+} and Mg^{2+} into calcite under karst-analogue experimental conditions. *Geochimica et Cosmochimica Acta* 65: 47-62.
Huang, Y., Fairchild, I. J., Borsato, A., Frisia, S., Cassidy, N. J., McDermott, F. and Hawkesworth, C. J. (2001). Seasonal variations Sr, Mg and P in modern speleothems (Grotta di Ernesto, Italy). *Chemical Geology* 175: 429-448.
Imbrie, J. (1982). Astronomical theory of the Pleistocene ice ages: A brief historical review. *Icarus* 50: 408-422.
IOCI (1999). Towards understanding climate variability in south western Australia (Research reports of the Indian Ocean Climate Initiative). Melbourne: Bureau of Meteorology and Commonwealth Science and Industry Research Organisation.
Ishikawa, M. and Ichikuni, M. (1984). Uptake of sodium and potassium by calcite. *Chemical Geology* 42: 137-146.

Ivanovich, M. (1982). The Phenomenon of Radioactivity. In: M. Ivanovich and R. S. Harmon (Eds.). Uranium Series Disequilibria Applications to Environmental Problems. Oxford: Claredon Press.
Ivanovich, M. and Harmon, R. S. (Eds.). Uranium Series Disequilibria Applications to Environmental Problems. Oxford: Claredon Press.
Jones, P. D., Briffa, K. R., Barnett, T. P. and Tett, S. F. B. (1998). High-resolution palaeoclimatic records for the last millennium; interpretation, integration and comparison with general circulation model control-run temperatures. *The Holocene* 8: 455-471.
Jones, P. D., Osborn, T. J. and Briffa, K. R. (2001). The evolution of climate over the last millennium. *Science* 292: 662-667.
Jouzel, J. (1986). Isotopes in cloud physics: multiphase and multistage condensation processes. In: P. Fritz and J. C. Fontes (Eds.). Handbook of Environmental Isotope Geochemistry (pp. 61-112, Vol. 2, 2nd ed.). Amsterdam: Elsevier.
Jouzel, J. and Merlivat, L. (1984). Deuterium and oxygen 18 in precipitation: Modelling of the isotopic effects during snow formation. *Journal of Geophysical Research* 89: 11749-11757.
Jouzel, J., Lorius, C., Petit, J. R., Genthon, C., Barkov, N. I., Kotlyakov, V. M. and Petrov, V. M. (1987). Vostok ice core: a continuous isotope temperature record over the last climatic cycle (160,000 years). *Nature* 329: 403-408.
Jouzel, J., Alley, R. B., Cuffey, K. M., Dansgaard, W., Grootes, P., Hoffmann, G., Johnsen, S. J., Koster, R. D., Peel, D., Shuman, C. A., Stievenard, M., Stuiver, M. and White, J. (1997a). Validity of the temperature reconstruction from water isotopes in ice cores. *Journal of Geophysical Research* 102(C12): 26471-26487.
Jouzel, J., Froehlich, K. and Schotterer, U. (1997b). Deuterium and oxygen-18 in present-day precipitation: data and modelling. *Hydrological Sciences-Journal-des Sciences Hydrologiques* 42: 747-763.
Kanamitsu, M., Ebisuzaki, W., Woolen, J., Potter, J. and Fiorino, M. (1999). Overview of NCEP/DOE Reanalysis-2. Second WCRP International Conference on Reanalyses. Reading, United Kingdom, World Meteorological Organisation.
Kato, K. (1978). Factors controlling oxygen isotopic composition of fallen snow in Antarctica. *Nature* 272: 46-48.
Katz, A. (1973). The interaction of magnesium with calcite during crystal growth at 25-95°C and one atmosphere. *Geochimica et Cosmochimica Acta* 36: 481-496.
Kaufman, A., Wasserburg, G., Porcelli, D., Bar-Matthews, M., Ayalon, A. and Halicz, L. (1998). U-Th isotope systematics from the Soreq cave, Israel and climatic correlations. *Earth and Planetary Science Letters* 156: 141-155.
Keywood, M. D., Ayers, G. P., Gillett, R. W. and Selleck, P. W. (2001). Precipitation chemistry. In: N. W. Tindale, N. Derek, R. J. Francey (Eds.). Baseline 97-98 (pp. 110-110). Melbourne: Bureau of Meteorology and Commonwealth Science and Industrial Research Organisation.
Kiernan, K. (1971). Caves and karst of Junee-Florentine, Tasmania. *Australian Speleological Federation News Letter* 53: 4-10.
Kiernan, K. (1989). Karst, caves and management at Mole Creek, Tasmania (Report no. 130). Hobart: Parks, Wildlife and Heritage.
Kim, S. T. and O'Neil, J. R. (1997). Equilibrium and nonequilibrium oxygen isotope effects in synthetic carbonates. *Geochimica et Cosmochimica Acta* 61: 3461-3475.
Kitagawa, H. and van der Plicht, J. (1998). Atmospheric radiocarbon calibration to 45,000 yr B.P.: Late glacial fluctuations and cosmogenic isotope production. *Science* 279: 1187-1190.
Koster, R. D., Jouzel, J., Suozzo, R. J., Russell, G. L., Broecker, W., Rind, D. and Eagleson, P. (1986). Global sources of local precipitation as determined by the NASA/GISS GCM. *Geophysical Research Letters* 13: 121-124.
Koster, R. D., Jouzel, J., Suozzo, R. J. and Russell, G. L. (1992). Origin of July Antarctic precipitation and its influence on deuterium content: a GCM analysis. *Climate Dynamics* 7: 195-203.
Koster, R. D., de Valpine, D. P. and Jouzel, J. (1993). Continental water recycling and $H_2{}^{18}O$ concentrations. *Geophysical Research Letters* 20: 2215-2218.

Kreutz, K. J., Mayewski, P. A., Meeker, L. D., Twickler, M. S., Whitlow, S. I. and Pittalwala, I. I. (1997). Bipolar changes in atmospheric circulation during the Little Ice Age. *Science* 277: 1294-1296.
Krinner, G. and Genthon, C. (1997). GCM analysis of local influences on ice core signals. *Geophysical Research Letters* 24: 2825-2828.
Ku, T. L. and Li, H. C. (1998). Speleothems as high-resolution paleoenvironment archives: Records from northeastern China. *Proceedings of the Indian Academy of Science (Earth and Planetary Sciences)* 107: 321-330.
Ku, T. L. and Liang, Z. C. (1984). The dating of impure carbonates with decay-series isotopes. *Nuclear Instruments, methods and physics research* 223: 563-571.
Kutzbach, J. E., Prell, W. L. and Ruddiman, W. F. (1993). Sensitivity of Eurasian climate to surface uplift of the Tibetan Plateau. *Journal of Geology* 101: 177-190.
Lamb, H. H. (1977). Climate: present, past and future. London: Methuen and Co.
Lambeck, K. and Chappell, J. (2001). Sea level change through the last glacial cycle. *Science* 292: 679-686.
Langmuir, D. (1978). Uranium solution-mineral equilibria at low temperatures with applications to sedimentary ore deposits. *Geochmica et Cosmochmica Acta* 42: 547-569.
Lauritzen, S. (1995). High-resolution paleotemperature proxy record for the Last Interglaciation based on Norwegian speleothems. *Quaternary Research* 43: 133-146.
Lauritzen, S. E. and Lundberg, J. (1999). Calibration of the speleothem delta function: an absolute temperature record for The Holocene in northern Norway. *The Holocene* 9: 659-669.
Lavery, B., Kariko, A. and Nicholls, N. (1992). A historical rainfall data set for Australia. *Australian Meteorology Magazine* 40: 33-39.
Lawrence, J. R. and Gedzelman, S. D. (1996). Low stable isotope ratios of tropical cyclone rains. *Geophysical Research Letters* 23: 527-530.
Lawrence, J. R., Gedzelman, S. D., White, J. W. C., Smiley, D. and Lazov, P. (1982). Storm trajectories in eastern US D/H isotopic composition of precipitation. *Nature* 296: 638-640.
Lawrence, J. R., Gedzelman, S. D., Zhang, X. and Arnold, R. (1998). Stable isotope ratios of rain and vapour in 1995 hurricanes. *Journal of Geophysical Research* 103(D10): 11381-11400.
Lawver, L. A. and Gahagan, L. M. (1998). Opening of Drake Passage and its impact on Cenozioc ocean circulation. In: T. C. Crowley and K. C. Burke (Eds.). Tectonic boundary conditions for climate reconstructions. Oxford: Oxford University Press.
Lea, D. W., Pak, D. K. and Spero, H. J. (2000). Climate impact of late Quaternary equatorial Pacific temperature variations. *Science* 289: 1719-1724.
Lebron, I. and Suarez, D. L. (1998). Kinetics and mechanisms of precipitation of calcite as affected by PCO_2 and organic ligands at 25C. *Geochimica et Cosmochimica Acta* 62: 405-416.
Lorens, R. B. (1981). Sr, Cd, Mn and Co distribution coefficients in calcite as a function of calcite precipitation rate. *Geochimica et Cosmochimica Acta* 45: 553-561.
Lorius, C., Jouzel, J., Ritz, C., Merlivat, L., Barkov, N., Y, K. and Kotlyakov, V. (1985). A 150,000-year climatic record from Antarctic ice. *Nature* 316: 591-596. Data provided by the National Snow and Ice Data Center, University of Colorado at Boulder, and the WDC-A for Paleoclimatology, National Geophysical Data Center, Boulder, Colorado.
Ludwig, K. R. and Paces, J. B. (2002). Uranium-series dating of pedogenic silica and carbonate, Crater Flat, Nevada. *Geochimica et Cosmochimica Acta* 66: 487-506.
Ludwig, K. R. and Titterington, D. M. (1994). Calculation of ^{230}Th/U isochrons, ages, and errors. *Geochimica et Cosmochimica Acta.* 58: 5031-5042.
Ludwig, K. R., Simmons, K. R., Szabo, B. J., Winograd, I. J., Landwehr, J. M., Riggs, A. C. and Hoffman, R. J. (1992). Mass-spectrometric ^{230}Th-^{234}U-^{238}U dating of Devils Hole calcite vein. *Science* 258: 284-287.
Luo, S. and Ku, T. L. (1991). U-series isochron dating; a generalized method employing total-sample dissolution. *Geochimica et Cosmochimica Acta* 55: 555-564.
Mann, M., Bradley, R. and Hughes, M. (1998). Global-scale temperature patterns and climate forcing over the past six centuries. *Nature* 392: 779-787.
Manning, M. R. and Melhuish, W. H. (1994). Atmospheric D^{14}C record from Wellington. In: Trends: a compendium of data on global change. Carbon Dioxide Information Analysis Center,

Oak Ridge National Laboratory, U.S. Department of Energy, Oak Ridge, Tennessee. Retrieved from the World Wide Web: http:cdiac.esd.ornl.gov/trends/co2/welling.html.
Marshall, J. F. (1983). Submarine cementation in a high-energy platform reef; One Tree Reef, southern Great Barrier Reef. *Journal of Sedimentary Petrology* 53: 1133-1149.
Martinson, D. G., Pisias, N. G., Hays, J. D. and more (1987). Age dating and the orbital theory of the ice ages: development of a high-resolution 0 to 300,000 year chronostratigraphy. *Quaternary Research* 27: 1-29.
Matthews, A., Ayalon, A. and Bar-Matthews, M. (2000). D/H ratios of fluid inclusions of Soreq cave (Israel) speleothems as a guide to the Eastern Mediterranean meteoric water line relationships in the last 120 years. *Chemical Geology* 166: 183-191.
Matthews, P. G. (1985). Australian karst index. Melbourne: Australian Speleological Federation.
McConnaughey, T. (1989a). ^{13}C and ^{18}O isotope disequilibrium in biological carbonates: I Patterns. *Geochimica et Cosmochimica Acta* 53: 151-162.
McConnaughey (1989b). ^{13}C and ^{18}O isotope disequilibrium in biological carbonates: II In vitro simulation of kinetic isotope effects. *Geochimica et Cosmochimica Acta* 53: 163-171.
McCrea, J. M. (1950). On the isotopic chemistry of carbonates and a paleotemperature scale. *Journal of Chemical Physics* 18: 849-857.
McDermott, F., Stringer, C., Grun, R., Williams, C. T., Din, V. K. and Hawkesworth, C. J. (1996). New Late-Pleistocene uranium-thorium and ESR dates for the Singa hominid (Sudan). *Journal of Human Evolution* 31: 507-516.
McDermott, F., Mattey, D. P. and Hawkesworth, C. (2001). Centennial-scale Holocene climate variability revealed by a high-resolution speleothem $\delta^{18}O$ record from SW Ireland. *Science* 294: 1328-1330.
McGarry, S. F. and Baker, A. (2000). Organic acid fluorescence: applications to speleothem palaeoenvironmental reconstruction. *Quaternary Science Reviews* 19: 1087-1101.
McGarry, S., Bar-Matthews, M., Matthews, A. and Ayalon, A. (2002). Palaeohydrology in the Eastern Mediterranean from speleothem fluid inclusion D/H analyses. Goldschmidt conference abstract, Davos, Switerland, *Geochimica et Cosmochimica Acta* 66 (15A): A500-A500 Suppl. 1 August 2002.
McKeegan, K. D., Leshin, L. A., Russell, S. S. and MacPherson, G. J. (2002). Oxygen isotopic abundances in calcium-aluminum-rich inclusions from ordinary chondrites: Implications for nebular heterogeneity. *Science* 295: 1051-1054.
Meadows, J. W., Armani, R. J., Callis, E. L. and Essling, A. M. (1980). Half-life of ^{230}Th. *Physical Review* C22: 750-754.
Merlivat, L. (1978). Molecular diffusivities of $H_2{}^{16}O$, $HD^{16}O$, and $H_2{}^{18}O$ in gases. *Journal of Chemical Physics* 69: 2864-2871.
Metservice (2002). Mean Air temperatures 1961-1998, New Zealand climate service. Retrieved from the World Wide Web: http://www.metservice.co.nz/home/index.asp.
Miller, G., Magee, J. and Jull, A. (1997). Low-latitude glacial cooling in the Southern Hemisphere from amino-acid racemization in emu eggshells. *Nature* 385: 241-244.
Millero, F., Huang, F., Zhu, X., Liu, X. and Zhang, J.-Z. (2001). Adsorption and desorption of phosphate on calcite and aragonite in seawater. *Aquatic Chemistry* 7: 33-56.
Morgan, V. I. and van Ommen, T. D. (1997). Seasonality in late-Holocene climate from ice-core records. *The Holocene* 7: 351-354.
Morse, J. W. and Bender, M. L. (1990). Partition coefficients in calcite: Examination of factors influencing the validity of experimental results and their application to natural systems. *Chemical Geology* 82: 265-277.
Morse, J. W. and Casey, W. H. (1988). Ostwald processes and mineral paragenesis in sediments. *American Journal of Science* 288: 537-560.
Morse, J. W. and Mackenzie, F. T. (1990). Geochemistry of sedimentary carbonates. Amsterdam: Elsevier.
Mucci, A. (1987). Influence of temperature on the composition of magnesian calcite overgrowths: precipitation from seawater. *Geochimica et Cosmochimica Acta* 51: 1977-1987.

Mucci, A. and Morse, J. W. (1983). The incorporation of calcite overgrowths: influences of growth rate and solution composition. *Geochimica et Cosmochimica Acta* 47: 217-233.
Nägler, T. F. and Müller, A. E. a. A. (2000). The ^{44}Ca-temperature calibration on fossil and cultured Globigerinoides sacculifer: New tool for reconstruction of past sea surface temperatures. Geochemistry, Geophysics, Geosystems 1: 1-9.
Nicholls, N. and Lavery, B. (1992). Australian rainfall trends during the twentieth century. *International Journal of Climatology* 12: 153-163.
Noone, D. and Simmonds, I. (1998). Implications for the interpretation of ice-core isotope data from analysis of modelled Antarctic precipitation. *Annals of Glaciology* 27: 398-402.
Oomori, T., Kaneshima, H., Maezato, Y. and Kitano, Y. (1987). Distribution coefficient of Mg^{2+} ions between calcite and solution at 10-50°C. *Marine Chemistry* 20: 327-336.
Paillard, D., Labeyrie, L. and Yiou, P. (1996). Macintosh Program Performs Time-Series Analysis. *Eos, Transactions, American Geophysical Union* 77: 379.
Paquette, J. and Reeder, R. J. (1990). New type of compositional zoning in calcite: insights into crystal-growth mechanisms. *Geology* 18: 1244-1247.
Paquette, J. and Reeder, R. J. (1995). Relationship between surface structure, growth mechanism, and trace element incorporation in calcite. *Geochimica et Cosmochimica Acta* 59: 735-749.
Paquette, J., Chien, J., Mucci, A. and Vali, H. (2002). Abiotic calcites: crystal morphology, zoning and microstructure. Goldschmidt conference abstract, Davos, Switerland, *Geochimica et Cosmochimica Acta* 66 (15A): A138-A138 Suppl. 1 August 2002.
Pearce, N. J. G., Perkins, W. T., Westgate, J. A., Gorton, M. P., Jackson, S. E., Neal, C. R. and Chenery, S. P. (1996). A compilation of new and published major and trace element data for NIST SRM 610 and NIST SRM 612 glass reference materials. *Geostandards Newsletter* 21: 115-144.
Petit, J. R., White, J. W. C., Young, N. W., Jouzel, J. and Korotkevich, Y. S. (1991). Deuterium excess in recent Antarctic snow. *Journal of Geophysical Research* 96(D3): 5113-5122.
Pillans, B. (1991). New Zealand Quaternary stratigraphy: An overview. *Quaternary Science Reviews* 10: 405-418.
Pingitore, N. E. and Eastman, M. P. (1984). The experimental partitioning of Ba^{2+} into calcite. *Chemical Geology* 45: 113-120.
Pingitore, N. E. and Eastman, M. P. (1985). Barium partitioning during the transformation of corals from aragonite to calcite. *Chemical Geology* 48: 183-187.
Porter, S. C. (1975a). Glaciation limit in New Zealand's Southern Alps. *Arctic and Alpine Research* 7: 33-37.
Porter, S. C. (1975b). Equilibrium-line altitudes of Late Quaternary glaciers in the Southern Alps, New Zealand. *Quaternary Research* 5: 27-47.
Price, D. M., Brooke, B. P. and Woodroffe, C. D. (2001). Thermoluminescence dating of aeolianites from Lord Howe Island and South-West Western Australia. *Quaternary Science Reviews* 20: 841-846.
Rindsberger, M., Jaffe, S., Rahamim, S. and Gat, J. R. (1990). Patterns of the isotopic composition of precipitation in time and space: data from the Israeli storm water collection program. *Tellus* 42B: 263-271.
Roberts, M., Smart, P., Perkins, W., Pearce, N. J. G., Hawkesworth, C. J. (1996). Trace elements in Holocene speleothems. In: Climate Change: The Karst Record University of Bergen, Norway, Karst Waters Institute Special Publication 2.
Roberts, M. S., Smart, P. L. and Baker, A. (1998). Annual trace element variations in a Holocene speleothem. *Earth and Planetary Science Letters* 154: 237-246.
Roberts, M. S., Smart, P. L., Hawkesworth, C. J., Perkins, W. T. and Pearce, N. J. G. (1999). Trace element variations in coeval Holocene speleothems from GB Cave southwest England. *The Holocene* 9: 707-713.
Romanek, C., Grossman, E. and Morse, J. (1992). Carbon isotopic fractionation in synthetic aragonite and calcite: effects of temperature and precipitation rate. *Geochimica et Cosmochimica Acta* 56: 419-430.

Rozanski, K., Sonntag, C. and Munnich, K. O. (1982). Factors controlling stable isotope composition of European precipitation. *Tellus* 34: 142-150.
Rozanski, K., Araguas-Araguas, L. and Gonfiantini, R. (1993). Isotopic patterns in modern global precipitation. In: P. K. Swart, K. C. Lohmann, J. McKenzie and S. Savin (Eds.). Climate change in continental isotopic records. Washington: American Geophysical Union. Geophysical Monograph Series 78.
Salati, E., Dali'Olio, A., Matsui, E. and Gat, J. R. (1979). Recycling of water in the Amazon Basin: An isotopic study. *Water Resources Research* 15: 1250-1258.
Schrag, D. P., Hampt, G. and Murray, D. W. (1996). Pore fluid constraints on the temperature and oxygen isotopic composition of the glacial ocean. *Science* 272: 1930-1932.
Schwarcz, H. P. (1980). Absolute age determination of archaeological sites by uranium series dating of travertines. *Archaeometry* 22: 3-24.
Schwarcz, H. P. (1986). Geochronology and isotopic geochemistry of speleothems. In: P. Fritz and J. C. Fontes (Eds.). Handbook of Environmental Isotope Geochemistry (Vol. 2, pp. 271-304, 2nd ed.). Amsterdam: Elsevier.
Schwarcz, H. P. (1996). Paleoclimate inferences from stable isotopic studies of speleothem. In: Climate Change: The Karst Record University of Bergen, Norway, Karst Waters Institute Special Publication 2.
Schwarcz, H. P. and Latham, A. G. (1989). Dirty calcites 1. Uranium series dating of contaminated calcite using leachates alone. *Chemical Geology* 80: 35-43.
Schwarcz, H. P. and Yonge, C. (1983). Stable isotopes of fluid inclusions in speleothems and their paleoclimatic significance. *Geochimica et Cosmochimica Acta* 40: 657-665.
Serefiddin, F., Schwarcz, H. P. and Ford, D. C. (2002). Paleotemperature reconstruction using isotopic variation in speleothem fluid inclusion water. Goldschmidt conference abstract, Davos, Switerland, *Geochimica et Cosmochimica Acta* 66 (15A): A697-A697 Suppl. 1 August 2002.
Shackleton, N. J. (2000). The 100,000-year Ice-Age cycle identified and found to lag temperature, carbon dioxide and orbital eccentricity. *Science* 289: 1897-1902.
Sinclair, D. J., Kinsley, L. P. J. and McCulloch, M. T. (1998). HIgh resolution analysis of trace elements in corals by laser ablation ICP-MS. *Geochimica et Cosmochimica Acta* 62: 1889-1901.
Singh, G., Opdyke, N. D. and Bowler, J. M. (1981). Late Cainozoic stratigraphy, palaeomagnetic chronology and vegetation history from Lake George, NSW. *Journal of the Geological Society of Australia* 28: 435-452.
Smart, P. L., Roberts, M. S., Baker, A. and Richards, D. A. (1996). Palaeoclimate determination from speleothems - a critical appraisal of the state of the art. In: Climate Change: The Karst Record University of Bergen, Norway, Karst Waters Institute Special Publication 2.
Smith, I. N., McIntosh, P., Ansell, T. J., Reason, C. J. C. and McInnes, K. (2000). South-west Western Australian winter rainfall and its association with Indian Ocean climate variability. *International Journal of Climatology* 20: 1913-1930.
Soons, J. M. (1979). Late Quaternary environments in the central South Island of New Zealand. *New Zealand Geographer* 35: 16-23.
Spotl, C. and Mangini, A. (2002). Stalagmite from the Austrian Alps reveals Dansgaard-Oeschger events during isotope stage 3: Implications for the absolute chronology of Greenland ice cores. *Earth and Planetary Science Letters* 6356: 1-12.
Stewart, M. K. (1975). Stable isotope fractionation due to evaporation and isotopic exchange of falling water drops. *Journal of Geophysical Research* 80: 1133-1146.
Stewart, M. K., Cox, M. A., James, M. R. and Lyon, G. L. (1983). Deuterium in New Zealand rivers and streams (Report no. 17). Lower Hutt: New Zealand Institute of Nuclear Sciences.
Stirling, C. H., Esat, T. M., McCulloch, M. T. and Lambeck, K. (1995). High-precision U-series dating of corals from Western Australia and implications for the timing and duration of the last interglacial. *Earth and Planetary Science Letters* 135: 115-130.
Stirling, C. H., Esat, T. M., Lambeck, K. and McCulloch, M. T. (1998). Timing and duration of the last interglacial; evidence for a restricted interval of widespread coral reef growth. *Earth and Planetary Science Letters* 160: 745-762.

Stuiver, M. and Grootes, P. (2000). GSIP2 oxygen isotope ratios. *Quaternary Research* 53: 277-284.
Stuiver, M. and Polach, H. A. (1977). Discussion: reporting of ^{14}C data. *Radiocarbon* 19: 355-363.
Stuiver, M. and Reimer, P. J. (1993). Extended ^{14}C database and revised CALIB radiocarbon calibration program. *Radiocarbon* 35: 215-230.
Stuiver, M., Reimer, P. J., Bard, E., Beck, J. W., Burr, G. S., Hughen, K. A., Kromer, B., McCormac, G., Plicht, J. v. d. and Spurk, M. (1998). Intcal98 radiocarbon age calibration, 24,000-0 cal BP. *Radiocarbon* 40: 1041-1083.
Sturman, A. and Tapper, N. (1996). The weather and climate of Australia and New Zealand. Melbourne: Oxford University Press.
Suggate, R. P. (1965). Late Pleistocene Geology of the northern part of the South Island, New Zealand. New Zealand Department of Science and Industry Research Bulletin 77.
Suggate, R. P. (1990). Late Pliocene and Quaternary glaciations of New Zealand. *Quaternary Science Reviews* 9: 175-197.
Talma, A. S. and Vogel, J. C. (1992). Late Quaternary palaeotemperatures derived from a speleothem from Cango Caves, Cape Province, South Africa. *Quaternary Research* 37: 203-213.
Tang, K. and Feng, X. (2001). The effect of soil hydrology on the oxygen and hydrogen isotopic compositions of plants' source water. *Earth and Planetary Science Letters* 185: 355-367.
Thomas, R. (2002). A beginner's guide to ICP-MS. *Spectroscopy* 17(4): 34-39.
Thompson, L. G., Mosely-Thompson, E., Dansgaard, W. and Grootes, P. M. (1986). The Little Ice Age as recorded in the stratigraphy of the tropical Quelccaya ice cap. *Science* 234: 361-364.
Thorne, A., Grun, R., Mortimer, G., Spooner, N. A., Simpson, J. J., McCulloch, M., Taylor, L. and Curnoe, D. (1999). Australia's oldest human remains: age of the Lake Mungo 3 skeleton. *Journal of Human Ecology* 36: 591-612.
Tindale, N. W., Derek, N. and Francey, R. J. (2001). Baseline atmospheric program Australia 1997-1998 (Report no. 122). Melbourne: Bureau of Meteorology and Commonwealth Science and Industrial Research Organisation.
Treble, P. C. (1998). Late Quaternary palaeoclimates inferred from two Tasmanian speleothems. Unpublished Honours dissertation. University of Sydney, Sydney.
Tsesorio, A. J. and Pankow, J. F. (1996). Solid solution partitioning of Sr^{2+}, Ba^{2+}, and Cd^{2+} to calcite. *Geochimica et Cosmochimica Acta* 60: 1053-1063.
Turner, J. V. (1982). Kinetic fractionation of carbon-13 during calcium carbonate precipitation. *Geochimica et Cosmochimica Acta* 46: 1183-1191.
Valley, J. W., Graham, C. M., Harte, B., Eiler, J. M. and Kinny, P. D. (2001). Ionmicroprobe analysis of oxygen, carbon and hydrogen isotope ratios. In: M. A. McKibben, W. C. Shanks, and W. I. Ridley (Eds.). Applications of microanalytical techniques to understanding mineralising processes (Report no. 7). Society of Economic Geologists.
van de Geer, G., Fitzsimmons, S. J. and Colhoun, E. A. (1989). Holocene to middle Last Glaciation vegetation history at Newall Creek, western Tasmania. *New Phytologist* 111: 549-558.
van Ommen, T. D. and Morgan, V. (1997). Calibrating the ice core paleothermometer using seasonality. *Journal of Geophysical Research* 102(D8): 9351-9357.
Veizer, J. (1983a). Trace elements and isotopes in sedimentary carbonates. In: R. J. Reeder (Ed.). Carbonates: Mineralogy and Chemistry. (pp. 265-300, Vol. 11). Virginia: Mineralogical Society of America.
Veizer, J. (1983b). Chemical diagenesis of carbonates: theory and application of trace element technique. In: M. A. Arthur, T. F. Anderson, I. R. Kaplan, J. Veizer, and L. S. Land (Eds.). Stable isotopes in sedimentary geology. (Society of Economic Paleontologists and Mineralogists Short course no. 10). Dallas: Society of Economic Paleontologists and Mineralogists.
Veizer, J., Compston, W., Clauer, N. and Schidlowski, M. (1983). $^{87}Sr/^{86}Sr$ in late Proterozoic carbonates; evidence for a "mantle" event at approximately 900 Ma ago. *Geochimica et Cosmochimica Acta* 47: 295-302.

Verheyden, S., Keppens, E., Fairchild, I., McDermott, F. and Weis, D. (2000). Mg, Sr and Sr isotope geochemistry of a Belgian Holocene speleothem: implications for paleoclimate reconstructions. *Chemical Geology* 169: 131-144.
Vogel, J. C. (1983). ^{14}C Variations during the Upper Pleistocene. *Radiocarbon* 25: 213-218.
Wang, Y. J., Cheng, H., Edwards, R. L., An, Z. S., Wu, J. Y., Shen, C. C. and Dorale, J. A. (2001). A high-resolution absolute dated late Pleistocene monsoon record from Hulu Cave, China. *Science* 294: 2345-2348.
Watson, E. B. (1996). Surface enrichment and trace-element uptake during crystal growth. *Geochimica et Cosmochimica Acta* 60: 5013-5020.
Welker, J. M. (2000). Isotopic ($\delta^{18}O$) characteristics of weekly precipitation collected across the USA: an initial analysis with application to water source studies. *Hydrological Processes* 14: 1449-1464.
Wenk, H.-R., Barber, D. J. and Reeder, R. J. (1983). Microstructures in carbonates. In: R. J. Reeder (Ed.). Carbonates: Mineralogy and Chemistry. (pp. 301-367, Vol. 11). Virginia: Mineralogical Society of America.
White, J. W. C. and Gedzelman, S. D. (1984). The isotopic composition of atmospheric water vapour and the concurrent meteorological conditions. *Journal of Geophysical Research* 89(D3): 4937-4939.
Williams, P. (1996). A 230 ka record of glacial and interglacial events from Aurora Cave, Fiordland, New Zealand. *New Zealand Journal of Geology and Geophysics* 39: 225-241.
Williams, P. W., Marshall, A., Ford, D. C. and Jenkinson, A.V. (1999). Palaeoclimatic interpretation of stable isotope data from Holocene speleothems of the Waitomo district, North Island, New Zealand. *The Holocene* 9: 649-657.
Wilson, R. (1990). Soils and soil erosion. In: A. P. Scanlon, G. J. Fish, and M. L. Yaxley (Eds.). Behind the scenery: Tasmania's landform and Geology. (Report no. 163). Hobart: Tasmanian Department of Education and the Arts.
Winograd, I. J., Coplen, T. B., Landwehr, J. M., Riggs, A. C., Ludwig, K. R., Szabo, B. J., Kolesar, P. T. and Revesv, K. M. (1992). Continuous 500,000 year climate record from vein calcite in Devils Hole, Nevada. *Science* 258: 255-260.
Yapp, C. J. (1982). A model for the relationship precipitation D/H ratios and precipitation intensity. *Journal of Geophysical Research* 87: 9614-9620.
Yokoyama, Y. (1999). Sea-level change in Australasia and the radiocarbon time scale calibration during the last 50,000 years. Unpublished doctoral dissertation. The Australian National University, Canberra.
Yonge, C. J., Ford, D. C., Gray, J. and Schwarcz, H. P. (1985). Stable isotope studies of cave seepage water. *Chemical Geology* 58: 97-105.
Yurtsever, Y. and Gat, J. R. (1981). Atmospheric waters. In: J. R. Gat and R. Gonfiantini (Eds.). Stable isotope hydrology: deuterium and oxygen-18 in the water cycle (pp. 103-139). Vienna: International Atomic Energy Agency.
Zachos, J., Pagani, M., Sloan, L., Thomas, E. and Billups, K. (2001). Trends, rhythms, and aberrations in global climate 65 Ma to present. *Science* 292: 686-693.

Appendix I

Sample	Median distance above base (mm)	Sample fired?	Mass (g)	$^{238}U_{conc}$ ($\mu g\ g^{-1}$)	[$^{230}U/^{238}U$] activity	$\delta^{234}U_T$ ± 2σ error	[$^{230}Th/^{232}Th$] activity	Age ± 2σ error (ka)
FC-S8 U1	5	Y	5.12	0.096	0.0427 ± 0.0025	569 ± 4.43	2.596	2.99 ± 0.17
FC-S7 U1	5	Y	4.49	0.104	0.0817 ± 0.0031	587.83 ± 3.58	7.60	5.73 ± 0.22
LY-STAL1 U1	28	N	5.27	0.031	0.3292 ± 0.0108	1664.30 ± 115.67	43.26 ± 1.84	14.54 ± 1.13
LY-STAL1 U2	2320	N	5.50	0.019	0.1291 ± 0.0130	1246.48 ± 7.01	12.60 ± 1.34	6.47 ± 0.76
LY-F1 U2	55	Y	4.77	0.026	0.2394 ± 0.0186	1576.95 ± 29.90	14.783	10.51 ± 0.82
ES-F1 U1	190	N	5.26	0.066	0.0225 ± 0.0011	84.40 ± 1.89	1.87 ± 0.15	2.28 ± 0.50
ES-F1 U2	110	N	4.81	0.062	0.0795 ± 0.0015	61.02 ± 1.10	78.51 ± 1.20	8.47 ± 0.90
ES-F1 U6	20	N	5.03	0.017	0.2265 ± 0.0218	79.44 ± 4.62	2.01 ± 0.12	25.54 ± 2.37
NC U1	4	Y	3.19	0.152	2.3225 ± 0.0211	2910.66 ± 5.17	122.34	86.16 ± 0.78
NW U1	367	Y	1.67	0.378	1.9330 ± 0.0753	3426.30 ± 13.73	4002.97	57.69 ± 2.25
YB1_1	-	N	1.91	0.116	0.436 ± 0.008	748.92 ± 5.37	330.62 ± 30.60	30.56 ± 0.81
YB1_3	-	N	1.89	0.117	0.418 ± 0.004	745.60 ± 1.35	349.15 ± 4.30	29.166 ± 0.38
YB1_5	-	N	0.94	0.117	0.408 ± 0.019	745.89 ± 1.14	318.13 ± 16.13	28.36 ± 0.21
YB1_6	-	N	1.08	0.117	0.398 ± 0.018	742.21 ± 2.00	235.73 ± 34.97	27.68 ± 1.99

FC-S7: Stalagmite 190 mm tall collected from Frankcombe Cave, Florentine Valley, Tasmania.

LY-F1: Small section of broken flowstone (60 mm tall) collected in Lynds Cave, Mole Creek, Tasmania.

NC/NW: Two pieces of broken stalagmite (NC basal 215 mm tall; NW top 390 mm tall) collected from Newdegate Cave, Hastings, Tasmania.

YB1: RSES internal speleothem standard prepared by J. C. Hellstrom (Hellstrom, 1998).

All other speleothems are described in Chapter 2.

Appendix II

LA-ICP-MS trace element concentrations for entire length of MND-S1 (32 µm spot)

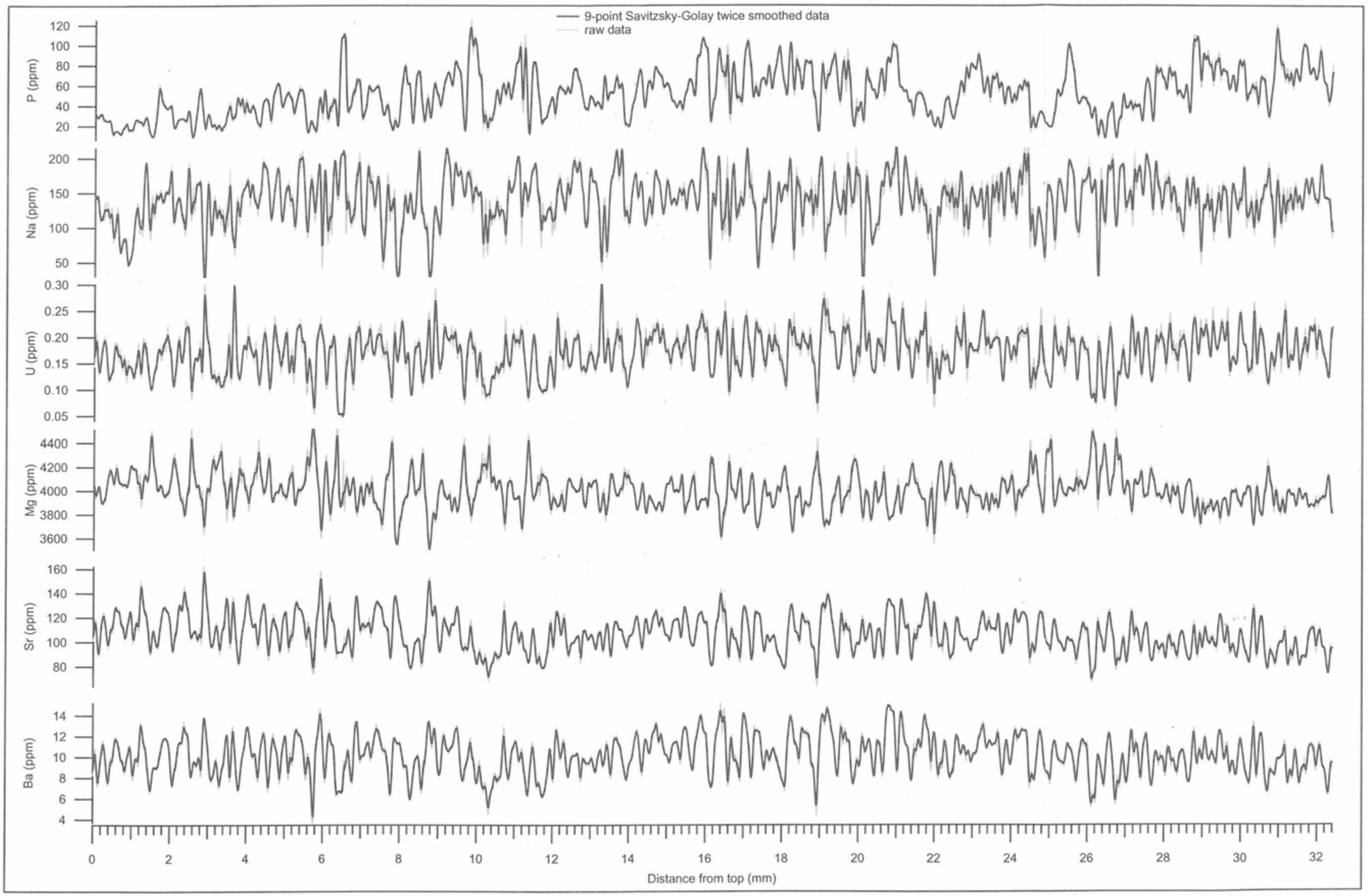

APPENDIX III

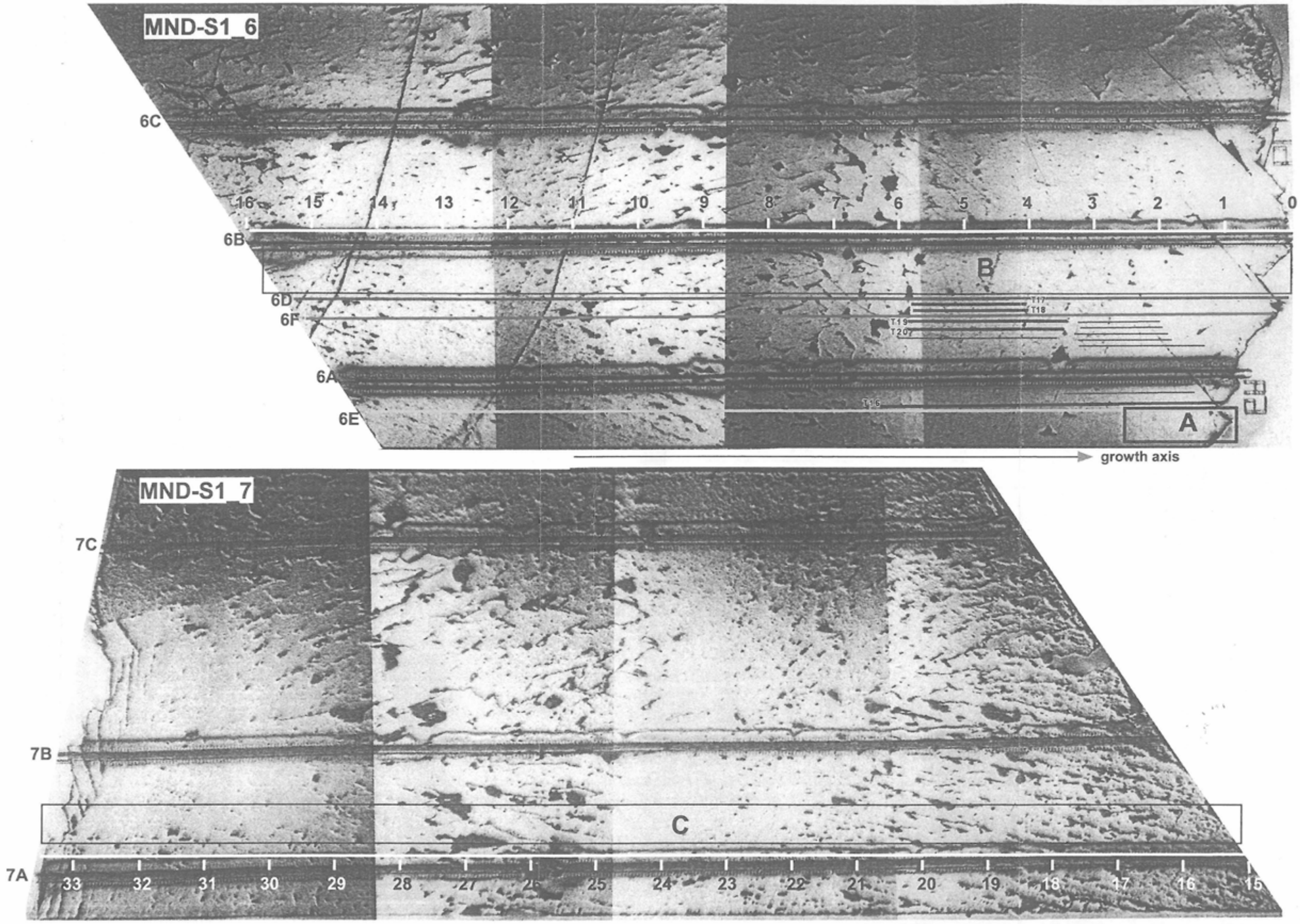

Image is a mosaic of photographs taken under reflected light on gold-coated samples. Scale units are in mm. The labels MND-S1_6 and MND-S1_7 refer to sections cut from MND-S1.

Box A: Ba concentration map constructed from LA-ICP-MS acquisition of 7 adjacent tracks using the 5x50 μm slit.
Box B: Area of 11 32μm spot LA-ICP-MS transects on MND-S1_6.
Box C: Area of 11 32μm spot LA-ICP-MS transects on MND-S1_7 .
6A, 6B, 6C, 6D, 6E, 6F, 7A, 7B and 7C are LA-ICP-MS tracks acquired using the 5x50 μm slit; dark area alongside these tracks is the condensation blanket created during LA-ICP-MS acquisition.
Shorter lines in the lower right corner of MND-S1_6 are $\delta^{18}O$ ion-microprobe tracks.